Oceanologia

Official Journal of the Polish Academy of Sciences

EDITOR-IN-CHIEF
Jacek Piskozub
Institute of Oceanology, Polish Academy of Sciences, Sopot, Poland

MANAGING EDITOR
Agata Bielecka — abielecka@iopan.pl

Editorial Office Address
Institute of Oceanology, Polish Academy of Sciences (IO PAN)
Powstańców Warszawy 55
81—712 Sopot, Poland
e-mail address: editor@iopan.pl

THEMATIC EDITORS

Katarzyna Błachowiak-Samołyk — Institute of Oceanology, Polish Academy of Sciences, Sopot, Poland

Artur Burzyński — Institute of Oceanology, Polish Academy of Sciences, Sopot, Poland

Piotr Kowalczuk — Institute of Oceanology, Polish Academy of Sciences, Sopot, Poland

Krzysztof Opaliński — Institute of Ecology and Bioethics, Warsaw, Poland

Żaneta Polkowska — Gdańsk University of Technology, Gdańsk, Poland

Krzysztof Rychert — Pomeranian University in Słupsk, Poland

Marek Zajączkowski — Institute of Oceanology, Polish Academy of Sciences, Sopot, Poland

ADVISORY BOARD

Xosé Antón Álvarez Salgado
Marine Research Institute, Spanish Research Council (CSIC), Vigo, Spain
Mirosław Darecki
Institute of Oceanology, Polish Academy of Sciences, Sopot, Poland
Jerzy Dera
Institute of Oceanology, Polish Academy of Sciences, Sopot, Poland
Jan Harff
University of Szczecin, Poland; Leibniz-Institute for Baltic Sea Research, Warnemünde, Germany
Agnieszka Herman
Institute of Oceanography, University of Gdańsk, Gdynia, Poland
Alicja Kosakowska
Institute of Oceanology, Polish Academy of Sciences, Sopot, Poland
Matti Leppäranta
Institute of Atmospheric and Earth Sciences, University of Helsinki, Finland
Ewa Łupikasza
Faculty of Earth Sciences, University of Silesia, Sosnowiec, Poland
Hanna Mazur-Marzec
Institute of Oceanography, University of Gdańsk, Gdynia, Poland
David McKee
University of Strathclyde, Glasgow, Scotland, United Kingdom
Dag Myrhaug
Norwegian University of Science and Technology (NTNU), Trondheim, Norway
Tarmo Soomere
Tallinn University of Technology, Estonia
Hans von Storch
Institute of Coastal Research, Helmholtz Center Geesthacht, Germany
Piotr Szefer
Department of Food Sciences, Medical University of Gdańsk, Poland
Muhammet Türkoğlu
Çanakkale Onsekiz Mart University, Turkey
Jan Marcin Węsławski
Institute of Oceanology, Polish Academy of Sciences, Sopot, Poland

---

This journal is supported by the Ministry of Science and Higher Education, Warsaw, Poland

Indexed in: ISI Journal Master List, Science Citation Index Expanded, Scopus, Current Contents, Zoological Record, Thomson Scientific SSCI, Aquatic Sciences and Fisheries Abstracts, DOAJ

IMPACT FACTOR ANNOUNCED FOR 2022 IN THE ‘JOURNAL CITATION REPORTS’ IS 2.9; 5-year IF is 2.8. CITESCORE ANNOUNCED FOR 2022 IS 4.3

Publisher
Elsevier B.V.
Radarweg 29
1043 NX Amsterdam
The Netherlands

Senior Publisher
Tobias Wesselius
+31 6 5370 3539

ISSN 0078-3234

Oceanologia 65 (2023) 517—533

Available online at www.sciencedirect.com

ScienceDirect

journal homepage: www.journals.elsevier.com/oceanologia

ORIGINAL RESEARCH ARTICLE

The influence of biochemical parameters on primary production in the Gulf of Gdańsk region: A model study

Maciej Janecki*, **Dawid Dybowski**, **Lidia Dzierzbicka-Głowacka**

Ecohydrodynamics Laboratory, Physical Oceanography Department, Institute of Oceanology, Polish Academy of Sciences, Sopot, Poland

Received 31 March 2023; accepted 23 May 2023
Available online 7 June 2023

KEYWORDS
Gulf of Gdańsk;
Biochemical parameters;
Primary production;
Phytoplankton;
Numerical modelling

Abstract Understanding the changing levels of biochemical parameters and the factors that influence them throughout the seasons is crucial for comprehending the dynamics of marine ecosystems. It also helps us identify potential threats that could harm their condition, aiding decision-making processes related to their protection. This study focuses on examining the variations in nutrients (such as nitrates, phosphates, and silicates), dissolved oxygen, and phytoplankton within the Gulf of Gdańsk. Additionally, we analyze the primary production process at three representative locations. To achieve this, we used data from the *EcoFish* biochemical numerical model. To ensure the model's accuracy, we compared its results with in situ data from the ICES database. The comparison revealed high correlations and minimal errors. Furthermore, we investigated how limiting factors impact primary phytoplankton production and demonstrated how the intensity of spring diatom blooms influences the nature of cyanobacterial blooms in the summer.

1. Introduction

Primary production in marine environments is associated with the process of photosynthesis, in which organisms such as phytoplankton (and other photosynthesizing organisms) use sunlight, water, and carbon dioxide to produce organic matter. Phytoplankton is a key component of the marine food web and plays an important role in shaping the ecosystem of the Gulf of Gdańsk (Verity and Smetacek, 1996). It serves as the primary source of food for many organisms, such as zooplankton (for example invertebrates) or small

---

* Corresponding author at: Ecohydrodynamics Laboratory, Physical Oceanography Department, Institute of Oceanology, Polish Academy of Sciences, Powstańców Warszawy 55, 81—712 Sopot, Poland. Tel.: (+48) 587-311-912.
E-mail addresses: mjanecki@iopan.pl (M. Janecki), ddybowski@iopan.pl (D. Dybowski), dzierzb@iopan.pl (L. Dzierzbicka-Głowacka).

Peer review under the responsibility of the Institute of Oceanology of the Polish Academy of Sciences.

Production and hosting by Elsevier

https://doi.org/10.1016/j.oceano.2023.05.001

fish, which then are consumed by larger fish, birds, and marine mammals. Various factors, including water temperature, nutrient availability, and sunlight, influence primary production in the Gulf of Gdańsk. Its location at the mouth of the Vistula River (and other smaller rivers), which provides nutrient-rich freshwater, makes it a particularly productive area (Tomczak et al., 2016).

The Baltic Sea is exposed to a range of natural processes and anthropogenic stressors (von Storch, 2023). These include climate change, rising sea levels, coastal processes, excessive nutrient loads resulting in eutrophication, hypoxia, acidification, agriculture, fisheries, organic pollution, sunken munitions, marine litter, underwater noise and tourism (Reckermann et al., 2022; Szymczycha et al., 2019).

During the latest socioecological assessment, the Baltic Sea achieved a Baltic Health Index (BHI) score of 76 out of 100, indicating that its overall condition is suboptimal and achieving management objectives and associated targets requires significant effort (Blenckner et al., 2021). Regionally, the Gulf of Gdańsk achieved the lowest BHI score of 55 among all regions considered, mainly due to a low assessment in relation to contaminants, carbon storage, and lasting special places. Therefore, continuous monitoring of the state of the Gulf of Gdańsk and appropriate management of human maritime activities is particularly important to minimize their negative impact on the condition of its waters.

The project *Knowledge transfer platform FindFISH* (short: *FindFISH*) (Dzierzbicka-Głowacka et al., 2018) is perfectly suited to the implementation of the aforementioned tasks (monitoring and management of human activities). The project aimed to develop a user-friendly platform to provide fishermen and scientists with accessible knowledge and information regarding the Gulf of Gdańsk's physical and biological state. As part of the project, a *Fish Module* was designed to generate maps indicating the best environmental conditions for specific commercially caught fish species in the Gulf of Gdańsk, such as herring, sprat, and flounder. This tool enables targeted fishing, reducing unintended catch and minimizing pollution caused by fishing expeditions, thus promoting environmental protection.

The heart of *FindFISH* is the 3D prognostic eco-hydrodynamic model *EcoFish*, developed within the project. The *EcoFish* model (www.findfish.pl) operates in real-time mode, creating 48-hour forecasts of hydrodynamic parameters (water temperature, salinity, sea currents, sea surface height) and biochemical parameters (nitrate, phosphate, silicate, chlorophyll *a*, phytoplankton and microzooplankton biomass, dissolved oxygen and dissolved organic carbon concentration).

The hydrodynamic part of the *EcoFish* model was described in separate papers (Janecki et al., 2021, 2022), along with the analysis of the variability of the physical parameters, confirming a very good agreement between the model results and environmental data. In this work, we focus on the biochemical part of the *EcoFish* model. The following chapters present the results for the biochemical parameters, their variability, and a comparison with *in situ* data from the ICES database.

One of the three groups of phytoplankton implemented in the *EcoFish* model is cyanobacteria. Cyanobacteria are prokaryotes but have historically been grouped with eukaryotic "algae" and at varying times have been referred to as "blue-greens" or "blue-green algae" (Carmichael, 2008; O'Neil et al., 2012). This name does not reflect any relationship between cyanobacteria and other organisms called algae. Cyanobacteria are a distinct group of bacteria that perform oxygenic photosynthesis, and it is only the chloroplast in eukaryotic algae to which the cyanobacteria are related (Sato, 2021).

Although we are aware of the updated classification of cyanobacteria, for the purposes of our study, we have chosen to treat cyanobacteria as a component of phytoplankton as it was traditionally understood. This decision is motivated by the need to maintain consistency with previous studies and the existing literature, ensuring comparability and facilitating model-based analyses. By acknowledging the revised systematic position of cyanobacteria while using the term "phytoplankton" within the scope of our research, we aim to strike a balance between the historical perspective and the contemporary scientific understanding.

The purpose of the paper is not only to prove, that the *EcoFish* model provides reliable results on biochemical variables for the Gulf of Gdańsk. By analyzing the variability of nutrients (nitrates, phosphates and silicates), dissolved oxygen and phytoplankton in the Gulf of Gdańsk, we wanted to describe their impact on the pattern and intensity of the primary production. The rich nutrient deposition from rivers can significantly alter the biomass distribution of all phytoplankton groups.

The analysis of the seasonal variability dynamics of the primary production process is extremely important in the context of the conducted research, as it is a process directly related to the production and consumption of oxygen in the waters of the Gulf of Gdańsk. Dissolved oxygen concentration is one of the four parameters (along with temperature, salinity, and depth) that constitute an input variable crucial for the *Fish Module*.

2. Material and methods

2.1. Study area

The *EcoFish* model domain encompasses an enlarged area of the Gulf of Gdańsk (Figure 1). It is one of the most important coastal areas in the southern part of the Baltic Sea, with unique oceanographic and hydrological conditions. The western part of the Gulf of Gdańsk can be divided into a shallow part called the Puck Bay, and further west into the semiclosed Puck Lagoon (Majewski, 1972). The Vistula, which is the largest river flowing into the gulf and carrying nutrients and other substances originating from industry and other human activities, has a significant impact on the hydrology of the Gulf of Gdańsk (Voss et al., 2005; Witek et al., 1997). The Gulf of Gdańsk also contains the largest Polish ports, such as Gdańsk and Gdynia, which have a significant impact on its environment due to pollution, maritime transport, and fishing (HELCOM, 2010).

2.2. *In situ* data

To verify whether the *EcoFish* model accurately reproduces the variability of biochemical parameters in the Gulf of

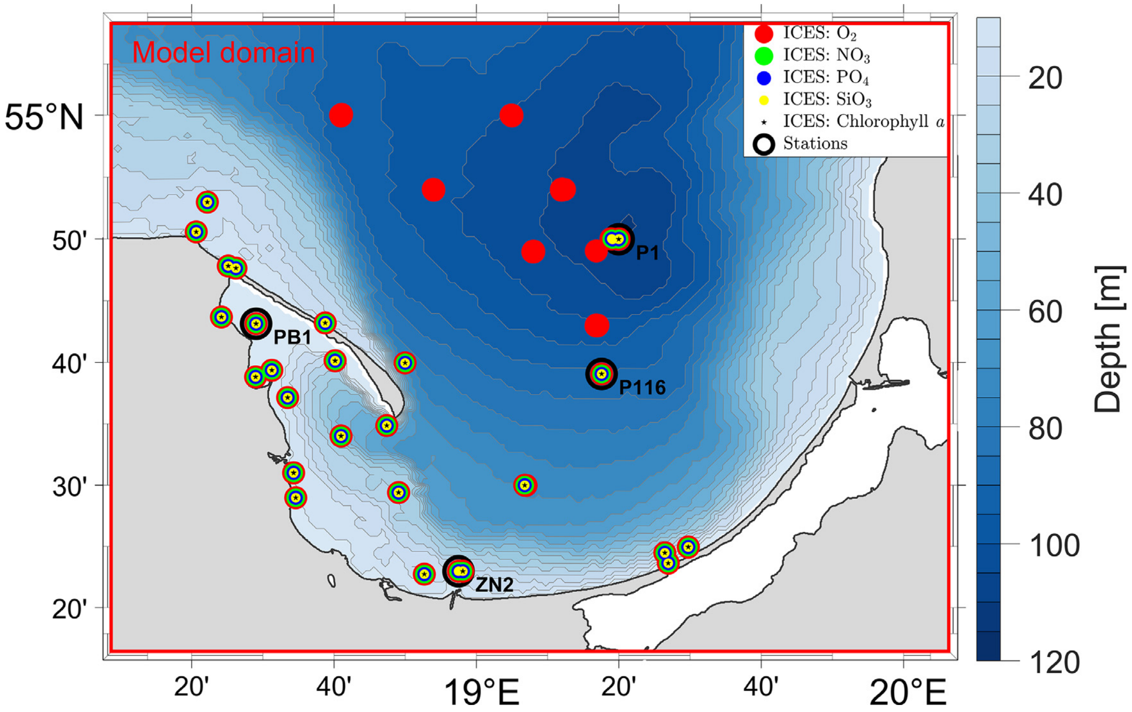

Figure 1 The *EcoFish* model domain with bathymetry, the location of environmental data from the ICES database, and the stations where primary production was investigated.

Gdańsk, the International Council for the Exploration of the Sea[1] (ICES) database was used. The ICES database for the years 2017—2020 contained 3329 measurements of oxygen (O_2), 2370 measurements of nitrate (NO_3), 2592 measurements of phosphate (PO_4), 2610 measurements of silicate (SiO_3), and 972 measurements of chlorophyll *a*. Most of the data originated from the shallow waters in the Puck Bay area and the southern part of the Gulf of Gdańsk. Only a small fraction (mainly for oxygen concentration) was located at greater depths in the open sea (Figure 1).

2.3. The *EcoFish* model

2.3.1. Configuration

The *EcoFish* model is a three-dimensional, numerical prognostic model of the Gulf of Gdańsk ecosystem with a horizontal resolution of 575 m, which was developed as part of the *FindFISH* project. The model is divided into 26 vertical levels, each with a thickness of 5 m. The *EcoFish* model consists of:

- Hydrodynamic component — this is an ocean model based on the Parallel Ocean Program (POP) code, which has been described and validated (for water temperature and salinity) in a separate article (Janecki et al., 2021);
- Biochemical component — this is an NPZD-type biochemical model, which is described and validated in this paper;
- *Fish Module* — this is an additional element created within the *FindFISH* project, which, based on data from the hydrodynamic and biochemical components, allows for the creation of maps of optimal environmental conditions for the habitat of fish (sprat, herring, and flounder) commercially caught in the Gulf of Gdańsk region.

In addition to the three main components in which simulations are conducted, the *EcoFish* model includes dedicated modules for processing input and output data, data assimilation modules (for surface temperature and chlorophyll *a*), and a module coordinating the model in the operational mode. Its task is to control the components, handle errors, and transmit data between modules.

2.3.2. Water — water border

The *EcoFish* model domain is connected with the Baltic Sea from the north and northwest, which creates the need to provide the model with boundary conditions (open boundary). These forcings are transmitted to the *EcoFish* model using the results from the *3D CEMBS* model with a horizontal resolution of 2 km (Dzierzbicka-Głowacka et al., 2013a,b).

2.3.3. Atmosphere forcing

At the water-atmosphere boundary, the *EcoFish* model is driven by meteorological forcing. These forcings are derived from the UM (Unified Model)[2], developed at the Interdisciplinary Centre for Mathematical and Computational Modelling of the University of Warsaw (ICM UW). Some of the obtained parameters (wind speed, air temperature, specific humidity, atmospheric pressure, precipitation, radiation) are directly used as forcings after interpolation onto the *EcoFish* model grid. The missing parameters are calcu-

---

[1] https://data.ices.dk.

[2] www.meteo.pl.

Table 1 Rivers mouths' locations included within the *EcoFish* model domain and mean runoff.

	Source	River name	Longitude	Latitude	Mean runoff [$m^3 s^{-1}$]
1	HYPE	Vistula	18.95	54.35	1064
2	HYPE	Bold Vistula	18.78	54.37	2.05
3	HYPE	Still Vistula	18.66	54.41	6.06
4	HYPE	Oliwski Stream	18.60	54.42	0.31
5	HYPE	Kamienny Stream	18.56	54.46	0.45
6	HYPE	Kacza	18.56	54.48	0.29
7	HYPE	Sewage Canal	18.51	54.61	0.21
8	SWAT	Zagórska Stream	18.47	54.63	0.11
9	SWAT	Reda	18.47	54.64	0.48
10	SWAT	Mrzezino Canal	18.46	54.66	0.20
11	SWAT	Gizdepka	18.46	54.66	0.30
12	SWAT	Żelistrzewo Canal	18.45	54.70	0.17
13	SWAT	Płutnica	18.39	54.72	0.91

lated by the atmospheric data module, which is an integral part of the *EcoFish* model.

2.3.4. Land-water linkage

In the *EcoFish* model, 13 rivers that flow into the Gulf of Gdańsk are taken into account (Table 1). Information about the volume of freshwater (runoff) and nutrients deposition for six rivers whose mouths are located in the area of the Puck Commune comes from the SWAT model (Kalinowska et al., 2020, 2018; Wielgat et al., 2021). SWAT was developed as part of the *Integrated Information-Predictive Service WaterPUCK* project (Dybowski et al., 2019; Dzierzbicka-Głowacka et al., 2019, 2022). The remaining seven rivers use runoff data from the Hydrological Predictions for the Environment (HYPE) model (Arheimer et al., 2012; Donnelly et al., 2016). Data on the amount of nutrient deposition in the HYPE model were available only in the form of monthly averages for the period 1980—2010. As a result of the HELCOM directives, the actual amounts of these substances entering the Baltic Sea from the territory of the Republic of Poland have been significantly reduced over the past 30 years (Pastuszak et al., 2018). The use of 30—year averages would lead to overestimation and distortion of the actual flow. Therefore, nutrient deposition for HYPE rivers was set based on the work of Pastuszak et al. (2018). Nitrate concentrations were established at 0.9 mg dm^{-3}, ammonia at 0.07 mg dm^{-3}, phosphate at 0.07 mg dm^{-3}, and silicate at 1.1 mg dm^{-3}. Concentrations were linked to daily volumes of freshwater introduced by these rivers, obtaining a satisfactory estimate of deposition (Dybowski et al., 2020).

2.3.5. NPZD-type biochemical model

The implementation of environmental variables in the *EcoFish* model was carried out by determining the source and sink functions for four types of nutrients (phosphates — PO_4, nitrates — NO_3, ammonia — NH_4, and silicates — SiO_3), three groups of phytoplankton and microzooplankton. There are two things that the general equation of turbulent diffusion with an advection component does in the *EcoFish* model (Equation (1)). First, it describes the dynamics of changes in concentrations. Second, it serves as the link where the transfer of forcings between the hydrodynamic and biochemical components takes place.

$$\frac{\partial S}{\partial t} + (V + w_s) \cdot \nabla S = \frac{\partial}{\partial z}\left(K_z \frac{\partial S}{\partial z}\right) + \sum_{i-1}^{2} \frac{\partial}{\partial x_i}\left(K_{x_i} \frac{\partial S}{\partial x_i}\right) + F_s \quad (1)$$

where S is each model variable, V (u, v, w) is the velocity vector, w_S is the sinking velocity of pelagic detritus, K_z, K_{xi}, are vertical and horizontal turbulent diffusion coefficients and F_S is the biogeochemical source-sink term which describes possible sources and losses of the diffusing substance in the space being studied.

The source code of the biochemical part was filled with interrelated dependencies describing the variability of the primary production of phytoplankton biomass, as well as the concentration of chlorophyll *a*, microzooplankton biomass, nutrients concentrations (phosphates, nitrates, ammonia and silicates), dissolved oxygen, pelagic and benthic detritus (for NO_3 and PO_4). Source and sink functions were determined based on knowledge of the biological and chemical processes that occur in the marine environment and their mutual relationships (Dzierzbicka-Głowacka et al., 2013b; Moore et al., 2001).

The biochemical component of the *EcoFish* model requires information about the state and physical conditions of the ecosystem it represents. Therefore, it depends on the hydrodynamic component and operates in the same domain (Figure 1).

3. Results

In the following chapters, we present monthly average concentrations of dissolved oxygen (O_2), nitrate (NO_3), phosphate (PO_4), silicate (SiO_3), and phytoplankton (as chlorophyll *a*) for a four-year period from January 1, 2017 to December 31, 2020.

Furthermore, each biochemical variable was validated by comparing it with the available measurements from the ICES database (Figure 1). Basic statistical measures were deter-

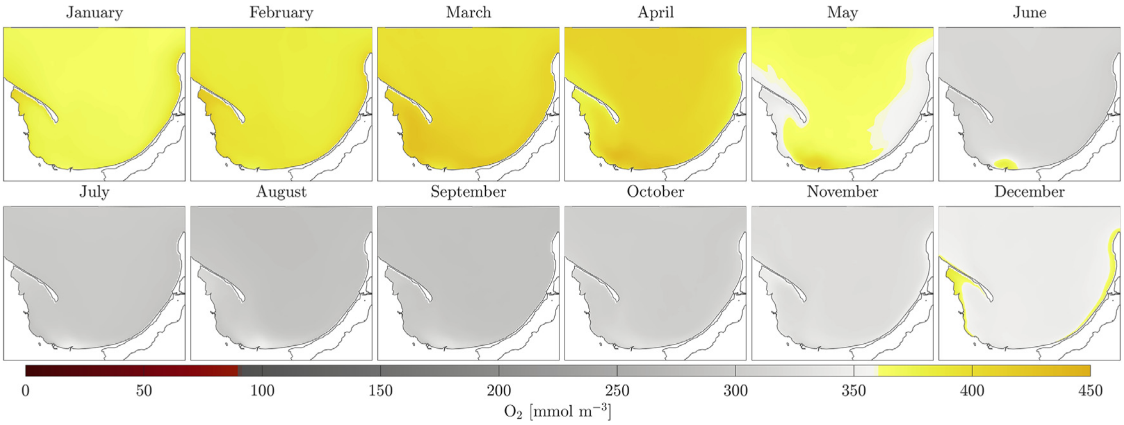

Figure 2 Average monthly concentrations of dissolved oxygen (O_2) in the surface layer for the period 2017—2020.

mined: means, standard deviations (STD), Pearson's correlation coefficients (r) and root mean square errors (RMSE).

In the *EcoFish* model, all depth levels have a thickness of 5 meters. However, the ICES data had non-uniform sampling density in the water column (e.g., 0 m, 1 m, 2.5 m, 4 m, 5 m, 10 m, 20 m). This resulted in several ICES measurements that differed from each other but corresponded to the same EcoFish model value, or an ICES measurement was taken from a depth at the boundary of two adjacent model levels. This could cause unnatural distortion of the validation results. To eliminate the negative impact of the non-uniform data density, interpolation (and extrapolation) between *EcoFish* model levels with a step of 0.1 m was applied. Among the available methods of interpolation and extrapolation, the third-order simplified Hermite polynomial method (PCHIP) was chosen, which interpolates both the function and its first derivative.

3.1. Dissolved oxygen — O_2

Seasonal changes in water oxygenation are influenced by both climatic factors and primary production. Maximum concentrations of dissolved oxygen occur in the winter-spring season, with the combination of low water temperature and the beginning of the phytoplankton bloom period (Figure 2). The maximum monthly average concentration of dissolved oxygen in the surface layer of the *EcoFish* model (calculated for the entire domain area) occurred in March and April, and was 398.79 mmol m^{-3} and 401.03 mmol m^{-3}, respectively. In the following months, as the temperature increases, the solubility decreases, and so the oxygen concentration in the water drops. However, there are areas where an increase in dissolved oxygen is noticeable as a result of intensive primary production. The minimum concentration of dissolved oxygen in the surface layer occurred in August with a mean value of 269.50 mmol m^{-3}. The average annual concentration of dissolved oxygen in the surface layer was 344.07 mmol m^{-3} with a standard deviation of 40.33 mmol m^{-3}.

When examining the vertical profiles of mean monthly oxygen concentrations (Figure 3) at station P1 situated in the Gdańsk Deep area (Figure 1), it becomes apparent that there is a distinct variation as depth increases. In all months except summer months (May, June, July, and August), the oxygen concentration remains constant (homogeneous) until a depth of approximately 40—50 meters. Then it begins to drop with increasing depth until it stabilizes at a depth of about 90 meters. In the winter months, this stable concentration at the greatest depths is higher (up to approximately 250 mmol m^{-3} in February). This is due to stronger vertical mixing, pushing the cold, oxygenated water from the surface to greater depths. In the summer, such strong vertical mixing does not occur, and the average oxygen concentration at greater depths drops to 150 mmol m^{-3} and below.

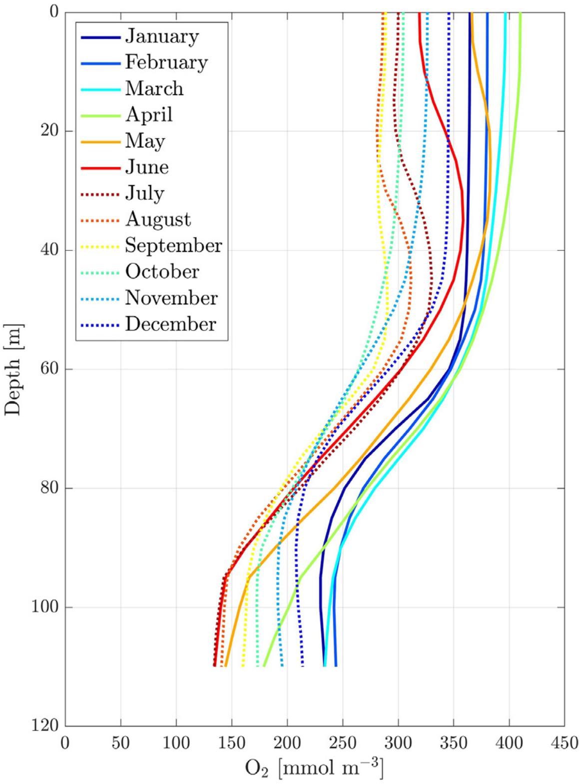

Figure 3 Vertical profiles of the mean monthly dissolved oxygen concentrations (O_2) for the period 2017—2020.

The concentration of dissolved oxygen is the most important modeled variable that needed to be verified for accu-

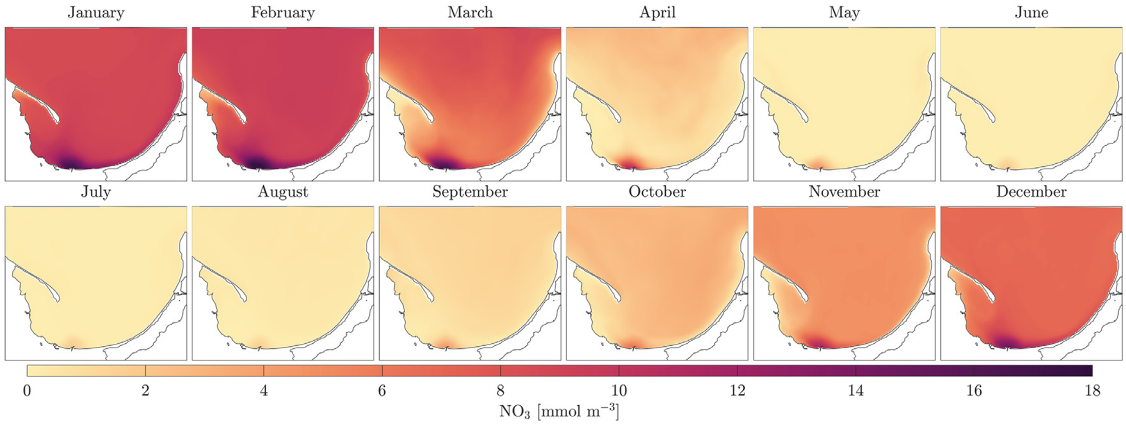

Figure 4 Average monthly concentrations of nitrates (NO_3) in the surface layer for the period 2017—2020.

racy. This is because it is used as an input parameter for the *Fish Module*. In the ICES database for the years 2017—2020, there were 3329 measurements available within the *EcoFish* model domain. After comparing ICES measurements with their corresponding values from the *EcoFish* model, a good reproduction of oxygen concentration variability was obtained for high O_2 concentrations. However, for measurements from great depths with concentrations dropping below 200 mmol m^{-3} the *EcoFish* model tended to slightly overestimate the results. The validation results for oxygen are presented in Table S1. Pearson's correlation coefficients ranged from 0.70 to 0.80 and RMSE from 61.14 to 86.85 mmol m^{-3}. For the entire period 2017—2020, a Pearson correlation coefficient of 0.75 and a root mean square error of 70.86 mmol m^{-3} were obtained.

3.2. Nitrates — NO_3

The highest concentrations of nitrates in the *EcoFish* model were observed in winter and early spring, before the start of the growing season. The lowest concentrations were observed in the summer months (Figure 4). The highest average monthly concentration of nitrates in the surface layer of the *EcoFish* model (calculated for the entire domain area) occurred in February (8.66 mmol m^{-3}), and the lowest in June (0.03 mmol m^{-3}).

By examining the vertical profiles of the nitrate concentrations at station P1 (Figure 5), we can observe that the highest amounts of this compound (concentrations greater than 9 mmol m^{-3}) accumulate at depths from 60 meters to the seabed. Nitrates are also present closer to the surface, but there is a clear seasonal variability associated with the intensity of primary production and phytoplankton blooms. Nitrates in the euphotic zone begin to decline in the spring due to diatom blooms, and subsequently decrease until July, when they are completely depleted in the layer to about 20 meters. In September, slow extraction of nitrates from deeper layers to the surface occurs because of fall storms, causing an increase in their concentrations. In October, due to low primary production, nitrate concentrations in the surface layer can reach values greater than 3 mmol m^{-3}. In the following months, nitrate concentrations on the surface gradually increase, reaching their maximum of around 9 mmol m^{-3} in January and February.

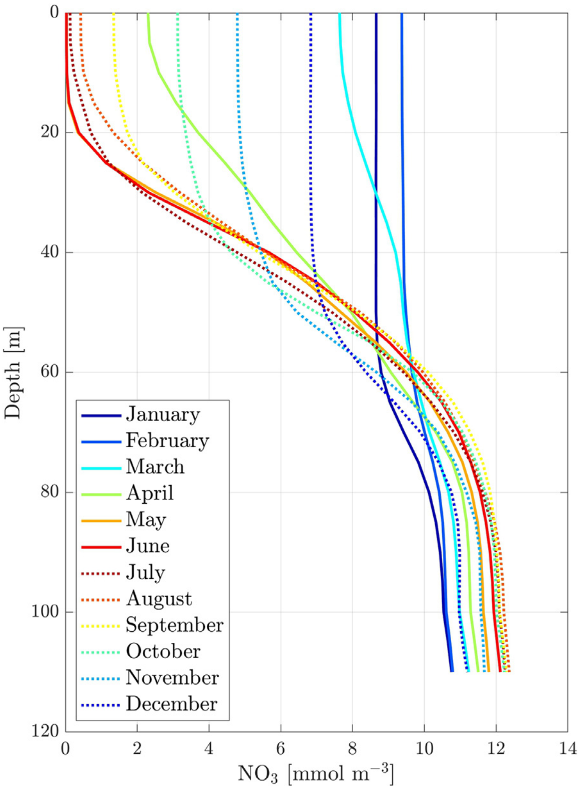

Figure 5 Vertical profiles of mean monthly concentrations of nitrates (NO_3) for the period 2017—2020.

In the ICES database for the years 2017—2020, there were 2370 nitrate concentration measurements available. After comparing the ICES measurements with their corresponding values from the *EcoFish* model, a moderately good representation of the dynamics of nitrate concentrations was obtained. This is because the ICES measurements came mainly from locations that are under strong pressure from the land, in the form of nutrient deposition from rivers flowing into the Puck Bay and Gulf of Gdańsk. The results of the nitrate validation are presented in Table S2. Pearson's correlation coefficients ranged from 0.40 to 0.59 and the root mean square errors ranged from 3.28 to 4.02 mmol m^{-3}. For the entire period 2017—2020, a Pearson correlation coefficient

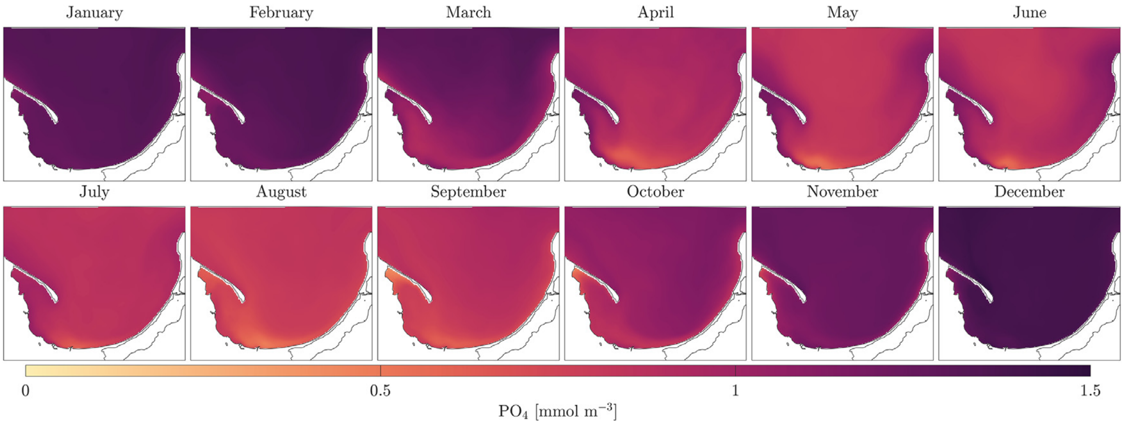

Figure 6 Average monthly concentrations of phosphates (PO_4) in the surface layer for the period 2017—2020.

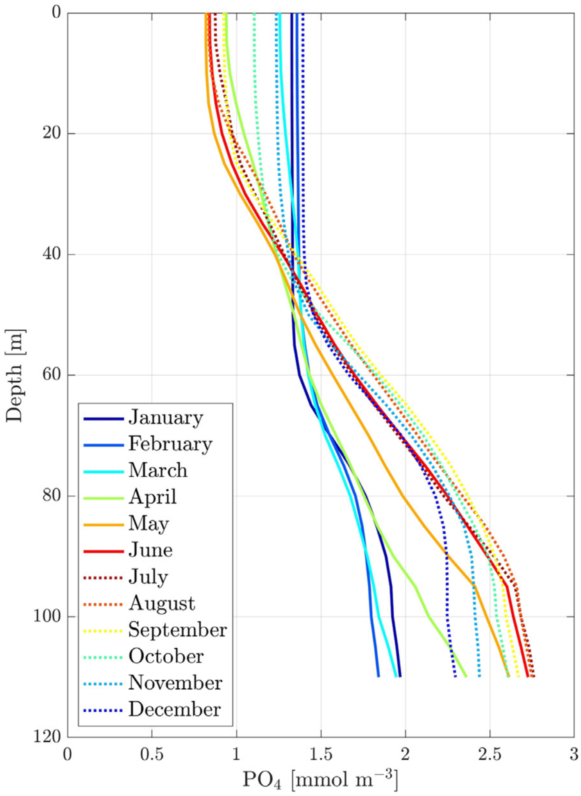

Figure 7 Vertical profiles of mean monthly concentrations of phosphates (PO_4) for the period 2017—2020.

of 0.46 and a mean squared error of 3.77 mmol m^{-3} were obtained.

3.3. Phosphates — PO_4

The highest average monthly concentration of phosphates in the surface layer of the *EcoFish* model (calculated for the entire domain area) occurred in December (1.34 mmol m^{-3}), while the lowest occurred in August (0.89 mmol m^{-3}) (Figure 6).

The vertical profiles of the monthly mean concentrations of phosphates at station P1 (Figure 7) have a similar character to that of nitrates. The largest amounts of this compound (concentrations of about 2 mmol m^{-3} and higher) also lie at great depths (below 60 meters). Variations in this parameter in the euphotic zone are related to primary production and the vegetative cycle of phytoplankton. Phosphorus is a limiting factor for the growth of all groups of phytoplankton, which means that it is consumed more or less intensively throughout the year.

The decrease in phosphate concentrations in the euphotic zone begins in March with the beginning of diatom blooms and lasts until August, when the highest intensity of primary production associated with cyanobacterial blooms occurs (caused by the highest water temperatures in the surface layer). From September, phosphate concentrations begin to systematically increase (as water temperature drops) until December, when they reach their maximum value for the whole year (approximately 1.4 mmol m^{-3}).

In the bottom layer, the situation is reversed. The highest concentrations occur in summer due to the settling of dead organic matter. There, as a result of the mineralization process, phosphorus is released back into the water column by microorganisms, leading to elevated concentrations. In winter months, because of vertical mixing, phosphate deposits are transported to the surface, replenishing the resources used after the vegetative period of phytoplankton.

In the ICES database for the years 2017—2020, there were 2592 phosphate concentration measurements available. After comparing the ICES measurements with the corresponding values from the *EcoFish* model, we observed that the model systematically overestimates phosphate concentrations. Despite this, high correlations were obtained in individual years, as well as acceptable RMSEs. The results of the phosphate validation are presented in Table S3. Pearson's correlation coefficients were in the range of 0.66 to 0.77, and the root mean squared errors ranged from 0.37 to 0.75 mmol m^{-3}. For the entire comparison period (2017—2020), we obtained a Pearson correlation coefficient of 0.65 and a root mean square error of 0.63 mmol m^{-3}.

3.4. Silicates — SiO_3

Nitrogen and phosphorus are the main factors that limit biological production, however, the primary production of diatoms is also limited by silicates. The *EcoFish* model shows

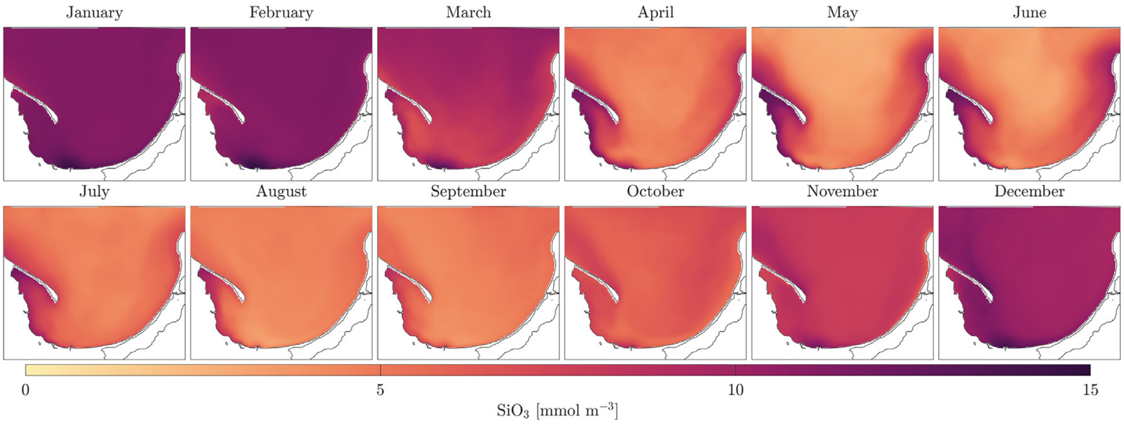

Figure 8 Average monthly concentrations of silicates (SiO_3) in the surface layer for the period 2017—2020.

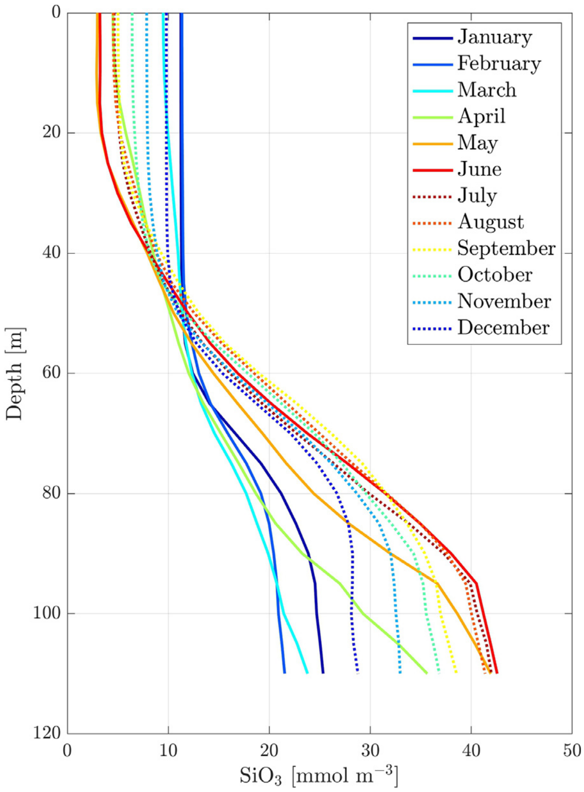

Figure 9 Vertical profiles of mean monthly concentrations of silicates (SiO_3) for the period 2017—2020.

the highest concentrations of silicates in winter and early spring, before the start of the growing season (Figure 8). In March, when intense spring diatom blooms begin, silicate concentrations begin to decrease and remain at lower levels until autumn. The highest average monthly concentrations of silicates in the surface layer occurred in February (10.69 mmol m^{-3}) and January (10.67 mmol m^{-3}), while the lowest occurred in May (6.49 mmol m^{-3}).

Analysis of vertical profiles of mean monthly silicate concentrations at station P1 reveals large differences between values at depths below 80 meters (Figure 9). Silicate concentrations from May to August are up to twice as high as concentrations in winter months (from December to March). In the layer between 40 and 60 meters, silicates remain at similar levels (usually between 10 and 15 mmol m^{-3}) regardless of the month analyzed. In the euphotic layer, there is an inverse relationship compared to the bottom. Silicate concentrations are higher in the winter months, outside of the phytoplankton growing season. Lower values are observed from spring to fall and are closely related to their consumption in the primary production process to increase the biomass of diatoms.

In the ICES database for the years 2017—2020, there were 2610 silicate concentration measurements available. A comparison of *in situ* data from the ICES database with the corresponding values from the *EcoFish* model confirmed that the model performs well in reproducing the dynamics of silicate concentrations, although there is a noticeable tendency to underestimate the results, mainly for high SiO_3 concentrations above 40 mmol m^{-3}. The results of the silicate validation are presented in Table S4. Pearson correlation coefficients ranged from 0.51 to 0.74, and root mean square errors ranged from 7.45 to 12.58 mmol m^{-3}. For the entire comparison period (2017—2020), we obtained a Pearson correlation coefficient of 0.62 and a root mean square error of 10.32 mmol m^{-3}.

3.5. Chlorophyll *a*

In the *EcoFish* model, phytoplankton is divided into three groups. The first group represents nano- and pico-sized phytoplankton, whose growth is limited by nitrogen, phosphorus, temperature, and light. The second group represents large phytoplankton, mainly diatoms, whose production is limited by the same factors plus silica. The third group is cyanobacteria, which have the ability to fix nitrogen directly from the atmosphere and whose production is limited only by phosphorus, light, and temperature.

The highest concentrations of chlorophyll *a* are observed relatively close to the shore, where the access to nutrients is greatest due to the deposition of biogenic substances carried by rivers. The highest modeled monthly mean chlorophyll *a* concentration for the period 2017—2020 in the surface layer occurred in April and was 3.91 mg m^{-3} (Figure 10). The lowest concentrations were observed in the winter months, with a minimum of 0.29 mg m^{-3} (in December).

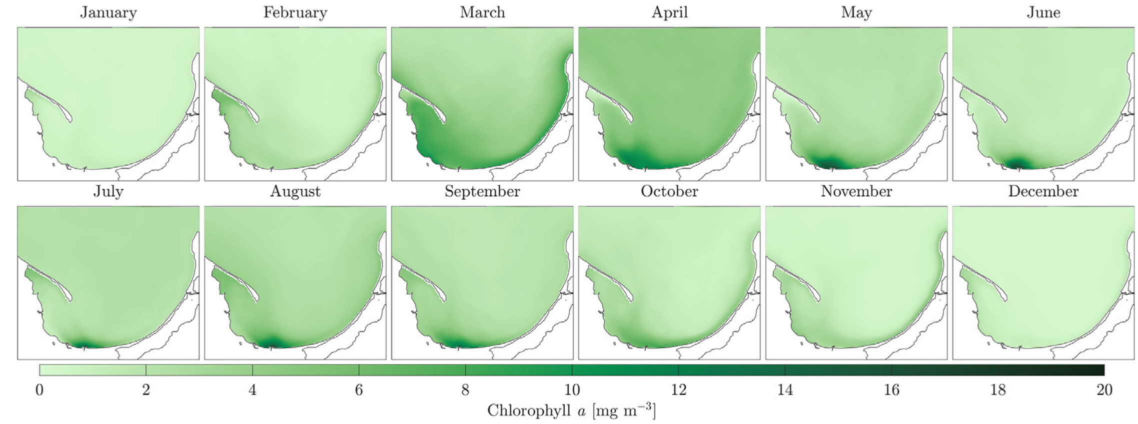

Figure 10 Average monthly concentrations of chlorophyll *a* in the surface layer for the period 2017—2020.

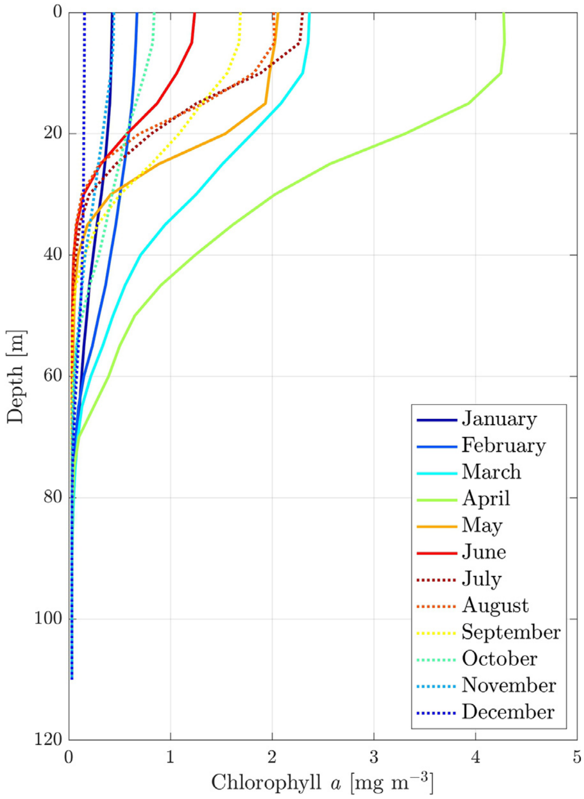

Figure 11 Vertical profiles of mean monthly concentrations of chlorophyll *a* for the period 2017—2020.

In vertical distribution, chlorophyll *a* concentrations reach their highest values in the upper layer of the water column. Then the concentration values decrease with depth. Below 60 meters deep, chlorophyll *a* occurs in negligible amounts or is not detected at all (Figure 11).

The highest chlorophyll *a* concentration values occur in spring (in April and March) when there is a maximum in phytoplankton biomass due to the spring diatom bloom and in July due to the growth of cyanobacteria. In months with primary production, concentrations rapidly decrease with depth. This is particularly visible in summer. There are no longer nitrates in the euphotic zone, and cyanobacteria grow only in the surface layer, where they are in direct contact with nitrogen fixed from the atmosphere.

In the ICES database for the years 2017—2020, only 972 chlorophyll *a* concentration measurements were available. Most of the measurements were taken in the area of Puck Bay and the southern part of the Gulf of Gdańsk, close to the coast (Figure 1). After comparing the ICES measurements with the corresponding values from the *EcoFish* model, we obtained a moderately good representation of the chlorophyll *a* variability. The results of the chlorophyll *a* validation are presented in Table S5. Pearson's correlation coefficients ranged from 0.50 to 0.63, and root mean square errors ranged from 1.77 to 3.63 mg m^{-3}. For the entire comparison period (2017—2020), we obtained a Pearson correlation coefficient of 0.50 and a root mean square error of 2.77 mg m^{-3}.

3.6. Primary production

An important aspect studied in this article is primary production, which is a key function of marine ecosystems. Primary production is a process in which photosynthetic organisms, such as phytoplankton, use solar energy to produce organic compounds. In this way, primary production forms the basis for the entire marine food chain, providing energy and organic compounds for zooplankton and other marine organisms. Studying the seasonal variability of primary production in the Gulf of Gdańsk is important to understand the impact of climate change and other factors on marine ecosystems and their ability to adapt to changing conditions.

Primary production in the water column was calculated for each of the modeled phytoplankton groups at three selected locations (Figure 1).

- PB1 — (54°43'N, 18°29'E) — the inner part of the Puck Bay, depth of about 10 m,
- ZN2 — (54°22'N, 18°57'E) — the mouth of the Vistula River, depth of about 20 m,
- P116 — (54°39'N, 19°17'E) — the central part of the Gulf of Gdańsk, depth of about 90 m.

The location PB1 comes from a very shallow area (inner part of Puck Bay), which is geographically limited from the northeast by the Hel Peninsula and from the east by the Rybitwia Mielizna, effectively preventing the mixing of water from Puck Bay with both the open Baltic Sea and the

Outer Puck Bay. Six rivers flow into the inner part of Puck Bay (Zagórska Stream, Reda, Mrzezino Canal, Gizdepka, Żelistrzewo Canal and Płutnica), causing the PB1 station to be regularly supplied with moderate amounts of nutrients.

The ZN2 station is located in the shallow coastal part of the Gulf of Gdańsk, close to the mouth of the Vistula River. The Vistula is the largest river in the region and carries more than 1000 m^3 s^{-1} of freshwater on average, along with huge amounts of nutrients, strongly affecting the primary production of phytoplankton at this location.

The P116 station, with a depth of approximately 90 meters, is located in the open waters of the central part of the Gulf of Gdańsk. It is located far from the river mouths and is not geographically constrained by any factors.

The rate of primary production in the chosen locations was determined from the *EcoFish* model for a one-year period, from January 1 to December 31, 2021. Production values were calculated for the entire water column and compared with the limiting functions. The temperature of the water, the availability of light and the phosphates are limiting factors for the growth of all phytoplankton groups implemented in the *EcoFish* model. The growth of the group representing nano- and pico-sized phytoplankton is additionally limited by the availability of nitrates, while the growth of diatoms is additionally limited by the availability of nitrates and silicates.

The beginning of phytoplankton bloom in the first weeks of the year is primarily dependent on the amount of light available. At station PB1, the annual cycle of primary production begins in mid-February with a low intensity (up to 1000 mg C m^{-2} d^{-1}) and a short-lived diatom bloom, which ends in the first days of March (Figure 12a). This is due to the shallow depth at this location. All available nitrogen in the water column is rapidly depleted and reaches zero values at the end of February (Figure 12d). As a result of such a short diatom bloom period, a very small amount of phosphate is consumed. It remains in the water column in large amounts until mid-June, when a bloom of cyanobacteria begins due to the appropriately high water temperature (Figure 12b). Due to favorable conditions (available light, high water temperature, and a large amount of phosphates), this process is very intense (more than 2000 mg C m^{-2} d^{-1}) and lasts until mid-September, when it is stopped due to decreasing water temperature and replaced by a bloom of small phytoplankton (Figure 12c). The cycle of primary production at this station in 2021 slows down in the first days of November, which is due to a low amount of available light and a drop in the water temperature. The period of unfavorable conditions for phytoplankton bloom, which lasts until next spring, allows the replenishment of the nutrient fields (Figure 12d).

In the P116 station, the annual cycle of primary production (similar to the PB1 station) begins in mid-February. It is initiated by the appearance of appropriately strong light and favorable water temperature (Figure 13a). However, unlike station PB1, this bloom does not end in the first half of March due to the depletion of available nitrate. Station P116 is located at a great depth in the central part of the Gulf of Gdańsk. Because of the vertical mixing, nitrates are carried from greater depths toward the surface, sustaining the bloom of diatoms until mid-April. Then, the nitrate resources are depleted (Figure 13d), leading to a slowdown in production (around 200 to 300 mg C m^{-2} d^{-1}), but not enough to completely stop it (Figure 13a). Diatoms remain in the water column at a level of around 10—20 mmol C m^{-3} until the first days of July. In mid-July, a cyanobacterial bloom begins (Figure 13b). This is a month later than at the PB1 station (Figure 12b), which is a consequence of the lower water temperature in the open water. The shallow, enclosed coastal zone where station PB1 is located heats up much faster than the deep waters of the central part of the Gulf of Gdańsk. However, cyanobacterial production is not as intense as at station PB1. In addition to the lower water temperature, the decisive factor here may be a smaller amount of available phosphate (Figure 13d), which was partially consumed during the diatom bloom that began in mid-February. In 2021, small phytoplankton practically does not occur at this station (Figure 13c), which is also related to lower levels of phosphate in summer compared to the PB1 station and competition for access to nitrogen and phosphorus with diatoms.

At the ZN2 station located at the mouth of the Vistula River, the diatom bloom begins in a period similar to that of the other stations, i.e., in mid-February (Figure 14a). The highest intensity of diatom primary production occurs here in May and June, reaching rates of up to 4000 mg C m^{-2} d^{-1}. In July 2021, diatom production is slowed and a very intense bloom of small phytoplankton begins, which lasts until the end of October, with peak production in August.

However, the cyanobacteria bloom has a completely different pattern than at the other stations. The station is located in a shallow coastal area, which means that the water temperature is high enough for the cyanobacterial blooms to start in mid-May (Figure 14b). However, cyanobacteria do not appear until the end of July, competing for phosphate with small phytoplankton (Figure 14c) that grow at the same time. This leads to a very low primary production rate associated with this species (below 1000 mg C m^{-2} d^{-1}) causing suppression of cyanobacterial blooms. The production of cyanobacteria ends in October because the water temperature is too low.

It should be noted that station ZN2 is located at the mouth of the Vistula River. Nitrates and silicates do not deplete here after spring diatom bloom and are available throughout the year (Figure 14d). This is related to the massive deposition of nutrients from the Vistula.

4. Discussion

4.1. The *EcoFish* model evaluation

The article presents the biochemical component of the three-dimensional numerical model *EcoFish*, which was used to analyze the basic biochemical parameters that characterize the dynamics of the Gulf of Gdańsk ecosystem. To increase the accuracy of the results obtained in the *EcoFish* model, a module was implemented to assimilate satellite data for SST and chlorophyll *a*. The source of these data is the *SatBałtyk*[3] system (Woźniak et al. 2011a,b).

Statistical validation of the *EcoFish* model, allowed us to verify the accuracy of the results in terms of the spatiotemporal variability of nitrate, phosphate, silicate, dis-

---

[3] www.satbaltyk.pl.

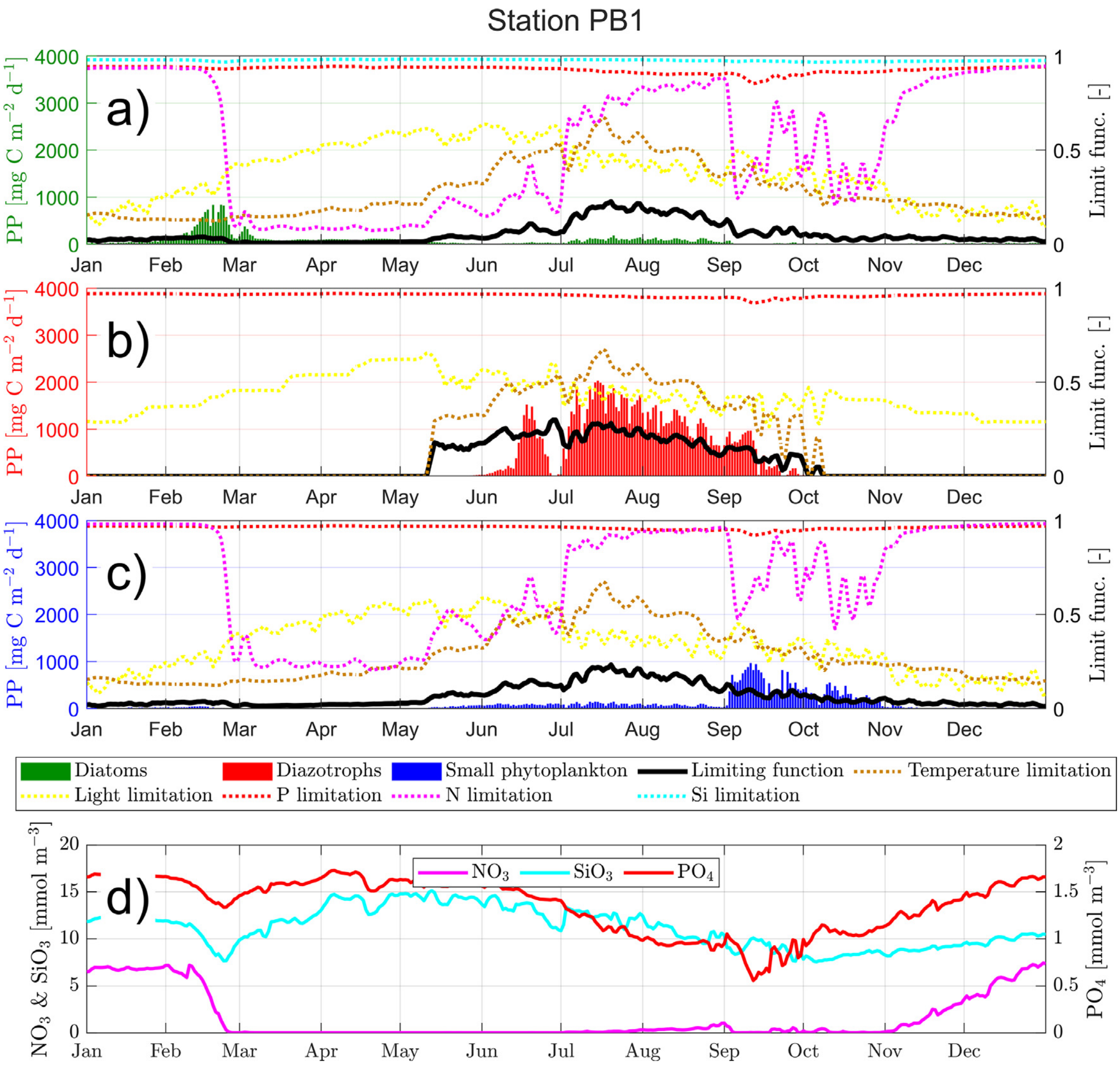

Figure 12 Primary production rate in 2021 for the entire water column at PB1 station for a) diatoms, b) cyanobacteria, and c) small phytoplankton, compiled with limiting factors, and d) concentrations of nutrients.

solved oxygen, and chlorophyll *a* concentrations. Validation was carried out using available *in situ* data from the ICES database for the period from January 1, 2017 to December 31, 2020, and basic statistical quantities were determined.

The *EcoFish* model tends to systematically overestimate (for oxygen, nitrates, and phosphates) and underestimate (for chlorophyll *a* and silicates) the results. However, these values are not significantly different from the measurement data and are acceptable after careful examination of the causes. The main reason for the lower correlations, especially in the validation of chlorophyll *a* and nitrates, is the specificity of the ICES experimental database itself. The map with the distribution of measurements for individual variables (Figure 1) shows that the vast majority of measurements come from shallow coastal areas with depths that generally do not exceed 30 meters. Approximately half of all measurements were taken within 2 km from the shore. Only a small number of points are located in the open sea or at greater depths. More open-water measurements can only be found in the ICES database for oxygen concentration, resulting in the highest correlation (0.75) between all biochemical variables we analyzed.

Another cause is the construction of the numerical model itself. The *EcoFish* model is a z-type model. It means that the model maintains the thickness of layers in a cell rather than the number of layers, in contrast to sigma-type models, where the same number of layers exists at each point, but they differ in their thickness. Z-type models are less capable of dealing with shallow water areas, where the water column often consists of only two or three layers. This configuration of the model, combined with the measurement database, where most measurements come from shallow coastal locations, negatively affects the validation results.

Worse results in the validation of nutrients may be related to inaccurate data for rivers (especially the Vistula) and the constant concentrations adopted for some rivers (according to Pastuszak et al., 2018). The volume of fresh water carried into the Gulf of Gdańsk by rivers was determined on the basis of long—term averages, which can result in insufficiently accurate deposition modeling, es-

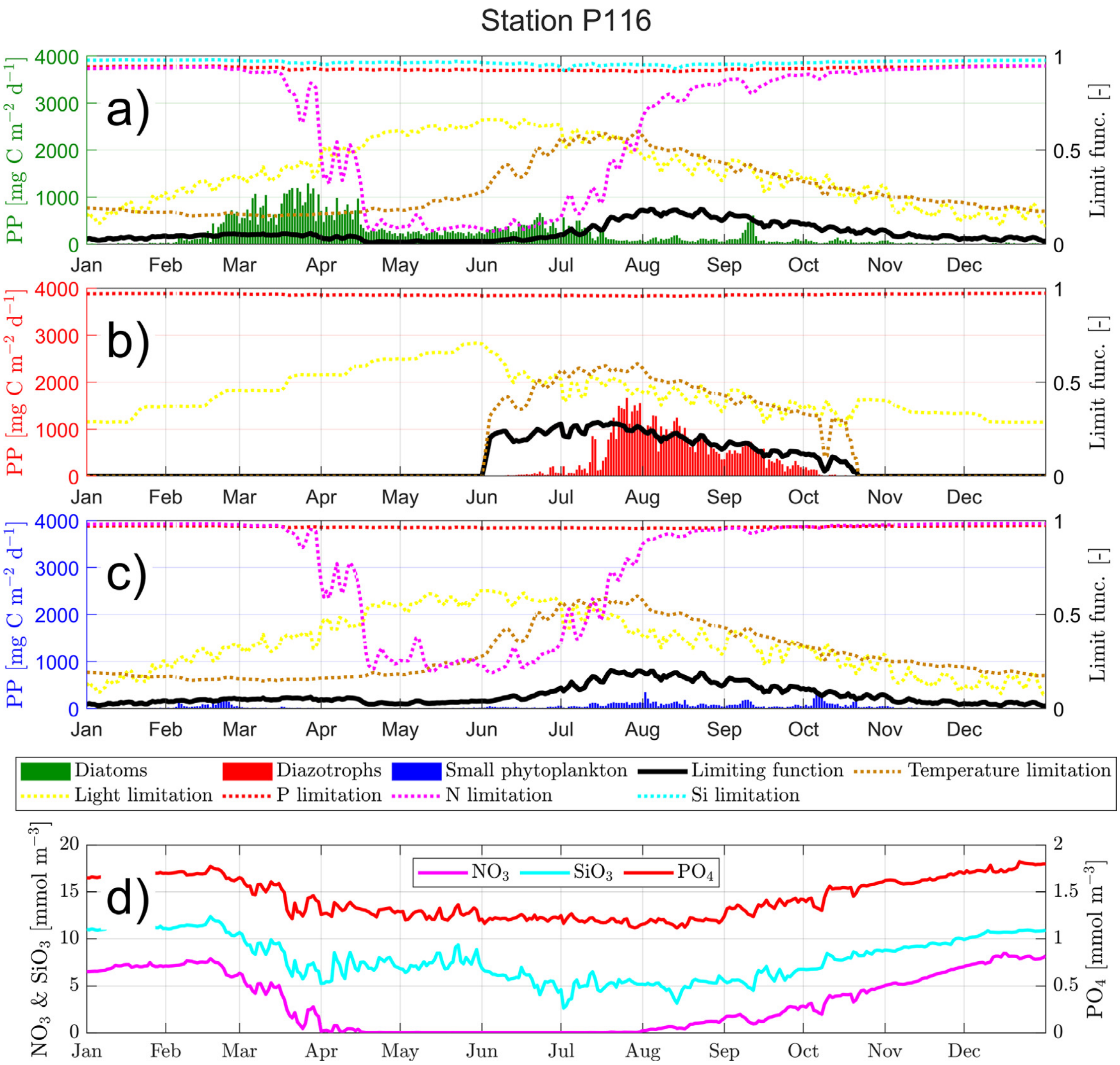

Figure 13 Primary production rate in 2021 for the entire water column at P116 station for a) diatoms, b) cyanobacteria, and c) small phytoplankton, compiled with limiting factors, and d) concentrations of nutrients.

pecially during periods of high daily variability. To ensure the numerical stability of the *EcoFish* model, large rivers were subjected to distribution, that is, the volume of fresh water along with the nutrients carried by them was divided into several model cells (several dozen for the Vistula).

4.2. Nutrients

The oxygen present in seawater primarily comes from photosynthesis and gas exchange with the atmosphere. However, when organic matter decomposes, oxygen is consumed, leading to potential deficits. In the central Baltic Sea, there are regular periods of stagnation in deep waters due to limited water exchange with the North Sea and consistent haline stratification (Conley et al., 2009, 2002; Meier et al., 2017). During these periods, nitrates are depleted, phosphates and ammonia concentrations increase, and dissolved oxygen levels decrease significantly at greater depths. Consequently, toxic hydrogen sulfide can emerge (Kuliński et al., 2022). The situation can improve temporarily when salty and oxygen-rich waters from the North Sea enter the Baltic Sea. However, such strong inflows have become increasingly infrequent in recent times, with only a few events occurring every decade (Mohrholz, 2018). In the deep basins of the Baltic Sea (including the area of the Gdańsk Deep), hypoxia and anoxia have increased significantly over the past century (Carstensen et al., 2014), and in 2019, the area of hypoxia covered approximately 32% of the surface of the Baltic Proper (Hansson et al., 2019). Despite efforts made to substantially decrease nutrient deposition in the waters of the Baltic Sea over the past few decades, areas suffering from oxygen deficiency (mainly caused by eutrophication) have not experienced reoxygenation. This is because a considerable amount of nutrients has accumulated in the sediments and is gradually released into the water column, leading to prolonged oxygen depletion (McCrackin et al., 2018).

Nitrogen is one of the main limiting factors for primary production and an element causing eutrophication of the marine environment (Andersen et al., 2017; Malone and Newton, 2020). It is present in the water column in the form

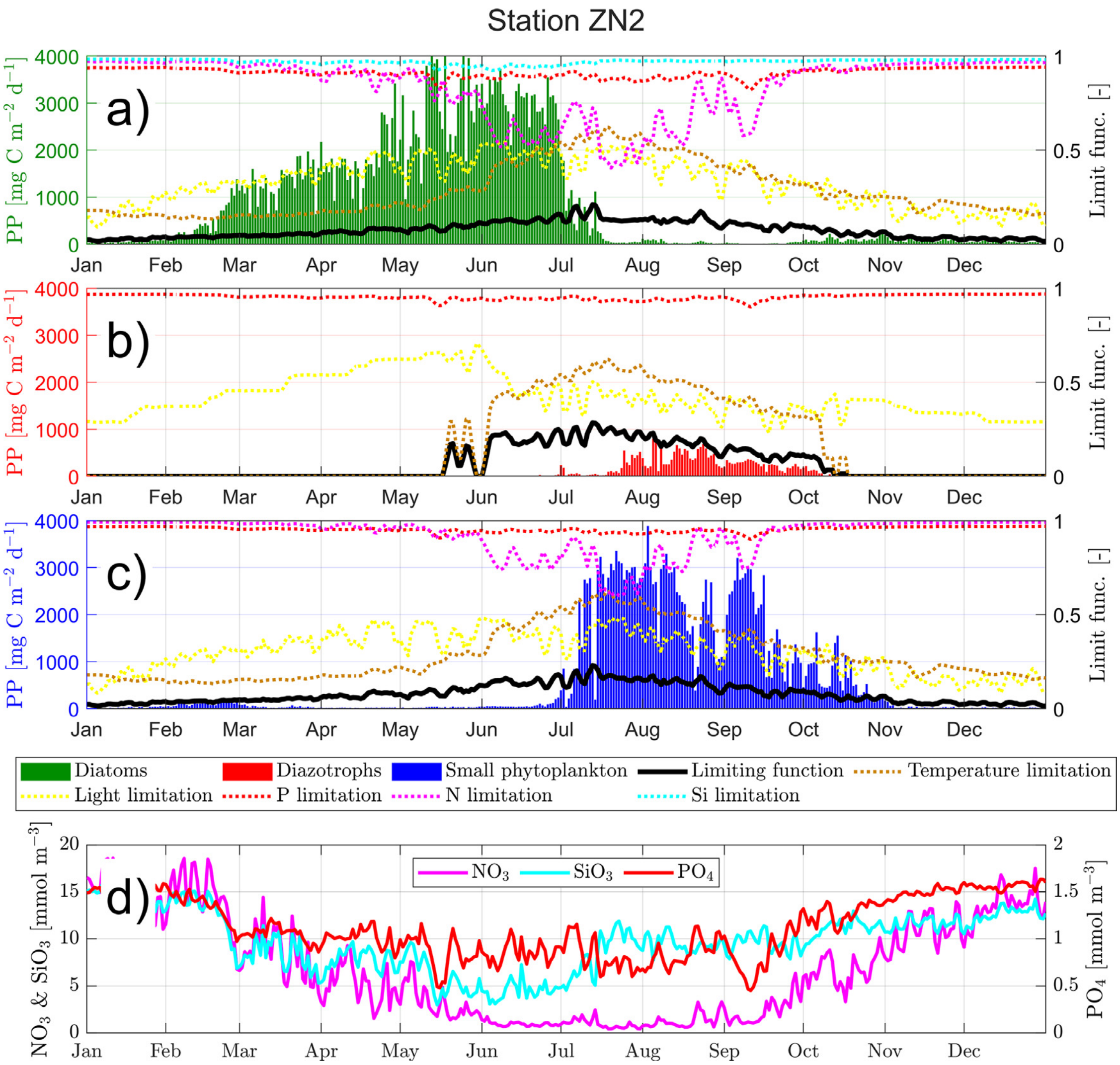

Figure 14 Primary production rate in 2021 for the entire water column at ZN2 station for a) diatoms, b) cyanobacteria, and c) small phytoplankton, compiled with limiting factors, and d) concentrations of nutrients.

of nitrates (NO_3), nitrites (NO_2) and ammonia (NH_4). Nitrogen concentrations in surface waters of the Gulf of Gdańsk vary spatially — higher concentrations occur at the mouth of the Vistula River, and lower in the central part of the Gulf. These compounds show a strongly marked seasonal cycle. The highest concentrations are recorded in early spring (March), when the melting waters of the Vistula River flow into the Gulf. Then, as a result of nitrogen consumption by phytoplankton and underwater plants, nitrogen compound concentrations decrease, eventually falling below the measurement capabilities of the methods used.

The basic difference between nitrogen and phosphorus is that the most plant-available forms (nitrates and nitrites) are not as easily regenerated as phosphates (Paytan and McLaughlin, 2007; Vitousek and Howarth, 1991). Therefore, practically every year from May to the end of September, seawater is devoid of nitrates and nitrites, which should limit the development of phytoplankton in summer. However, existing phosphate resources promote the development of Cyanobacteria, which can directly fixate nitrogen (N_2) from the atmosphere. Among them are species that produce toxins, such as *Nodularia spumigena* and *Aphanizomenon flos-aquae*, which pose a potential threat to other organisms that live in the Gulf of Gdańsk and to the health and lives of people resting by the sea.

Phosphorus, along with nitrogen, is the main element that causes eutrophication of the marine environment (Tamminen and Andersen, 2007). Phosphates in the Gulf of Gdańsk exhibit a strong seasonal cycle, similar to that of nitrates. The highest concentrations of phosphates are recorded in winter and early spring, before the start of the growing season. Then, as a result of the consumption of phosphorus by phytoplankton and underwater vegetation, phosphate concentrations decrease to low levels but are not completely depleted, as is the case with nitrates. Phosphates are compounds with a short regeneration period, which means that they are easily and quickly released by microorganisms (bacteria) from dead organic matter (Paytan and McLaughlin, 2007). Therefore, shortly after the spring bloom, they appear in marine waters in amounts sufficient to provide a food base for species developing in the summer (e.g., cyanobacteria).

Although chlorophyll *a* concentration is not a direct measure of phytoplankton biomass, it is one of the parameters often used in oceanographic and limnological studies as an indicator of the quantitative presence of phytoplankton in water (Boyer et al., 2009; Gons et al., 2002; Randolph et al., 2008). The increase in phytoplankton biomass in the waters of the Gulf of Gdańsk has a seasonal cycle. The stages of phytoplankton development are similar throughout the area. The cycle begins in early spring (usually around February and March) with high nitrate concentrations and seawater temperatures of a few degrees Celsius. The rate of primary production is usually very high during this period. Due to the short life span of these microscopic plants and the high productivity of the euphotic layer, phytoplankton is the main source of energy for other components of the ecosystem (Mosharov et al., 2022). Some phytoplankton is directly consumed by herbivorous zooplankton, but a large amount of phytoplankton sinks to the bottom.

4.3. Primary production cycle

The analysis of primary production (for the year 2021) is presented in Results (see 3.6. Primary production). The results were compared with the limiting functions and concentrations of nitrates, phosphates, and silicates, which are the most important nutrients that limit the growth of phytoplankton.

As a result of this analysis, we confirm that in the first weeks of the year, the factors determining the beginning of the vegetation period are the availability of light and water temperature. At each of the three locations analyzed (PB1, P116, and ZN2), the first group that began the annual production cycle in mid-February 2021 was diatoms. However, the length and intensity of this bloom varied depending on the location. The diatoms bloomed for the shortest time (only until mid-March) at the PB1 station, where the available nitrate was rapidly depleted due to the shallow depth. The availability of nitrates also determined the end of the diatom bloom at station P116, but it lasted a bit longer, until mid-April. After the spring diatom bloom, there was a period without production (or with very low production) at these stations until the water temperature reached the optimal level for the start of cyanobacterial blooms (June/July). These species can directly fix atmospheric nitrogen, so their growth is not dependent on the availability of nitrates in the water column.

A completely different situation prevailed at the ZN2 station, where due to the continuous supply of nutrients (mostly nitrates and silicates) deposited with the Vistula waters, the diatoms grew very intensively until July. Due to this long growth period, diatoms consumed a very large amount of phosphorus and, despite its continuous supply by the Vistula, their level was lower than at the other stations, effectively suppressing the intensity and duration of toxic cyanobacterial blooms.

In the available scientific literature, many articles can be found that analyze primary production in the Gulf of Gdańsk (Mosharov et al., 2022; Ostrowska et al., 2022; Wasmund et al., 2001; Witek et al., 1997; Zdun et al., 2021). In the study by Ostrowska et al. (2022), the total yearly primary production in the Gulf of Gdańsk (for the period 2010—2019) ranged from 124 to 145 g C m^{-2} year^{-1}. The values we obtained for the year 2021 were higher, reaching 160.1 g C m^{-2} year^{-1} at station P116, 168.2 g C m^{-2} year^{-1} at station PB1, and 553.1 g C m^{-2} year^{-1} at station ZN2.

The lowest monthly means of daily primary production occur In December, reaching 19.7 mg C m^{-2} day^{-1} at station P116, 25.9 mg C m^{-2} day^{-1} at station PB1 and 64.9 mg C m^{-2} day^{-1} at station ZN2. This result is consistent with previous studies for this region (e.g., Ostrowska et al., 2022; Zdun et al., 2021).

The highest monthly means of daily primary production occur during the summer months. At station P116, it was observed in August, with a value of 1021.6 mg C m^{-2} day^{-1}. The highest average of 1690.1 mg C m^{-2} day^{-1} was recorded in July at station PB1. Station ZN2, on the other hand, exhibited the highest primary production in June, with a value of 3111.5 mg C m^{-2} day^{-1}.

The maximum primary production in the Gulf of Gdańsk, as reported by Ostrowska et al. (2022), is most often observed in July and does not extend to August. The values obtained in that study range from 603 mg C m^{-2} day^{-1} in 2017 to 1066 mg C m^{-2} day^{-1} in 2010. Zdun et al. (2021), obtained the highest values in April and May, with primary production exceeding 2000 mg C m^{-2} day^{-1}.

The beginning of the vegetation period, as reported by other studies (Ostrowska et al., 2022; Zdun et al., 2021), is also in good agreement with our results. Furthermore, our results agree with the experiment conducted by Sommer et al. (2012), where it was confirmed that light availability and temperature are the most important factors for the timing of the spring bloom.

5. Conclusions

The *EcoFish* numerical model is part of the *Knowledge transfer platform FindFISH* service, providing information on hydrodynamic and biochemical variables for the Gulf of Gdańsk area. Thanks to the numerical simulations from the *EcoFish* model and the results for temperature, salinity (presented in Janecki et al. 2021), and oxygen concentration, it is possible to operate the key element of the platform, the *Fish Module*. Using these variables and the applied fuzzy logic method, the *Fish Module* allows the creation of maps of the most favorable environmental conditions (Habitat Suitability Index) for the industrial fishing of herring, sprat, and flounder in the Gulf of Gdańsk area.

By presenting the most important biochemical variables of the *EcoFish* model and conducting the validation, we have confirmed that the results of numerical simulations are consistent with *in situ* data and will provide a reliable set of input data for the *Fish Module*.

In the analysis of primary production, we show that geomorphological conditions and the deposition of nutrients from rivers have a significant impact on its pattern and intensity. The availability of nutrients can significantly alter the biomass distribution of all phytoplankton groups.

An overly strong focus on limiting nitrate deposition in river waters to inhibit marine eutrophication may ultimately lead to the opposite situation, where short and weak diatom blooms in spring will be followed by long and intense cyanobacterial blooms in summer. This is consistent with the results obtained from a numerical experiment conducted for Puck Bay by Dybowski et al. (2022). A reasonable approach to any legislative decisions in this regard is particularly important in the era of climate change and increasing water temperatures in seas and oceans, which will further prolong the period of optimal temperature for the bloom of this toxic and unwanted species from the perspective of the region's specificity.

Declaration of competing interest

The authors declare that they have no known competing financial interests or personal relationships that could have appeared to influence the work reported in this paper.

Acknowledgments

Calculations were carried out at the Academic Computer Centre in Gdańsk.

We are grateful to the anonymous reviewers for valuable comments on earlier versions of the manuscript.

Funding

Partial support for this study was provided by the project "Knowledge transfer platform FindFISH — Numerical Forecasting System for the Marine Environment of the Gulf of Gdańsk for Fisheries," funded by the European Union through European Regional Development Fund Contract RPPM.01.01.01-22-0025/16-00.

Some elements of the EcoFish model (i.e., river runoff data) are based on the solutions developed during the WaterPUCK project funded by National Centre for Research and Development of Poland within the BIOSTRATEG III program BIOSTRATEG3/343927/3/NCBR/2017.

Supplementary materials

Supplementary material associated with this article can be found, in the online version, at https://doi.org/10.1016/j.oceano.2023.05.001.

References

Andersen, J.H., Carstensen, J., Conley, D.J., Dromph, K., Fleming-Lehtinen, V., Gustafsson, B.G., Josefson, A.B., Norkko, A., Villnäs, A., Murray, C., 2017. Long-term temporal and spatial trends in eutrophication status of the Baltic Sea. Biol. Rev. 92 (1), 135—149. https://doi.org/10.1111/brv.12221

Arheimer, B., Dahné, J., Donnelly, C., Lindström, G., Strömqvist, J., 2012. Water and nutrient simulations using the HYPE model for Sweden vs. the Baltic Sea basin — influence of input-data quality and scale. Hydrol. Res. 43, 315—329. https://doi.org/10.2166/nh.2012.010

Blenckner, T., Möllmann, C., Stewart Lowndes, J., Griffiths, J.R., Campbell, E., De Cervo, A., Belgrano, A., Boström, C., Fleming, V., Frazier, M., Neuenfeldt, S., Niiranen, S., Nilsson, A., Ojaveer, H., Olsson, J., Palmlöv, C.S., Quaas, M., Rickels, W., Sobek, A., Viitasalo, M., Wikström, S.A., Halpern, B.S., 2021. The Baltic Health Index (BHI): Assessing the social—ecological status of the Baltic Sea. People and Nature 3, 359—375. https://doi.org/10.1002/pan3.10178

Boyer, J.N., Kelble, C.R., Ortner, P.B., Rudnick, D.T., 2009. Phytoplankton bloom status: Chlorophyll a biomass as an indicator of water quality condition in the southern estuaries of Florida, USA. Ecol. Indic. 9, 56—67. https://doi.org/10.1016/j.ecolind.2008.11.013

Carmichael, W., 2008. A world overview — One-hundred-twenty-seven years of research on toxic cyanobacteria — Where do we go from here?. In: Hudnell, H.K. (Ed.), Cyanobacterial Harmful Algal Blooms: State of the Science and Research Needs, AEMB vol. 619. Springer, New York, NY. https://doi.org/10.1007/978-0-387-75865-7_4

Carstensen, J., Andersen, J.H., Gustafsson, B.G., Conley, D.J., 2014. Deoxygenation of the Baltic Sea during the last century. P. Natl. Acad. Sci. USA 111, 5628—5633. https://doi.org/10.1073/pnas.1323156111

Conley, D.J., Björck, S., Bonsdorff, E., Carstensen, J., Destouni, G., Gustafsson, B.G., Hietanen, S., Kortekaas, M., Kuosa, H., Markus Meier, H.E., Müller-Karulis, B., Nordberg, K., Norkko, A., Nürnberg, G., Pitkänen, H., Rabalais, N.N., Rosenberg, R., Savchuk, O.P., Slomp, C.P., Voss, M., Wulff, F., Zillén, L., 2009. Hypoxia-Related Processes in the Baltic Sea. Environ. Sci. Technol. 43, 3412—3420. https://doi.org/10.1021/es802762a

Conley, D.J., Humborg, C., Rahm, L., Savchuk, O.P., Wulff, F., 2002. Hypoxia in the Baltic Sea and Basin-Scale Changes in Phosphorus Biogeochemistry. Environ. Sci. Technol. 36, 5315—5320. https://doi.org/10.1021/es025763w

Donnelly, C., Andersson, J.C.M., Arheimer, B., 2016. Using flow signatures and catchment similarities to evaluate the E-HYPE multi-basin model across Europe. Hydrolog. Sci. J. 61, 255—273. https://doi.org/10.1080/02626667.2015.1027710

Dybowski, D., Dzierzbicka-Głowacka, L., 2022. Analysis of the impact of nutrients deposited from the land side on the waters of Puck Lagoon (Gdańsk Basin, Southern Baltic): A model study. Oceanologia 65 (2), 386—397. https://doi.org/10.1016/j.oceano.2022.11.005

Dybowski, D., Jakacki, J., Janecki, M., Nowicki, A., Rak, D., Dzierzbicka-Glowacka, L., 2019. High-Resolution Ecosystem Model of the Puck Bay (Southern Baltic Sea)—Hydrodynamic Component Evaluation. Water-SUI 11, 2057. https://doi.org/10.3390/w11102057

Dybowski, D., Janecki, M., Nowicki, A., Dzierzbicka-Glowacka, L.A., 2020. Assessing the Impact of Chemical Loads from Agriculture Holdings on the Puck Bay Environment with the High-Resolution Ecosystem Model of the Puck Bay, Southern Baltic Sea. Water-SUI 12, 2068. https://doi.org/10.3390/w12072068

Dzierzbicka-Glowacka, L., Dybowski, D., Janecki, M., Wojciechowska, E., Szymczycha, B., Potrykus, D., Nowicki, A., Szymkiewicz, A., Zima, P., Jaworska-Szulc, B., Pietrzak, S., Pazikowska-Sapota, G., Kalinowska, D., Nawrot, N., Wielgat, P., Dembska, G., Matej-Łukowicz, K., Szczepańska, K., Puszkarczuk, T., 2022. Modelling the impact of the agricultural holdings and land-use structure on the quality of inland and coastal waters with an innovative and interdisciplinary toolkit. Agr. Water Manage. 263, 107438. https://doi.org/10.1016/j.agwat.2021.107438

Dzierzbicka-Głowacka, L., Jakacki, J., Janecki, M., Nowicki, A., 2013a. Activation of the operational ecohydrodynamic model (3D CEMBS) — the hydrodynamic part. Oceanologia 55 (3), 519—541. https://doi.org/10.5697/oc.55-3.519

Dzierzbicka-Głowacka, L., Janecki, M., Dybowski, D., Szymczycha, B., Obarska-Pempkowiak, H., Wojciechowska, E., Zima, P., Pietrzak, S., Pazikowska-Sapota, G., Jaworska-Szulc, B., Nowicki, A., Kłostowska, Ż., Szymkiewicz, A., Galer-Tatarowicz, K., Wichorowski, M., Białoskórski, M., Puszkarczuk, T., 2019. A New Approach for Investigating the Impact of Pesticides and Nutrient Flux from Agricultural Holdings and Land-Use Structures on Baltic Sea Coastal Waters. Pol. J. Environ. Stud. 28, 2531—2539. https://doi.org/10.15244/pjoes/92524

Dzierzbicka-Głowacka, L., Janecki, M., Nowicki, A., Jakacki, J., 2013b. Activation of the operational ecohydrodynamic model (3D CEMBS) — the ecosystem module. Oceanologia 55 (3), 543—572. https://doi.org/10.5697/oc.55-3.543

Dzierzbicka-Głowacka, L., Nowicki, A., Janecki, M., Szymczycha, B., Piotrowski, P., Pieckiel, P., Łukasiewicz, G., 2018. Structure of the FindFish Knowledge Transfer Platform. Fisheries & Aquatic Life 26, 193—197. https://doi.org/10.2478/aopf-2018-0021

Gons, H.J., Rijkeboer, M., Ruddick, K.G., 2002. A chlorophyll-retrieval algorithm for satellite imagery (Medium Resolution Imaging Spectrometer) of inland and coastal waters. J. Plankton Res. 24, 947—951. https://doi.org/10.1093/plankt/24.9.947

Hansson, M., Viktorsson, L., Andersson, L., 2019. Oxygen Survey in the Baltic Sea 2019 — Extent of Anoxia and Hypoxia, 1960—2019 (No. 67), Report Oceanography. SMHI, Göteborg, Sweden.

HELCOM, 2010. Ecosystem Health of the Baltic Sea 2003—2007: HELCOM Initial Holistic Assessment (No. 122). In: Balt. Sea Environ. Proc. Helsinki Commission, Helsinki, Finland.

Janecki, M., Dybowski, D., Jakacki, J., Nowicki, A., Dzierzbicka-Glowacka, L., 2021. The Use of Satellite Data to Determine the Changes of Hydrodynamic Parameters in the Gulf of Gdańsk via EcoFish Model. Remote Sens. 13 (18), 3572. https://doi.org/10.3390/rs13183572

Janecki, M., Dybowski, D., Rak, D., Dzierzbicka-Glowacka, L., 2022. A New Method for Thermocline and Halocline Depth Determination at Shallow Seas. J. Phys. Oceanogr. 52, 2205—2218. https://doi.org/10.1175/JPO-D-22-0008.1

Kalinowska, D., Wielgat, P., Kolerski, T., Zima, P., 2018. Effect of GIS parameters on modelling runoff from river basin. The case study of catchment in the Puck District. In: E3S Web Conf., 63, 00005. https://doi.org/10.1051/e3sconf/20186300005

Kalinowska, D., Wielgat, P., Kolerski, T., Zima, P., 2020. Model of Nutrient and Pesticide Outflow with Surface Water to Puck Bay (Southern Baltic Sea). Water-SUI 12, 809. https://doi.org/10.3390/w12030809

Kuliński, K., Rehder, G., Asmala, E., Bartosova, A., Carstensen, J., Gustafsson, B., Hall, P.O.J., Humborg, C., Jilbert, T., Jürgens, K., Meier, H.E.M., Müller-Karulis, B., Naumann, M., Olesen, J.E., Savchuk, O., Schramm, A., Slomp, C.P., Sofiev, M., Sobek, A., Szymczycha, B., Undeman, E., 2022. Biogeochemical functioning of the Baltic Sea. Earth Syst. Dynam. 13, 633—685. https://doi.org/10.5194/esd-13-633-2022

Majewski, A., 1972. Hydrological characteristics of estuarine waters at the Polish Coast. Państwowy Instytut Hydrologiczno-Meteorologiczny, 3—40.

Malone, T.C., Newton, A., 2020. The Globalization of Cultural Eutrophication in the Coastal Ocean: Causes and Consequences. Front. Mar. Sci. 7. https://doi.org/10.3389/fmars.2020.00670

McCrackin, M.L., Muller-Karulis, B., Gustafsson, B.G., Howarth, R.W., Humborg, C., Svanbäck, A., Swaney, D.P., 2018. A Century of Legacy Phosphorus Dynamics in a Large Drainage Basin. Global Biogeochem. Cy. 32, 1107—1122. https://doi.org/10.1029/2018GB005914

Meier, H.E.M., Höglund, A., Eilola, K., Almroth-Rosell, E., 2017. Impact of accelerated future global mean sea level rise on hypoxia in the Baltic Sea. Clim. Dyn. 49, 163—172. https://doi.org/10.1007/s00382-016-3333-y

Mohrholz, V., 2018. Major Baltic Inflow Statistics — Revised. Front. Mar. Sci. 5. https://doi.org/10.3389/fmars.2018.00384

Moore, J.K., Doney, S.C., Kleypas, J.A., Glover, D.M., Fung, I.Y., 2001. An intermediate complexity marine ecosystem model for the global domain. Deep-Sea Res. Pt. II 49, 403—462. https://doi.org/10.1016/S0967-0645(01)00108-4

Mosharov, S.A., Mosharova, I.V., Dmitrieva, O.A., Semenova, A.S., Ulyanova, M.O., 2022. Seasonal Variability of Plankton Production Parameters as the Basis for the Formation of Organic Matter Flow in the Southeastern Part of the Baltic Sea. Water-SUI 14, 4099. https://doi.org/10.3390/w14244099

O'Neil, J.M., Davis, T.W., Burford, M.A., Gobler, C.J., 2012. The rise of harmful cyanobacteria blooms: The potential roles of eutrophication and climate change. Harmful Algae 14, 313—334. https://doi.org/10.1016/j.hal.2011.10.027

Ostrowska, M., Ficek, D., Stoltmann, D., Stoń-Egiert, J., Zdun, A., Kowalewski, M., Zapadka, T., Majchrowski, R., Pawlik, M., Dera, J., 2022. Ten years of remote sensing and analyses of the Baltic Sea primary production (2010—2019). Remote Sensing Applications: Society and Environment 26, 100715. https://doi.org/10.1016/j.rsase.2022.100715

Pastuszak, M., Bryhn, A.C., Håkanson, L., Stålnacke, P., Zalewski, M., Wodzinowski, T., 2018. Reduction of nutrient emission from Polish territory into the Baltic Sea (1988—2014) confronted with real environmental needs and international requirements. Oceanol. Hydrobiol. St 47, 140—166. https://doi.org/10.1515/ohs-2018-0015

Paytan, A., McLaughlin, K., 2007. The Oceanic Phosphorus Cycle. Chem. Rev. 107, 563—576. https://doi.org/10.1021/cr0503613

Randolph, K., Wilson, J., Tedesco, L., Li, L., Pascual, D.L., Soyeux, E., 2008. Hyperspectral remote sensing of cyanobacteria in turbid productive water using optically active pigments, chlorophyll *a* and phycocyanin. Remote Sens. Environ. 112, 4009—4019. https://doi.org/10.1016/j.rse.2008.06.002

Reckermann, M., Omstedt, A., Soomere, T., Aigars, J., Akhtar, N., Bełdowska, M., Bełdowski, J., Cronin, T., Czub, M., Eero, M., Hyytiäinen, K.P., Jalkanen, J.-P., Kiessling, A., Kjellström, E., Kuliński, K., Larsén, X.G., McCrackin, M., Meier, H.E.M., Oberbeckmann, S., Parnell, K., Pons-Seres de Brauwer, C., Poska, A., Saarinen, J., Szymczycha, B., Undeman, E., Wörman, A., Zorita, E., 2022. Human impacts and their interactions in the Baltic Sea region. Earth Syst. Dynam. 13 (1), 1—80. https://doi.org/10.5194/esd-13-1-2022

Sato, N., 2021. Are Cyanobacteria an Ancestor of Chloroplasts or Just One of the Gene Donors for Plants and Algae? Genes 12 (6), 823. https://doi.org/10.3390/genes12060823

Sommer, U., Aberle, N., Lengfellner, K., Lewandowska, A., 2012. The Baltic Sea spring phytoplankton bloom in a changing climate: an experimental approach. Mar. Biol. 159, 2479—2490. https://doi.org/10.1007/s00227-012-1897-6

Szymczycha, B., Zaborska, A., Bełdowski, J., Kuliński, K., Beszczyńska-Möller, A., Kędra, M., Pempkowiak, J., 2019. Chapter 4 — The Baltic Sea. In: Sheppard, C. (Ed.), World Seas: An Environmental Evaluation. Acad. Press, 85—111. https://doi.org/10.1016/B978-0-12-805068-2.00005-X

Tamminen, T., Andersen, T., 2007. Seasonal phytoplankton nutrient limitation patterns as revealed by bioassays over Baltic Sea gradients of salinity and eutrophication. Mar. Ecol. Prog. Ser. 340, 121—138. https://doi.org/10.3354/meps340121

Tomczak, M.T., Szymanek, L., Pastuszak, M., Grygiel, W., Zalewski, M., Gromisz, S., Ameryk, A., Kownacka, J., Psuty, I., Kuzebski, E., Grzebielec, R., Margoński, P., 2016. Evaluation of Trends and Changes in the Gulf of Gdańsk Ecosystem — an Integrated Approach. Estuar. Coast. 39, 593—604. https://doi.org/10.1007/s12237-015-0026-4

Verity, P.G., Smetacek, V., 1996. Organism life cycles, predation, and the structure of marine pelagic ecosystems. Mar. Ecol. Prog. Ser. 130, 277—293. https://doi.org/10.3354/meps130277

Vitousek, P.M., Howarth, R.W., 1991. Nitrogen limitation on land and in the sea: How can it occur? Biogeochemistry 13, 87—115. https://doi.org/10.1007/BF00002772 von Storch, H., 2023. Perceptions of an endangered Baltic Sea. Oceanologia 65 (1), 44—49. https://doi.org/10.1016/j.oceano.2021.08.005

Voss, M., Liskow, I., Pastuszak, M., Rüß, D., Schulte, U., Dippner, J.W., 2005. Riverine discharge into a coastal bay: A stable isotope study in the Gulf of Gdańsk, Baltic Sea. J. Marine Syst. 57, 127—145. https://doi.org/10.1016/j.jmarsys.2005.04.002

Wasmund, N., Andrushaitis, A., Łysiak-Pastuszak, E., Müller-Karulis, B., Nausch, G., Neumann, T., Ojaveer, H., Olenina, I., Postel, L., Witek, Z., 2001. Trophic Status of the South-Eastern Baltic Sea: A Comparison of Coastal and Open Areas. Estuar. Coast. Shelf. S. 53 (6), 849—864. https://doi.org/10.1006/ecss.2001.0828

Wielgat, P., Kalinowska, D., Szymkiewicz, A., Zima, P., Jaworska-Szulc, B., Wojciechowska, E., Nawrot, N., Matej-Lukowicz, K., Dzierzbicka-Glowacka, L.A., 2021. Towards a multi-basin SWAT model for the migration of nutrients and pesticides to Puck Bay (Southern Baltic Sea). PeerJ 9, e10938. https://doi.org/10.7717/peerj.10938

Witek, Z., Ochocki, S., Maciejowska, M., Pastuszak, M., Nakonieczny, J., Podgórska, B., Kownacka, J.M., Mackiewicz, T., Wrzesinska-Kwiecien, M., 1997. Phytoplankton primary production and its utilization by the pelagic community in the coastal zone of the Gulf of Gdansk (southern Baltic). Mar. Ecol. Prog. Ser. 148, 169—186. https://doi.org/10.3354/meps148169

Woźniak, B., Bradtke, K., Darecki, M., Dera, J., Dudzińska-Nowak, J., Dzierzbicka-Głowacka, L., Ficek, D., Furmańczyk, K., Kowalewski, M., Krężel, A., Majchrowski, R., Ostrowska, M., Paszkuta, M., Stoń-Egiert, J., Stramska, M., Zapadka, T., 2011a. SatBałtyk — A Baltic environmental satellite remote sensing system — an ongoing project in Poland. Part 1: Assumptions, scope and operating range. Oceanologia 53 (4), 897—924. https://doi.org/10.5697/oc.53-4.897

Woźniak, B., Bradtke, K., Darecki, M., Dera, J., Dudzińska-Nowak, J., Dzierzbicka-Głowacka, L., Ficek, D., Furmańczyk, K., Kowalewski, M., Krężel, A., Majchrowski, R., Ostrowska, M., Paszkuta, M., Stoń-Egiert, J., Stramska, M., Zapadka, T., 2011b. SatBałtyk — A Baltic environmental satellite remote sensing system — an ongoing project in Poland. Part 2: Practical applicability and preliminary results. Oceanologia 53 (4), 925—958. https://doi.org/10.5697/oc.53-4.925

Zdun, A., Stoń-Egiert, J., Ficek, D., Ostrowska, M., 2021. Seasonal and spatial changes of primary production in the Baltic Sea (Europe) based on in situ measurements in the period of 1993—2018. Front. Mar. Sci. 7. https://doi.org/10.3389/fmars.2020.604532

Oceanologia 65 (2023) 534—547

Available online at www.sciencedirect.com

ScienceDirect

journal homepage: www.journals.elsevier.com/oceanologia

ORIGINAL RESEARCH ARTICLE

Projections of wind climate and wave energy resources in Lithuanian territorial waters of the Baltic Sea in the 21st century

Darius Jakimavičius*, **Vytautas Akstinas**

Laboratory of Hydrology, Lithuanian Energy Institute, Kaunas, Lithuania

Received 15 September 2022; accepted 9 June 2023
Available online 24 June 2023

KEYWORDS
Wave energy flux;
Baltic Sea;
Wind projections;
Wave height;
SSP scenarios

Abstract Wave energy is still insufficiently explored and exploited as a future energy source. Climate change is an additional force that affects energy potential changes. Therefore, this study aims to evaluate the wave energy under climate change and to project it for the near (2025—2044) and far (2081—2100) future by applying the wave energy flux (WEF) approach and statistical relations between wind speeds and wave heights. The study was concentrated on the Baltic Sea nearshore at the Lithuanian territorial water. The analysis of existing relations between wind speeds and wave heights was found based on historical observations of the reference period (1995—2014), and the projections of WEF were created using the downscaled output of best-fit global climate models (GCMs) according to four scenarios of Shared Socioeconomic Pathways (SSP). The results indicated strong relations between wind speed and wave height, especially for the west-origin winds. Depending on the selected scenarios, the projected WEF may increase up to 10% (SSP5-8.5) and 11% (SSP1-2.6) in the near and far future respectively. The absence of large differences between the periods may be caused by the rough resolution of grid cells of GCMs. The comparison with the results based on regional climate models output could be a future perspective in order to reach a better representation of regional forces and to introduce more clarity to the obtained results. The results of this study may be advantageous for the primary planning of renewable energy sources (RES) development, especially in the face of climate change.

---

* Corresponding author at: Laboratory of Hydrology, Lithuanian Energy Institute, Breslaujos St. 3, LT—444003 Kaunas, Lithuania.
E-mail addresses: darius.jakimavicius@lei.lt (D. Jakimavičius), vytautas.akstinas@lei.lt (V. Akstinas).

Peer review under the responsibility of the Institute of Oceanology of the Polish Academy of Sciences.

Production and hosting by Elsevier

https://doi.org/10.1016/j.oceano.2023.06.004

1. Introduction

Due to the growth of energy needs, many countries all around the world are seeking to transform their energy system from the fossil fuel-based to the RES, such as solar, wind, hydropower and biofuels. Based on the data from 2020, around 22.1% of the electricity consumed in Europe was produced from RES (Eurostat, 2020). The progress of renewable energy sources consumption corresponds to the rest of the world — 27.4% (Statistics Lithuania, 2022). The European Union (EU) has set itself the goal of becoming the world's first climate-neutral continent by 2050 following the European Green Deal (European Parliament, 2009). This means that a large part of the consumed energy could be produced from RES. Currently, Iceland, Norway and Sweden are moving towards successfully to be climate-neutral countries, because 83.7%, 77.4% and 60.1% of the consumed energy respectively is produced by RES (Eurostat, 2020). These leading countries are followed by Finland and Latvia (43.8 and 42.1% respectively). According to the official statistics, Lithuania from RES produces about 27% of the consumed energy, and the remaining part is produced by other sources (e.g. thermal power plants) or imported. However, these numbers are much higher than the EU average. And more than currently produced by economically stronger EU countries such as Germany and France (19.3 and 19.1% respectively). Talking about the distribution of energy production between RES, on average 70% of renewable energy comes from hydropower and wind by equal share. A smaller part of RES consists of solar (19%), solid biofuel (8%) and other sources (9%) (Eurostat, 2020). Hydropower forms an important part in the overall balance. Many types of water-based energy production exist. Expanding the types of hydropower, we can see that hydropower consists of the kinetic and potential energy of rivers, tidal energy, and wave energy. The theoretical wave energy potential of the World Ocean is estimated to be 32,000 TWh/year, while the total global electricity consumption is 16,800 TWh/year (Mørk et al., 2010). Accordingly, wave energy hid its enormous potential for a long time till scientists discerned its applicability to human needs. The pioneer of wave energy is Pierre-Simon Girard, who published the first patent related to wave energy in 1799 (Ross, 1995). Since then, many important studies and scientific works have been carried out and finally, the first commercial wave energy plant installed on the coast of Portugal began its operation. The plant consisted of three 750 kW Pelamis units (Aquaret, 2008). Despite the hidden great potential and wide geographical distribution of wave energy, many different obstacles step into the universal applicability. The main challenges are related to the creation of wave energy converters and their connection to the network. Moreover, the proper assessment of the wave energy potential and perspectives is an important task for each country towards the development of such kind of energy source.

According to the data of Statistics Lithuania, 27.4% of the consumed electricity was produced from renewable energy sources in 2020 (Statistics Lithuania, 2022). It is worth evaluating the current status of Lithuania in order to achieve the set goal to produce 100% of the consumed electricity in the country only from RES by 2050. Nowadays, the largest part of the consumed electricity is produced by wind power plants (16.5%) and biofuel power plants (6.3%). Another 3.2% of consumed electricity is produced in hydropower and 1.4% in solar power plants. Mentioned amounts are still insufficient from the long-term perspective, therefore it is necessary to evaluate all possible options and pathways in which direction to move forward. Almost 100 hydropower plants are operating in Lithuania, as well as wind and solar power plants are expanding rapidly. The western part of the Lithuanian border is located along the Baltic Sea and consists of a 90 km coastline. However, there are still no wave power plants in operation. Previous studies have determined that the wave energy flux of the Baltic Sea averages varied from 0.5 to 8 kW/m (Kovaleva et al., 2017; Nilsson et al., 2019; Soomere and Eelsalu, 2014). Meanwhile, the WEF near the Lithuanian coastline of the Baltic Sea reaches from 1 to 2 kW/m (Jakimavičius et al., 2018a; Kasiulis et al., 2015). Considering the development of wind and solar power plants only on the mainland and the prohibition of the development of new hydropower plants on the rivers according to the national law, it is worth to begin the usage of waves of the Baltic Sea for electricity production. Energy generated by waves is available to estimate using empirical equations but predicting wave resources in the long term requires the use of physical or statistical models. Physical models are much more accurate because they are based on hydrodynamic equations and can more precisely describe the processes taking place in nature. On the other hand, physical models require a lot of additional input data that cannot be provided by climate models in evaluating future changes under climate change. Third-generation SWAN, WAM and WAVEWATCH III models are often used for the modelling of wave parameters. These models are often applied in Baltic Sea (Alari et al., 2016; Björkqvist et al., 2020; Kanarik et al., 2021; Sapiega et al., 2023), Mediterranean Sea (Elkut et al., 2021), in Black Sea (Islek and Yuksel, 2021; Soran et al., 2022), in Atlantic Ocean at Canada coastline (Reikard et al., 2015) and in the Indian Ocean at southwestern coast of Australia (Cuttler et al., 2020). In wave research, the MIKE21 model is also applied, with which wave parameters were simulated in the Baltic Sea (Kasiulis et al., 2015; Jakimavičius et al., 2018a), in the Black Sea (Anton et al., 2019; Divinsky and Kosyan, 2017), in the Mediterranean Sea (Ahn and Park, 2019) and elsewhere. However, the physical models require a large amount of input data and computational resources for relatively simple tasks, therefore the application of other approaches such as statistical models enables to simplify the obtaining of results with acceptable accuracy.

Statistical models are usually based on the relationship between the predictor and the predictand. They are much simpler to apply, which is why they are often used in various scientific studies (Camus et al., 2017; Toffoli and Bitner-Gregersen, 2017). The projections of the height of sea waves are closely related to the changes in wind speeds since the interrelationship between them is found. The variability of wind speed take place an important role in the context of climate change. The first steps in wind-projections related studies in the Baltic Sea region were carried out under the climate change scenarios published in 4th Assessment Report by the IPCC (Intergovernmental Panel on Climate Change) (Pryor et al., 2006). The study notes that even the slightest change in surface wind speeds can have both, positive or negative feedback to the rest of the climate system, and can further catalyse the already accelerating effects of climate change. The assessment of wind is not only limited to the studies of its origin and variability but at the same time attempts to link it to various parameters such as wind-induced sea waves in the face of climate change (Lobeto et al., 2021) or the projections of offshore wind resource (Vu Dinh et al., 2022). However, the mentioned studies still involve RCP scenarios and related changes, although the projections for new SSP scenarios are already available after the publication of GCMs outputs of the CMIP6 project (Eyring et al., 2016). One of the first detailed analyses of the wind changes in Europe disclosed differences between SSP scenarios and compared the wind patterns between CMIP5 and CMIP6 projects (Carvalho et al., 2021). The changes in wind energy resources in the North American continent and its coastal zone were also assessed according to the SSP scenarios and ensemble of even 18 selected GCMs (Martinez and Iglesias, 2022). Although the study involves the accuracy analysis of GCMs simulations in a historical period based on ERA-5 reanalysis database the whole ensemble was chosen instead of the selection of best-fit GCMs.

Continuing the described practices in wave energy flux evaluation, the main aim of this study is to project the WEF in the near (2025—2044) and far (2081—2100) future by applying statistical relationships between wind speeds and wave heights according to four SSPs. For the implementation of the main aim of this study, four tasks were set, i.e., to determine the relationship between wind speed and wave height, to select best-fit GCMs for wind climate representation at the territory of the Lithuanian coast, to identify changes in wind climate in the future, and to project wave heights and WEF in near (2025—2044) and far (2081—2100) future according to SSP scenarios.

This study is one of the first attempts to project wind and wave climate as well as wave energy resources in the south-eastern part of the Baltic Sea using a statistical model and SSP scenarios. Therefore, the applied approach and obtained findings of this research expanded the knowledge in the field of wave research of the Baltic Sea.

2. Study area and data

The Baltic Sea coast near Klaipėda (Lithuania) was chosen as the case study area (Figure 1). Lithuania has 90.66 km of the southeastern Baltic Sea coast. The coast of Lithuania is quite shallow. Here, an isobath of 5 m passes on average 0.45 km, 10 m — 1.0 km, and 20 m — 1.8—2.0 km away from the coastline. Meanwhile, the 40 m isobath is located between 13 and 30 km away from the coast. 51.03 km of total length belongs to the Curonian Spit, which separates the Baltic Sea from the Curonian Lagoon (Universal Lithuanian Encyclopedia, 2022). A National Park was established in the Curonian Spit and the whole territory is included in the UNESCO World Heritage List. Accordingly, any anthropogenic activity is strongly regulated in this stretch. Klaipėda State Seaport is located near the middle of the Lithuanian coastline. The port is unique as the northernmost frost-free port of the Baltic Sea. 18.7 million tons of cargo on average are handled in this port per year. Due to the volume of such works, it is the fourth largest port on the east coast of the Baltic Sea (Atvira Klaipeda.lt, 2021). Lithuanian coastline distinguishes by its position in terms of global atmospheric circulation. The coastline is situated longitudinally from south to north and it is the first barrier to the westerly flow in the Baltic Sea region. Therefore, the dominant winds and consequently wave heights are much higher than in other parts of the Baltic Sea, e.g. western shore, the Gulf of Riga or the Gulf of Finland (Bonaduce et al., 2019; Soomere, 2023). The growing demand for clean energy pushes forward to develop not only the rivers hydropower, solar and wind but also to start planning new sources such as wave energy plants in the Lithuanian coastal water of the Baltic Sea.

The observational data of wind and wave parameters for the period of 1995—2014 was used in this study. The data on wind speed and its direction were taken from the Klaipėda meteorological station of the Lithuanian Hydrometeorological Service under the Ministry of Environment of the Republic of Lithuania. This station is located on land (55.731350 N, 21.091570 E), about 400 meters away from the wave monitoring place. Measurements of wind parameters were carried out in an instrumental way at a height of 10 meters. For this purpose, Vaisala WMT700 ultrasonic sensor with WinCap technology was installed in the meteorological station, which performs measurements every 1 hour. The wave height and direction were taken from the monitoring station of the Marine Research Department under the Environmental Protection Agency of Lithuania. The waves' parameters were estimated visually twice a day (in the morning and in the afternoon) at a depth of 5—6 meters west of the Klaipėda harbour piers (55.730786 N, 21.069204 E) (Figure 1). A period is also determined during wave observations. However, it is not determined during each observation, but several times a month. Therefore, its data were not used in this study. Wind parameters were measured much more often than waves, so wind parameters were used only during the same hours when wave observations were carried out. For future projections, the output of zonal (u, m/s) and meridional (v, m/s) components of the wind at a height of 10 meters were taken from GCMs stored in CEDA (Centre for Environmental Data Analysis) database (https://data.ceda.ac.uk, accessed on 24 February 2022) for the reference (1995—2014) period and for the near (2025—2044) and far (2081—2100) future. The projections were based on four SSP climate scenarios (SSP1-2.6, SSP2-4.5, SSP3-7.0, and SSP5-8.5).

3. Methods

The concept of wave energy flux projections was based on the evaluation of interrelations of historical wind and wave data as well as the application of obtained relations for future periods. The scheme of this research displayed the main steps of the study implementation (Figure 2). The first level consisted of the creation of a database of necessary data for the historical period and future projections. The second level was the processing of collected data where the presence of the relations between wind speed and wave height were tested, and the selecting best-fit GCMs for the Lithuanian climatic conditions from the set of 24 GCMs.

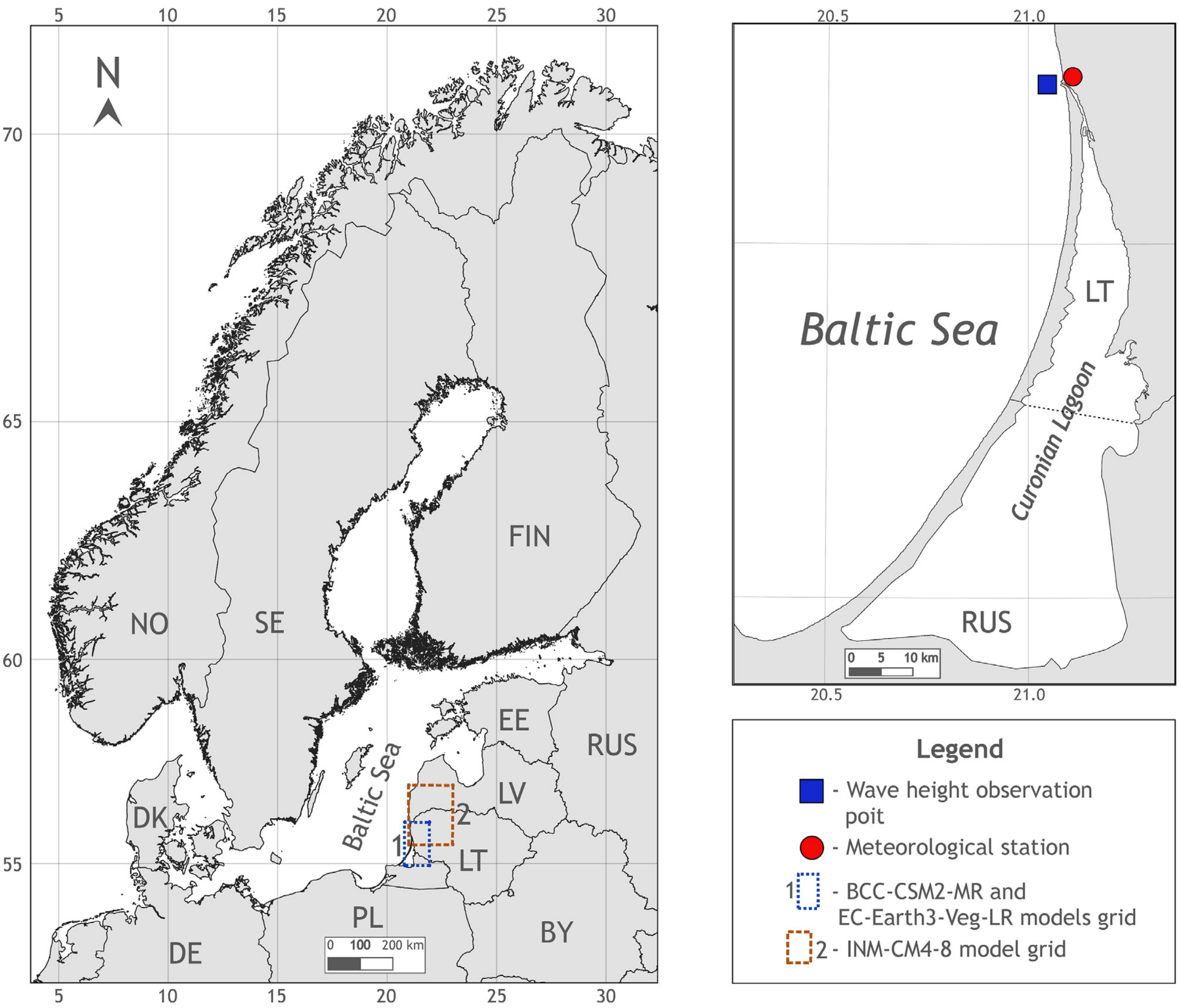

Figure 1 Study area.

The output of the selected GCMs and obtained relations were used for the projections of wave heights and following wave energy flux in the 21st century.

First of all, the existence of relations between wind speed and wave height was tested for the period of 1995—2014. The statistical relations were tested between the wind speed of a particular direction (according to classification in 8 directions) and the wave height at the same wind direction including one neighbouring direction clockwise and counterclockwise. The linear relations were described by the following equation:

$$y_i = ax_i + b \tag{1}$$

where x_i — wind speed of particular direction i, y_i — wave height of the same direction i as a wind speed, a — the change in wave height of i direction for each one-increment change in wind speed of i direction and b — intercept of wave height of i direction. The correlation coefficients were calculated for generated equations in order to verify the suitability of equations for the projections of wave heights under climate change. Moreover, the distribution percentage between directions of wave height was calculated for each of the 8 wind directions.

For the wind speed and following wave height projections in the near (2025—2044) and far (2081—2100) future, the meteorological data of zonal (u) and meridional (v) wind components according to four SSP scenarios (SSP1-2.6, SSP2-4.5, SSP3-7.0, and SSP5-8.5) were downloaded from CEDA database in netCDF data format. The R programming language was used to extract the necessary data from certain grid cells that represent Klaipėda meteorological station (MS). The wind speed and direction were recalculated from zonal (u) and meridional (v) wind components (ECMWF, 2022) as follows for wind speed:

$$V = \sqrt{u^2 + v^2} \tag{2}$$

and wind direction according to the following conditions:

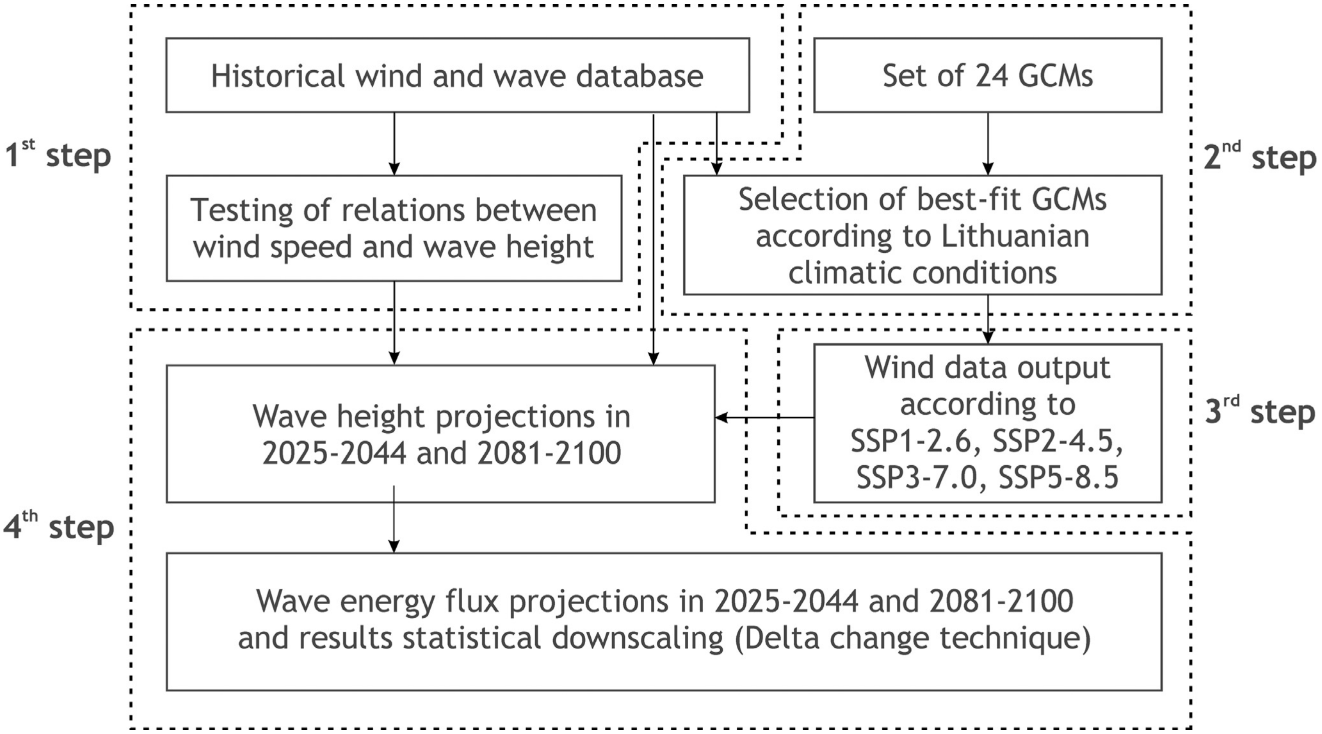

Figure 2 Workflow of the research.

$$\theta = arctan\left(\frac{u}{v}\right) + \Phi$$

where:

$$\Phi = \begin{cases} 0^\circ & if \quad u < 0 \quad and\ v < 0 \\ 180^\circ & if \quad v \geq 0 \\ 360^\circ & if \quad u \geq 0 \quad and\ v < 0 \end{cases} \tag{3}$$

According to the calculated values of wind speed and wind direction, three best-fit GCMs were selected from the set of 24 GCMs that simulated wind data output according to four previously mentioned SSP scenarios. The selection was done in three steps for the historical reference period (1995—2014). For the primary evaluation, the differences in average wind speed were calculated between simulated by GCMs and observed at MS. The obtained differences disclosed the potential deviations from the real observations and systematic errors of models. The models whose deviations did not exceed ±5% were analysed in the further step. The secondary evaluation step consisted of the comparison of the cases of wind directions. The mean absolute error of total wind cases according to 16 wind directions for each GCM was calculated. Finally, the correlation between the sum of wind directions simulated by GCM and observed in Klaipėda MS was evaluated for the period of 1995—2014. In total, 16 wind directions were considered since the wind observations were based on such a number of directions. The 3 GCMs with the smallest deviations of average wind speed and mean absolute error of wind directions, and the strongest correlation were selected for the output (*u* and *v* components) extraction and for the projections of wave height (H, m) and following wave energy flux (W/m).

Wave energy density estimated according to the flowing equation (Henfridsson et al., 2007):

$$E = \frac{\rho g H^2}{16} \tag{4}$$

where E — energy density, J/m^2, ρ — sea water density, kg/m^3 (Baltic Sea — 1010 kg/m^3), g — acceleration due to gravity, m/s^2, H — wave height, m.

For the group speed estimation was use shallow water condition, which is represented in the following equation used by Zaitseva-Pärnaste and Soomere (2013) for the evaluation of ice cover and wave energy flow variation in the north-eastern part of the Baltic Sea:

$$c_g = \sqrt{gd} \tag{5}$$

where c_g — group speed m/s, d — sea depth at the place of wave observations, m.

And finally, the wave energy flux of the Baltic Sea near Klaipėda estimated according to Falnes (2002):

$$P = Ec_g \tag{6}$$

where P — energy flux, W/m.

The projections of wave energy flux were adjusted to the Klaipėda location using the delta change technique of model output statistics according to the wind data output of GCMs. The main idea of this widely used delta-change method (Bosshard et al., 2011; Teutschbein and Seibert, 2012) is to use the ratio between the GCM simulated future parameter and GCM simulated parameter in the past (reference period), and use it as a change factor to the dataset that based on the real observations. The correction is used to avoid the uncertainties raised due to systematic errors in GCM output. GCM simulated parameter in the past is also known as base-line climatology, but it only corresponds to GCM future projections and can't be assumed as the observed climate and can't be used for a proper evaluation. Therefore, the GCM-simulated differences between the future scenario and reference simulation are superimposed upon the observational time series. A multiplicative correction is used for the ratio-based parameters and is described by the following equations (Bosshard et al., 2011):

$$P_{ref} = P_{obs} \tag{7}$$

$$P_{fut} = P_{obs} \cdot \frac{P_{sim\_fut}}{P_{sim\_ref}} \tag{8}$$

where P_{obs} — observed parameter, P_{ref} — reference parameter, P_{sim_ref} — GCM simulated parameter in the reference period, P_{sim_fut} — GCM projected parameter in the future, P_{fut} — adjusted future projection of analysed parameter to the study area.

It was determined how the WEF values of the 5, 25, 50, 75 and 95% probabilities changed in the future compared to the reference period. Past and future WEF data series were ranked from highest value to lowest value. Using the following equation (Weibull, 1939), the probability of each value was calculated:

$$P_{WEF} = \frac{m}{n+1} \times 100\% \tag{9}$$

where P_{WEF} — the probability of WEF, %; m — rank number, n — number of ranked values.

In the last step, the WEF values corresponding to the selected probabilities were obtained.

4. Results

4.1. Wind-wave relations according to historical observations

The wave phenomenon is usually linked directly to the origin of the wind effect if the tidal cycle is absent. The Baltic Sea is a quite closed sea with a narrow strait that connects it with the Atlantic Ocean. Therefore, the wind remains the main source of origin for the formation of waves. The created wind speed and wave height roses for the Lithuanian coastline disclosed the primary connection between these parameters (Figure 3). The most of observed winds were concentrated in west-origin directions and southeast winds, especially those with a speed higher than 8 m/s. The distribution patterns for wave heights indicated the domination of west-origin waves as well. Meanwhile, east-origin waves accounted for a certain part of wave cases, however, the dominant heights were up to 1 m and did not reach 1.5 m. The statistical relations between the wind speed of eight directions and the wave height at the same wind direction were created for the period 1995—2014 (Figure 4). Additionally, the percentage of distribution of wave directions at each wind direction was calculated. The directions were considered for the equations of wave height prediction according to wind speed. For each wind direction, the wave height of the same direction plus one neighbouring direction clockwise and counterclockwise were chosen in order to cover possible fluctuations in wave directions due to steady wind.

The obtained results of the relations disclosed clear strong relation between wind speed and wave height. The established regularities showed a clear distribution of the relations across wind directions. The strongest relations between wind speed and wave height were obtained for the winds of west directions origin. Accordingly, the strongest correlation coefficients of 0.87 were found for the winds of west and southwest directions, and 0.84 for northwest. Under the influence of the west wind, the wave height increased by 1 meter on average at each increase of wind speed by 5 m/s. The most dominant wave directions were west and southwest at west winds, 73% and 24% of total cases respectively. Similar patterns were obtained for the northwest wind since the most dominant wave directions of total cases were northwest (70%) and west (26%). During the southeast winds, the major cases (82%) of wave directions were southwest as well. Only 11% of waves were south direction. Weaker correlation coefficients were found for north, south and southeast winds. But the worst relations between wind speed and wave height were found for easterly winds, especially, from east and northeast directions. The winds of aforementioned directions had the worst correlation coefficients between wind speed and wave height because the obtained coefficients were 0.54 for the northeast and 0.66 for the east wind.

The found differences in the strength of the relations are closely related to the location of the case study coastline. Lithuanian coastline is located on the east coast of the Baltic Sea and is oriented from south to north. Accordingly, the westerly flow of northern hemisphere is met by the case study area perpendicularly. The acceleration distance of west directions wind has no orographic barriers, therefore the effect on the wave height and direction are more fluent. The opposite effect is for the eastern winds. Here land and topography cause surface roughness for the wind acceleration, turbulence, and direction. Additionally, the waves during the eastern winds may be caused by other local factors and may be induced by swell left after wind change in a relatively short time period. Consequently, the effect of wind speed on the wave height decreased noticeably, e.g. even at 10 or 15 m/s wind speed of the northeast and east directions the wave heights did not change significantly and varied between 0.2 and 1.5 m. The obtained relations provided a basis for the wave height prediction on a daily scale according to wind speed and wind direction. Using daily wave height observations and their predictions generated by equations, the correlation coefficient between them reached 0.89 for the period 1995-2014. The results confirmed the suitability of obtained relations for the projections of the wave height based on the wind data under climate change.

4.2. Selection of best-fit GCMs in the reference period

For the projections of wind speed and further WEF according to previously obtained relations between wind speed and wave height, the selection of the GCMs with the best representation of local wind characteristics was performed. The analysis of the best-fit GCMs in the reference period was done according to the data of Klaipėda MS. The set of

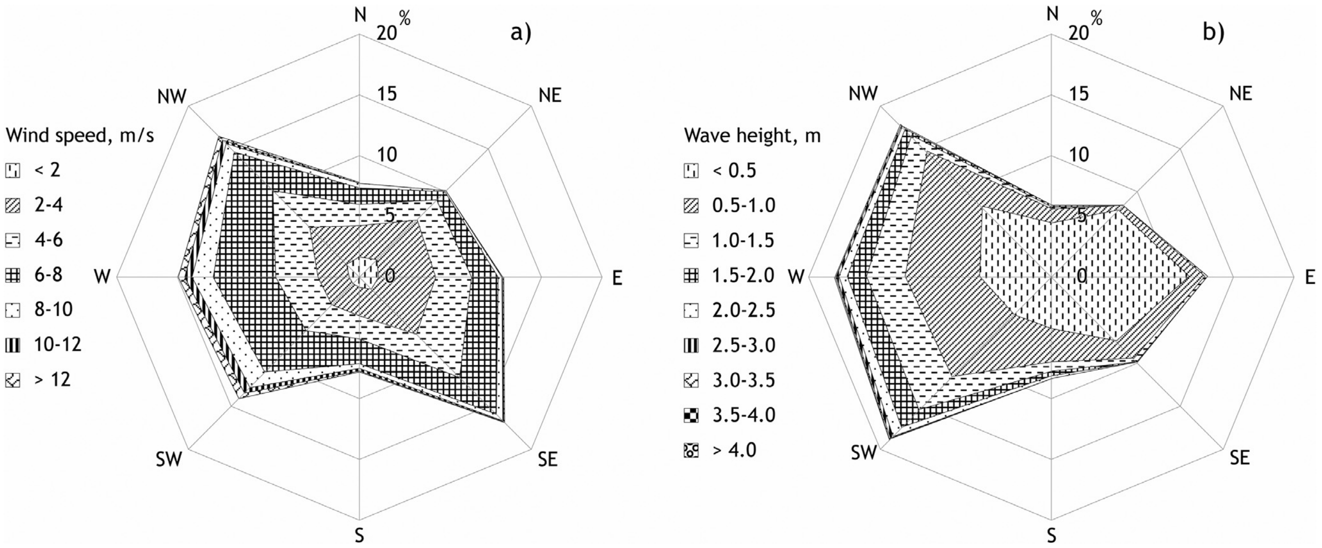

Figure 3 Wind rose of Klaipėda MS, a) and wave rose of wave monitoring station, b) according to 8 directions for the period of 1995—2014.

24 GCMs was selected for this purpose. Only the GCMs that contained all SSP scenarios were selected. Two main parameters, the average wind speed and the sum of days with the certain wind direction (each of 16 directions) were analysed for the period of 1995—2014. For the average wind speed, the deviation of GCM simulation from the historical observations and the mean absolute error of cases of 16 wind directions for each GCM were calculated, as well as the correlation between the sum of wind directions simulated by GCM and observed in Klaipėda MS was evaluated (Table 1). The deviations of the average wind speed of the selected 24 GCMs fluctuated in a wide range from —39.9 and 29.1%. Therefore, the models with the smallest deviations were indicated. Only the wind speed deviations of 8 models varied between ±5%. Those models were filtered in more detail using the distribution of the sum of the days between particular wind directions. The mean absolute error of wind directions showed the patterns of how well each GCM simulated the total amount of wind events according to 16 directions. The results defined three groups of GCMs that provided mean absolute errors of —8.50, —0.06 and 0.25 respectively. Therefore, the group of GCMs with the smallest error (—0.06) was considered for a potential selection. The correlation of wind direction between observed and GCMs simulated values indicated a wide range of correlation coefficients, thus the models with the relatively highest correlation were chosen in the next step. BCC-CSM2-MR and INM-CM4-8 models were chosen as the model with the smallest deviations in average wind speed and relatively high correlation coefficients in wind direction. Whereas EC-Earth3-Veg-LR was chosen as a model with relatively highest correlation in wind direction analysis from the Earth3 models group. The comparison of the wind roses of the selected GCMs with the Klaipėda MS showed a relatively similar distribution of wind speeds according to wind direction (Figure 5). Therefore, the mentioned GCMs represented local wind conditions well enough considering the fact that GCMs are created to simulate global climate. The ensemble was formed of three selected GCMs that were indicated as the best-fit models for the following wind speed and direction projections in the Lithuanian coastline according to SSP climate scenarios in the near (2025—2044) and far (2081—2100) future.

4.3. Wind speed projections in the near and far future

Based on the ensemble of three selected GCMs the projections of wind speed were calculated for the near and far future (Table 2). For the final projections, 8 wind directions were chosen since wave observations were based on 8 directions. The deviations in wind speed projections did not show any significant changes between SSP scenarios in the near future. The overall tendencies showed increased values for SSP2-4.5 and SSP5-8.5 scenarios. The larger differences in wind speed projections were found between the wind directions. The increase in wind speed was obtained for the winds of west, southwest and south directions. According to the ensemble of projections, the increase of mentioned winds may vary in the range of 1.2—3.6% compared with the historical reference period. Meanwhile, a decrease of 0.3—2.2% in wind speed was found for the southeast wind according to all SSP scenarios. In the far future, the wind speed projections gained a bit different character because the projected changes showed opposite tendencies between SSP scenarios. SSP3-7.0 and SSP5-8.5 mainly indicated the decrease of up to 6.3% in wind speed, especially for the winds in north and east directions. SSP1-2.6 scenario indicated a general increase of 0.8—3.9% in wind speed for all directions except southeast wind. In the far future, the decrease in wind speed of winds in southeast direction was projected by all SSP scenarios, as well as in the near future. Most of

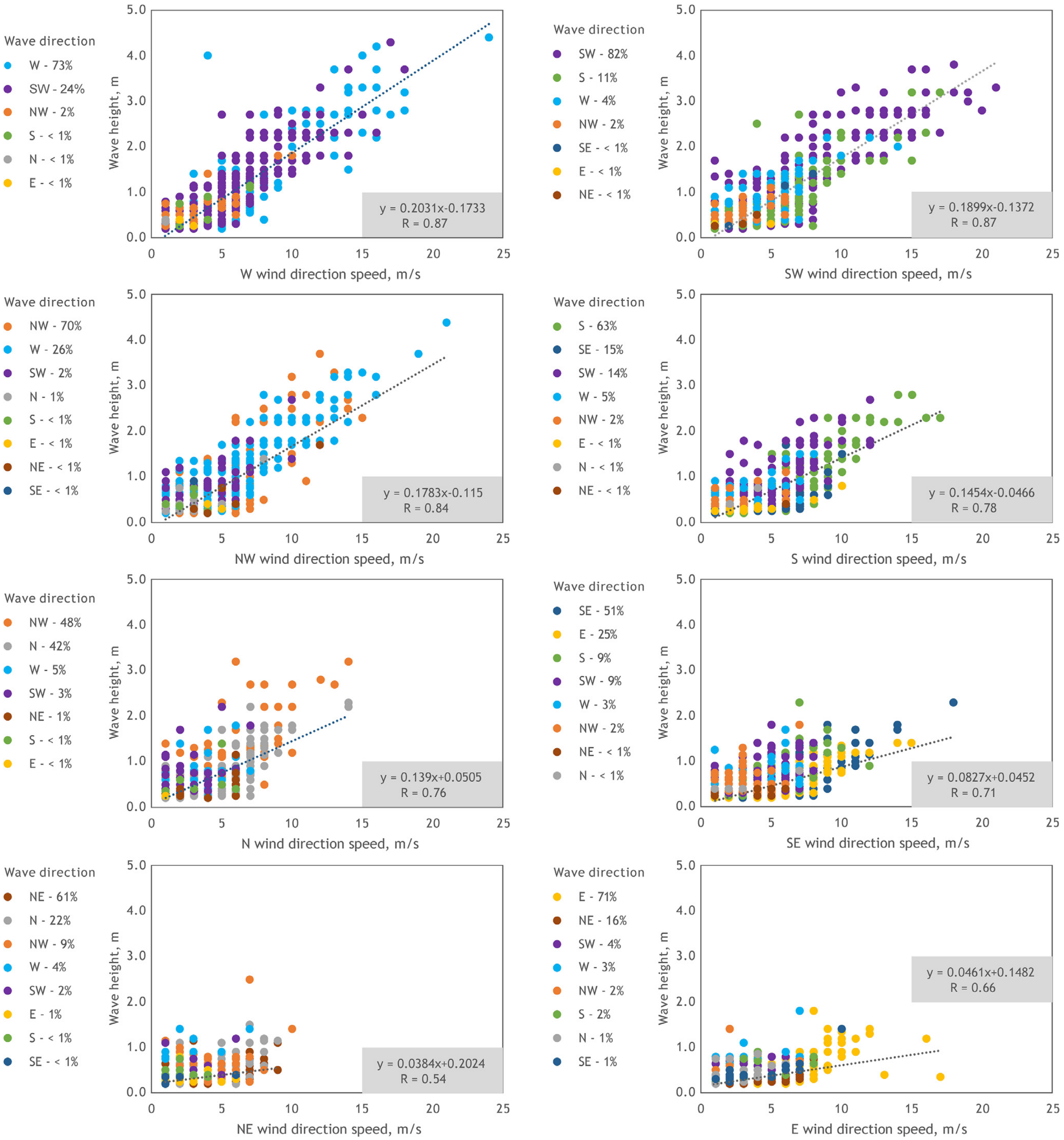

Figure 4 The relations between wind speed of a particular direction (horizontal axis) and wave height (vertical axis) obtained at the same wind direction for the period 1995—2014; distribution of wave directions in percentage at each wind direction; equations of the relationship according to the wind speed of certain wind direction and the wave height of the same direction plus one neighbouring direction clockwise and counterclockwise; and correlation of listed equations.

the projections showed an increase in the speed of west and southwest winds which are dominant wind directions for the Lithuanian coastline. Therefore, even a small increase or decrease in wind speed of mentioned origin of the direction may cause significant changes in the wave height since the obtained relations between wave height and winds of west origin were very strong.

4.4. Wave energy flux projection in the near and far future

The projections of wave energy flux were generated using wave height as a derived unit which was based on the projections of wind speed and its direction and the relations between wind speed and wave height. According to

Table 1 The deviations (%) of the GCM simulated wind speed comparing with the historical observations in the 1995—2014 reference period, the mean absolute error of wind directions and the correlation of 16 wind directions between direction cases (sum of the days) of observed and simulated according to GCM, and three selected best-fit GCMs (in bold).

GCM	Spatial resolution (lat. × lon.)	∆ wind speed, %	Mean absolute error of wind directions	Correlation of wind directions
ACCESS-CM2	1.25° × 1.875°	7.1	0.25	0.32
ACCESS-ESM1-5	1.25° × 1.875°	−16.9	0.25	0.51
AWI-CM-1-1-MR	0.935° × 0.938°	−19.4	0.25	0.51
BCC-CSM2-MR	1.121° × 1.125°	−0.9	−0.06	0.52
CMCC-CM2-SR5	0.942° × 1.25°	10.4	0.25	0.42
CMCC-ESM2	0.942° × 1.25°	8.7	0.25	0.46
EC-Earth3	0.702° × 0.703°	2.8	−0.06	0.50
EC-Earth3-AerChem	0.702° × 0.703°	3.1	−0.06	0.44
EC-Earth3-CC	0.702° × 0.703°	5.2	−0.06	0.47
EC-Earth3-Veg	0.702° × 0.703°	3.9	−0.06	0.51
EC-Earth3-Veg-LR	1.121° × 1.125°	−4.9	−0.06	0.58
GFDL-CM4	1.0° × 1.25°	6.4	0.25	0.47
GFDL-ESM4	1.0° × 1.25°	8.4	0.25	0.51
IITM-ESM	1.905° × 1.875°	27.0	0.25	0.76
INM-CM4-8	1.5° × 2.0°	1.5	−0.06	0.49
INM-CM5-0	1.5° × 2.0°	−1.5	−0.06	0.36
IPSL-CM5A2-INCA	1.895° × 3.75°	−15.9	−0.06	0.26
IPSL-CM6A-LR	1.2676° × 2.5°	−28.5	0.25	0.38
KACE-1-0-G	1.25° × 1.875°	29.1	−8.50	0.18
KIOST-ESM	1.865° × 1.875°	−33.7	−0.06	0.44
MIROC6	1.4° × 1.406°	−39.9	0.25	−0.13
MPI-ESM1-2-HR	0.935° × 0.9375°	−19.4	0.25	0.56
MPI-ESM1-2-LR	1.865° × 1.875°	1.1	0.25	0.39
MRI-ESM2-0	1.121° × 1.125°	−15.0	0.25	0.56

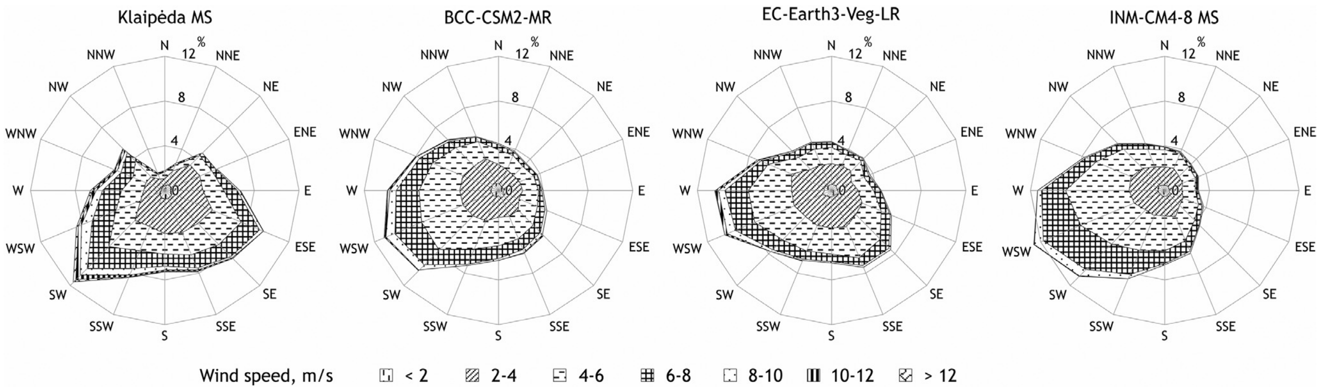

Figure 5 Wind roses for Klaipėda MS and for the corresponding grid cell of three selected GCMs according to 16 directions for the reference period of 1995—2014.

obtained values, the wave energy flux (WEF, kW/m) on average reached 3.11 kW/m, and the wave height (H, m) 0.65 m in the Baltic Sea at Klaipėda during the reference period (1995—2014). The highest WEF values were estimated in the autumn-winter time (from 2.89 to 5.42 kW/m), and the lowest in the spring-summer season (from 1.36 to 2.60 kW/m).

The projections of wave energy flux in the near (2025—2044) and far (2081—2100) future disclosed the main tendencies of change according to four SSP scenarios. The deviations in WEF values were calculated by comparing them with the reference period (Figure 6). The winter months were distinguished by a significant increase in WEF, while the autumn showed a decrease in WEF. These tendencies became obvious, especially in the far future. A slightly positive increase in WEF values was obtained in the spring and summer seasons. The deviations in wave energy flux values, expressed as a % from the reference period, differed between the near and far future despite the determined similar tendencies.

In the near future, on average the largest increase in WEF was found in February (8%) and January (22%) according to

Table 2 The deviations (%) of the ensemble of wind speed projections comparing with the historical reference period according to wind direction and SSP scenarios in near (N) and far (F) future.

Ensemble	Wind direction							
	N	NE	E	SE	S	SW	W	NW
SSP1-2.6_N	1.6	−0.8	1.0	−0.3	−0.5	0.0	1.7	−0.9
SSP2-4.5_N	−0.7	3.0	3.3	−0.7	2.1	1.3	2.1	1.2
SSP3-7.0_N	−0.5	0.8	0.6	−0.2	1.2	2.0	1.8	0.7
SSP5-8.5_N	2.2	-0.9	1.2	−2.2	3.6	2.0	3.3	−0.1
SSP1-2.6_F	0.8	2.1	1.5	−0.2	2.7	2.9	3.9	1.9
SSP2-4.5_F	−1.4	−2.6	0.7	−1.9	1.2	−0.8	0.9	−1.8
SSP3-7.0_F	−2.8	−6.3	−4.5	−3.8	−0.5	−1.3	−0.4	−2.0
SSP5-8.5_F	−1.3	−5.6	−1.7	−2.1	1.3	1.8	1.5	−0.9

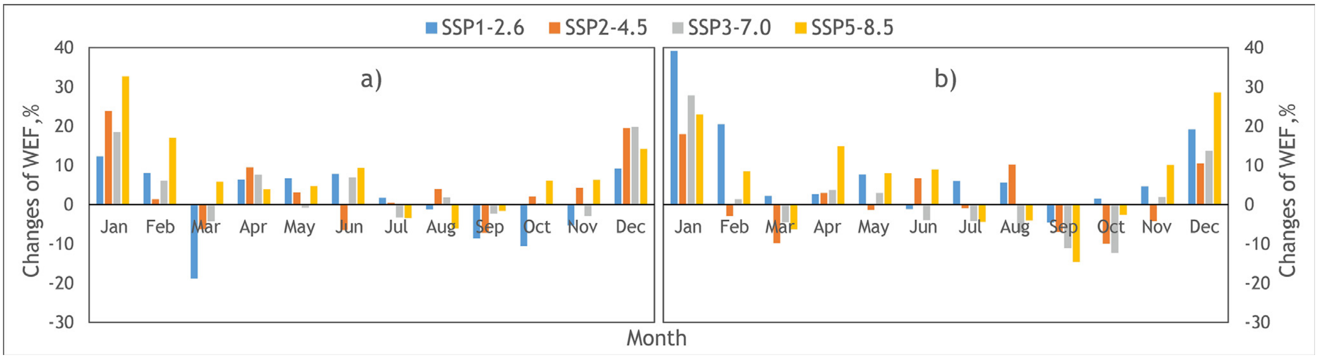

Figure 6 Changes (in %) of wave energy flux at the Baltic Sea Lithuanian nearshore in the near (a, 2025—2044) and far (b, 2081—2100) future comparing with 1995—2014.

three GCMs and four SSP scenarios (Figure 6a). During the spring seasons, the positive deviation in WEF was very slight and on average consisted of 0.5% higher values than in the reference period. The separate months of the spring season indicated from 6% decrease in March up to 7% increase in April compared with the reference period. A slight positive deviation of up to 1% in WEF values was projected during the summer season. The distribution of average deviation in WEF was from 4% increase in June to 1% decrease in July and August. In the autumn seasons, the projected WEF was on average 2% lower compared to the reference period. The tendencies between autumn months indicated a gradual increase in WEF from −5% in September up to −1% in October and 1% in November.

For the far future, the obtained deviations of wave energy flux projections were greater than in the near future. The main differences were determined by increased amplitude between different seasons (Figure 6b). Looking into individual seasons, the largest increase in WEF was in the winter time where the average increase of 17% was found. The projections of WEF in separate winter months highlighted high variability between the deviations. The WEF values based on 4 SSP scenarios average showed an increase for December, January and February by 18%, 27% and 7% respectively. In the spring and summer seasons, the projected wave energy flux increased by 1%. Compared with the near future, the deviation consisted only of 0.5% percentage points. From all spring months, the negative deviation of 5% was found only in March. An average increase of 4 and 6% is expected in the remaining two spring months. According to the far future projections for the summer season, WEF changed even less between the individual months. On average, the values fluctuated from an increase of 1% in July to an increase of 3% in June. The tendencies of the autumn season of WEF projections in the far future remained unchanged, as well as in the near future. The main difference was found in the amplitude of the projected WEF deviations. For September and October, the WEF values of the far future were 9% and 6% smaller, respectively, compared to the reference period. While 3% of an increase was projected for November.

After the analysis of the distribution of wave energy flux changes according to selected SSP scenarios, no clear tendencies were found in either the near or far future. The smallest increase in WEF values in the near future was found according to the SSP1-2.6 scenario (1%), the average ones (up to 6%) according to the SSP2-4.5 and SSP3-7.0 scenarios, and the largest according to the SSP5-8.5 scenario (10%). Meanwhile, the distribution of regularities of WEF projections changed in the far future because the largest increase of 11% was obtained according to the SSP1-2.6 scenario. The other scenarios projected from 2—3% (SSP2-4.5 and SSP3-7.0) up to 8% (SSP5-8.5) higher values of WEF compared with the reference period.

For a better understanding of the possible range of changes in the theoretical potential of wave energy flux, the deviations of different probabilities were calculated according to selected SSP scenarios (Table 3). The projected WEF values were close to the reference period for all probabilities in the near future according to the SSP1-2.6

Table 3 Deviations (%) of wave energy flux of different probabilities in the near and far future comparing with the reference period.

Probability, %	2025–2044				2081–2100			
	SSP1-2.6	SSP2-4.5	SSP3-7.0	SSP5-8.5	SSP1-2.6	SSP2-4.5	SSP3-7.0	SSP5-8.5
5	1.2	5.4	3.0	9.0	11.4	−0.2	0.7	5.9
25	−0.1	5.2	5.0	9.1	10.4	2.5	1.4	7.3
50	−3.1	4.5	6.9	9.0	7.5	1.4	3.5	6.6
75	−1.7	2.3	4.2	6.2	3.7	0.5	0.6	3.0
95	1.7	0.6	7.3	5.3	0.7	1.5	−3.6	0.2

scenario. SSP2-4.5 scenario projected small changes in WEF for 95–75% probabilities but for the values of medium to rare probabilities (50–5%) the increase of around 5% was obtained. Much bigger changes were projected according to the SSP3-7.0 scenario, when the values of wave energy flux of the selected probabilities were from 4 to 7% higher compared to the reference period. For the SSP5-8.5 scenario, values of 95–75% probability showed 6% higher WEF while values of 50–5% probability – an increase of 9%. For the far future, the changes in WEF projections according to SSP2-4.5 and SSP3-7.0 scenarios varied only slightly. The largest differences in far future projections were found in SSP1-2.6 scenario due to rarer probabilities, such as 25% and 5%, the projected increases in WEF values were 10 and 11%, respectively. For the SSP5-8.5 scenario, the increase in WEF was projected as well and the values were on average 6.6% higher for probabilities of 50–5% than in the reference period.

5. Discussion

The wave energy resources of the Baltic Sea have been studied quite well. Based on previous research, the average wave energy flux varies between 1 and 2 kW/m in the territorial waters of Lithuania (Jakimavičius et al., 2018a; Kasiulis et al., 2015), between 0.7 and 1.5 kW/m at Latvia's coastline (Soomere and Eelsalu, 2014), and from 0.5 to 8 kW/m in the Baltic Sea in general (Kovaleva et al., 2017; Nilsson et al., 2019). For the comprehensive evaluation of the sea wave's energy application for electricity production purposes, it is important to understand how WEF will change in the future. The projections based on the output of global climate models are used for mentioned tasks. Groll et al. (2017) used the scenarios of the SRES group and the WAM model for the evaluation of wind speed and wave height changes in the last thirty years of the 21st century. The results indicated an increase in wind speed by up to 5%, and wave height by up to 10% comparing to 1961–1990. Similar tendencies of a 10% increase in wave height were obtained according to RCP8.5 (Bonaduce et al., 2019). Dreier et al. (2021) using the SWAN model and data from regional climate models under RCP scenarios determined that at the end of the 21st century, the wind speed in the Baltic Sea off the coast of Germany will increase to 7% on average, and the wave height to 11% compared to the reference period of 1971–2000. The newest SSP scenarios for assemblages of many GCMs project a decrease in wind speed (Carvalho et al., 2021), however, the lacking of studies on SSP scenarios requires a broader assessment of future wind changes under CMIP6 in order to compare with the output of CMIP5 (Jung and Schindler, 2022), especially in terms of WEF analysis.

This study was based on the application of a statistical model to predict wave heights. The relationship between the wind speed of eight directions and the wave height at the same wind direction was determined according to the data of historical observations in 1995–2014 for the following WEF evaluation and projections according to four SSP climate scenarios. Additionally, the wind output of 24 global climate models was compared with real observational data for the selection of GCMs that adequately represent the wind climate in the studied area. Global climate models of BCC-CSM2-MR, EC-Earth3-Veg-LR, and INM-CM4-8 were selected as best-fit GCMs for the Lithuanian coastline. Based on their results, the deviations of projected wind speed values fluctuated between −6.3% and 3.9% comparing with the reference period. For the dominant wind directions including west and southwest, low impact SSP1-2.6 climate scenario projected an increase in wind speed while the east-origin winds under the SSP scenarios of higher impact tend to decrease. These findings highlighted the importance of evaluation according to wind directions, since general wind tendencies for a major part of Europe project a strong decline by the end of the 21st century, particularly under the SSP5-8.5 scenario (Carvalho et al., 2021). Moreover, the study applied an ensemble of 15 GCMs instead of the selection of best-fit GCMs. Distribution of wind change patterns across the SSP scenarios, i.e. increase for SSP1-2.6 and decrease for SSP5-8.5 may be explained by the change in pressure gradients induced by the change of air temperature. The increased global temperature reduces temperature gradients between high and low latitudes, consequently, the pressure gradients change in mid-latitudes as well by weakening the wind-driving forces (Gou et al., 2011). All these changes in wind speed had an important impact on wave height parameters and, accordingly, WEF values. For the wave height and WEF, the projections indicated an increase in their values for the near and far future, up to 5 and up to 11% respectively. Essential differences were found only between individual scenarios. The highest increase was estimated according to SSP1-2.6 in the far future, while other scenarios projected a slightly lower increase. Despite the reduced wind speed for east-origin winds, the overall WEF tendencies indicated the growth due to the increase of west-origin winds.

The comparison of the obtained results emphasized two methodological differences from previous studies in the Baltic Sea. The projections in many previous studies were simulated based on global and regional climate models according to SRES (IPCC AR4) and RCP (IPCC AR5) climate scenarios (Dreier et al., 2021; Groll et al., 2017). Moreover, the usage of physical models such as WAM, SWAN or WWIII was widely applied (Alari et al., 2016; Björkqvist et al., 2020; Kanarik et al., 2021; Sapiega et al., 2023). The physical modelling for the south-eastern part of the Baltic Sea coastline was done using MIKE21 model (Jakimavičius et al., 2018a). In this study, the statistical model was used instead with its certain limitations as well. Prediction of wave heights based on physical models is significantly more accurate but requires reliable input data at the boundary of the domain and large computational resources. Meanwhile, statistical models are based on equations of relationships between the predictor and the predictand, therefore statistical relations can only be applied to the specific area for which they were obtained. Observational data availability is another limiting factor for the extent of the application of statistical models. In the case of a physical model, once we have created one and calibrated it to a certain location, the simulation may be done for the whole study area. On the other hand, statistical models can be a good solution for the primary overview and rough evaluation of possible changes with the lowest costs. Nevertheless, the selection of appropriate predictors is one of the most important aspects in the application of statistical models (Austin, 2017; Xie, 2011). The relationship between predictor and predictand should be interrelated on a physical basis instead of random statistical relation. Despite these limitations, the advantage of statistical models is their relatively quick and broad applicability. They have been successfully applied in the natural sciences, where they were used to predict complex processes, e.g. to predict wind speed and wind power (Jankevičienė and Kanapickas, 2023; Liu et al., 2010), to estimate wind speed and solar radiation (Zeng et al., 2020), to predict the average annual salinity of the Curonian Lagoon in the 21st century (Jakimavičius et al., 2018b), to evaluate fish abundance according to river water temperature and river discharge (Kriaučiūnienė et al., 2019).

This study is one of the first attempts to project changes in WEF of the Baltic Sea using a statistical model and SSP scenarios. There is still room for improvement, but the obtained results could be a starting point for further research. The involvement of regional climate models with fine spatial resolution, the prediction for the entire Baltic Sea area or at least part of it, and the comparison between statistical and physical models results may be the future perspectives for such kind of research. The findings of this study may be applied to the primary overview of possible changes in WEF in the future and the planning of adaptation measures to climate change. Due to altered patterns of wind and wave parameters, the results might be beneficial in the preparation of a national energy strategy by predicting what part of RES could be generated from wave energy. The evaluation of the obtained results and findings of the other authors concluded that the wave climate will change in the future, especially under climate change forces. In contrast to the kinetic and potential energy of the rivers (Jakimavičius et al., 2020), wave energy is a “sleeping giant” in the world of renewable energy sources. Therefore, it is worth paying more interest to the investigation and exploitation of this resource on a wider scale. In this way, we could gradually shift away from fossil fuels and start moving faster towards a climate-neutral society.

6. Conclusions

- The study revealed a strong correlation between wind speed and visually observed wave height of the same direction.
- After the analysis of wind parameters of 24 GCMs, it was found that BCC-CSM2-MR, INM-CM4-8 and EC-Earth3-Veg-LR were best-fit GCMs for Lithuanian climatic conditions.
- According to wind speed projections, the average speed may increase for the W, SW and S wind directions in the near and far future. However, the decrease for the east-origin winds in the far future was found.
- For the WEF values, the largest deviations in the near future were obtained according to SSP5-8.5 (9.9%), the medium — SSP2-4.5 and SSP3-7.0, and the smallest — SSP1-2.6. In the far future, the largest positive deviations were found according to SSP1-2.6 (up to 11.3%), smaller ones by SSP5-8.5, and the smallest by SSP2-4.5 and SSP3-7.0.
- From the seasonal perspective, WEF deviations based on the average of four SSP scenarios indicated perceptible deviations in the winter (up to 17% increase) and only slight deviations (up to ±1%) in the remaining seasons.

Acknowledgement

The authors are grateful to the Marine Research Department under the Environmental Protection Agency of Lithuania, which so kindly facilitated the wind and wave observation data necessary for this study. Also we acknowledge the World Climate Research Programme, which, through its Working Group on Coupled Modelling, coordinated and promoted CMIP6. We thank the climate modelling groups for producing and making available their model output, the Earth System Grid Federation (ESGF) for archiving the data and providing access, and the multiple funding agencies who support CMIP6 and ESGF.

Declaration of competing interest

The authors declare that they have no known competing financial interests or personal relationships that could have appeared to influence the work reported in this paper.

References

Ahn, J., Na, Y., Park, S.W., 2019. Development of Two-Dimensional Inundation Modelling Process using MIKE21 Model. KSCE J. Civ. Eng. 23, 3968—3977. https://doi.org/10.1007/s12205-019-1586-9

Alari, V., Staneva, J., Breivik, Ø., Bidlot, J.-R., Mogensen, K., Janssen, P., 2016. Surface wave effects on water temperature in the Baltic Sea: simulations with the coupled NEMO-WAM model. Ocean Dynam. 66, 917–930. https://doi.org/10.1007/s10236-016-0963-x

Anton, I.A., Rusu, L., Anton, C., 2019. Nearshore Wave Dynamics at Mangalia Beach Simulated by Spectral Models. J. Mar. Sci. Eng. 7, 206. https://doi.org/10.3390/jmse7070206

Aquaret, 2008. Case Study — Okeanos Pelamis Wave Farm. Available online: https://www.aquaret.com/images/stories/aquaret/pdf/cswavepelamis.pdf (accessed on 9 August 2022).

Atvira Klaipeda.lt, 2021. Klaipėda port's cargo turnover is without significant fluctuations. Available online: https://www.atviraklaipeda.lt/2021/06/18/klaipedos-uosto-kroviniu-apyvarta-be-dideliu-svyravimu/ (accessed on 11 August 2022) (in Lithuanian).

Austin, P.C., 2017. A Tutorial on Multilevel Survival Analysis: Methods, Models and Applications. Int. Stat. Rev 85, 185–203. https://doi.org/10.1111/insr.12214

Bonaduce, A., Staneva, J., Behrens, A., Bidlot, J.-R., Wilcke, R.A.I., 2019. Wave Climate Change in the North Sea and Baltic Sea. J. Mar. Sci. Eng. 7, 166. https://doi.org/10.3390/jmse7060166

Bosshard, T., Kotlarski, S., Ewen, T., Schär, C., 2011. Spectral representation of the annual cycle in the climate change signal. Hydrol. Earth Syst. Sci. 15 (9), 2777–2788. https://doi.org/10.5194/hess-15-2777-2011

Björkqvist, J.-V., Rikka, S., Alari, V., Männik, A., Tuomi, L., Pettersson, H., 2020. Wave height return periods from combined measurement—model data: a Baltic Sea case study. Nat. Hazard. Earth Sys. 20, 3593–3609. https://doi.org/10.5194/nhess-20-3593-2020

Camus, P., Losada, I.J., Izaguirre, C., Espejo, A., Menéndez, M., Pérez, J., 2017. Statistical wave climate projections for coastal impact assessments. Earth's Future 5, 918–933. https://doi.org/10.1002/2017EF000609

Carvalho, D., Rocha, A., Costoya, X., deCastro, M., Gómez-Gesteira, M., 2021. Wind energy resource over Europe under CMIP6 future climate projections: What changes from CMIP5 to CMIP6. Renew. Sust. Energ. Rev. 151, 111594. https://doi.org/10.1016/j.rser.2021.111594

Cuttler, M.V.W., Hansen, J.E., Lowe, R.J., 2020. Seasonal and interannual variability of the wave climate at a wave energy hotspot off the southwestern coast of Australia. Renew. Energy 146, 2337–2350. https://doi.org/10.1016/j.renene.2019.08.058

Divinsky, B.V., Kosyan, R.D., 2017. Spatiotemporal variability of the Black Sea wave climate in the last 37 years. Cont. Shelf Res. 136, 1–19. https://doi.org/10.1016/j.csr.2017.01.008

Dreier, N., Nehlsen, E., Fröhle, P., Rechid, D., Bouwer, L., Pfeifer, S., 2021. Future Changes in Wave Conditions at the German Baltic Sea Coast Based on a Hybrid Approach Using an Ensemble of Regional Climate Change Projections. Water 13, 167. https://doi.org/10.3390/w13020167

Elkut, A.E., Taha, M.T., Abu Zed, A.B.E., Eid, F.M., Abdallah, A.M., 2021. Wind-wave hindcast using modified ECMWF ERA-Interim wind field in the Mediterranean Sea. Estuar. Coast. Shelf Sci. 252, 107267. https://doi.org/10.1016/j.ecss.2021.107267

European Centre for Medium-Range Weather Forecasts (ECMWF), 2022. ERA5: How to calculate wind speed and wind direction from u and v components of the wind? Available online: https://confluence.ecmwf.int/pages/viewpage.action?pageId=133262398 (accessed on 25 August 2022).

European Parliament, 2009. Directive 2009/28/EC of the European Parliament and of the Council of 23 April 2009 on the promotion of the use of energy from renewable sources and amending and subsequently repealing Directives 2001/77/EC and 2003/30/EC. European Council, Brussels, Belgium. 5 June 2009. Available online: https://eur-lex.europa.eu/legal-content/en/ALL/?uri=CELEX%3A32009L0028 (accessed on 12 August 2022).

Eurostat, 2020. Renewable energy statistics. Available online: https://ec.europa.eu/eurostat/statistics-explained/index.php?title=Renewable_energy_statistics#Share_of_renewable_energy_more_than_doubled_between_2004_and_2020 (accessed on 10 August February 2022).

Eyring, V., Bony, S., Meehl, G.A., Senior, C.A., Stevens, B., Stouffer, R.J., Taylor, K.E., 2016. Overview of the Coupled Model Intercomparison Project Phase 6 (CMIP6) experimental design and organization. Geosci. Model Dev. 9 (5), 1937–1958. https://doi.org/10.5194/gmd-9-1937-2016

Falnes, J., 2002. Ocean Waves and Oscillating Systems: Linear Interactions Including Wave-Energy Extraction. Cambridge University Press, UK, 286 pp. https://doi.org/10.1017/CBO9780511754630

Groll, N., Grabemann, I., Hünicke, B., Meese, M., 2017. Baltic Sea wave conditions under climatechange scenarios. Boreal Env. Res. 22, 1–12.

Guo, H., Xu, M., Hu, Q., 2011. Changes in near-surface wind speed in China: 1969–2005. Int. J. Climatol. 31, 349–358. https://doi.org/10.1002/joc.2091

Henfridsson, U., Neimane, V., Strand, K., Kapper, R., Bernhoff, H., Danielsson, O., Leijon, M., Sundberg, J., Thorburn, K., Ericsson, E., Bergman, K., 2007. Wave energy potential in the Baltic Sea and the Danish part of the North Sea, with reflections on the Skagerrak. Renew. Energ. 32, 2069–2084. https://doi.org/10.1016/j.renene.2006.10.006

Islek, F., Yuksel, Y., 2021. Inter-comparison of long-term wave power potential in the Black Sea based on the SWAN wave model forced with two different wind fields. Dynam. Atmos. Oceans 93, 101192. https://doi.org/10.1016/j.dynatmoce.2020.101192

Jakimavičius, D., Adžgauskas, G., Šarauskienė, D., Kriaučiūnienė, J., 2020. Climate change impact on hydropower resources in gauged and ungauged Lithuanian river catchments. Water 12, 3265. https://doi.org/10.3390/w12113265

Jakimavičius, D., Kriaučiūnienė, J., Šarauskienė, D., 2018a. Assessment of wave climate and energy resources in the Baltic Sea nearshore (Lithuanian territorial water). Oceanologia 60 (2), 207–218. https://doi.org/10.1016/j.oceano.2017.10.004

Jakimavičius, D., Kriaučiūnienė, J., Šarauskienė, D., 2018b. Impact of climate change on the Curonian Lagoon water balance components, salinity and water temperature in the 21st century. Oceanologia 60 (3), 378–389. https://doi.org/10.1016/j.oceano.2018.02.003

Jankevičienė, J., Kanapickas, A., 2023. Projected Wind Energy Maximum Potential in Lithuania. Appl. Sci. 13, 364. https://doi.org/10.3390/app13010364

Jung, C., Schindler, D., 2022. A review of recent studies on wind resource projections under climate change. Renew. Sust. Energ. Rev. 165, 112596. https://doi.org/10.1016/j.rser.2022.112596

Kanarik, H., Tuomi, L., Björkqvist, J.-V., Kärnä, T., 2021. Improving Baltic Sea wave forecasts using modelled surface currents. Ocean Dynam. 71, 635–653. https://doi.org/10.1007/s10236-021-01455-y

Kasiulis, E., Punys, P., Kofoed, J.P., 2015. Assessment of theoretical near-shore wave power potential along the Lithuanian coast of the Baltic Sea. Renew. Sust. Energ. Rev. 41, 134–142. https://doi.org/10.1016/j.rser.2014.08.044

Kovaleva, O., Eelsalu, M., Soomere, T., 2017. Hot-spots of large wave energy resources in relatively sheltered sections of the Baltic Sea coast. Renew. Sust. Energ. Rev. 74, 424–437. https://doi.org/10.1016/j.rser.2017.02.033

Kriaučiūnienė, J., Virbickas, T., Šarauskienė, D., Jakimavičius, D., Kažys, J., Bukantis, A., Kesminas, V., Povilaitis, A., Dainys, J., Akstinas, V., Jurgelėnaitė, A., Meilutytė-Lukauskienė, D., Tomkevičienė, A., 2019. Fish assemblages under climate change in Lithuanian rivers. Sci. Total Environ. 661, 563–574. https://doi.org/10.1016/j.scitotenv.2019.01.142

Liu, H., Tian, H.-Q., Chen, C., Li, Y., 2010. A hybrid statistical method to predict wind speed and wind power. Renew.

Energ. 35, 1857—1861. https://doi.org/10.1016/j.renene.2009.12.011

Lobeto, H., Menendez, M., Losada, I.J., 2021. Future behavior of wind wave extremes due to climate change. Sci. Rep. 11, 7869. https://doi.org/10.1038/s41598-021-86524-4

Martinez, A., Iglesias, G., 2022. Climate change impacts on wind energy resources in North America based on the CMIP6 projections. Sci. Total Environ. 806, 150580. https://doi.org/10.1016/j.scitotenv.2021.150580

Mørk, G., Barstow, S., Pontes, M.T., Kabuth, A., 2010. Assessing the global wave energy potential. 29th International Conference on Ocean, Offshore Mechanics and Arctic Engineering. Shanghai, China, 6—11. https://doi.org/10.1115/OMAE2010-20473

Nilsson, E., Rutgersson, A., Dingwell, A., Björkqvist, J.-V., Pettersson, H., Axell, L., Nyberg, J., Strömstedt, E., 2019. Characterization of Wave Energy Potential for the Baltic Sea with Focus on the Swedish Exclusive Economic Zone. Energies 12, 793 pp. https://doi.org/10.3390/en12050793

Pryor, S.C., Schoof, J.T., Barthelmie, R.J., 2006. Winds of change?: Projections of near-surface winds under climate change scenarios. Geophys. Res. Lett. 33, L11702. https://doi.org/10.1029/2006gl026000

Reikard, G., Robertson, B., Buckham, B., Bidlot, J.R., Hiles, C., 2015. Simulating and forecasting ocean wave energy in western Canada. Ocean Eng. 103, 223—236. https://doi.org/10.1016/j.oceaneng.2015.04.081

Ross, D., 1995. Power from the waves. Oxford University Press, USA, 224 pp.

Sapiega, P., Zalewska, T., Struzik, P., 2023. Application of SWAN model for wave forecasting in the southern Baltic Sea supplemented with measurement and satellite data. Environ. Modell. Softw. 105624. https://doi.org/10.1016/j.envsoft.2023.105624

Soomere, T., Eelsalu, M., 2014. On the wave energy potential along the eastern Baltic Sea coast. Renew. Energ. 71, 221—233. https://doi.org/10.1016/j.renene.2014.05.025

Soomere, T., 2023. Numerical simulations of wave climate in the Baltic Sea: a review. Oceanologia 65 (1), 117—140. https://doi.org/10.1016/j.oceano.2022.01.004

Soran, M.B., Amarouche, K., Akpınar, A., 2022. Spatial calibration of WAVEWATCH III model against satellite observations using different input and dissipation parameterizations in the Black Sea. Ocean Eng. 257, 111627. https://doi.org/10.1016/j.oceaneng.2022.111627

Statistics Lithuania, 2022. Total gross electricity production from renewables. Available online: https://osp.stat.gov.lt/statistiniu-rodikliu-analize?hash=e69dc4ad-15d0-4d55-a261-96b455a7a20b#/ (accessed on 11 August 2022).

Teutschbein, C., Seibert, J., 2012. Bias correction of regional climate model simulations for hydrological climate-change impact studies: Review and evaluation of different methods. J. Hydrol. 456—457, 12—29. https://doi.org/10.1016/j.jhydrol.2012.05.052

Toffoli, A., Bitner-Gregersen, E.M., 2017. Types of Ocean Surface Waves, Wave Classification. In: Encyclopedia of Maritime and Offshore Engineering. John Wiley & Sons, Ltd, Chichester, UK, 1—8. https://doi.org/10.1002/9781118476406.emoe077

Universal Lithuanian Encyclopedia, 2022. The Baltic Sea. Available online: https://www.vle.lt/straipsnis/baltijos-jura (accessed on 12 August 2022) (in Lithuanian).

Vu Dinh, Q., Doan, Q.-V., Ngo-Duc, T., Nguyen Dinh, V., Dinh Duc, N., 2022. Offshore wind resource in the context of global climate change over a tropical area. Appl. Energ. 308, 118369. https://doi.org/10.1016/j.apenergy.2021.118369

Weibull, W., 1939. A statistical study of the strength of material. Ing. Vetenskaps Akad. Handl. (Stockholm), 151, 45 pp.

Xie, Y., 2011. Values and limitations of statistical models. Res. Soc. Strat. Mobil. 29, 343—349. https://doi.org/10.1016/j.rssm.2011.04.001

Zaitseva-Pärnaste, I., Soomere, T., 2013. Interannual variations of ice cover and wave energy flux in the northeastern Baltic Sea. Ann. Glaciol. 54, 175—182. https://doi.org/10.3189/2013aog62a228

Zheng, C., Xu, J., Zhan, C., Wang, Q., 2020. 21st Century Maritime Silk Road: Wave Energy Resource Evaluation. Springer, Singapore, 170 pp. https://doi.org/10.1007/978-981-15-0917-9

Oceanologia 65 (2023) 548—555

Available online at www.sciencedirect.com

ScienceDirect

journal homepage: www.journals.elsevier.com/oceanologia

ORIGINAL RESEARCH ARTICLE

Stripe segmentation of oceanic internal waves in SAR images based on Gabor transform and K-means clustering

Kai-Tuo Qi[a], **Hong-Sheng Zhang**[a], **Ying-Gang Zheng**[b], **Yu Zhang**[c,*], **Long-Yu Ding**[a]

[a] *College of Ocean Science and Engineering, Shanghai Maritime University, Shanghai, China*
[b] *Translational Research Institute of Brain and Brain-Like Intelligence, Shanghai Fourth People's Hospital, School of Medicine, Tongji University, Shanghai, China*
[c] *College of Harbour, Coastal and Offshore Engineering, Hohai University, Nanjing, China*

Received 9 September 2022; accepted 9 June 2023
Available online 24 June 2023

KEYWORDS
Oceanic internal waves;
Synthetic aperture radar;
Gabor transform;
K-means clustering;
Stripe segmentation

Abstract Oceanic internal waves are an active ocean phenomenon that can be observed, and their relevant characteristics can be acquired using synthetic aperture radar (SAR). The locations of oceanic internal waves must be determined first to obtain the important parameters of oceanic internal waves from SAR images. An oceanic internal wave segmentation method with integrated light and dark stripes was described in this study. To extract the SAR image characteristics of oceanic internal waves, the Gabor transform was initially used, and then the K-means clustering algorithm was used to separate the light (dark) stripes of oceanic internal waves from the background in the SAR images. The regions of the dark (light) stripes were automatically determined based on the differences between the three classes, that is, the dark stripes, light stripes, and background area. Finally, the locations of the dark (light) stripes were determined by shifting a given distance along the normal direction of the long side with the minimum bounding rectangle of the light (dark) stripes. The best segmentation results were obtained based on the intersection over the union of the images, and the accuracy of segmen-

---

* Corresponding author at: College of Harbour, Coastal and Offshore Engineering, Hohai University, Nanjing, 210024, China.
E-mail addresses: 2932366338@qq.com (K.-T. Qi), hszhang@shmtu.edu.cn (H.-S. Zhang), ingopro@qq.com (Y.-G. Zheng), jessicazhang@hhu.edu.cn (Y. Zhang), 1938556272@qq.com (L.-Y. Ding).

Peer review under the responsibility of the Institute of Oceanology of the Polish Academy of Sciences.

Production and hosting by Elsevier

https://doi.org/10.1016/j.oceano.2023.06.006

tation was verified. Furthermore, the effectiveness and practicability of the proposed method in the light and dark stripe segmentation of SAR images of oceanic internal waves were illustrated. The proposed method prepares the foundation for future inversion studies of oceanic internal waves.

1. Introduction

Oceanic internal waves can influence the local oceanic ecological environment, affect the safety of oceanic structures, and play an important role in the transportation of energy and materials in oceans, therefore it is crucial to study oceanic internal waves. However, it is difficult to observe oceanic internal waves in situ. Therefore, remote sensing is a common tool.

Many studies on the extraction features of oceanic internal waves from remote sensing images have yielded considerable progress (Dong et al., 2016; Kao et al., 2007; Lindsey et al., 2018; Rodenas and Garello, 1997, 1998; Simonin et al., 2009; Zheng et al., 2021b).

Wang et al. (2019) classified and detected oceanic internal waves in images captured by unmanned aerial vehicles (UAVs) using a principal component analysis network (PCANet) and support vector machine (SVM). Their approach can identify the locations of oceanic internal waves through a rectangular box. However, it cannot easily quantify the precise locations of their stripes. Similarly, Bao et al. (2020) detected oceanic internal waves with rectangular boxes based on faster regions with a convolutional neural network (Faster R-CNN) and discriminated between the characteristics of oceanic internal waves and those of ship wakes to a certain extent, avoiding confusion between the latter and the former. Using a modified U-Net framework, Li et al. (2020) extracted information on oceanic internal waves from Himawari-8 satellite images. Based on SegNet, Zheng et al. (2021a) proposed a method to identify whether synthetic aperture radar (SAR) images contain oceanic internal waves and obtain the respective locations of the light and dark stripes from SAR images.

As the characteristics of light and dark stripes in oceanic internal waves can directly represent their propagation and evolution, it is important to extract the features of oceanic internal waves in SAR images. In this study, the Gabor transform was used to extract the characteristics of these waves, and the K-means clustering algorithm was employed in the stripe segmentation of SAR images. The clustering results were morphologically processed to separate the light (dark) stripes of the waves from the background. Finally, the segmented image was compared with the manually generated stripe segmentation image, and the intersection over union (IoU) value was computed to validate the feature extraction quantitatively. After selecting the optimal segmentation image by IoU, the full light and dark stripe information is further segmented by comparing the differences between the three classes, that is, the dark stripes, light stripes, and background area.

2. Material and methods

2.1. Dataset

The image selected, shown in Figure 1, was obtained by the Advanced Land Observing Satellite (ALOS), taken at 02:19:28 on February 23, 2011. The image with a size of 1024 × 1024 pixels of Figure 1 is chosen as a sample for simplicity of calculation, as illustrated in Figure 2.

2.2. Method

The feature extraction procedure for oceanic internal waves in SAR images is shown in Figure 3.

Because of their functional properties, unlike those of optical images, the images acquired from SAR are prone to speckle noise, making subsequent identification and classification difficult. Therefore, the images must be filtered before segmentation. The Gabor transform (Gabor, 1946) introduced a time-localized window function and obtained its Fourier transform to extract the local information from the signal. The phase parameter controls the return value of the Gabor function, which consists of real and imaginary parts. The imaginary part is an odd symmetric filter, whereas the real part is an even symmetric filter. Even symmetric filters were chosen because odd symmetric filters cannot discern texture features (Malik and Perona, 1990). The real part of the two-dimensional Gabor filter is expressed as

$$\left.\begin{array}{l} g_{\lambda\theta\psi\sigma\gamma}(x,y)=e^{\left(-\frac{x'^2+\gamma^2y'^2}{2\sigma^2}\right)}\cos\left(2\pi\frac{x'}{\lambda}+\psi\right) \\ x'=x\cos(\theta)+y\sin(\theta) \\ y'=y\cos(\theta)-x\sin(\theta) \end{array}\right\} \quad (1)$$

where x, y represent the pixel location coordinates, x', y'represent the new coordinates generated by rotating the Gabor kernel function, λ is the wavelength of the cosine function, θ is the normal direction of a parallel strip, that is, the texture direction, ψ is the phase parameter of the cosine function, σ is the standard deviation of the Gaussian function, and γ is the aspect ratio of space.

Because the size and direction of each image feature are different, it is necessary to design filters with different sizes and directions for filtering. After testing, the optimal interval is 30° between 0° and 180°. As the real part of the Gabor filter is used, the ψ value is chosen as 0°, and γ is 1, which represents the circular Gabor filter. The spatial frequency can be changed between −0.5 and 0.5 through normalization. Because of the symmetry of the Fourier function, only the spatial frequency value between 0 and 0.5 is considered (Zhang et al., 2002). σ is related to b and λ, that is,

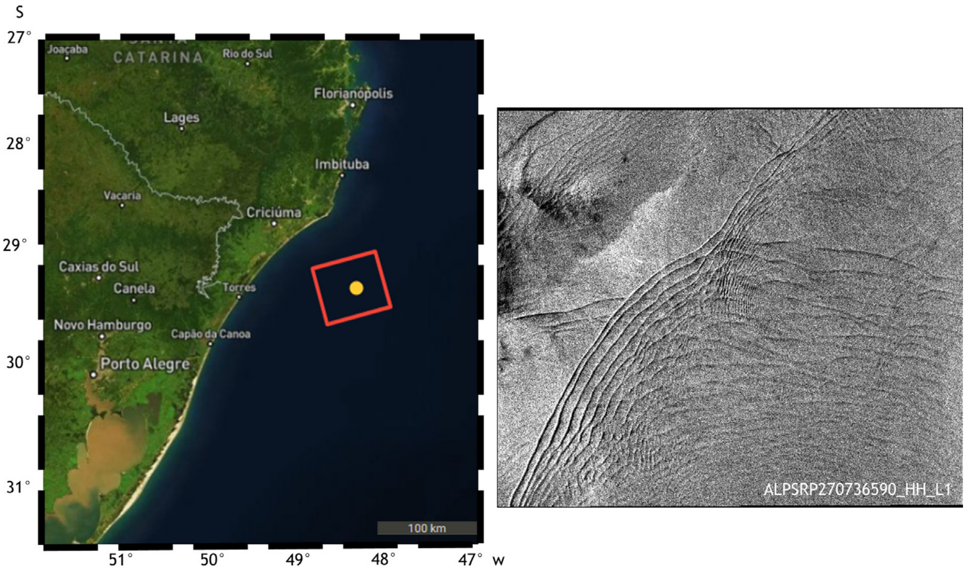

Figure 1 SAR images of oceanic internal waves from ALOS satellite (11200 × 9600).

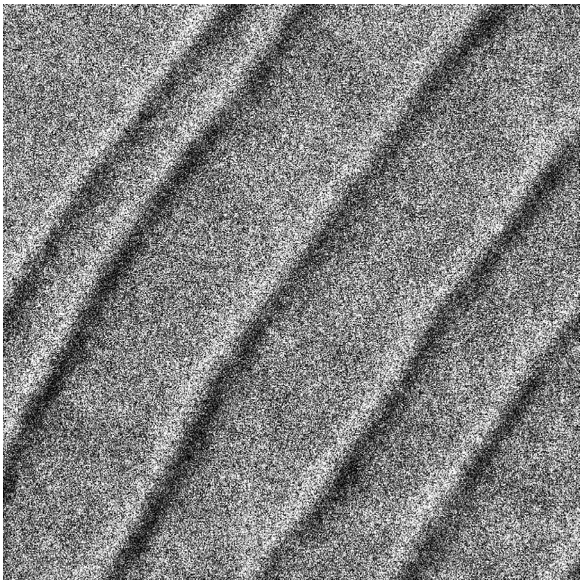

Figure 2 Selected area of oceanic internal waves (1024 × 1024). The location is shown in Figure 1.

$\sigma = \frac{\lambda}{\pi}\sqrt{\frac{\ln 2}{2}}\frac{2^b+1}{2^b-1}$ (Clausi and Jernigan, 2000), where b is the half-response spatial frequency bandwidth, and the default value, 2, is used in this study.

Different Gabor kernel functions can be obtained by combining different wavelengths and directions, and filter images of different characteristics can be obtained by convoluting the corresponding kernel functions with the images. After Gaussian smoothing, the feature images for classification were extracted. In this study, the Gaussian function was expressed as

$$G(x,y) = e^{\left(-0.5\left(\frac{x^2}{\sigma_G^2}+\frac{y^2}{\sigma_G^2}\right)\right)} \tag{2}$$

where σ_G denotes the standard deviation. This study uses the $\sigma_G = 3\sigma$, which was obtained by Jain and Farrokhnia (1991).

The K-means algorithm (MacQueen, 1967) has been extensively employed to construct an initial partition randomly for a specified number of clusters K, assign the cluster an initial center, and use an iterative approach to improve the partitioning effect by continually shifting the cluster center until the criteria function converges. The function is expressed as

$$E = \sum_{i=1}^{k}\sum_{x\in C_i}\left|x-\bar{x}_i\right|^2 \tag{3}$$

where $\overline{x_i}$ is the average value of the category C_i, x is the category, E is the sum of squared errors, and k is the number of clusters.

Light and dark stripes exist in the region where oceanic internal waves are located in SAR images. When k is set to 3 for segmentation, we observed that regardless of whether the stripes are light or dark, one of the grey values was close to the background in several images, which leads to confusion and makes subsequent classification difficult. Therefore, this study segmented the light or dark stripes whose grey values are different from those of the background and regarded them as one type and the rest as another type. That is, the value of k was 2. The class center point was initialized randomly, the number of changes of the center point was set to 3, and the change rate of the class center was set to 0.05. The images filtered by Gaber were segmented by K-means clustering and divided into background and light (dark) stripes. In Figure 2, the dark stripes are segmented because a significant difference exists between them and the background.

The light or dark stripes of oceanic internal waves were manually extracted to assess and screen the classification results. The dark stripes in Figure 2 are manually extracted, as shown in Figure 4.

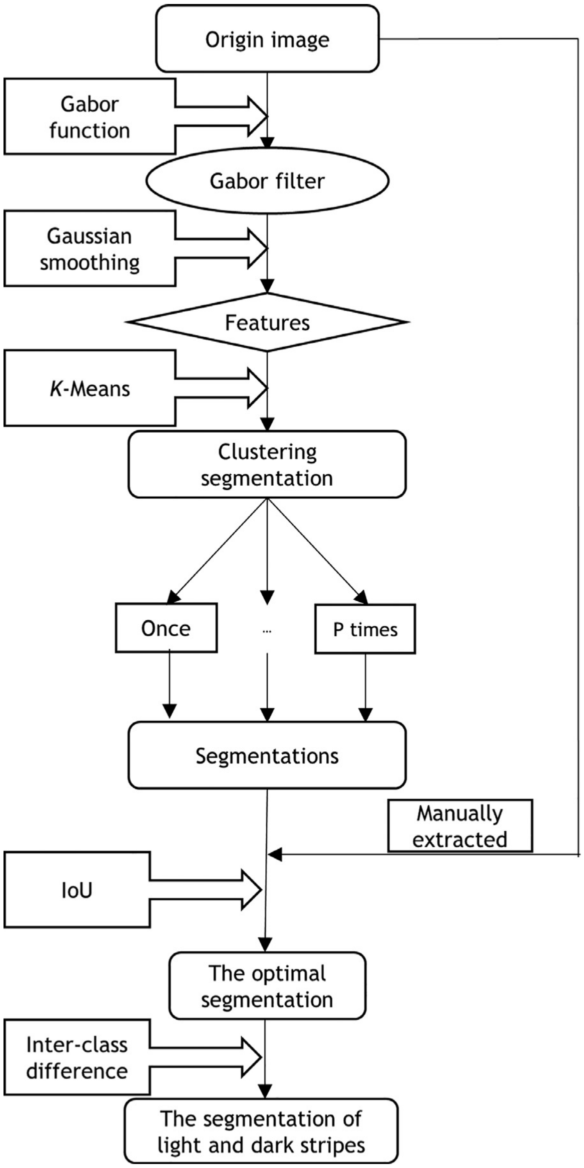

Figure 3 Flowchart for extracting the features of oceanic internal wave stripes, IoU — intersection over union.

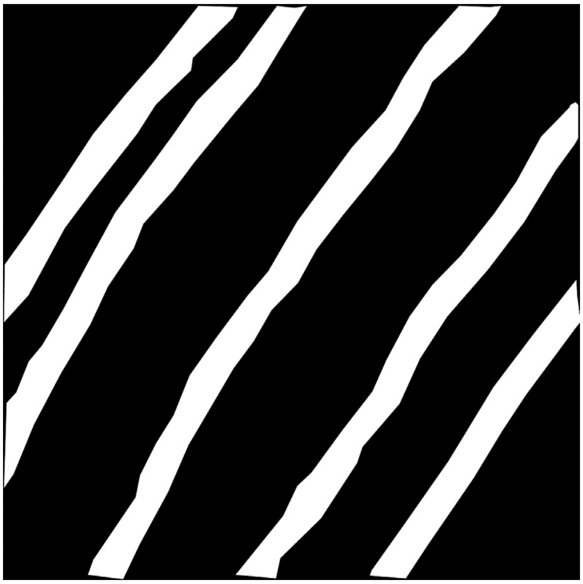

Figure 4 Effect of manual segmentation for dark stripes.

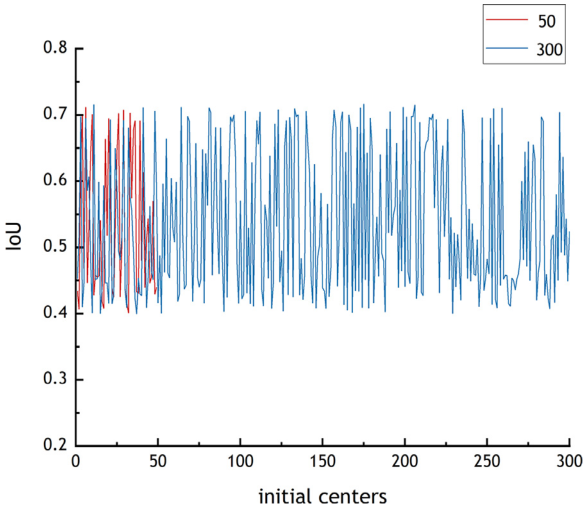

Figure 5 Intersection over union (IoU) variation with segmentation results for different initial centers.

3. Results

Because the initialization center of the K-means algorithm is random, different initial centers were selected for the tests. The segmentation results were compared with the manual extraction results, and IoU values were calculated. The optimal value of IoU remains the same after comparing the running results of 300 and 50 different initial centers. In Figure 5, the initial center is the number of randomly selected center points of Kmeans, that is, the number of tests. 50 and 300 were the number of tests. As shown in Figure 5, to reduce processing time and improve efficiency, selecting the segmented image corresponding to the optimal solution from the results of 50 runs is sufficient. In Figure 5, the IoU corresponding to the best dark stripe segmentation result was 0.71, and the segmentation results are shown in Figure 6.

The segmentation regions of the dark stripes are marked in red and overlaid with Figure 2 to make the segmentation effect easier to observe and verify, as shown in Figure 7.

The segmented image must be processed to further obtain the locations of the light stripes from Figure 2. Because of the characteristics of oceanic internal wave images, the minimum bounding rectangle of each dark-striped contour can be used (Li et al., 2021). Each light stripe was located at a specific distance D_i along the long side of the rectangle in the normal direction. In this study, D_i was approximately equal to the width of the contour of each stripe. Because the width of each stripe after segmentation is not a constant value, as shown in Figure 6, each stripe should be translated independently based on the varying distances. When the width of the stripe is constant, as shown in Figure 8 in blue, the long side of the minimum bounding rectangle and tangent point C_i of the stripe outline can be

Figure 6 Effect of segmentation for dark stripes under optimal intersection over union (IoU).

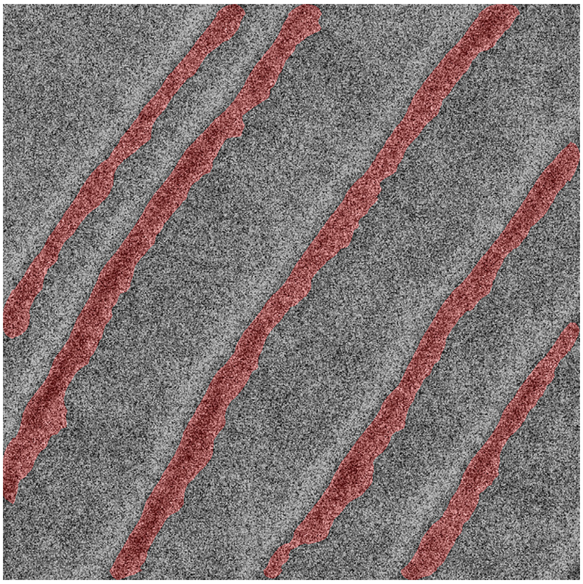

Figure 7 Comparison of the segmentation effect for dark stripes under optimal intersection over union (IoU).

used to create a line segment parallel to the short edge of the minimum bounding rectangle. The line segment intersects the contour at point B_i and intersects with the other long side of the minimum bounding rectangle at point A_i, therefore, the stripe width is $D_i \doteq \overline{A_iC_i} - \overline{A_iB_i}$. When the width of a stripe is not constant, translation distance D_i can be considered the average value of the width of the stripe. For the purpose of simplification, the width of each stripe was assumed to be a constant.

To obtain the real selection of green stripes in the process of translation, the dark stripe region obtained by segmentation is denoted as set m, and the two regions obtained by shifting the region along the inner and outer normal directions are denoted as sets n and p in Figure 8, respectively. Thus, three sets of light stripes, dark stripes, and background are formed. Because set m corresponds to dark stripes, set n corresponds to light stripes or the background area, and set p is determined accordingly. In the original image, the differences in grey values between the light stripes and dark stripes are relatively large. Therefore, the side that is the region of the light stripe can be automatically judged. The code is used to find the minimum bounding rectangle of the dark stripe outline, calculate the average width of the stripe, and determine the translation direction. Finally, the automatic extraction of light stripes was realized. Based on automatic judgment, the segmentation result of the light stripe is shown in the green area in Figure 9.

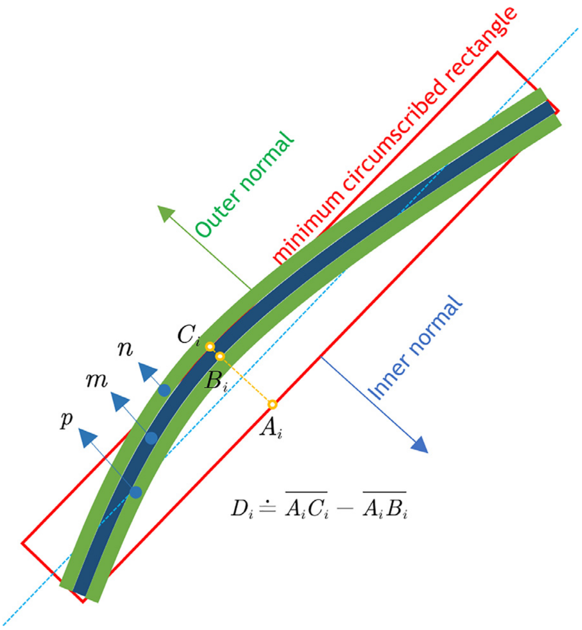

Figure 8 Stripe translation diagram.

The segmentation regions of the stripes were overlaid with Figure 2 to make the segmentation effect easier to observe and verify, as shown in Figure 10. Because of the significant differences in the grey values between the light and dark stripes, the fitted grey value curve exhibits fluctuations. Based on these observations, the relative locations of the light and dark stripes were determined, and their accuracies were further confirmed. To eliminate the influence of noise, 33 × 33 mean filtering was used to process the original image data. Figure 11 shows the mean change of the row and column grey values of the center point of the image.

As shown in Figure 11, regardless of the grey values of the row or column pixels, the grey values change from light to dark. The highest point of each line segment corresponds to the light stripe; the lowest point is the dark stripe; and the rest is the background color. The order of the grey value change is light-dark-background color, and the five segmented internal wave stripes are cycled five times in every run. Thus, the segmentation result, which was automatically selected based on the difference between classes, was verified.

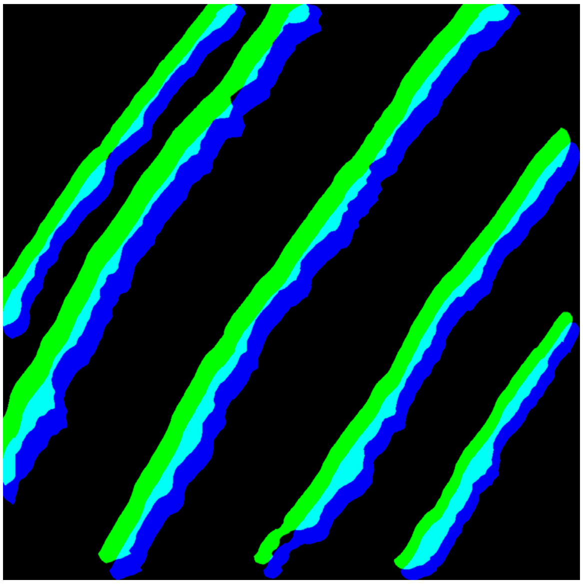

Figure 9 Segmentations of light and dark stripes after translation. (Blue is the segmented dark stripe, green is the light stripe obtained by translation, light blue is the intersection of light and dark stripes, and black is the background.) (For interpretation of the references to colour in this figure legend, the reader is referred to the web version of this article.)

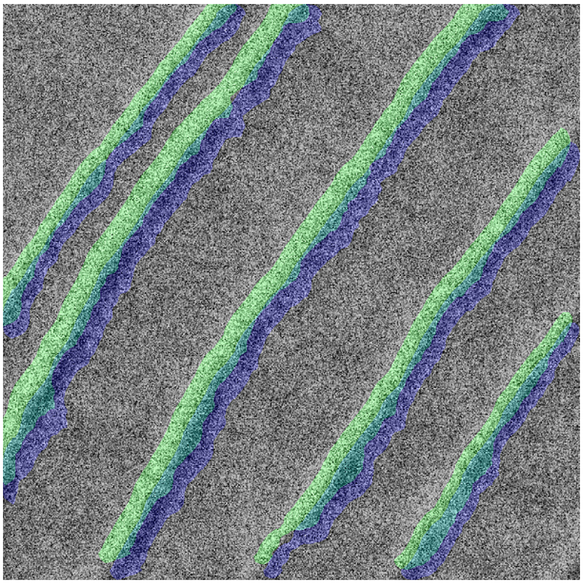

Figure 10 Comparisons of light and dark stripes in the original image after translation. (Blue is the segmented dark stripe, green is the light stripe obtained by translation, and light blue is the intersection of light and dark stripes.) (For interpretation of the references to colour in this figure legend, the reader is referred to the web version of this article.)

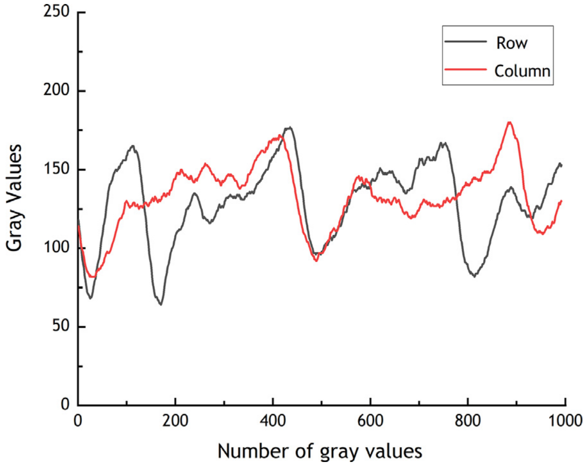

Figure 11 Variations in the grey values of the rows and columns at the center of the image. (For interpretation of the references to colour in this figure legend, the reader is referred to the web version of this article.)

Table 1 The intersection over union (IoU) of samples.

Sample	Proposed algorithm	U-Net
A	0.581	0.179
B	0.461	0.258
C	0.561	0.172

Five other samples containing oceanic internal wave SAR images were segmented to verify this method's robustness and stability. The selected images were numbered A, B, C, D, and E, respectively. Sample B is sourced from ALPSRP_270 736590_H1.1, imaging on January 16, 2007; samples A and C are from ALPSRP0521 44120_H1.1, imaging on February 23, 2011; sample D is from ALPSRP121523360 -H1.1, imaging on May 6, 2008; and sample E is from ALPSRP138520130-H1.1, imaging on August 30, 2008.

The segmentation results for D and E are shown in Figure 12. The segmentation results in the images are better for light stripes only or dark, indicating that the proposed method can completely segment oceanic internal waves using only light stripes or dark stripes.

The segmentation results were compared with those of U-Net (Ronneberger et al., 2015) segmentation, as shown in Figure 13. A total of 703 oceanic internal wave data points were used in the U-Net experiment. Envisat (Environmental Satellite), ERS-1 (the first European Remote Sensing Satellite), and ALOS were used as the sources of the SAR image data. In the obtained data, the color of the oceanic internal wave stripes is primarily dark and light, and there are few light-only or dark-only samples; therefore, it is difficult to identify samples D and E. In the training process, an SGD optimizer with a learning rate of 0.001, a batch size of 16, a momentum of 0.9, and a weight decay of 1×10^{-4} were used for training.

Table 1 show the IoUs of samples A, B, and C. It can be seen from Table 1 that the segmentation result of the proposed algorithm is better than that of U-Net. As shown in Figure 13, the segmentations of samples A and B agree with the regions where the oceanic internal waves were located. Moreover, the segmentation results of the Gabor filter are better than those of the U-Net results. In sample C, compared with C(II) and C(III) in Figure 13, the proposed method can roughly segment the contour of the internal waves, while U-Net is less effective for complex internal wave stripes. However, from C(VI) in Figure 13, the value of the inter-class difference at A and B is affected by the qual-

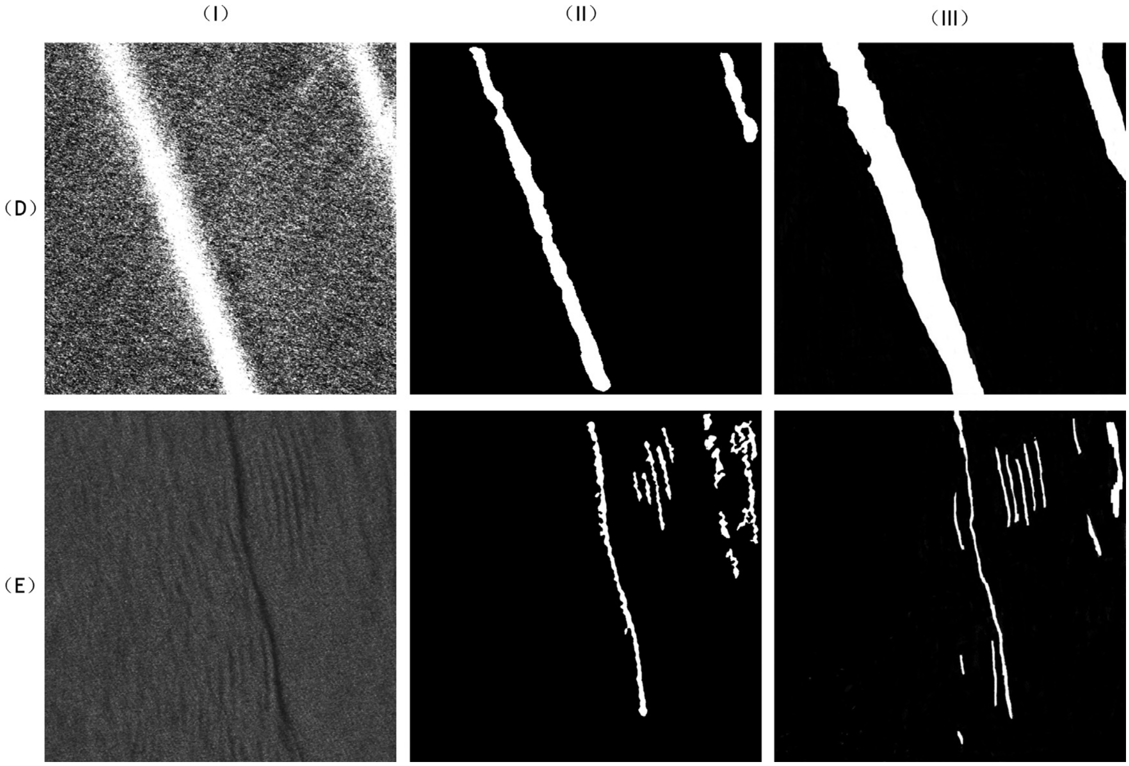

Figure 12 Oceanic internal wave light and dark stripe segmentation map for the ALOS satellite (I. original image of oceanic internal waves; II. segmentation after Gabor filtering; III. manual extraction).

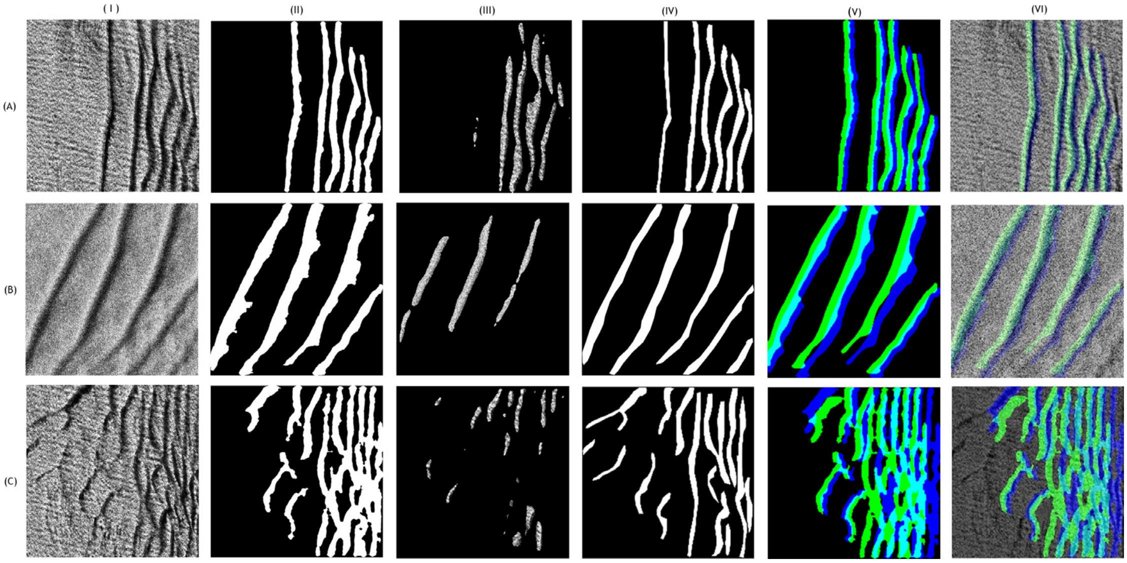

Figure 13 Segmentation for light and dark stripes of oceanic internal waves (each column from left to right represents the original image of internal waves, segmentation under the Gabor filter, U-Net segmentation, manual segmentation, segmentations of light and dark stripes, comparison between light and dark stripes in the original image, respectively).

ity of the grey values when the light stripes are obtained by the translation of the dark stripes. This leads to an error in the translation direction. However, this problem can be corrected using the frequency distribution of the translation direction of the stripes in the images. In addition, because of the complexity at C in C(VI), the dark stripes are connected after segmentation, and simultaneously affecting the translation distance of the stripe.

4. Discussion

By comparing the segmentation results of the light and dark stripes from different samples, the proposed method was observed to be robust and highly accurate. However, there were still defects. For example, image quality affects the translation distance and direction in the stripe translation process. Nevertheless, the segmentation method is effective and practical for the segmentation of light and dark stripes in oceanic internal wave images.

5. Conclusions

The light and dark stripes of oceanic internal waves were segmented based on Gabor filtering and the K-means clustering algorithm. The results show that the integrated algorithm proposed in this study has better effects on the segmentation of light and dark stripes in the SAR images. If the light or dark stripes are more distinct from the background, they can be better identified, and the relative locations of the corresponding dark or light stripes can be automatically determined by comparing inter-class differences. As a result, feature extraction for light and dark stripes in oceanic internal waves was realized, creating a foundation for the subsequent parameter inversion of oceanic internal waves.

The quality of the SAR images is unstable. For SAR images with poor imaging quality, the difference in the grey value of the image is small, making it challenging to extract the light and dark stripes, or the light and dark stripes extracted are discontinuous. However, the translation distance and direction in the process of stripe translation are affected. Although the error of the translation direction can be corrected by the frequency distribution, for intricate stripes, the stripes are connected after the segmentations, which has a negative impact on the subsequent translation. As a result, a certain degree of deficiency needs to be addressed in future studies.

Acknowledgments

The authors are grateful to the websites of Envisat, Sentinel, and ASF, which were used to collect the SAR images, and for the support of MATLAB. In addition, they are grateful to the Shanghai Frontiers Science Center of "Full Penetration" Far-Reaching Offshore Ocean Energy and Power.

Funding

This work was supported by the Science and Technology Commission of Shanghai Municipality (grants Nos. 21ZR1427000 and 17040501600).

Declaration of competing interest

The authors declare that they have no known competing financial interests or personal relationships that could have appeared to influence the work reported in this paper.

References

Bao, S., Meng, J., Sun, L., Liu, Y., 2020. Detection of ocean internal waves based on Faster R-CNN in SAR images. J. Ocean. Limnol. 38 (1), 55—63. https://doi.org/10.1007/s00343-019-9028-6

Clausi, D.A., Jernigan, E.M., 2000. Designing Gabor filters for optimal texture separability. Pattern Recogn. 33 (11), 1835—1849. https://doi.org/10.1016/S0031-3203(99)00181-8

Dong, D., Yang, X., Li, X., Li, Z., 2016. SAR Observation of Eddy-Induced Mode-2 Internal Solitary Waves in the South China Sea. IEEE T. Geosci. Remote 54 (11), 6674—6686. https://doi.org/10.1109/tgrs.2016.2587752

Gabor, D., 1946. Theory of communication. Part 1: The analysis of information. J. Inst. Electr. Eng. Pt. III Radio Comm. Eng. 93 (26), 429—441. https://doi.org/10.1049/ji-3-2.1946.0074

Jain, A.K., Farrokhnia, K., 1991. Unsupervised texture segmentation using Gabor filters. Pattern Recogn. 24 (12), 1167—1186. https://doi.org/10.1016/0031-3203(91)90143-s

Kao, C.C., Lee, L.H., Tai, C.C., Wei, Y.C., 2007. Extracting the ocean surface feature of nonlinear internal solitary waves in MODIS satellite images. In: International Conference on Intelligent Information Hiding and Multimedia Signal Processing, 1, 27—30. https://doi.org/10.1109/IIHMSP.2007.4457485

Li, Z., Guo, B., Ren, X., Liao, N.N., 2021. Vertical interior distance ratio to minimum bounding rectangle of a shape. In: Abraham, A., Hanne, T., Castillo, O., Gandhi, N., Nogueira Rios, T., Hong, T.P. (Eds.), Hybrid Intelligent Systems. HIS 2020. Advances in Intelligent Systems and Computing. Springer, Cham Vol. 1375. https://doi.org/10.1007/978-3-030-73050-5_1

Li, X.F., Liu, B., Zheng, G., Ren, Y., Zhang, S., Liu, Y.J., Gao, L., Liu, Y.H., Zhang, B., Wang, F., 2020. Deep learning-based information mining from ocean remote sensing imagery. Natl. Sci. Rev. 7 (10), 1584—1605. https://doi.org/10.1093/nsr/nwaa047

Lindsey, D.T., Nam, S., Miller, S.D., 2018. Tracking oceanic nonlinear internal waves in the Indonesian seas from geostationary orbit. Remote Sens. Environ. 208, 202—209. https://doi.org/10.1016/j.rse.2018.02.018

MacQueen, J., 1967. Some methods for classification and analysis of multivariate observations. Proc. Fifth Berkeley Symp. Math. Statistics Probab. 1, 281—298.

Malik, J., Perona, P., 1990. Preattentive texture discrimination with early vision mechanisms. J. Opt. Soc. Am. 7 (5), 923—932. https://doi.org/10.1364/josaa.7.000923

Rodenas, J.A., Garello, R., 1998. Internal wave detection and location in SAR images using wavelet transform. IEEE T. Geosci. Remote 36 (5), 1494—1507. https://doi.org/10.1109/36.718853

Ronneberger, O., Fischer, P., Brox, T., 2015. U-Net: Convolutional networks for biomedical image segmentation. In: Navab, N., Hornegger, J., Wells, W., Frangi, A. (Eds.), Medical Image Computing and Computer-Assisted Intervention — MICCAI 2015. MICCAI 2015. Lecture Notes in Computer Science, Vol. 9351. Springer, Cham, 234—241. https://doi.org/10.1007/978-3-319-24574-4_28

Rodenas, J.A., Garello, R., 1997. Wavelet analysis in SAR ocean image profiles for internal wave detection and wavelength estimation. IEEE T. Geosci. Remote 35 (4), 933—945. https://doi.org/10.1109/36.602535

Simonin, D., Tatnall, A.R., Robinson, I.S., 2009. The automated detection and recognition of internal waves. Int. J. Remote Sens. 30 (17), 4581—4598. https://doi.org/10.1080/01431160802621218

Wang, S., Dong, Q., Duan, L., Sun, Y., Jian, M., Li, J., Dong, J., 2019. A fast internal wave detection method based on PCANet for ocean monitoring. J. Intell. Syst. 28 (1), 103—113. https://doi.org/10.1515/jisys-2017-0033

Zhang, J.G., Tan, T.N., Ma, L., 2002. Invariant texture segmentation via circular Gabor filters. In: 2002 International Conference on Pattern Recognition, Vol. 2, IEEE, Quebec City, QC, Canada, 901—904. https://doi.org/10.1109/ICPR.2002.1048450

Zheng, Y.G., Zhang, H.S., Qi, K.T., Ding, L.Y., 2021a. Stripe segmentation of oceanic internal waves in SAR images based on SegNet. Geocarto Int. 37 (25), 8567—8578. https://doi.org/10.1080/10106049.2021.2002430

Zheng, Y.G., Zhang, H.S., Wang, Y.Q., 2021b. Stripe detection and recognition of oceanic internal waves from synthetic aperture radar based on support vector machine and feature fusion. Int. J. Remote Sens. 42 (17), 6710—6728. https://doi.org/10.1080/01431161.2021.1943040

Oceanologia 65 (2023) 556—563

Available online at www.sciencedirect.com

ScienceDirect

journal homepage: www.journals.elsevier.com/oceanologia

ORIGINAL RESEARCH ARTICLE

Modified logarithmic distribution of wind-driven flow velocity in remote foreshore of the non-tidal sea

Rafał Ostrowski, Magdalena Stella-Bogusz*

Institute of Hydro-Engineering, Polish Academy of Sciences, Gdańsk, Poland

Received 18 November 2022; accepted 9 June 2023
Available online 20 June 2023

KEYWORDS
Wave-induced nearbed velocities;
Wind-driven current;
Bed shear stresses;
Modified logarithmic velocity distribution

Abstract The paper presents the results of the novel modelling of the wind-driven current in the southern Baltic Sea. The steady current is accompanied by wave-induced orbital velocities. The bed boundary layer related to wave-induced oscillatory flow gives rise to the appearance of additional shear stresses affecting the wind-driven current. This impact included in the wind-driven current model yields a modified logarithmic velocity distribution. Theoretical velocity profiles are compared with the field data. The measurement database includes wind, wave and current parameters. The velocities and directions of the wind were collected from the anemometer installed at the Coastal Research Station (CRS) in Lubiatowo. Wave-current parameters at a depth of about 17 m were obtained from a location of approx. 1.5 Nm from the shoreline in the vicinity of CRS Lubiatowo. The study site hydrodynamics is typical of the south Baltic coast. The analysis shows good agreement between the measured flow velocities and the theoretical vertical distributions in the form of the modified logarithmic profile.

1. Introduction

In the case of the Baltic Sea (which belongs to shallow non-tidal seas), the remote foreshore zone stretches seawards from a so-called depth of closure h_c. This depth constitutes an offshore limit of the seabed changes (Dean, 2002) where even extreme storm waves are estimated not to generate high sediment transport rates. Hallermeier (1978, 1981) and Birkemeier (1985) derived unsophisticated formulas enabling the determination of the depth of closure h_c on the basis of "effective" parameters of deep-water waves (significant wave height H_{es0} and period T_{es0}). The effective wave height H_{es0} corresponds to the extreme, significant deep-water wave height which is exceeded 12 hours

---

* Corresponding author at: Institute of Hydro-Engineering, Polish Academy of Sciences, ul. Kościerska 7, 80—328 Gdańsk, Poland.
E-mail address: m.stella@ibwpan.gda.pl (M. Stella-Bogusz).

Peer review under the responsibility of the Institute of Oceanology of the Polish Academy of Sciences.

https://doi.org/10.1016/j.oceano.2023.06.003

per year or 0.137% of the considered time. It is obvious that the depth of closure h_c can also be found from long-term bathymetric changes.

For the south Baltic multi-bar shore, Cerkowniak et al. (2015a) obtained actual depth of closure values (from bathymetric surveys) equal to $h_c = 6.0–7.7$ m, greater than those calculated using the effective significant wave parameters ($h_c = 4.9–6.5$ m). On a second front, however, Cerkowniak et al. (2015b) found out that the extreme stormy wave-induced bed shear stresses (generated by the significant deep-water waves higher than 3.5 m) can give rise to considerable sediment transport (sheet flow) even at depths of 13—15 m. Such conditions, however, last at most several hours per year and presumably cannot cause distinct changes to the sea bottom. Further, Cerkowniak et al. (2015b) concluded that even extreme storms cannot induce a sheet flow regime at water depths greater than 15 m, resulting in the development of bedforms. Large subaqueous forms within this region can occur and develop only if stormy waves are superimposed with strong sea currents (see Ostrowski and Stella, 2020). In the North Sea, such big sandy bedforms that occur at depths of 20—30 m, are called sand waves or sand banks, and their presence is surely associated with tidal currents. Similar sea bottom dynamic effects have also been observed, although rarely, in non-tidal environment, i.e. in the south Baltic coastal zone at depths between 15 and 30 m, see Rudowski et al. (2008). According to recent measurements by Stella (2021), such bedforms occur commonly in this region at depths of 16—20 m, and their movement results in the seabed elevation changes of magnitude from a few to 70 cm during the year.

In view of the above, within the present study, the remote foreshore region of the south Baltic Sea was assumed to lie between the depths of 15 m and 25 m.

Wind-driven flows in the nearshore zone are dominated by wave-driven currents, while wind-driven currents prevail in regions more distant from the shoreline. The boundary between the above zones cannot be determined precisely. For the south Baltic coast, basing on theoretical modelling and the field data collected at the Coastal Research Station (CRS) in Lubiatowo, Sokolov and Chubarenko (2012) found a relatively high wind-induced component of currents in the surf zone. They concluded that the wind blowing parallel to the shore can contribute almost 50% to the generation of the longshore current and more than 20% in case it blows at an angle of 45% to the shoreline. The wave-driven longshore current always predominates in the surf zone, whereas the situation in the remote foreshore, seawards of the surf zone, is somewhat different.

The interaction between waves and currents is a complex phenomenon. Each component of wave-current flow characteristics can significantly affect various processes occurring in the sea. For example, the angle between the wave and the current affects the configuration and type of seabed forms (Baas et al., 2021), the current velocity and impact of the current itself on the seabed (Lacy et al., 2007, Lim and Madsen, 2016), as well as the magnitude of the shear stress and the bottom roughness (Malarkey and Davies, 1998; Wiberg, 2005). Research on combined wave and current flow over the rough bed has shown that the presence of boundary layer effects in a nonlinear interaction between them, and mean-velocity profiles or shear stresses cannot be described by a linear superposition of wave and current velocities or shear stresses (Grant and Madsen, 1979; Kemp and Simons, 1982). Wave-current interactions play a crucial role in sediment dynamics. Outside the nearshore zone higher waves alone are able to entrain the sediment from the sea bottom but are ineffective at sediment transport, however, the appearance of even a weak current can lead to net transport when current alone is often unable to initiate the sediment motion (Grant and Madsen, 1979; Wiberg, 2005). Some research showed that the bottom is rougher for currents in the presence of waves and bottom drag coefficients for near-bed currents can be increased by up to an order of magnitude (Egan et al., 2019; Wiberg, 2005).

The Coriolis force in coastal areas of the Baltic Sea may be neglected. The surface and the bottom Ekman layers overlap. Therefore, the Ekman spiral does not develop and the wind-induced current is collinear with the wind direction (Krauss, 2001; Trzeciak, 2000; Valle-Levinson, 2016). On the basis of velocity profile measurements in the south Baltic coastal zone at a depth of 17 m, Ostrowski et al. (2018) found out that the direction of flow velocities is the same in the entire water column, almost identical to the wind. Hence, the vertical profile of the wind-driven current velocity can be modelled using a directionally invariable distribution.

The logarithmic distribution is a simple theoretical model providing a good fit to steady flow profiles. This distribution is commonly applied to both river flows (see, e.g. Meyer, 2009) and sea currents (Nielsen, 1992, 2009). The logarithmic velocity profile results from the Boussinesq hypothesis and the assumption of the turbulent viscosity increasing linearly from zero value at the bottom. The inclination of the growth line depends on the value of friction velocity. In order to improve this theoretical approach and obtain better agreement between the calculated and measured velocity profiles, modifications of the logarithmic distribution were proposed (Meyer, 2009; Nielsen, 1992; Stella et al., 2019). The present study is a novel attempt of such a modification. Within the proposed new approach, the vertical turbulent viscosity distribution ruling the wind-driven current is modified by the inclusion of the impact of the wave bed boundary layer. Contrary to the abovementioned concepts, this aim is achieved by the assumption of a non-zero turbulent viscosity at the bottom, obtained from the solution to the momentum equation in the wave bed boundary layer.

2. Material and methods

2.1. Site and data

The measurements of parameters of wind, waves and currents were carried out at the Coastal Research Station (CRS) in Lubiatowo and its vicinity in the period from 26th April 2014 to 30th June 2014. CRS Lubiatowo is a field experimental post of the Institute of Hydro-Engineering of the Polish Academy of Sciences (IBW PAN), see Figure 1. Hydrodynamic, lithodynamic and morphodynamic processes near CRS Lubiatowo display features typical for the sandy coast of the south Baltic Sea (see Cerkowniak et al., 2017; Ostrowski et al., 2016). In the remote foreshore, approxi-

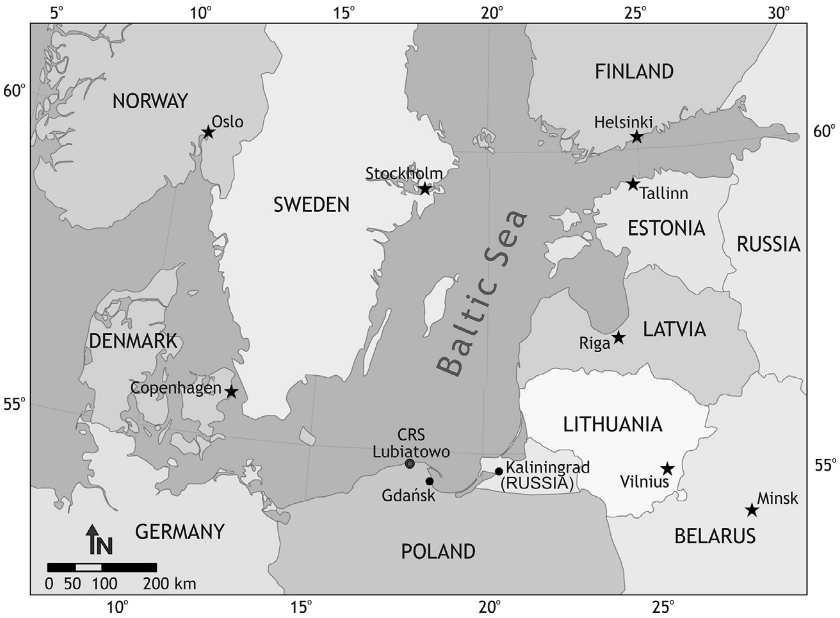

Figure 1 Location of the study site.

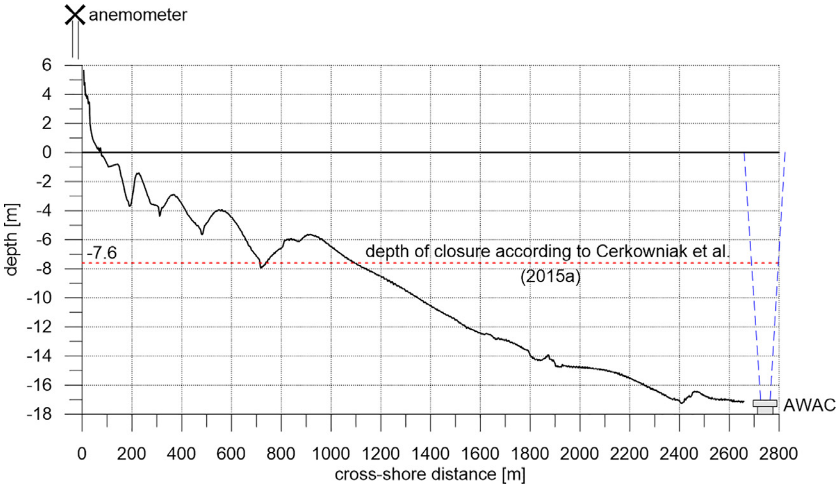

Figure 2 Example of the cross-shore seabed profile at CRS Lubiatowo, depth of closure after Cerkowniak et al. (2015a) and approximate location of measuring instruments.

mately 1.5 NM from the coastline where CRS Lubiatowo is located, wave parameters are periodically collected since 1997.

The coastal bottom at the study site is mildly inclined (1—2%) and built of fine sand. Cross-shore bathymetric transects display 3—4 bars which favours the multiple wave breaking, with the gradual wave energy dissipation, see Pruszak et al. (2008). The example of the cross-shore bottom profile at CRS Lubiatowo, with the marked depth of closure according to Cerkowniak et al. (2015a) and the approximate location of the measuring instruments, is shown in Figure 2.

Flow velocities were recorded using an acoustic current profiler (AWAC, produced by Nortek, with transmission frequency of 600 kHz) coupled with the surface wave measurement module. The meter was installed on a bottom-resting frame with transducers facing up at the position 54°50.48′N, 17°53.09′E (about 2.7 km from the shoreline, at the depth of $h = 17$ m). Free surface elevation was recorded once an hour for about 17 minutes with a frequency of 2 Hz and then processed to determine statistical and stochastic wave parameters (height, period and direction). Water flow velocities were measured with 1 Hz frequency in 1 m thick layers once an hour and then averaged for 2-minute records. Current measurements were not performed in the nearbed layer (about 1 m thick), because of technical reasons (height of the frame on which the instrument was mounted and the so-called blanking distance i.e. direct water body thickness to transducers where the accuracy of measurements is not acceptable). The velocity data in the surface water layer (up to 10% of the total depth) are not fully reliable due to side-lobe interference. Measurements carried out in this layer are therefore not fully reliable.

The parameters of the wind (direction and speed averaged over 10 minutes and maximum gust in 10 minutes), were recorded by a cup anemometer SW-48 (produced by MORS, Poland) mounted on a 22 m mast, placed next to CRS Lubiatowo, 150 m from the shoreline (54°48.70′N, 17°50.43′E).

The mast is 12 m higher than required by the meteorological monitoring standards (10 m) but the high trees growing around the mast increase the terrain roughness resulting in the recorded wind speed lower than it would have been over flat ground. Further, wind parameters on land differ from wind parameters at sea. This issue was already solved by Ostrowski et al. (2018) and Stella (2021), who derived the following equations, describing the relationship between the "sea" wind velocity W_{sea} (10 m above sea level) the "land" wind velocity W_{land} at CRS Lubiatowo:

$$W_{sea} = 3.68\,W_{land} \;\; \text{for} \;\; W_{land} \le 1 \text{ m/s} \tag{1}$$

$$W_{sea} = 1.76\,W_{land} + 1.92 \;\; [\text{m/s}] \;\; \text{for} \;\; W_{land} > 1 \text{ m/s} \tag{2}$$

The seabed at the deep-water locations in the vicinity of the wave buoy consists of well-sorted quartz sediments (having the density of $\rho_s = 2650$ kg/m^3) with the grain diameter d_{50} equal to about 0.13 mm. The IBW PAN divers spotted sandy bedforms at some locations there. They were mostly small forms (ripple marks), about 5—15 cm high and 1—2 m long, respectively.

Deep water wave-current data measured by AWAC, namely the wave parameters and the current velocities, were used directly while the wind velocity values W_{land} were recalculated to W_{sea} using Eqs. (1) and (2). The above data, together with the seabed sand features, were the input to the theoretical model of the wind-driven current interacting with the wave bed boundary layer.

2.2. Theoretical model

2.2.1. Wind-driven current

It is assumed that the shear stresses τ in the water column, where the wind-driven current occurs, satisfy the Boussinesq hypothesis as follows:

$$\tau = \rho \nu_t \frac{du(z)}{dz} \tag{3}$$

where ρ denotes the water density, ν_t is the kinematic turbulent viscosity (eddy viscosity) in the vertical direction z, and $u(z)$ is the velocity of the steady flow.

Further, the turbulent viscosity is assumed to increase linearly from the bottom, being proportional to von Karman's constant κ and the friction velocity u_f:

$$\nu_t = \kappa u_f z \tag{4}$$

Having the shear stress defined as $\tau = \rho {u_f}^2$, it is possible to obtain the logarithmic vertical distribution of the flow velocity $u(z)$:

$$u(z) = \frac{u_f}{\kappa} \ln\left(\frac{z}{z_0}\right) \tag{5}$$

in which z_0 denotes the ordinate at which the velocity u is equal to zero.

The quantity z_0 is thus a theoretical seabed level from which the profile of the velocity $u(z)$ starts. This level is determined as depending on the bottom roughness height, namely as $z_0 = k_f/30$, where k_f is the bedform height (a so-called Nikuradse roughness), assumed to be equal to 0.1 m.

The velocity of the wind-driven current within the surface layer $u_{surface}$ can be determined from the wind speed W_{sea} as follows (Stella et al., 2019):

$$u_{surface} = 0.03\,W_{sea} \;\; \text{for} \;\; W_{sea} < 8 \text{ m/s}$$

$$u_{surface} = 0.035\,W_{sea} \;\; \text{for} \;\; W_{sea} \ge 8 \text{ m/s} \tag{6}$$

With a given superficial velocity $u_{surface}$, using the assumption of the wind-driven current velocity described by the logarithmic vertical distribution, the friction velocity u_f can be determined from Eq. (5) with $z = h$ and $u(h) = u_{surface}$. The resulting formula, after the rearrangement of Eq. (5), reads as follows:

$$u_f = \frac{\kappa u_{surface}}{\ln\left(\frac{h}{z_0}\right)} \tag{7}$$

A hydrodynamic effect, which appears for the stationary current due to the occurrence of wave bed boundary layer, ought to be somehow incorporated in the model. This effect was taken into account by Nielsen (1992) by the inclusion of the so-called apparent bottom roughness k_a, which represents the additional bottom roughness causing larger roughness than the natural roughness of the rippled bed. Comparison of the calculated flow velocity profiles with the measured ones led Stella et al. (2019) to distinguish wave- and current-dominated flows in dependence on the apparent roughness k_a magnitude. According to Stella et al. (2019), the mean flow velocity profile can be reliably described by the logarithmic distribution if the wind-driven current is dominant. This is obtained with the turbulent viscosity ν_t increasing linearly from zero value at the bed, see Eq. (4) and Figure 3.

For the wave-dominated flows, Stella et al. (2019) proposed a two-layer mean velocity profile, namely the logarithmic distribution in the nearbed layer (equivalent to the wave bed boundary layer) and the linear distribution higher in the water column. The latter velocity profile resulted from the assumed turbulent viscosityν_t increasing linearly in the nearbed layer as defined by Eq. (4) and ν_t being a constant value in higher layers, see Figure 3.

In the present study, we permit the turbulent viscosity ν_t to be non-zero at the bottom, namely at $z = z_0$. First, this is due to the wave bed boundary layer effect mentioned previously. Second, the sea bottom, being built of fine sand, is assumed to be moveable, particularly under the joint impact of stormy waves and wind-induced currents. In such a situation, one can expect motion of the water-sand mixture at the theoretical bed level and the related turbulence. This turbulence at the ordinate z_0 is represented by the bottom kinematic turbulent viscosity ν_0, see Figure 3.

Such a modified linearly variable kinematic turbulent viscosity ν_t is described by the following formula:

$$\nu_t = \kappa u_f (z - z_0) + \nu_0 \tag{8}$$

Assuming the validity of the Boussinesq hypothesis as given by Eq. (3) and having the shear stress defined as $\tau = \rho {u_f}^2$, one obtains a modified logarithmic vertical distribution of the flow velocity $u(z)$:

$$u(z) = \frac{u_f}{\kappa} \ln\left(\frac{\kappa u_f (z - z_0) + \nu_0}{\nu_0}\right) \tag{9}$$

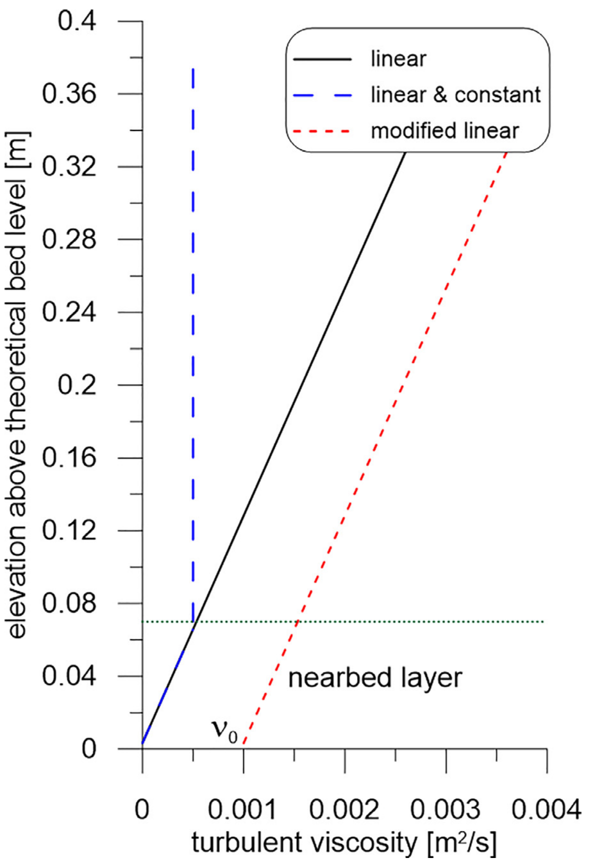

Figure 3 Vertical distributions of the kinematic turbulent viscosity $\nu_t(z)$.

in which a non-zero turbulent viscosity ν_0 at the bottom is determined from the solution of the momentum equation (equation of motion) in the wave bed boundary layer.

For a given superficial velocity $u_{surface}$, the friction velocity u_f (and consequently the shear stress $\tau = \rho {u_f}^2$ related to the water flow) can be calculated from the modified logarithmic vertical distribution of the wind-driven current velocity described by Eq. (9) with $z = h$ and $u(h) = u_{surface}$. Contrary to Eq. (5), Eq. (9) must be solved numerically.

It should be noted that $\nu_t(z_0) = \kappa u_f z_0$ within the classical logarithmic approach. If $\nu_t(z_0)$ is greater than ν_0 the application of the modified logarithmic approach is not justified because of a negligibly small effect of the wave turbulent bed boundary layer.

2.3. Wave bed boundary layer

According to Nielsen (1992, 2009), the wave boundary layer and the wave-related bed shear stresses are almost unaffected by the presence of a steady flow. Hence, for practical purposes, the shear stresses in the wave bed boundary layer can be calculated as if the current was not there.

Within the proposed modelling system, the integral momentum method of Fredsøe (1984) is used to solve the equation of motion in the wave bed boundary layer. Fredsøe (1984) integrated the relevant equation over the wave bed boundary layer thickness δ and, assuming the logarithmic velocity profile in this layer, obtained the following differential equation:

$$\frac{dz_1}{d(\omega t)} = \frac{30\kappa^2 U}{k_f \omega [e^{z_1}(z_1 - 1) + 1]} - \frac{z_1(e^{z_1} - z_1 - 1)}{e^{z_1}(z_1 - 1) + 1} \frac{1}{U} \frac{dU}{d(\omega t)} \tag{10}$$

in which ω is the angular frequency of wave motion and z_1 is a dimensionless variable:

$$z_1 = \frac{U}{u_{fw}} \kappa \tag{11}$$

where $U(\omega t)$ is a free stream velocity (at the top of the wave bed boundary layer). The velocity $U(\omega t)$ depends on the wave height H and period T (available directly from the measurements), as well as the wave length L. The latter is determined from the dispersion relationship which takes the wave-current interaction into account and has the following form (Nielsen, 2009):

$$\left(\frac{2\pi}{T} - \frac{2\pi}{L} u_{surface} \cos\gamma \right)^2 = g \frac{2\pi}{L} \tanh\left(\frac{2\pi}{L} h \right) \tag{12}$$

in which γ is an angle between the steady current direction and the wave propagation direction, while g denotes the acceleration due to gravity.

From the solution of Eqs. (10) and (11), the wave friction velocity $u_{fw}(\omega t)$ can be calculated, as well as the wave boundary layer thickness δ (ωt):

$$\delta = \frac{k_f}{30}(e^{z_1} - 1) \tag{13}$$

Exemplary results of computations for typical south Baltic storm wave parameters, namely height $H = 3$ m and period $T = 8$ s, at water depth of $h = 17$ m, are shown in Figure 4.

Two quantities characterising the wave bed boundary layer are assumed to be representative for the entire wave period. They are the root-mean-square friction velocity $u_{fw,\mathrm{RMS}}$ and the "mean" boundary layer thickness δ_m at the moment corresponding to wave crest (or trough), see Figure 4.

The wave-related turbulent viscosity in the bed boundary layer ν_{tw} is described by the linear distribution:

$$\nu_{tw} = \kappa u_{fw,\mathrm{RMS}} z \tag{14}$$

As has been assumed before, the wave bed boundary layer generates a non-zero turbulent viscosity for the steady current at the bottom (ν_0). Thus, for $z = \delta_m$, i.e. at the upper limit of the wave boundary layer, $\nu_{tw} = \nu_0$. Consequently, one has the following:

$$\nu_0 = \kappa u_{fw,\mathrm{RMS}} \delta_m \tag{15}$$

The above constitutes a quantity sought to be applied in Eq. (9). For the assumed exemplary conditions ($H = 3$ m, $T = 8$ s, $h = 17$ m and $k_f = 0.1$ m) one obtains $\nu_0 = 0.002048$ m^2/s from Eqs. (10), (11), (13) and (15). If the wind-driven current superficial velocity $u_{surface} = u(h)$ amounts to, for instance, 0.5 m/s, Eq. (9) yields $u_f = 0.04071$ m/s. The respective friction velocity u_f within the "classical" logarithmic model, calculated by use of Eq. (7), amounts to 0.02343 m/s. The wind-driven current velocity profiles for the case in question resulting from the classical logarithmic model and the modified logarithmic model, i.e. Eq. (5) and Eq. (9), respectively, are plotted in Figure 5.

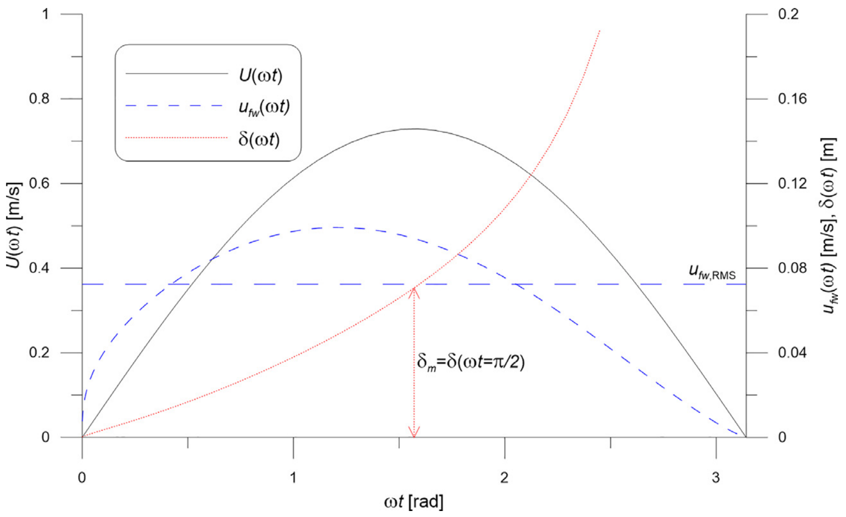

Figure 4 Free stream velocity U, friction velocity u_{fw} and the wave bed boundary layer thickness δ calculated for $H = 3$ m, $T = 8$ s, $h = 17$ m and $k_f = 0.1$ m.

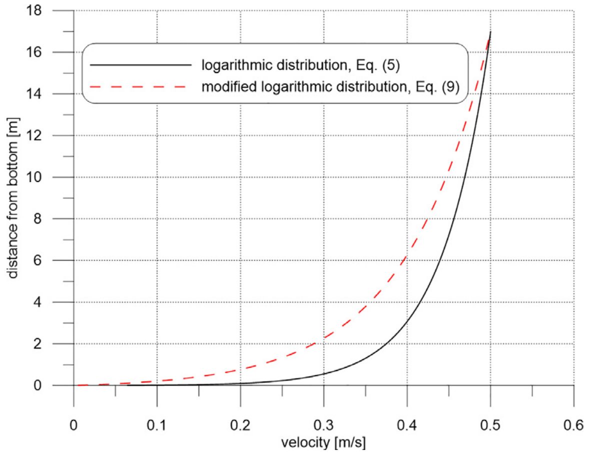

Figure 5 Velocity profiles according to Eq. (5) and Eq. (9), respectively, for $u_{surface} = 0.5$ m/s, $H = 3$ m, $T = 8$ s, $h = 17$ m and $k_f = 0.1$ m, $u_f = 0.02343$ m/s (logarithmic), $u_f = 0.03375$ m/s and $\nu_0 = 0.000614$ m^2/s (modified logarithmic).

It can be seen in Figure 5 that the presence of the wave bed boundary layer, resulting in an increase of the nearbed turbulent viscosity, causes a considerable growth of the friction (shear stress) and in consequence a reduction of the flow velocities in the water column.

3. Results and discussion

Computations were carried out for numerous wind-wave-current situations occurring in the period from 26th April 2014 to 30th June 2014. The number of wind-wave-current data sets examined amounts to more than one thousand. Some of the analysed hydrodynamic situations are current-dominated while some of them are wave-dominated. The exemplary measured velocity profiles, together with the distributions theoretically modelled by the use of both the logarithmic and modified logarithmic approach, are shown in Figures 6 and 7.

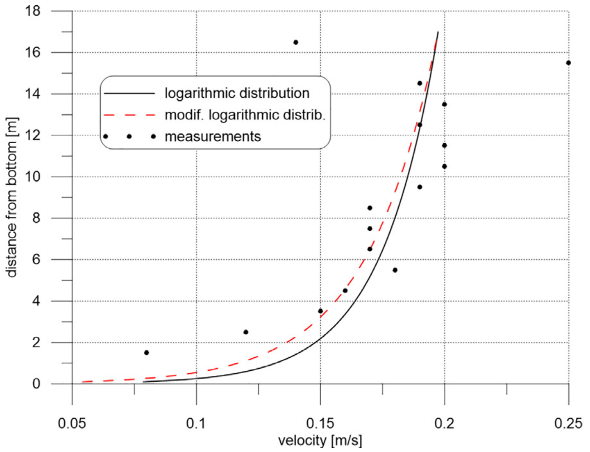

Figure 6 Exemplary theoretical and measured velocity profiles (15th May 2014, 18:00 UTC): wind direction (from) 28.85°, $W_{sea} = 6.6$ m/s, $u_{surface} = 0.197$ m/s, $H = 1$ m, $T = 4.9$ s, $h = 17$ m, $k_f = 0.1$ m, $u_f = 0.00925$ m/s (logarithmic), $u_f = 0.01143$ m/s and $\nu_0 = 0.000078$ m^2/s (modified logarithmic).

The examples presented in Figures 6 and 7 have been selected as they represent almost the same theoretical superficial current velocity, resulting from very similar wind speed, Eq. (6). The wave conditions, however, differ much for these cases, as the first one is current-dominated (Figure 6) while the second one is wave-dominated (Figure 7).

As one could have expected, the modified logarithmic velocity distribution is similar to the (traditional) logarithmic one for the current-dominated case (Figure 6). This is due to a minor wave impact and the low value of the wave-related turbulent viscosity ν_0.

The modified logarithmic profile is distinctly different from the logarithmic distribution for the wave-dominated hydrodynamic regime, with significantly smaller velocities, particularly in the lower part of the water column (Figure 7). This effect results from additional drag (friction)

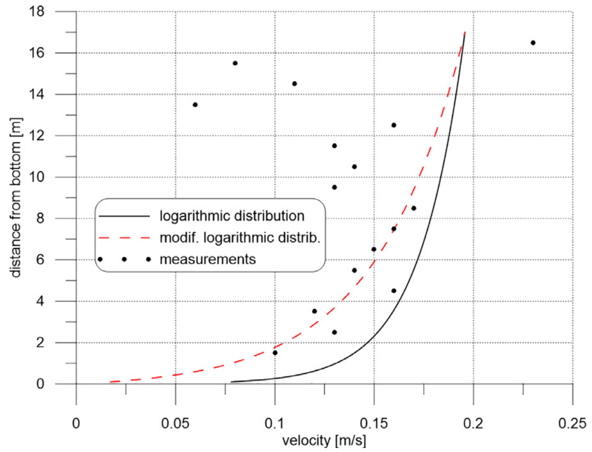

Figure 7 Exemplary theoretical and measured velocity profiles (14th June 2014, 14:00 UTC): wind direction (from) 339.50°, $W_{sea} = 6.5$ m/s, $u_{surface} = 0.196$ m/s, $H = 2.4$ m, $T = 7.9$ s, $h = 17$ m, $k_f = 0.1$ m, $u_f = 0.00917$ m/s (logarithmic), $u_f = 0.01767$ m/s and $\nu_0 = 0.001449$ m^2/s (modified logarithmic).

caused by the turbulent wave bed boundary layer generating a relatively high nearbed turbulent viscosity ν_0 (cf. ν_0 values given in the captions of Figures 6 and 7). In such a case, the modified logarithmic velocity profile is more consistent with the field data than in the classical logarithmic distribution.

The agreement between the measured velocity profile and the theoretical distribution in the upper part of the water column in Figure 7 is not as satisfactory as in Figure 6. It is, however, quite good in the nearbed layer, important in the context of sediment transport mechanisms.

3.1. Final remarks and conclusions

The paper presents the theoretical modelling yielding the modified logarithmic vertical distributions of the wind-driven current velocities in the remote foreshore, namely at depths bigger than the conventionally estimated depth of closure. The research conducted there have revealed different velocity distributions depending on the instantaneous predominance of wave motion or wind-induced currents. The present study has led to the following major conclusions:

- The presence of the wave bed boundary layer affects the wind-driven steady current by increased (non-zero) turbulent viscosity at the sea bottom.
- The modification of the turbulent viscosity distribution yields the modified logarithmic velocity profile.
- The above results in decreased flow velocities in the lower part of the water column, providing a theoretical velocity profile more consistent with the field data than in the case of the classical logarithmic distribution.

It seems that a gap in understanding of hydrodynamics of the non-tidal sea beyond the depth of closure has been filled in. The presented modelling approach can be helpful, for instance, in a more accurate assessment of nearbed wave-current velocities and parameters of lithodynamic processes in the remote foreshore of any non-tidal or micro-tidal sea.

Within further research, it would be worthwhile investigating superficial wind-induced current velocities interacting with surface waves, together with the dynamics of the sea bottom, including migration of the bedforms. The respective field measurements are under preparation. They will be carried out using the wave buoy Directional Waverider DWR4 with the Acoustic Current Meter (produced by Datawell B.V., the Netherlands) and a side-scan sonar, as well as a multi-beam echo-sounder.

Acknowledgements

The study was sponsored by the Ministry of Education and Science, Poland, under the IBW PAN statutory programme No. 2 ("Dynamics of Coastal-Estuarine Zone") and by the National Science Centre, Poland, within the research project No. 2021/41/B/ST8/01943 ("Dynamics of bottom in the remote foreshore of the non-tidal sea") which are hereby gratefully acknowledged.

Declaration of competing interest

The authors declare that they have no known competing financial interests or personal relationships that could have appeared to influence the work reported in this paper.

References

Baas, J., Malarkey, J., Lichtman, I., Amoudry, L., Thorne, P., Hope, J., Peakall, J., Paterson, D., Bass, S., Cooke, R., Manning, A., Parsons, D., Ye, L., 2021. Current- and Wave-Generated Bedforms on Mixed Sand—Clay Intertidal Flats: A New Bedform Phase Diagram and Implications for Bed Roughness and Preservation Potential. Front. Earth Sci. 9. https://doi.org/10.3389/feart.2021.747567

Birkemeier, W.A., 1985. Field data on seaward limit of profile change. J. Waterw. Port C. 111 (3), 598—602. https://doi.org/10.1061/(ASCE)0733-950X(1985)111:3(598)

Cerkowniak, G.R., Ostrowski, R., Stella, M., 2015a. Depth of closure in the multi-bar non-tidal nearshore zone of the Baltic Sea: Lubiatowo (Poland) case study. Bull. Marit. Inst. Gdańsk 30 (1), 180—188. http://doi.org/10.5604/12307424.1185577.

Cerkowniak, G.R., Ostrowski, R., Stella, M., 2015b. Wave-Induced Sediment Motion Beyond the Surf Zone: Case Study of Lubiatowo (Poland). Arch. Hydro-Eng. Environ. Mech. 62 (1—2), 27—39. https://doi.org/10.1515/heem-2015-0017

Cerkowniak, G.R., Ostrowski, R., Pruszak, Z., 2017. Application of Dean's curve to the investigation of the long-term evolution of the southern Baltic multi-bar shore profile. Oceanologia 59 (1), 18—27. https://doi.org/10.1016/j.oceano.2016.06.001

Dean, R.G., 2002. Beach Nourishment. Theory and Practice. Advanced Series on Ocean Engineering — Volume 18. World Sci. Publ., 399 pp. https://doi.org/10.1142/2160

Egan, G., Cowherd, M., Fringer, O., Monismith, S., 2019. Observations of near-bed shear stress in a shallow, wave- and current-driven flow. J. Geophys. Res. Oceans 124, 6323—6344. https://doi.org/10.1029/2019JC015165

Fredsøe, J., 1984. Turbulent boundary layer in combined wave-current motion. J. Hydraul. Eng. 110 (HY8), 1103—1120. https://doi.org/10.1061/(ASCE)0733-9429(1984)110:8(1103)

Grant, W.D., Madsen, O.S., 1979. Combined wave and current interaction with a rough bottom. J. Geophys. Res. Oceans 84 (C4), 1797—1808. https://doi.org/10.1029/JC084iC04p01797

Hallermeier, R.J., 1978. Uses for a calculated limit depth to beach erosion. In: Proceedings of 16th Coastal Engineering Conference, Am. Soc. Civil Eng., 1493—1512. https://doi.org/10.9753/icce.v16.88

Hallermeier, R.J., 1981. A profile zonation for seasonal sand beaches from wave climate. Coastal Eng. 4 (3), 253—277. https://doi.org/10.1016/0378-3839(80)90022-8

Kemp, P., Simons, R., 1982. The interaction between waves and a turbulent current: Waves propagating with the current. J. Fluid Mech. 116, 227—250. https://doi.org/10.1017/S0022112082000445

Krauss, W., 2001. Baltic Sea circulation. Encyclopedia of Ocean Sciences. https://doi.org/10.1006/rwos.2001.0381

Lacy, J.R., Rubin, D.M., Ikeda, H., Mokudai, K., Hanes, D.M., 2007. Bed forms created by simulated waves and currents in a large flume. J. Geophys. Res. 112, C10018. https://doi.org/10.1029/2006JC003942

Lim, K.Y., Madsen, O.S., 2016. An experimental study on near-orthogonal wave—current interaction over smooth and uniform fixed roughness beds. Coastal Eng. 116, 258—274. https://doi.org/10.1016/j.coastaleng.2016.05.005

Malarkey, J., Davies, A.G., 1998. Modelling wave—current interactions in rough turbulent bottom boundary layers. Ocean Eng. 25, 119—141. https://doi.org/10.1016/S0029-8018(96)00062-5

Meyer, Z., 2009. Modified Logarithmic Tachoida Applied to Sediment Transport in a River. Acta Geophysica 57 (3), 743—759. https://doi.org/10.2478/s11600-009-0010-0

Nielsen, P., 1992. Coastal bottom boundary layers and sediment transport. Advanced Series on Ocean Engineering — Vol. 4. World Sci. Publ. 340 pp. https://doi.org/10.1142/1269

Nielsen, P., 2009. Coastal and Estuarine Processes. Advanced Series on Ocean Engineering — Vol. 29. World Sci. Publ. 360 pp. https://doi.org/10.1142/7114

Ostrowski, R., Schönhofer, J., Szmytkiewicz, P., 2016. South Baltic representative coastal field surveys, including monitoring at the Coastal Research Station in Lubiatowo. Poland. J. Marine Syst. 162, 89—97. https://doi.org/10.1016/j.jmarsys.2015.10.006

Ostrowski, R., Stella, M., 2020. Potential dynamics of non-tidal sea bed in remote foreshore under waves and currents. Ocean Eng. 207, 107398. https://doi.org/10.1016/j.oceaneng.2020.107398

Ostrowski, R., Stella, M., Szmytkiewicz, P., Kapiński, J., Marcinkowski, T., 2018. Coastal hydrodynamics beyond the surf zone of the south Baltic Sea. Oceanologia 60 (3), 264—276. https://doi.org/10.1016/j.oceano.2017.11.007

Pruszak, Z., Szmytkiewicz, P., Ostrowski, R., Skaja, M., Szmytkiewicz, M., 2008. Shallow-water wave energy dissipation in a multi-bar coastal zone. Oceanologia 50 (1), 43—58.

Rudowski, S., Łęczyński, L., Gajewski, Ł., 2008. Fale piaszczyste na dnie głębokiego przybrzeża i ich rola w kształtowaniu brzegu. Landform Analysis 9, 214—216.

Sokolov, A., Chubarenko, B., 2012. Wind Influence on the Formation of Nearshore Currents in the Southern Baltic: Numerical Modelling Results. Arch. Hydro-Eng. Environ. Mech. 59 (1—2), 37—48. https://doi.org/10.2478/v10203-012-0003-3

Stella, M., 2021. Morphodynamics of the south Baltic seabed in the remote nearshore zone in the light of field measurements. Mar. Geol. 439, 106546. https://doi.org/10.1016/j.margeo.2021.106546

Stella, M., Ostrowski, R., Szmytkiewicz, P., Kapiński, J., Marcinkowski, T., 2019. Driving forces of sandy sediment transport beyond the surf zone. Oceanologia 61 (1), 50—59. https://doi.org/10.1016/j.oceano.2018.06.003

Trzeciak, S., 2000. Marine Meteorology with Oceanography. Wydawnictwo Naukowe PWN, 249 pp. (in Polish).

Valle-Levinson, A., 2016. Lecture 13. Equations of Motion. http://www.essie.ufl.edu/~arnoldo/ocp6050/notes_pdf/

Wiberg, P.L., 2005. Wave-Current Interaction. In: Schwartz, M.L. (Ed.), Encyclopedia of Coastal Science. Encyclopedia of Earth Science Series. Springer, Dordrecht. https://doi.org/10.1007/1-4020-3880-1_343

Oceanologia 65 (2023) 564—570

Available online at www.sciencedirect.com

ScienceDirect

journal homepage: www.journals.elsevier.com/oceanologia

ORIGINAL RESEARCH ARTICLE

Excitation of an extreme wave by standing current

Pavlo Anakhov*

Department of Infrastructure Systems, National Power Company "Ukrenergo", Kyiv, Ukraine

Received 19 October 2022; accepted 12 June 2023
Available online 23 June 2023

KEYWORDS
Damping of oscillations;
Excitation of oscillations;
Standing current;
Standing wave;
Sustaining of oscillations

Abstract The statistics suggest that extreme waves cause more damage in shallow waters and at the coast than in the deep sea. In the linear theory of the formation of extreme waves, their existence is interpreted as a local superposition of surface monochromatic waves. The event of excitation of extreme waves can be understood as an increase in natural oscillations of the water basin. The conditions for the excitation and sustaining of natural oscillations are the proximity of the periods of exciting traveling waves to the period of traveling waves and the speed of movement of the exciting current to the phase speed of propagation of traveling waves of the reservoir. Examples of stimulating natural oscillations are presented. We determined the range of expected periods of natural oscillations, which range from 30 seconds to 24 hours. Synchronously and in common-mode with the oscillations of standing waves between their antinodes, a "standing" current occurs with a measured speed of up to 11 km/h. We presented a hypothesis about the possibility of stimulating natural oscillations of water bodies by a standing current, which changes its direction due to the movement of the water surface from the trough of the wave to its crest, and back. A model of stimulating oscillations by the waves with a constant period and currents with constant and variable speeds has been developed.

1. Introduction

In recent decades, coastal populations have grown rapidly. Extreme sea levels have become an increasing threat to coastal populations (due to flooding), which are projected to amount to 630 million by 2100 (Vilibić et al., 2021).

Inside semi-enclosed water bodies, such as bays or harbors, arises harbor resonance — trapping and amplification of wave energy. Seiches and surf beats may be induced by infragravity waves, steady-state wave groups, atmospheric fluctuations, tsunami waves, or shear flows traveling into the semi-enclosed water body and so on (Gao et al., 2017; Gao et al., 2020; Jueza and Navas-Montilla, 2022).

---

* Corresponding author at: Department of Infrastructure Systems, National Power Company “Ukrenergo”, Kyiv, Ukraine.
E-mail address: anakhov@i.ua

Peer review under the responsibility of the Institute of Oceanology of the Polish Academy of Sciences.

Production and hosting by Elsevier

https://doi.org/10.1016/j.oceano.2023.06.005
0078-3234/

Large-scale experiments of unidirectional irregular waves propagating over a variable bottom profile considering different transition water depths have shown that the transition of water depth from a deeper to a shallower zone increases the occurrence probability of large waves (Gao et al., 2017, 2019; Zhang et al., 2019).

In modern times, there are usually destructive transient harbor oscillations induced by tsunamis. Tsunamis are triggered by submarine earthquakes, undersea volcanic eruptions or offshore landslides. As tsunamis approach the coastal area, the wave height increases significantly due to the continuous decrease of the water depth (Gao et al., 2017).

Among various generation mechanisms, a number of catastrophic meteotsunamis have been recorded. Meteotsunamis are documented to impact certain coastlines. In some bays, the meteotsunami waves have been recorded with heights of several metres and associated currents of several knots (Vilibić et al., 2021).

The evidence of rogue wave existence all over the world during 2006—2010 has been collected based mainly on mass media sources. From the total number of 131 reported events, 78 were identified as evidence of rogue waves. The statistics built on the selected 78 events suggest that extreme waves cause more damage in shallow waters and at the coast than in the deep sea. 39 such events were reported on the coast (Nikolkina and Didenkulova, 2011).

Descriptions and records of phenomena similar to tsunamis in Russian closed basins: rivers, lakes, and artificial water supply reservoirs are collected. During the period of the last 400 years, nine events of such type were found, seven of which can be considered reliable (Didenkulova and Pelinovsky, 2006). Events of extreme waves in Ukrainian closed basins are presented in the manuscript (Anakhov, 2021).

Gao et al. (2021) consider two kinds of stimulating harbor oscillations — directly by the regular long waves (linear theory of the formation of extreme waves), or by bichromatic short-wave groups (nonlinear harbor resonance).

In the linear theory of the formation of extreme waves, their existence is interpreted as a local superposition of surface monochromatic waves. The event of excitation of extreme wave can be understood as an increase of natural oscillations of the water basin, represented by standing waves of (1) a stable spatial structure (see Figure 1), (2) a fixed period, that determines the morphometric characteristics of the basin, and (3) high level of availability (30—50% of the duration of the ice-free period). Examples of observations of events of excitation and amplification of standing waves by tides, storm waves and tsunami waves are given (Anakhov, 2021).

The purpose of the article is to study possible sources of stimulation of natural oscillations of a water basin, which can provoke the excitation of an extreme wave. It is proposed to translate the results into the development of measures to counter catastrophic events.

2. Methods

According to the theory (see, for example, Rabinovich, 2009; Sudol'skij, 1991; Shuleykin, 1968), standing waves arise, when two oppositely directed traveling waves, moving with phase speeds V_{ph} towards each other, collide, — incident on the obstacle $A_{inciden\,t} = A_0 \sin(kx\text{-}\omega t)$ and reflected from the obstacle $A_{reflected} = A_0 \sin(kx+\omega t)$. As a result of the collision, a wave is formed:

$$A_{sw} = A_{inc} + A_{ref} = 2A_0 \cos(\omega t)\sin(kx) \tag{1}$$

where A_{inc}, A_{ref}, A_{sw}, and A_0 are the amplitudes of the incident, reflected, standing waves and the initial wave amplitude, respectively;

ω — angular frequency ($\omega = 2\pi/T$);
T is the period of the wave;
k is the wavenumber ($k = 2\pi/\lambda$);
λ is the wavelength;
x, t — variables for length and time.

The condition for the excitation of a standing wave is the closeness of the periods of traveling waves T_{inc} ($T_{inc} = T_{ref}$) to the period of standing wave T_{sw}. The gain (amplification factor for long waves) is calculated using the formula (Rabinovich, 2009):

$$H^2(T) = \frac{1}{\left(1 - \frac{T_{sw}}{T_{inc}}\right)^2 + Q^{-2}\left(\frac{T_{sw}}{T_{inc}}\right)^2},\; T_{sw} = \frac{\lambda_{sw}}{V_{ph}} = const \tag{2}$$

where Q is the quality factor of the basin, which determines the energy losses in the oscillatory system and the width of the resonance band;

λ_{sw} is the length of the standing wave of the reservoir, which is determined by its morphometric characteristics.

The condition for the excitation of a standing wave can be represented by the Froude number, which is the ratio of the traveling wave speed V_{inc} ($V_{inc} = V_{ref}$) to the phase speed of shallow water waves in the basin V_{ph} (Dogan et al., 2021):

$$Fr = \frac{V_{inc}}{V_{ph}} \approx 1 \tag{3}$$

which is calculated by the formula (Dogan et al., 2021; Forrester, 1983; Ivanov et al., 1946; Labzovsky, 1971; Rabinovich, 2009; Sudol'skij, 1991):

$$V_{ph} = \sqrt{g\overline{D}} \tag{4}$$

under the condition that distinguishes long-period standing waves (Forrester, 1983):

$$\lambda \gg \overline{D}$$

where g is the gravitational acceleration ($g = 9.81$ m/s^2);

$\overline{D}$ is the average depth of the water.

A unique property of standing wave oscillations is the coexistence of two forms of horizontal movement of water masses. Synchronously and in phase with the oscillations of standing waves between their antinodes, occurs a "standing" current with speed V_{sw} (Rabinovich, 2009; Sudol'skij, 1991).

The author has no information on the excitation of standing waves by standing currents.

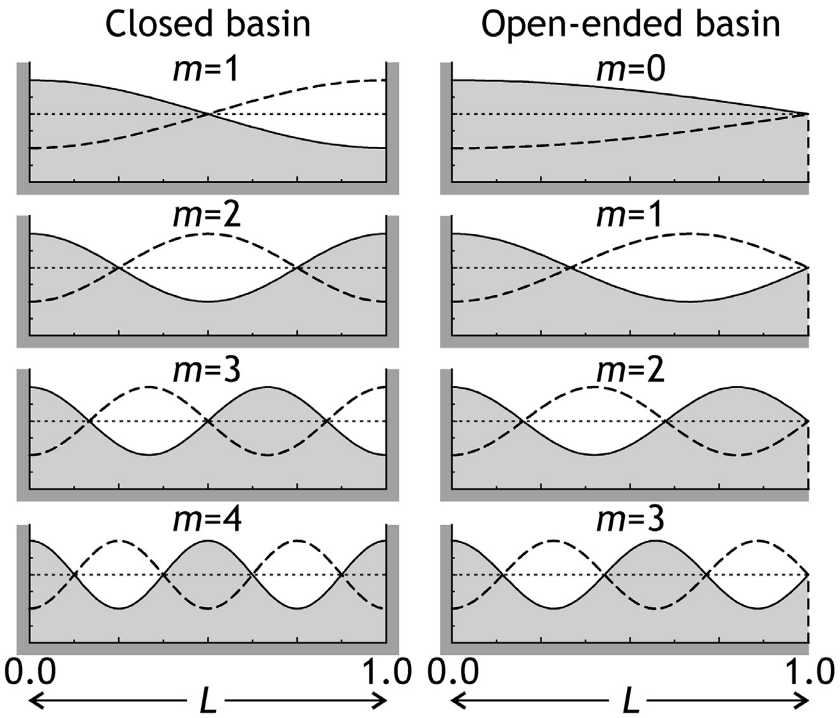

Figure 1 Profiles of the first four modes of longitudinal seiches in closed and open-ended rectangular basins with a horizontal bottom (Rabinovich, 2009).

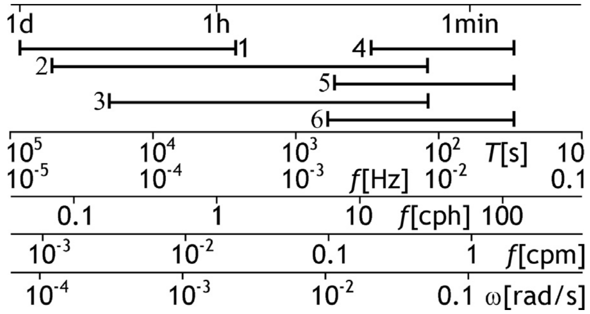

Figure 2 The ranges of periods of natural oscillations of water bodies: (1) seiches — according to Arsen'eva et al. (1963); (2) according to Kodomari (1982); (3) according to Kinsman (1965); (4) according to Titov (1971); (5) surf beats — according to Ivus et al. (1991); (6) according to Gao et al. (2019).

3. Results and discussion

3.1. Stimulation of natural oscillations by wave with constant period

According to the available data, the range of periods of natural oscillations (waves and currents) is from 30 seconds to 24 hours (see Figure 2).

The cases of stimulation of natural oscillations by the action of a wave with a constant period ($T_{inc} = const$)→($T_{sw} = const$) are described. First of all, this is the excitation and sustaining of standing waves by waves, produced by the constantly acting lunisolar tide.

The wave spectrum of the Kandalaksha Gulf of White Sea, Russia, clearly expressed level fluctuations with a period of 6 hours and 12 minutes. Academician Shuleykin (1968) determined, that this phenomenon is caused by the resonance of natural oscillations of water in the bay with the first harmonic of the lunar tide.

The analysis of observations revealed the effect of modulation of natural oscillations by a tidal wave for Terpeniya Bay in the water area near Poronaisk (Sakhalin Island, Russia) (Kovalev et al., 2022).

In a number of coastal seas, there are double high waters — on the southern coast of England in the Solent and the port of Southampton, as well as about Portland, located 90 km west of Southampton; at Den Helder port (Netherlands); and in Buzzards Bay (USA). The condition for the emergence of double high waters is adding to the main tone of the lunar tide of oscillations of a higher frequency — a seiche wave (Bowers et al., 2013).

3.2. Stimulation of natural oscillations by current with constant speed

Cases of excitation and sustaining of natural oscillations by the action of a constant speed current ($V_{inc} = const$)→($V_{ph} = const$) are described. The experience of studying the deformations of the ice cover under the influence of various loads (motor vehicles, cars and other vehicles) moving at different speeds along the Road of Life (ice road transport routes across Lake Ladoga to Leningrad, Russia, during the Second World War, in 1942—1943) showed the possibility of resonance at speeds of cargo movement equal to the speed of propagation of waves in ice (Ivanov et al., 1946).

With an average depth of Lake Ladoga of 47 m, the phase speed of wave propagation will be 21.5 km/h. Figure 3 shows the experimental data on the deflections of ice cover at different speeds of the load.

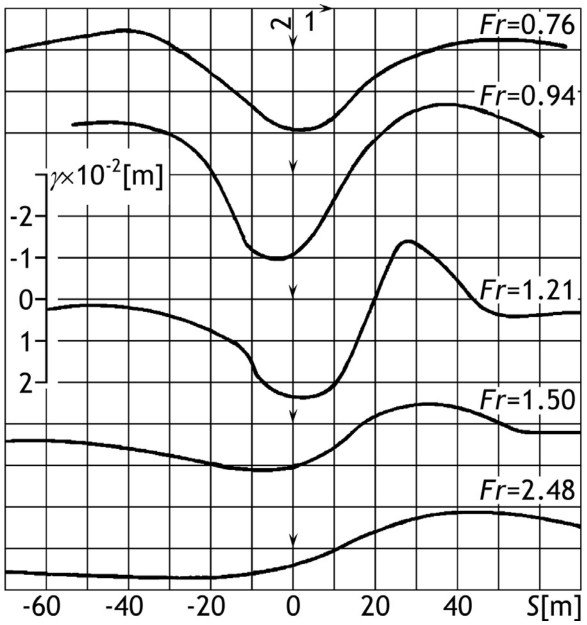

Figure 3 Flexures of the ice cover during cargo movement: 1 — direction of movement; 2 — load axis; γ — flexure scale, S — distance (Kozin, 2007).

When a moving weight acts on the ice, which excites a so called "flexural" wave in the ice cover, gravitational waves will arise in the water. If the load is moving in a particular direction with velocity $V_{inc}<V_{ph}$, the shape of the ice deflection is similar to the static one and is somewhat elongated in the direction of movement. When $V_{inc}\rightarrow V_{ph}$, the amplitude of the deflections increases significantly, at $V_{inc}=V_{ph}$ there is a flexural-gravitational resonance; the period of standing waves excited in the water coincides with the period of oscillations of the ice cover. When moving with velocity $V_{inc}>V_{ph}$, two systems of damped waves arise. Flexural waves with group velocity $U_1>V_{inc}$ go forward, and gravitational waves with group velocity $U_2<V_{inc}$ propagate behind.

3.3. Stimulation of natural oscillations by current with variable speed

Cases of excitation and sustaining of natural oscillations by the action of current with variable speed ($V_{inc}\neq const$)$\rightarrow$($V_{inc}=const$) are described. Based on the analysis of the Kamchatka (1952), Chilean (1960), Niigat (1964), Moneron (1971), and Akita (1983) tsunamis, the speeds of which are not constant, in the spectra of water level fluctuations in the Kholmskaya Bay, Russia, a well-defined peak with a period of about 80 minutes, which corresponds to a single-node longitudinal standing wave. It is present in calm weather, and in stormy situations, its energy increases by about an order of magnitude (Shevchenko, 2006).

The article (Dogan et al., 2021) considers a model of long-period wave excitation during atmospheric pressure, moving with variable speed. In this case, when the speeds of the landslide and water surface are equal (Froude number Fr=1), a resonant amplification of the wave occurs.

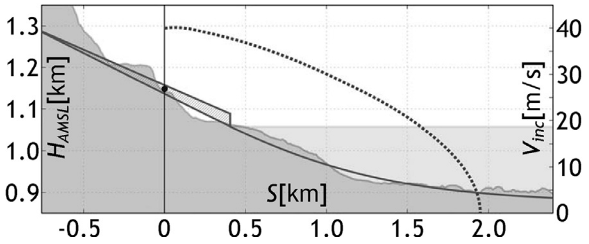

Figure 4 Cross section of the landslide crater of Askja volcano; the velocity graph of the center of mass is represented by a dashed line, the initial velocity is 40 m/s (144 km/h) (Gylfadottir et al., 2017).

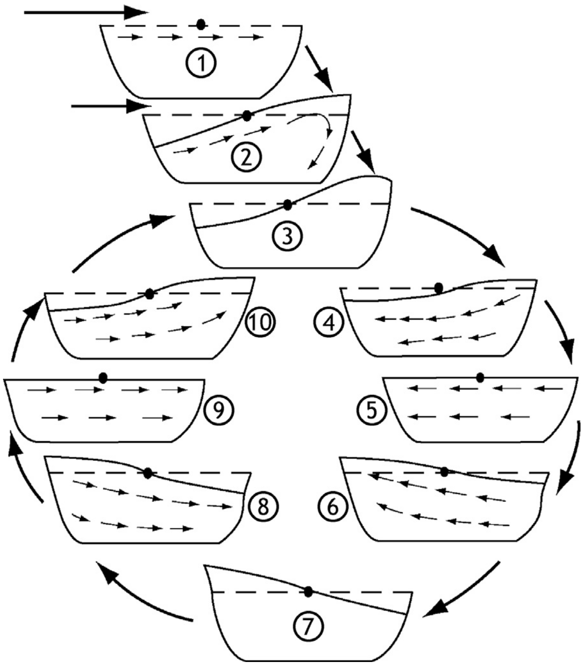

Figure 5 The sequence of longitudinal profiles of a single-node undamped standing wave in an unstratified water body (according to C. Mortimer, quoted from Boegman (2009)).

Landslides have been reported, to cause waves of significant height. The events described were accompanied by fluctuations of standing waves: July 9, 1958, in Lituya Bay, Alaska, USA (Miller, 1960); October 9, 1963, in Vajont reservoir, Italy (Ward and Day, 2011); July 21, 2014, in Askja Lake, Iceland (Gylfadottir et al., 2017). The reconstruction of the latter is shown in Figure 4.

According to calculations, the phase speed of the wave in a rectangular basin of constant depth, corresponding to the average depth of Askja Lake $\overline{D}=114$m, is $V_{ph}=33.4$ m/s.

3.4. Stimulation of natural oscillations by influencing standing current

Figure 5 shows a sequence of longitudinal profiles of a long-period single-node (uninodal) standing wave in an unstratified basin, at times $t=0.25\pi n$, where $n=0,1,2,\ldots$

In Figure 5, the point indicates the node of the wave, the dashed line is the level of the unwave surface; arrows are the generalized direction of movement of the water mass.

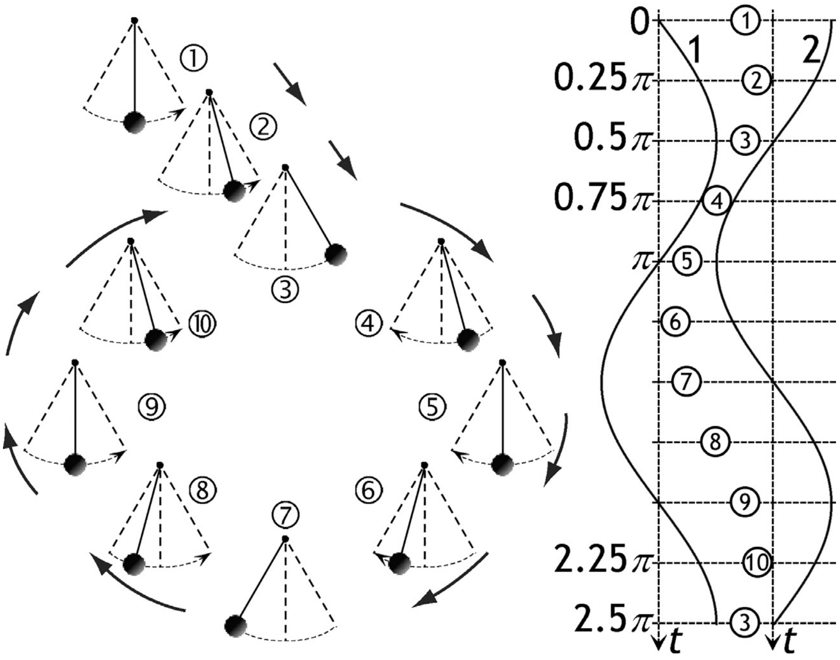

Figure 6 Oscillations of a standing wave: on the left is a sequence of positions of an oscillating mathematical pendulum corresponding to the profiles of a standing wave Figure 5; on the right are the water levels at the antinode (1) and the current speed at the node (2), at times t = 0.25πn, n = 0,1,2,...

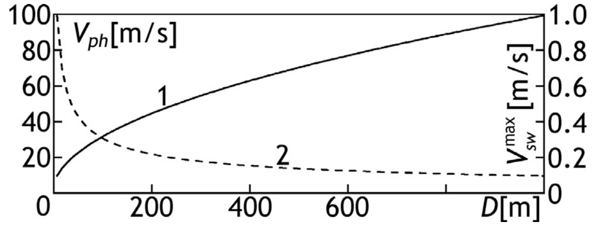

Figure 7 Comparative characteristics of phase speed of the wave Vph (1) and speed of standing current V_{sw} (2) in a rectangular basin with a horizontal bottom, at $A = 1$ m.

In Figure 6, standing wave profiles in Figure 5, according to the proposal of M. Longuet-Higgins, 1953, are represented by the corresponding positions of oscillations of a mathematical pendulum.

The second form of horizontal movement of standing waves, reversible currents, has a number of characteristic features, due to which it can be relatively easily distinguished from other types of currents. These features include: 1) the sinusoidal course of speed in time; 2) the periodic change of direction by 180°; 3) the functional connection of the speed course with the amplitude course (Sudol'skij, 1991).

Figure 7 shows a comparative characteristic of the speeds of both forms of horizontal movement of water masses with fluctuations of standing waves.

The maximum speed of the standing current, which changes the direction of movement due to the movement of the water surface from the bottom of the wave to its crest and back, is calculated by the formula (Arsen'eva et al., 1963; Rabinovich, 2009; Sudol'skij, 1991):

$$V_{sw}^{\max} = A_{sw}\sqrt{\frac{g}{D}} \tag{5}$$

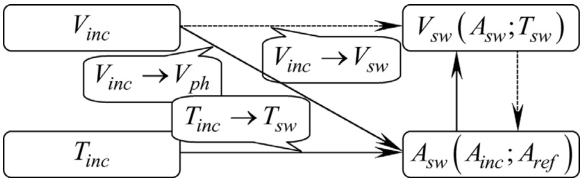

Figure 8 The block diagram of the stimulation of natural (eigen) oscillations of water bodies.

Field observations have shown that the speed of the standing current in narrow straits of reservoirs can reach 3 m/s (10.8 km/h), and in wide straits, it usually does not exceed 1.0 m/s (3.6 km/h). In coastal areas of large inland water bodies, current speeds are measured at 0.3 m/s (1.08 km/h). In particular, the highest speeds of currents in Lake Baikal, Russia, reach 10 cm/s (0.36 km/h), in Lake Balkhash, Kazakhstan, – up to 1.25 m/s (4.5 km/h), in the narrowing of the Kakhovka Reservoir, Ukraine, – 0.58 m/s (2.09 km/h) (Sudol'skij, 1991); in the Yakimvarsky Bay of Lake Ladoga – 78 cm/s (2.8 km/h) at the narrow entrance to the Big Bear Lake (Canada) – 2.7 m/s (9.7 km/h) in the strait connecting a small lagoon with the Sary-Chiganak bay of the Aral Sea (Kazakhstan, Uzbekistan) – more than 1.3 m/s (4.7 km/h) (Labzovsky, 1971).

According to the studies, natural oscillations are stimulated when exposed to an external wave with a period, close to the period of natural oscillations of the reservoir, by a current with a constant speed, close to the phase speed of wave movement in the reservoir. The possibility of excitation and sustenance by a wave with a variable speed is especially noted. This suggests that the effect of current with constant or variable speed on a reversible wave with a variable speed can also stimulate natural oscillations. This condition will be written as

$$[(V_{inc} = const) \vee (V_{inc} \neq const)] \rightarrow \left[\left(Fr = \frac{V_{inc}}{V_{sw}}\right) \rightarrow 1\right] \quad (6)$$

where $\vee$ is a disjunction symbol.

The process of stimulating standing waves is shown in the form of a diagram in Figure 8.

4. Conclusions

The reservoir is considered an oscillator of natural vibrations. These include vertical oscillations of standing waves and two forms of horizontal current — unidirectional, with the phase speed depending on the water depth, and reversible, which is a function of the depth, period and amplitude of the wave.

The mechanisms of stimulation of natural oscillations of the water body, which can provoke the excitation of extreme waves, have been identified. A model has been developed for stimulating natural oscillations by waves with a constant period, and currents with constant and variable speeds.

A hypothesis is presented about the possibility of stimulating natural oscillations of water bodies by influencing the standing current, which changes the direction of movement due to the movement of the water surface from the bottom of the wave to the crest, and vice versa.

The range of expected periods of natural oscillations of water bodies is established, which ranges from 30 seconds to 24 hours, and the speed of the standing current is up to 11 km/h.

Declaration of competing interest

Given that I am, Pavlo Anakhov, the sole author of the article “Excitation of rogue wave by standing current”, there are no conflicts of interests.

References

Anakhov, P.V., 2021. Excitation of rogue wave by natural oscillations of the water body. Hydrology, Hydrochem. Hydroecol. 1, 106—114, (in Ukrainian). https://doi.org/10.17721/2306-5680.2021.1.10

Arsen’eva, N.M., Davydov, L.K., Dubrovina, L.N., Konkina, N.G., 1963. Seiches on the lakes of the USSR. Leningrad Univ., Leningrad, 184 pp. (in Russian).

Boegman, L., 2009. Currents in Stratified Water Bodies 2: Internal Waves. In: Likens, G.E. (Ed.), Encyclopedia of Inland Waters Vol. 1. Elsevier, Oxford, 539—558.

Bowers, D.G., Macdonald, R.G., McKee, D., Nimmo-Smith, W.A.M., Graham, G.W., 2013. On the formation of tide-produced seiches and double high waters in coastal seas. Estuar. Coast. Shelf Sci. 134, 108—116. https://doi.org/10.1016/j.ecss.2013.09.014

Didenkulova, I.I., Pelinovsky, E.N., 2006. Phenomena similar to tsunami in Russian internal basins. RJES 8, ES6002. https://doi.org/10.2205/2006ES000211

Dogan, G.G., Pelinovsky, E., Zaytsev, A., Metin, A.D., Tarakcioglu, G.O., Yalciner, A.C., Yalciner, B., Didenkulova, I., 2021. Long wave generation and coastal amplification due to propagating atmospheric pressure disturbances. Nat. Hazards. 106, 1195—1221. https://doi.org/10.1007/s11069-021-04625-9

Forrester, W.D., 1983. Canadian Tidal Manual. Dept., Fisher. Oceans, Ottawa, 138 pp.

Gao, J., Ji, C., Gaidai, O., Liu, Y., Ma, X., 2017. Numerical investigation of transient harbor oscillations induced by N-waves. Coast. Eng. 125, 119—131. https://doi.org/10.1016/j.coastaleng.2017.03.004

Gao, J., Ma, X., Dong, G., Chen, H., Liu, Q., Zang, J., 2021. Investigation on the effects of Bragg reflection on harbor oscillations. Coast. Eng. 170, 103977. https://doi.org/10.1016/j.coastaleng.2021.103977

Gao, J., Ma, X., Zang, J., Dong, G., Ma, X., Zhu, Y., Zhou, L., 2020. Numerical investigation of harbor oscillations induced by focused transient wave groups. Coast. Eng. 158, 103670. https://doi.org/10.1016/j.coastaleng.2020.103670

Gao, J., Zhou, X., Zhou, L., Zang, J., Chen, H., 2019. Numerical investigation on effects of fringing reefs on low-frequency oscillations within a harbor. Ocean Eng. 172, 86—95. https://doi.org/10.1016/j.oceaneng.2018.11.048

Gylfadottir, S.S., Kim, J., Helgason, J.K., Brynjólfsson, S., 2017. The 2014 Lake Askja rockslide-induced tsunami: Optimization of numerical tsunami model using observed data. J. Geophys. Res.-Oceans. 122 (5), 4110—4122. https://doi.org/10.1002/2016JC012496

Ivanov, K.E., Kobeko, P.P., Shulman, A.R., 1946. Deformation of ice cover during the movement of loads. J. Tech. Phys. 16, 257—262 (in Russian).

Ivus, G.P., Raevskij, A.N., Kivganov, A.F., Gulyaev, E.N., Vorobyov, V.I., 1991. Specialized weather forecasts. Leningrad Hydrometeorol. Inst. Leningrad, 112 pp. (in Russian).

Jueza, C., Navas-Montilla, A., 2022. Numerical characterization of seiche waves energy potential in river bank lateral embayments. Renew. Energ. 186 (1), 143—156. https://doi.org/10.1016/j.renene.2021.12.125

Kinsman, B., 1965. Wind waves: their generation and propergation on the ocean surface. Prentice-Hall, Englewood Cliffs, New Jersey, 676 pp.

Kodomari, S. , 1982. On the Studies of the Periodic Motions in a Lake (2): Effect of the Lake Basin Shape on the Periodic Motion. J. Fac. Sci., Hokkaido Univ., Ser. 7 (Geophysics), 185—226. https://doi.org/https://eprints.lib.hokudai.ac.jp/dspace/bitstream/2115/8736/1/7(2)_p185-226.pdf

Kovalev, D., Kovalev, P., Borisov, A.S., Zarochintsev, V.S., Kirillov, K.V., 2022. Features of seiche excitation in the water area near Poronaisk (Sakhalin Island). Geosystems of Transition Zones. https://doi.org/10.30730/gtrz.2022.6.2.114-123.

Kozin, V.M., 2007. Resonant method of breaking ice cover. Inventions and experiments. Acad. Natural Sci. Moscow, 355 pp. (in Russian).

Labzovsky, N.A., 1971. Noncyclic sea level fluctuations. Gidrometeoizdat, Leningrad, 238 pp. (in Russian).

Longuet-Higgins, M.S., 1953. Can Sea Waves Cause Microseisms? In: Symposium on Microseisms (4—6 September 1952). National Academy of Sciences, National Research Council, 74—86.

Miller, D.J., 1960. Giant Waves in Lituya Bay Alaska. Geological survey professional paper 354-C. United States Government Printing Office, Washington, 86 pp.

Nikolkina, I., Didenkulova, I., 2011. Rogue waves in 2006—2010. Nat. Hazards Earth Syst. Sci. 11 (11), 2913—2924. https://doi.org/10.5194/nhess-11-2913-2011

Rabinovich, A.B., 2009. Seiches and Harbor Oscillations. In: Kim, Y.C. (Ed.), Handbook of Coastal and Ocean Engineering. World Scientific Publ., Singapoure, 193—236. https://doi.org/10.1142/9789812819307_0009

Shevchenko, G.V., 2006. Dynamic processes on the shelf and the forecast of marine hazardous phenomena (on the example of Sakhalin island). Institute of Marine Geology and Geophysics Far

Eastern Branch, Russian Acad. Sci., Vladivostok, 34 pp. (in Russian).

Shuleykin, V.V., 1968. Marine physics, 4th edn., Nauka, Moscow, 1083 pp. (in Russian).

Sudol'skij, A.S., 1991. Dynamic phenomena in reservoirs. Gidrometeoizdat, Leningrad, 263 pp. (in Russian).

Titov, L.F., 1971. Wind-Driven Waves. [Translated from Russian by D. Lederman; edited by P. Greenberg]. Israel Program for Scientific Translations, Springfield, Va., Jerusalem, 244.

Vilibić, I., Rabinovich, A.B., Anderson, E.J., 2021. Special issue on the global perspective on meteotsunami science: editorial. Nat. Hazards. 106, 1087—1104. https://doi.org/10.1007/s11069-021-04679-9

Ward, S.N., Day, S., 2011. The 1963 Landslide and Flood at Vaiont Reservoir Italy. A tsunami ball simulation. Ital. J. Geosci. 130 (f.1), 16—26. https://doi.org/10.3301/IJG.2010.21

Zhang, J., Benoit, M., Kimmoun, O., Chabchoub, A., Hsu, H.-C., 2019. Statistics of Extreme Waves in Coastal Waters: Large Scale Experiments and Advanced Numerical Simulations. Fluids 4 (2), 99. https://doi.org/10.3390/fluids4020099

Oceanologia 65 (2023) 571—594

Available online at www.sciencedirect.com

ScienceDirect

journal homepage: www.journals.elsevier.com/oceanologia

ORIGINAL RESEARCH ARTICLE

Dinoflagellate cysts and benthic foraminifera from surface sediments of Svalbard fjords and shelves as paleoenvironmental indicators

Maciej M. Telesiński[a,*], Vera Pospelova[b], Kenneth Neil Mertens[c], Małgorzata Kucharska[a], Marek Zajączkowski[a]

[a] *Institute of Oceanology, Polish Academy of Sciences, Sopot, Poland*
[b] *University of Minnesota, Department of Earth and Environmental Sciences, College of Science & Engineering, Minneapolis, USA*
[c] *LITTORAL, Ifremer, Concarneau, France*

Received 6 October 2022; accepted 14 June 2023
Available online 28 June 2023

KEYWORDS
North Atlantic;
Nordic Seas;
Sea ice;
Primary productivity;
Fjords;
Sediments;
Chlorophyll-*a*

Abstract Due to the Arctic amplification effect, the Svalbard archipelago is an important area for studying ongoing environmental changes. However, its marine ecosystem is extremely complex. In this study, we analyze modern assemblages of dinoflagellate cysts (dinocysts) and benthic foraminifera from surface sediment samples around Svalbard. We use multivariate statistical analyses to examine relationships between environmental conditions (summer and winter sea surface temperature and salinity, sea-ice cover, etc.) and both microfossil groups to evaluate their use as proxies for reconstructions of the marine environment in the region. Our results show that the most important factor controlling the environment around Svalbard is the Atlantic Water which mostly impacts the western coast, but its influence reaches as far as the eastern coast of Nordaustlandet. However, on a local scale, such factors as the sea-ice cover, the presence of tidewater glaciers, or even the morphology and hydrology of fjords become increasingly important. We found that two dinocyst species, cysts of *Polarella glacialis* and *Echinidinium karaense*, can be considered regional winter drift ice indicators. The relationships between environmental parameters and benthic foraminiferal assemblages are much more difficult to interpret. Although statistical analysis shows a correlation of benthic foraminiferal species with various environmental parameters, this correlation might be some-

---

[*] Corresponding author at: Institute of Oceanology Polish Academy of Sciences, Powstańców Warszawy 55, Sopot 81—712, Poland.
E-mail address: mtelesinski@iopan.pl (M.M. Telesiński).

Peer review under the responsibility of the Institute of Oceanology of the Polish Academy of Sciences.

Production and hosting by Elsevier

https://doi.org/10.1016/j.oceano.2023.06.007

what coincidental and caused by other factors not analyzed in this study. Nevertheless, the use of two complementary microfossil groups as (paleo)environmental indicators can provide a more comprehensive picture of the environmental conditions.

List of abbreviations

AF	Arctic Front
AW	Atlantic Water
ArW	Arctic Water
dinocysts	dinoflagellate cysts
ESC	East Spitsbergen Current
NAC	North Atlantic Current
SSS	sea surface salinity
SST	sea surface temperature
TAW	Transformed Atlantic Water
WCW	Winter-cooled Water
WSC	West Spitsbergen Current

List of taxa (mentioned in the text)

Dinoflagellate cysts:
Ataxiodinium spp.
Cysts of *Biecheleria* cf. *baltica*
Brigantedinium spp.
Dubridinium spp.
Echinidinium karaense
Echinidinium spp.
Islandinium? cezare
Islandinium minutum
Nematosphaeropsis labyrinthus
Operculodinium centrocarpum sensu Wall and Dale (1966)
Cysts of *Pentapharsodinium dalei*
Cysts of *Polarella glacialis*
Cysts of *Protoperidinium nudum*
RBC, round brown cyst
SBC, spiny brown cyst
Selenopemphix quanta
Spiniferites elongatus
unidentified 1 & 2
Foraminifera:
Adercotryma glomeratum
Buccella frigida
Cassidulina reniforme
Cibicides lobatulus
Elphidium clavatum
Globobulimina arctica-turgida
Islandiella helenae
Islandiella norcrossi
Labrospira crassimargo
Melonis barleeanus
Nonionellina labradorica
Portatrochammina karica
Recurvoides turbinatus
Reophax scorpiurus
Spiroplectammina spp.
Stainforthia loeblichi
Textularia earlandi-kattegatensis
Trifarina fluens

1. Introduction

The Svalbard archipelago is one of the crucial areas to study ongoing global warming. First of all, it is located in high northern latitudes where any environmental changes can be easily observed due to the Arctic amplification effect (e.g., Balazy and Kuklinski, 2019; Schiermeier, 2007; Serreze and Barry, 2011; Serreze and Francis, 2006). Secondly, the archipelago constitutes a frontal area between relatively warm Atlantic waters and cold, sea ice-bearing Arctic waters, which enables the study of the influence of their interplay on both terrestrial and marine environments, especially in numerous fjords cutting deep into landmasses and creating a unique interface between the land and the sea (e.g., Cottier et al., 2005; Syvitski and Shaw, 1995). The effect of sea ice is particularly important as the sea ice-albedo feedback is thought to be associated with a decrease in the snow and ice cover and a corresponding increase in the surface temperature, further decreasing the snow and ice cover. It is shown that the sea ice-albedo feedback can operate even in multiyear pack ice, without the disappearance of this ice, associated with internal processes occurring within the multiyear ice pack (e.g., duration of the snow cover, sea-ice thickness and distribution, lead fraction, and melt pond characteristics) (Curry et al., 1995). The presence of ice caps and glaciers, including tidewater ice margins (e.g., Dowdeswell, 1989), is another characteristic feature of Svalbard allowing the investigation of feedback between land-based ice masses and the ocean. Finally, Svalbard's relative ease of access, compared to other Arctic regions, makes it one of the most important natural Arctic laboratories concentrating scientific efforts of a wide range of disciplines.

To understand modern changes in the environment, studies of its natural variability reaching beyond historical observations are necessary. Remains of microorganisms are often used in paleoceanographic reconstructions as they are usually abundant in marine sediments and provide information on numerous parameters of the environment in which they lived. Unfortunately, in the Svalbard fjords, some microfossil groups like planktic foraminifera or diatoms are absent or have a poor fossil record which limits the possibilities of (paleo)environmental studies (e.g., Korsun et al., 1995; Zgrundo et al., 2017). On the other hand, fjords in the region are described as "hot spots" for other microfossil groups such as dinoflagellate cysts (e.g., Grøsfjeld et al., 2009; Howe et al., 2010) and benthic foraminifera (e.g., Pawłowska et al., 2017; Szymańska et al., 2021).

Dinoflagellates are a major group of microscopic plankton commonly found in marine environments (e.g., Taylor et al., 2008; Zonneveld et al., 2013). This group is very diverse in coastal waters, and about half of the dinoflagellates are phototrophic (commonly called autotrophic) and directly contribute to marine primary productivity, whereas the other half is heterotrophic, i.e., feeding on a wide range of microorganisms, including diatoms and small flagellates (e.g., Jacobson and Anderson, 1996; Jeong, 1999; Taylor, 1987). Mixotrophy among dinoflagellates is now known to be widespread (e.g., Stoecker, 1999). In the fossil record, dinoflagellates are represented by their resting stages called cysts, generally produced during the sexual reproduction phase (e.g., Dale, 1983; Taylor, 1987). Dinoflagellate cysts (dinocysts) have organic walls that are highly resistant to physical, chemical, and biological degradation and can be preserved in sediments for hundreds of millions of years (e.g., Dale, 1996; Fensome et al., 1993). Dinocyst diversity, relative and absolute abundances, and the presence of specific taxa in sediments encode information about some of the dinoflagellate populations in the upper water column and, thus, environmental factors that influence their distributions (e.g., Dale, 1976; Zonneveld et al., 2013). Biogeographical distribution of dinocysts has been widely documented over the years (e.g., Dale, 1996) and it demonstrated that these microfossils can be successfully used for qualitative and quantitative reconstructions of sea-surface temperature (SST), salinity (SSS), primary productivity, coastal eutrophication, and pollution in the Late Quaternary (e.g., Dale, 2009; Dale and Dale, 2002). Furthermore, the sea-ice cover appears to be another driving factor in cyst distributions in high latitudes, and some taxa have affinities for polar environments and are potential sea-ice indicators (e.g., de Vernal et al., 2020, 2013, 2001; de Vernal and Marret, 2007; Marret et al., 2020; Matthiessen et al., 2005; Obrezkova et al., 2023; Rochon et al., 1999). The seafloor sediments of areas characterized by multiyear perennial pack-ice are usually barren of dinocysts (e.g., de Vernal et al., 2020, 2005, 2001). Nevertheless, there are a few dinocyst taxa that are known to occur in sediments of areas marked by seasonal sea ice and even in high abundances (e.g., Grøsfjeld et al., 2009; Harland, 1982; Head et al., 2001; Heikkilä et al., 2014; Howe et al., 2010; Mudie and Rochon, 2001; Zonneveld et al., 2013). Neritic settings of Arctic seas with seasonal sea ice are usually characterized by *Islandinium minutum*, *Islandinium*? *cezare*, *Echinidinium karaense* and *Polykrikos*? sp. — Arctic morphotypes, whereas dinocyst assemblages from offshore regions have high abundances of *Impagidinium pallidum* and *Spiniferites elongatus* (e.g., de Vernal et al., 2020). Only a few cyst-forming species are known to dwell in the ice-pack environment. The most common examples are cysts of *Polarella glacialis* which were first described from sea-ice brine channels in Antarctica (Montresor et al., 1999) and the Canadian Arctic (Montresor et al., 2003).

Another key group of microorganisms thriving in Svalbard fjords and shelves with high biodiversity are benthic foraminifera (e.g., Murray, 1991). Their short life cycle and sexual reproduction allowing high genetic changeability make them good bioindicators for both short- and long-term environmental changes on a local as well as global scale (e.g., Barbieri et al., 2006). Due to the high preservation potential of the foraminiferal tests in sediment, they can be used as a proxy to reconstruct paleoenvironmental changes such as water temperature, salinity as well as oxygen and nutrients availability (e.g., Hald et al., 2001; Ślubowska et al., 2005). Benthic foraminiferal distribution in Svalbard fjords is conditioned by environmental gradients (e.g., Jernas et al., 2018). Close to tidewater glaciers, the conditions are unstable and the foraminiferal assemblages are characterized by low abundance and dominance of a few opportunistic species. In the outer parts of fjords, the conditions are more stable allowing for higher abundance and diversity of foraminiferal assemblages as well as a higher percentage of Atlantic Water-related species (Fossile et al., 2022; Hald and Korsun, 1997; Hansen and Knudsen, 1995; Jima et al., 2021; Korsun et al., 1995; Korsun and Hald, 2000; Kucharska et al., 2019; Mackensen et al., 2017; Majewski and Zajączkowski, 2007; Włodarska-Kowalczuk et al., 2013; Zajączkowski and Włodarska-Kowalczuk, 2007). As the water temperature is one of the main abiotic factors controlling benthic foraminifera distribution (e.g., Murray and Alve, 2016) it is important to study changes in benthic foraminiferal assemblages in the face of ongoing oceanographic and climatic changes.

In this study, we analyze modern assemblages of both dinocysts and benthic foraminifera and their relationships with environmental conditions to evaluate their use as proxies for reconstructions of the marine environment in Svalbard fjords and surrounding coastal waters. Although both groups have great potential to be used as bioindicators for modern and past environments, when combined, they can provide an even more complete image of the marine environment around Svalbard. We analyze the relationships between the two groups and surface water parameters, such as the dominant water masses, temperature and salinity, and sea-ice occurrence. We decided to focus only on surface water conditions, as these are available over extended periods of time from satellite observations. Even though surface water parameters might not influence benthic foraminiferal assemblages in a straightforward way, they certainly influence them indirectly, e.g., by regulating the food flux reaching the bottom.

2. Study area and oceanographic conditions

The Svalbard archipelago is influenced by two main water masses, Atlantic Water (AW) and Arctic Water (ArW). The relatively warm and saline AW ($T > 3°C$, $S > 34.65$, Cottier et al., 2005) is transported by the West Spitsbergen Current (WSC), the northernmost branch of the North Atlantic Current (Figure 1). Its flow is mainly confined to the continental slope (e.g., Saloranta and Svendsen, 2001), although the expansion of AW across the shelf and into the fjords, mostly below a 20—30 m thick surface layer (Figure 2A), occurs frequently (e.g., Cottier et al., 2005; Nilsen et al., 2016, 2008) as also confirmed by our CTD measurements (Figure 2). North of Svalbard, the WSC splits

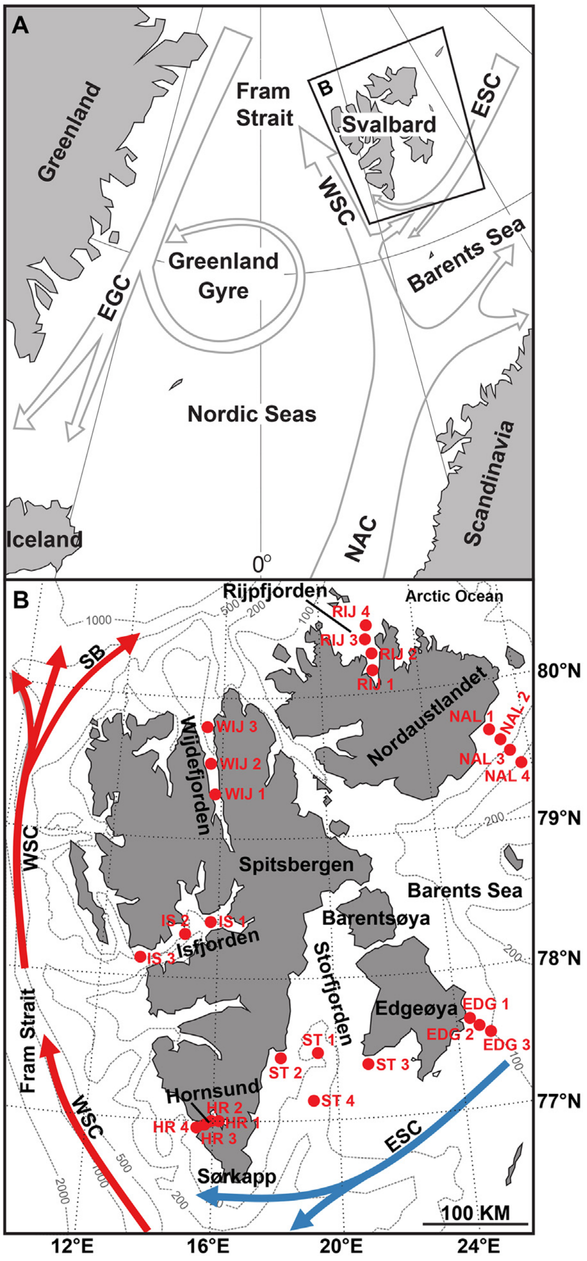

Figure 1 Location map showing the present-day surface water circulation (A) in the Nordic Seas and (B) around Svalbard. Positions of sampled stations are marked with red dots. Red arrows indicate AW, blue arrows — ArW. The surface currents are: EGC — East Greenland Current; ESC — East Spitsbergen Current; NAC — North Atlantic Current; SB — Svalbard branch of the WSC; WSC — West Spitsbergen Current.

into three primary branches. The easternmost Svalbard branch of the WSC encompasses the northern coasts of the archipelago (Aagaard et al., 1987) and represents the largest input of AW into the Arctic Ocean (Manley, 1995). The relatively cold and less saline ArW ($-1.5°C < T < 1°C$, $34.3 < S < 34.8$, Cottier et al., 2005) is transported from the northeast by the East Spitsbergen Current (ESC), together with drift ice from the Barents Sea (e.g., Saloranta and Svendsen, 2001; Skogseth et al., 2005). ArW mostly influences the eastern and southern coasts of Svalbard, though even here traces of AW can be found (Figure 2D, F and G). After passing the Sørkapp, the ESC turns northward and continues along the Svalbard continental shelf where it is influenced by the outflow from the adjacent fjords (e.g., Cottier et al., 2005). The mixing of the two water masses (i.e. AW and ArW) on the shelf leads to the formation of Transformed Atlantic Water (TAW) ($1°C < T < 3°C$, $S > 34.65$, Cottier et al., 2005). Other water masses, such as Winter-Cooled Water (WCW), and Local Water are restricted to the inner parts of all Svalbard fjords.

Sea-ice conditions around Svalbard are strictly related to water mass dominance. On the western coast, where waters are generally warmer and saltier, pack ice (e.g., WMO, 2014) is rarely seen, especially during the last few years (e.g., Dahlke et al., 2020). An exception is the area near Sørkapp where the ESC often brings pack ice from the Barents Sea. On the other hand, the sea surface around the eastern and northern coasts of the archipelago is rarely ice-free even during summer as pack ice from the high Arctic is often drifting here with water masses from the north (e.g., Comiso, 2002). Fast ice forming during winter and melting in spring often occurs in the inner parts of Svalbard fjords (e.g., Fossile et al., 2020).

The study area includes seven locations around Svalbard — five fjords (Storfjorden, Hornsund, Isfjorden, Wijdefjorden and Rijpfjorden) and coastal zones of two ice-covered islands: Nordaustlandet and Edgeøya (Figure 1). Based on the general oceanography of the region, as well as on our CTD results, the locations can be divided into three major areas: AW-dominated (including Isfjorden, Wijdefjorden and Rijpfjorden), ArW-dominated (Storfjorden and Hornsund), and locally/glacier-influenced (Nordaustlandet and Edgeøya).

Isfjorden is the largest fjord system on Svalbard. It is located on the western coast of Spitsbergen and is orientated north-east to south-west. The fjord has a length of 70 km and a water depth of up to 425 m (e.g., Rasmussen et al., 2012). The Isfjorden system is widely open to the inflow of Transformed Atlantic Water (TAW, Figure 2A) from the shelf as it has no sill at its mouth (e.g., Nilsen et al., 2016). The sea-ice cover in Isfjorden is seasonal, i.e. all ice in the fjord melts during summer. Freezing usually starts in late November and lasts until mid-May. The ice cover normally consists of locally formed fast ice with some drift ice entering from the shelf areas. In the mouth area, the ice cover is normally weak or non-existent (e.g., Nilsen et al., 2008).

Wijdefjorden is a 110 km long, south-north oriented fjord, located on the northern coast of Spitsbergen (Figure 1). The fjord has its prolongation (without a threshold) as a wide depression on the shelf (Kowalewski et al., 1990). Two basins can be identified in the inner part of the fjord with maximum water depths of 245 m and 170 m (e.g., Hald and Korsun, 1997). Five glaciers are discharging into the fjord. Despite its northern location, this fjord is exposed to the influence of AW from the WSC (Figure 2B) (Loeng et al., 1997; Maslowski et al., 2004; Pfirman et al., 1994; Rudels et al., 1994; Rudels and Friedrich, 2000), while the analysis of ice charts indicates frequent presence of drift ice in the fjord (NMI Ice Services, http://cryo.met.no accessed on 19.01.2021).

Rijpfjorden is a north-facing fjord located on the northern coast of Nordaustlandet (Figure 1). The fjord has a max-

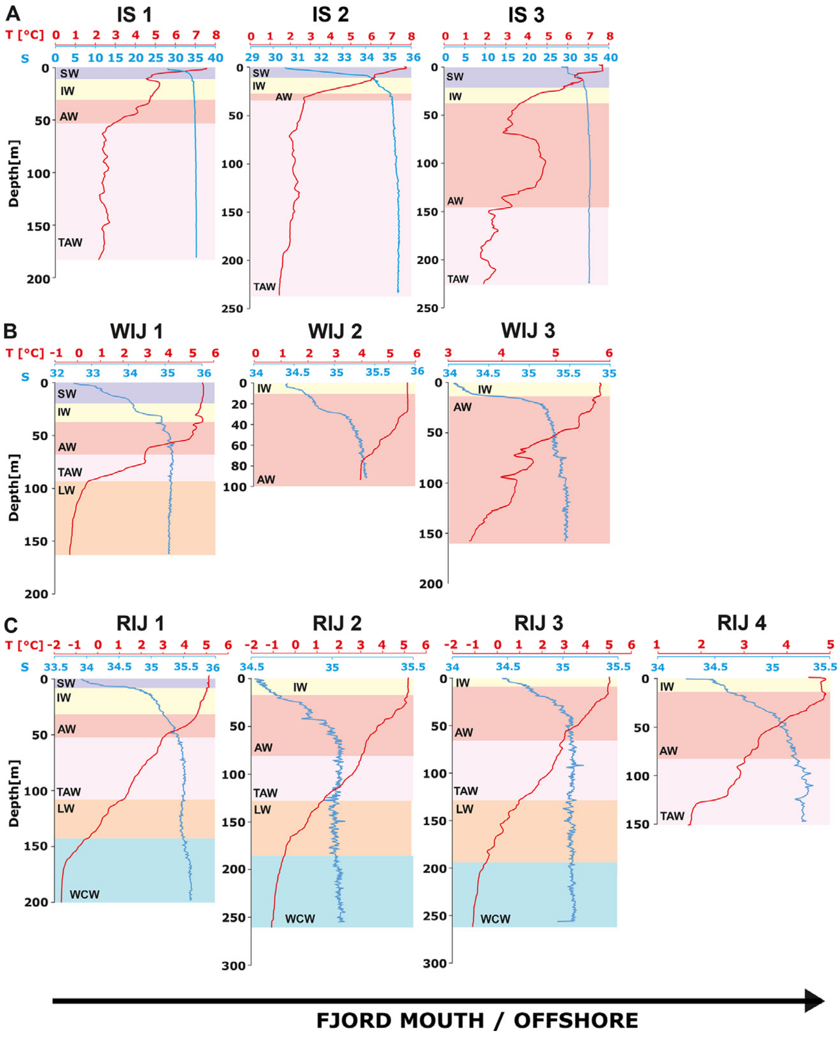

Figure 2 Water temperature [°C] (in red) and salinity (in blue) profiles measured at the sampling stations. Sampling dates are given in Table 1. Water masses at different depths are labelled (classification after Cottier et al., 2005). ArW — Arctic Water, AW — Atlantic Water, IW — Intermediate Water, LW — Local Water, SW — Surface Water, TAW — Transformed Atlantic Water, WCW — Winter-Cooled Water.

imum water depth of 270 m and is widely open towards the broad and shallow shelf (100—200 m deep). Rijpfjorden has generally been considered a ‘true’ Arctic fjord, as it was dominated by cold ArW, with a weak AW inflow. However, in recent years, the influence of AW has been steadily increasing (Figure 2C). In most years, sea ice lasts there from October until July (e.g., Ambrose et al., 2006; Søreide et al., 2010; Wallace et al., 2010) with some interannual variability in sea ice abundance and its thickness (Leu et al., 2011).

Nordaustlandet (Figure 1) is covered with the three main ice masses: Austfonna, Vestfonna, and Vegafonna (Dowdeswell and Drewry, 1985). Austfonna accounts for ~45% of the total calving flux from the Svalbard archipelago (Dowdeswell et al., 2008). The forefield of Austfonna is mostly covered with multiyear ice from the Arctic Ocean. Since the late 1970s, a progressive decrease in the sea-ice cover in the Barents Sea is observed (e.g., Comiso, 2002), causing an increase in moisture transport across Nordaustlandet and the growth of its ice masses (e.g., Bamber et al., 2004). The structure of the water column near the glaciated coastline is the result of the mixing of different water masses, including glacial meltwater. Further offshore, ArW becomes dominant. However, AW can also be traced (Figure 2D).

Edgeøya (Figure 1) is located on the eastern side of the Svalbard archipelago. It borders the Barents Sea to the east and Storfjorden to the west. In the north, the Freemansundet strait separates Edgeøya from Barentsøya. Edgeøya is covered by several glaciers, the largest of which is Edgeøyjøkulen on its eastern side. ArW dominance was observed close to the northeastern coast of Edgeøya, while AW was found beneath the surface layer of ArW off the southeastern coast (Carroll et al., 2008). Our CTD measurements confirm the dominance of ArW further offshore, while mixed water masses were identified closer to the coast. AW has not been traced (Figure 2E). Similar to Austfonna, mostly multiyear ice from the Arctic Ocean can be found off the eastern coast of Edgeøya.

Storfjorden is an approximately 190-km-long glacial trough that is enclosed by the landmasses of Spitsbergen to the west and Edgeøya and Barentsøya to the east and is

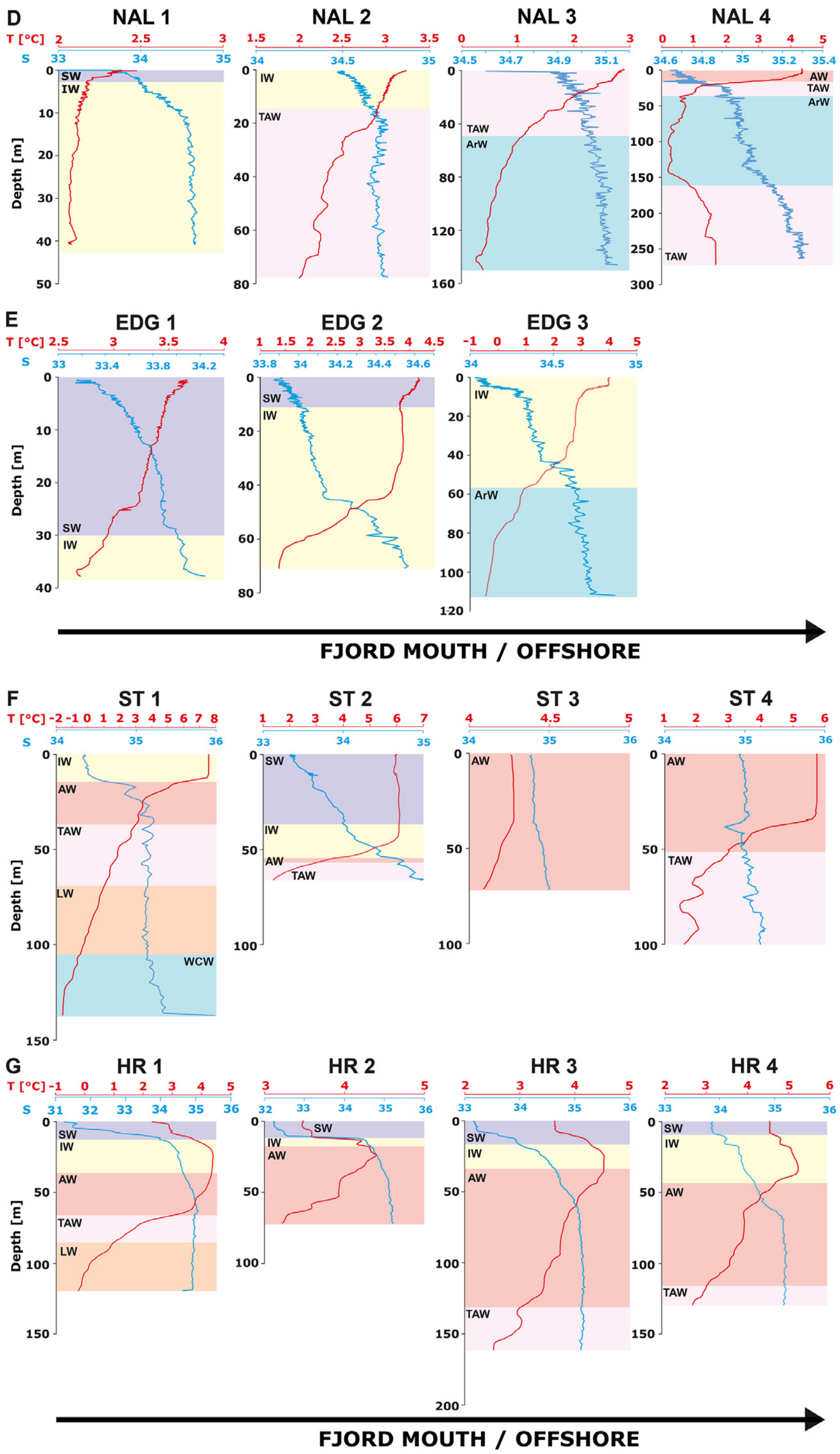

Figure 2 *Continued.*

limited by the shallow Storfjordbanken in the south-east. Storfjorden consists of two basins about 190 m deep, bordered by shallow (ca. 40 m) shelves. A 120-m deep sill crosses the mouth of Storfjorden at about 77°N and separates the main basin from Storfjordrenna, a continuation of the trough that extends beyond the shelf break (Skogseth et al., 2005). The water column in Storfjorden is composed of a mixture of two exogenous water masses and mixed waters that are formed locally (Figure 2F). ArW is transported by the ESC. AW, carried by the WSC, enters Storfjorden at a depth of 50—70 m (Akimova et al., 2011; Fer et al., 2003) though we have found it also on the surface. Brine-enriched shelf water is produced during sea-ice formation within the fjord (Haarpaintner et al., 2001; Skogseth et al., 2005, 2004). As fast ice forms in the inner part of Storfjorden starting in mid-November (Haarpaintner et al., 2001), the subsequently coming pack ice cannot enter the bay and is directed further towards Sørkapp and Hornsund.

Table 1 Sampling stations with their geographic position, water depth and sampling date.

Station	Latitude	Longitude	Depth [m]	Sampling date
Isfjorden				
IS 1	78°24.000′N	15°35.690′E	251	13.08.2016
IS 2	78°15.890′N	14°51.200′E	250	13.08.2016
IS 3	78°09.800′N	14°07.100′E	230	13.08.2016
Wijdefjorden				
WIJ 1	79°53.815′N	15°19.066′E	165	14.08.2016
WIJ 2	79°29.359′N	15°33.475′E	93	14.08.2016
WIJ 3	79°09.464′N	16°00.085′E	160	15.08.2016
Rijpfjorden				
RIJ 1	80°05.374′N	22°12.966′E	202	16.08.2016
RIJ 2	80°18.464′N	22°10.951′E	258	16.08.2016
RIJ 3	80°22.354′N	22°05.736′E	258	15.08.2016
RIJ 4	80°30.288′N	22°02.996′E	154	15.08.2016
Nordaustlandet				
NAL 1	79°42.727′N	26°34.955′E	43	18.08.2016
NAL 2	79°40.506′N	26°48.952′E	80	18.08.2016
NAL 3	79°36.241′N	27°30.196′E	147	18.08.2016
NAL 4	79°33.185′N	28°00.347′E	277	18.08.2016
Edgeøya				
EDG 1	77°42.925′N	24°12.853′E	41	19.08.2016
EDG 2	77°41.147′N	24°39.384′E	72	19.08.2016
EDG 3	77°39.751′N	25°00.162′E	112	19.08.2016
Storfjorden				
ST 1	77°27.163′N	19°14.230′E	251	14.08.2014
ST 2	77°24.138′N	17°51.734′E	67	14.08.2014
ST 3	77°14.728′N	20°53.185′E	72	15.08.2014
ST 4	76°53.181′N	19°27.559′E	158	14.08.2014
Hornsund				
HR 1	76°59.571′N	16°25.254′E	120	13.08.2014
HR 2	77°00.057′N	16°06.554′E	73	13.08.2014
HR 3	76°59.115′N	15°50.573′E	162	13.08.2014
HR 4	76°57.415′N	15°22.585′E	130	13.08.2014

Hornsund, the southernmost fjord of Svalbard (Figure 1), is 34 km long and 5—10 km wide. It is divided into several basins separated by sills with water depths usually over 100 m. The central basin is more than 250 m deep and the ice-proximal basins are 55-180 m deep (Zajączkowski et al., 2010). AW has been identified along the entire main axis of the fjord, below a ~40 m-thick layer of SW and IW (Figure 2G). Hornsund is the most 'glaciomarine' of the Spitsbergen fjords as almost 70% of the drainage area is covered by glaciers with thirteen tidewater glaciers entering the fjord (Błaszczyk et al., 2013; Hagen et al., 1993; Węsławski et al., 1991). Except for seasonal sea-ice cover in winter, Hornsund is often occupied by the pack ice brought there from the Barents Sea by the ESC in late spring and summer (e.g., Błaszczyk et al., 2013 and references therein; Węsławski et al., 1991).

3. Material and methods

3.1. Fieldwork

In total, 25 surface sediment samples were collected with a box corer (20 × 20 cm) for dinocyst analyses and with a small gravity corer (inner diameter 4.5 cm) for foraminiferal analyses during a cruise of r/v *Oceania*. Geographic positions, water depth, and sampling dates for each station are provided in Table 1. The samples were collected in August 2014 in Storfjorden (four stations; unfortunately, foraminiferal samples from station ST2 are missing) and Hornsund (four stations), and in August 2016 in Isfjorden (three stations), Wijdefjorden (three stations), Rijpfjorden (four stations) and in the coastal zones of Austfonna on Nordaustlandet (four stations) and Edgeøyjøkulen on Edgeøya (three stations, Figure 1). The temperature and salinity of the water column at each station were measured with a Mini CTD Sensordata SD202 at 1 s intervals. The depth of the water was measured with the hull-mounted echo sounder during sample retrieval.

3.2. Dinoflagellate cyst sample preparation and identification

The dinocyst analysis methodology used in this study is consistent with the standardized methodology described in Pospelova et al. (2005, 2010). The uppermost 2 cm of sediment from the box corer were collected into a zip bag and stored at a temperature of −20°C. With recent accumulation rates along the main axes of Svalbard fjords (e.g., 0.5–0.7 cm y^{-1} in Hornsund, Glud et al., 1998), 2 cm of sediment represents approximately four years of sedimentation. Close to tidewater glaciers, sediment accumulation rates increase to more than 10 cm y^{-1} (Filipowicz, 1990), resulting in a shorter time represented by the sampled sediment. However, our stations are located mainly in the middle and outer parts of the fjords, along their main axes (Figure 1). Therefore, we assume that 2 cm of sampled sediment should, on average, represent approximately two years of sedimentation. Although this approach might seem to be an oversimplification since the time interval represented by the 2 cm thick sample differs at each station, we consider it reasonable for the aim of the study as we assume that the environmental conditions did not change drastically over the last couple of years. After thawing, 3–4 cm^3 of well-mixed sediment was placed in a polypropylene test tube, dried at >40°C and weighed with an analytical balance. The samples were subsequently soaked with distilled water for 12 h, centrifuged at 3600 rpm for 6 min and then processed using a standard palynological technique (e.g., Pospelova et al., 2010, 2005).

Marker grains of a known number of *Lycopodium clavatum* spores (e.g., Mertens et al., 2012a, 2009) were added to allow quantitative estimates of the absolute concentrations of dinocysts. About 7 ml of hydrochloric acid (HCl, 10%) at room temperature was slowly added to samples to dissolve the *L. clavatum* spore tablets and remove carbonates. After 30 minutes samples were centrifuged and decanted. Subsequently, ~9 ml of distilled water was added and samples were centrifuged and decanted again. The procedure was repeated until the pH of the supernatant reached a neutral level. Afterwards, the samples were wet-sieved through 125 μm and 15 μm mesh to remove fractions of sediment above and below the maximal and minimal size of dinocysts.

After sieving, centrifuging, and decanting, ~7 ml of room-temperature hydrofluoric acid (HF, 48%) was added to the sediment to remove silicate. Samples were left in a fume hood for 72 hours, with regular digestion checking and stirring. After silicate dissolution, samples were once again centrifuged and decanted and ~7 ml of hydrochloric acid (HCl, 10%, at room temperature) was added. Samples were rinsed with distilled water as described above and sieved through a 15 μm mesh. Aliquots of a few drops of sample residue were placed on a glass slide and left for 24 h at room temperature to dry. Glycerine gel was used to mount a cover slide to the glass slide.

Approximately 300 specimens (min 281, max 319) were counted from each sample. Dinocysts were identified to the lowest possible taxonomical level. The paleontological taxonomy system used throughout this paper follows Zonneveld (1997), Kunz-Pirrung (1998), Montresor et al. (1999), Rochon et al. (1999), Head et al. (2001), Pospelova and Head (2002), Moestrup et al. (2009), Mertens et al. (2015, 2013, 2012b), and Zonneveld and Pospelova (2015). Cysts with unknown taxonomic affinity were classified into one of four groups: unidentified 1 – round transparent cyst, unidentified 2 – spiny transparent cyst, RBC – round brown cyst and SBC – spiny brown cyst. Cysts of *Biecheleria* cf. *baltica* are mostly very small (~5–10 μm) and were partly lost during sample preparation (sieving). Therefore, we excluded them from the total cyst concentrations and statistical analyses. Furthermore, it cannot be excluded that some thin-walled transparent *Impagidinium* spp. cysts have been missed during the counting.

3.3. Benthic foraminifera sample preparation and faunal analysis

Living benthic foraminifera can be found down to 10 cm in sediment (e.g., Kucharska et al., 2019; Zajączkowski et al., 2010). However, as the gravity corer did not penetrate deep enough at every station, the uppermost 4 cm of sediment was used for foraminiferal analysis to enable the comparison of the results between all the stations. Even though the 4 cm thick samples might contain some foraminiferal specimens older than ~2 years (as assumed for the 2 cm thick samples used for dinoflagellate cyst assemblage analysis), we find this a reasonable approach because, as mentioned before, we expect the environmental conditions to be roughly similar over the last couple of years. The sediments were weighed and wet-sieved through sieves with mesh sizes of 500 μm, 100 μm, and 63 μm. The 500 μm sieve was used only to protect foraminiferal shells from crushing by larger grains and the results of the analysis of >500 μm and 500–100 μm fractions (>100 μm) were analyzed together. The material was subsequently dried and weighed with an accuracy of ±0.1 mg. Benthic foraminifera census counts were conducted on representative splits (>300 specimens) in the >100 μm fraction using a Nikon SMZ1500 stereomicroscope. Individual species were identified and counted. The paleontological taxonomy system used throughout this paper follows Loeblich and Tappan (1987), Hald and Korsun (1997), Husum and Hald (2004), Darling et al. (2016), Łącka and Zajączkowski (2016), and Hayward et al. (2020). The number of benthic foraminifera per 1 g dry sediment (foram g^{-1}) was calculated.

3.4. Environmental data

The SST and SSS data were retrieved from the Copernicus website (https://www.copernicus.eu/; accessed October and November 2018). Monthly averaged data were read from available maps and average seasonal values were calculated over the period of two years prior to sediment sampling (August 2012–August 2014 for Hornsund and Storfjorden, August 2014–August 2016 for the rest of the stations; see Table 1 for sampling dates). Data on sea-ice coverage were retrieved from the website of the Norwegian Meteorological Institute (https://cryo.met.no/). Sea-ice concentrations at each station (in %) were manually read from Ice Charts at weekly intervals (four daily values per month) within two years prior to sediment sampling (the same as for the SST and SSS data). Subsequently, the average seasonal values (winter: December–February, spring: March–May, summer: June–August, autumn: September–November) were calculated. As fast ice was not present at any station during the studied time, only drift ice is included in the analysis. Despite ongoing global changes, we assume that environmental parameters over two years represent average 'modern' conditions and display general trends over the last couple of years. For this reason, we analysed the relationships between environmental parameters over a constant time interval (two years prior to sediment sampling) and the two groups of microorganisms, despite the variable time represented by the sediment samples studied.

3.5. Statistical analyses

To reduce noise in the data sets, all statistical analyses were performed on relative abundances of dinocysts and benthic foraminifera after grouping some less important species into genera and excluding taxa that contribute less than 1% to the assemblages (i.e., the maximum relative abundance at any station was lower than 1%). Only these taxa are presented and discussed hereafter. Multivariate statistical analyses were used to investigate the relationships between each microfossil group (dinocysts and benthic foraminifera) and environmental parameters using CANOCO 4.5 for Windows (ter Braak and Šmilauer, 2002). First, a Detrended Correspondence Analysis (DCA) was performed to identify the nature of variability within the assemblages in each group. The length of the first gradient determines whether the assemblages have unimodal variation (length >2) or linear variation (length <2) (Lepš and Šmilauer, 2003). We identified that the length of the first gradient was 1.9 standard deviations (SD) for dinocysts and 2.4 SD for foraminifera, indicating a linear variation for cysts and a unimodal variation for foraminifera. The DCA results justified the further use of a Redundancy Analysis (RDA) for dinocysts and Canonical Correspondence Analysis (CCA) for benthic foraminifera (Lepš and Šmilauer, 2003).

We applied a forward selection of environmental parameters to reduce the set of variables that could effectively explain the greatest amount of variance in the data sets. A total of seven environmental parameters were chosen for the analyses: water depth (WD), winter and summer sea-surface temperature (SST win, SST sum), salinity (SSS win, SSS sum), and sea ice cover (SI win, SI summer). Each environmental variable's statistical significance (P-value < 0.05) was determined using the forward selection Monte Carlo permutation test, with 499 unrestricted permutations.

4. Results

4.1. Oceanographic conditions

The results of CTD measurements, together with the identified water masses (following Cottier et al., 2005) are shown in Figure 2. Seasonally averaged sea-ice cover, SST and SSS data used for the multivariate statistical analysis are listed in Supplementary Table 1. We acknowledge that some of the salinity data retrieved from Copernicus appear anomalous, reaching up to 37.8 at station WIJ1 in March. Such high values might be caused by the quality of satellite measurements in inner parts of narrow fjords and/or in high latitudes in general. However, it should be noted that the highest salinities (>35.3) are associated with the lowest temperatures (≤ -2°C), generally high sea-ice concentrations, and occur in the inner parts of the north-facing fjords (Wijdefjorden and Rijpfjorden) in winter and spring (January to May). Altogether, it suggests that the high salinities might be related to brines formed by salt rejection during sea-ice formation (Haarpaintner et al., 2001). For this reason, we decided not to discard or correct the outlying data as they most probably reflect the natural variations even if the absolute values are indeed overestimated.

4.2. Dinoflagellate cyst abundances and assemblages

The total cysts concentrations calculated per gram of dry weight of sediments (cysts g^{-1}) vary from ~1,700 to 20,000, with an average of ~10,800 cysts g^{-1}. The highest cyst concentrations were found in Isfjorden and Rijpfjorden. The southern part of the studied region is characterized by lower cyst concentrations, with the lowest values recorded at the Hornsund and Edgeøya sites (Figure 3A). In total, dinocysts belonging to 39 taxa (23 genera) were identified in the analysed samples. A total of 19 of them were produced by autotrophic and 20 by heterotrophic dinoflagellates (Supplementary Table 2). The proportions of cysts produced by heterotrophic and autotrophic dinoflagellates in the assemblages are variable. Figure 3B shows the geographical distribution of the heterotrophic/autotrophic-related taxa in the cyst assemblages. The proportion of heterotrophic taxa ranges from 21 to 81%, averaging ~53%. In general, the highest abundances of heterotrophic taxa were observed at the sites near the mouth of each fjord and in coastal waters, with the highest average values recorded in Isfjorden. *Islandinium minutum*, *Brigantedinium* spp., cysts of *Pentapharsodinium dalei* and *Polarella glacialis* were present in every sample (Figure 4). Six further taxa (*Ataxiodinium* spp., cysts of *Protoceratium reticulatum* (or *Operculodinium centrocarpum* sensu Wall and Dale, 1966), *Nematosphaeropsis labyrinthus*, *Dubridinium* spp. *Echinidinium* spp., and *Selenopemphix quanta*) were present in each of the studied regions (though not in every sample). Light microscope micrographs of the most common dinocyst taxa are shown in Figure 5.

Four species were most abundant in the analyzed samples (Figure 4). *Islandinium minutum* constituted ~39% of all identified dinocysts and reached a maximum of 72% at station IS 3. The second most abundant species were cysts of *Polarella glacialis* (~24%) with a maximum abundance of 73% at station NAL 1. Cysts of *Pentapharsodinium dalei* and *Operculodinium centrocarpum* contributed an average of ~9% and ~7% in all identified assemblages, respectively with maximum abundances of ~39% at WIJ 1 and ~29% at IS 1, respectively. Among the remaining taxa, only *Islandinium*? *cezare* reached more than 22% at one of the stations (HR 2) but its average proportion among all identified taxa was only ~3%. Details on the relative abundances of individual taxa at each station can be found in Supplementary Table 2.

The results of the Redundancy Analysis (RDA) on the proportions of dinocyst taxa in the assemblages showed that the first ordination axis explains 43% of the variance, and it is positively but not significantly correlated with the winter sea-ice cover and negatively and significantly correlated with the water depth (Figure 6). A Monte Carlo permutation test under the reduced model with 499 permutations indicated that the first ordination axis and all canonical axes are

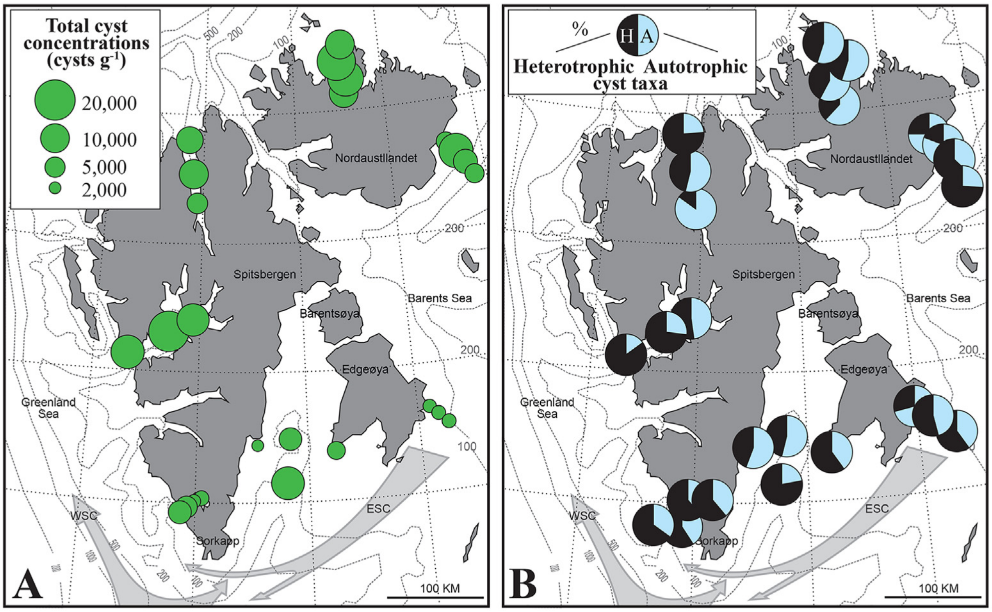

Figure 3 A: Total sedimentary concentrations [cysts g^{-1}] of dinocysts at each station. B: Proportion of autotrophic/heterotrophic dinocysts in each sample.

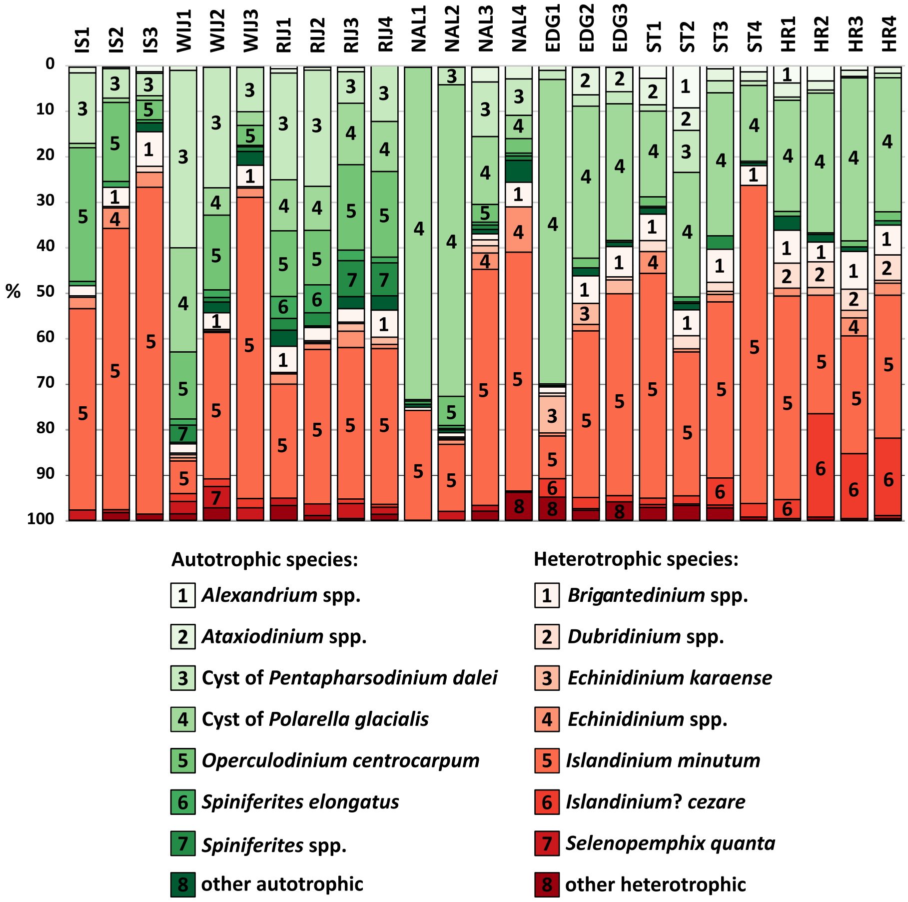

Figure 4 Percentages of the most common autotrophic (shades of green) and heterotrophic (shades of red) dinocyst taxa at each station.

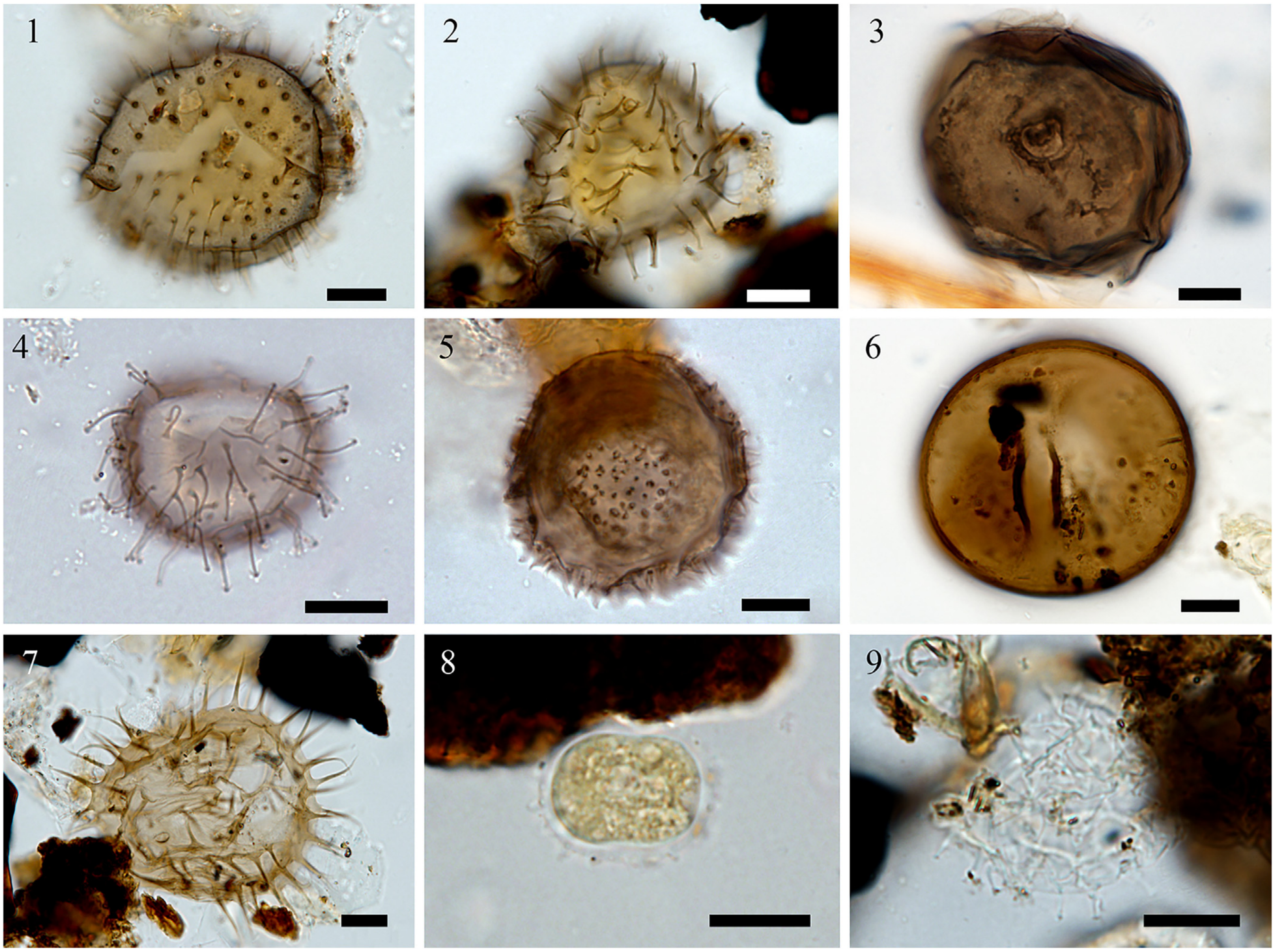

Figure 5 Plate presents light microscope micrographs. 1) High focus of *Islandinium minutum* (EDG 1). 2) High focus of *Echinidinium karaense* (EDG 1). 3) Mid focus of *Dubridinium* sp. with flagellar scar (HR 3). 4) High focus of *Islandinium*? *cezare* (EDG 1). 5) Mid focus of *Echinidinium sleipnerensis* (EDG 1). 6) Mid focus of *Brigantedinium simplex* with typical flagellar scars (NAL 4). 7) High focus of *Selenopemphix quanta* (EDG 1). 8) Mid focus of cyst of *Polarella glacialis* (EDG 1). 9) High focus of cyst of *Pentapharsodinium dalei* (IS 1). All scale bars = 10 μm.

statistically significant with P-values of 0.004 and 0.002, respectively. The second ordination axis explains an additional 19% of the variance, and it is positively and significantly correlated to the summer sea-ice cover and sea-surface salinity in winter. Figure 6 shows the ordination of sites, winter and summer environmental parameters, as well as the most common cyst taxa based on the first two RDA axes (RDA1 and RDA2). The first axis (RDA 1) demonstrates that the best fit corresponds to cysts of *Polarella glacialis* (67%), *Islandinium minutum* (37%), *Operculodinium centrocarpum* (24%), and *Echinidinium* species (~20%). The species with the best fit for the second axis (RDA 2) are cysts of *Pentapharsodinium dalei* (78%), *Spiniferites elongatus* (43%), *Selenopemphix quanta* and cysts of *Protoperidinium nudum* (both ~30%, respectively), and *Operculodinium centrocarpum* (27%).

The scores of RDA 1 and RDA 2 for each site are plotted on the satellite image of the area (NASA; https://landsat.visibleearth.nasa.gov/view.php?id=86468) that shows snow/ice cover in the summer of 2015 (Figure 7). It illustrates the impact of the warm WSC on the western side and the cool ESC on the southern and eastern coasts of Svalbard during the summer growing season. The figure shows that sites with the highest negative RDA 1 scores are in Isfjorden, Wijdefjorden, and Rijpfjorden, while the highest positive RDA1 values are in Nordaustlandet and Edgeøya. Sites with positive RDA 2 scores are primarily in Wijfjorden and Rijpfjorden, whereas sites with the highest negative scores of RDA 2 are found along the eastern and southern sites, as well as near the mouths of most of the fjords.

4.3. Benthic foraminiferal abundances and assemblages

The total benthic foraminifera concentrations calculated per gram of dry weight of sediments (forams g^{-1}) vary from 5 to ~1,300, with an average of ~214 forams g^{-1}. The highest benthic foraminiferal concentrations were found at Wijdefjorden and Nordaustlandet sites. The southern part of the studied region is characterized by lower foraminiferal concentrations, with the lowest values recorded at Stor-

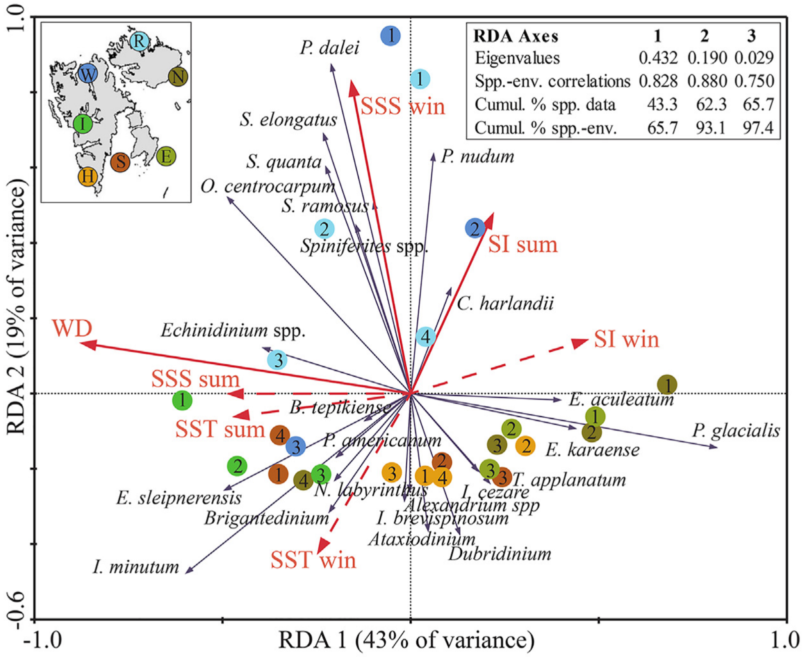

RDA Axes	1	2	3
Eigenvalues	0.432	0.190	0.029
Spp.-env. correlations	0.828	0.880	0.750
Cumul. % spp. data	43.3	62.3	65.7
Cumul. % spp.-env.	65.7	93.1	97.4

Marginal Effects

Variable	Lambda
WD	0.33
SSS win	0.15
SSS sum	0.11
SI win	0.11
SST sum	0.10
SST win	0.07
SI sum	0.07

Conditional Effects

Variable	Lambda	P-value
WD	0.330	**0.002**
SSS win	0.140	**0.002**
SI sum	0.100	**0.012**
SI win	0.030	0.270
SST win	0.040	0.076
SSS sum	0.020	0.402
SST sum	0.010	0.630

Study areas

- Ⓘ Isfjorden (IS 1-3)
- Ⓦ Wijdefjord (WIJ 1-3)
- Ⓡ Rijpfjorden (RIJ 1-4)
- Ⓝ Nordaustlandet (NAL 1-4)
- Ⓔ Edgeøya (EGD 1-3)
- Ⓢ Storfjorden (ST 1-4)
- Ⓗ Hornsund (HR 1-4)

Figure 6 The results of the Redundancy Analysis (RDA) on the proportions of dinocyst taxa in the assemblages showing the ordination of sites, winter (win) and summer (sum) environmental parameters (SI — sea-ice concentration, SSS — sea surface salinity, SST — sea surface temperature), as well as the most common dinocyst taxa based on the first two RDA axes (RDA1 and RDA2).

fjorden and Edgeøya sites (Figure 8A). In total, benthic foraminifera belonging to 27 taxa (24 genera) were identified in the analysed samples. A total of 15 of them were calcareous and 12 were agglutinated (Supplementary Table 3). The proportions of calcareous and agglutinated foraminifera in the assemblages are variable. Figure 8B shows the geographical distribution of the calcareous/agglutinated taxa in the foraminiferal assemblages. The proportion of calcareous taxa ranges from 21 to 100%, averaging ~76%. In general, the highest proportions of calcareous taxa were observed at the sites near the fjord heads and stations closest to the coast, with the highest average values recorded in Wijdefjorden. *Elphidium clavatum, Islandiella helenae* and *Nonionellina labradorica* were present in every sample (Figure 9). Fourteen further taxa (*Buccella frigida, Cassidulina reniforme, Cibicides, lobatulus, Globobulimina arctica-turgida, Islandiella norcrossi, Stainforthia loeblichi, Trifarina fluens, Adercotryma glomeratum, Labrospira crassimargo, Recurvoides turbinatus, Reophax scorpiurus, Spiroplectammina* spp., *Textularia earlandi-kattegatensis,* and *Portatrochammina karica*) were present in each of the studied regions (though not in every sample).

Five benthic foraminifera species were dominant in most of the analyzed samples (Figure 9). *E. clavatum* constituted ~22% of all identified forams and reached a maximum of ~52% at station HR 2. The second most abundant species were *Cassidulina reniforme* and *Cibicides lobatulus* (15%, respectively) with a maximum abundance of ~71% at station HR 1 and ~48% at station WIJ 2, respectively. *Nonionellina labradorica* reached ~11% with a maximum abundance of ~31% at station IS 2. *Adercotryma glomeratum*, the most abundant agglutinated species, constituted ~8% of all identified taxa with a maximum of ~23% at station RIJ 1. Among the remaining species, *Melonis barleeanus* reached a maximum of ~12% at station NAL 3 but its average share among all identified taxa reached only ~2%. Details on the relative abundances of individual taxa at each station can be found in Supplementary Table 3.

The results of the canonical correspondence analysis (CCA) on the proportions of benthic foraminifera in the assemblages showed that the first ordination axis (CCA 1) explains 21% of the variance, and the second ordination axis (CCA 2) describes an additional 11% of the variance (Figure 10). The first and all canonical axes are statistically significant with P-values of 0.02 and 0.004, respectively. CCA 1 is positively and significantly correlated with the summer sea-ice cover, whereas CCA 2 is positively and significantly correlated with the winter sea-ice cover.

The first axis (CCA 1) has the best fit with agglutinated foraminifera *Adercotryma glomeratum* (55%), *Ammodiscus* sp. (58%), *Portatrochammina karica* (46%) and calcareous

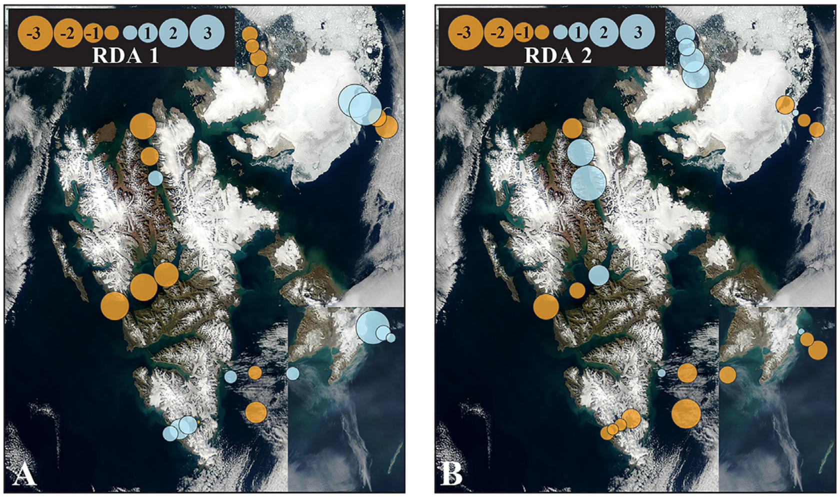

Figure 7 The scores of RDA 1 and RDA 2 for each site plotted on the satellite image of the area (NASA; https://landsat.visibleearth.nasa.gov/view.php?id=86468) showing snow/ice cover in the summer of 2015 (Data date: April 29, 2015—July 9, 2015).

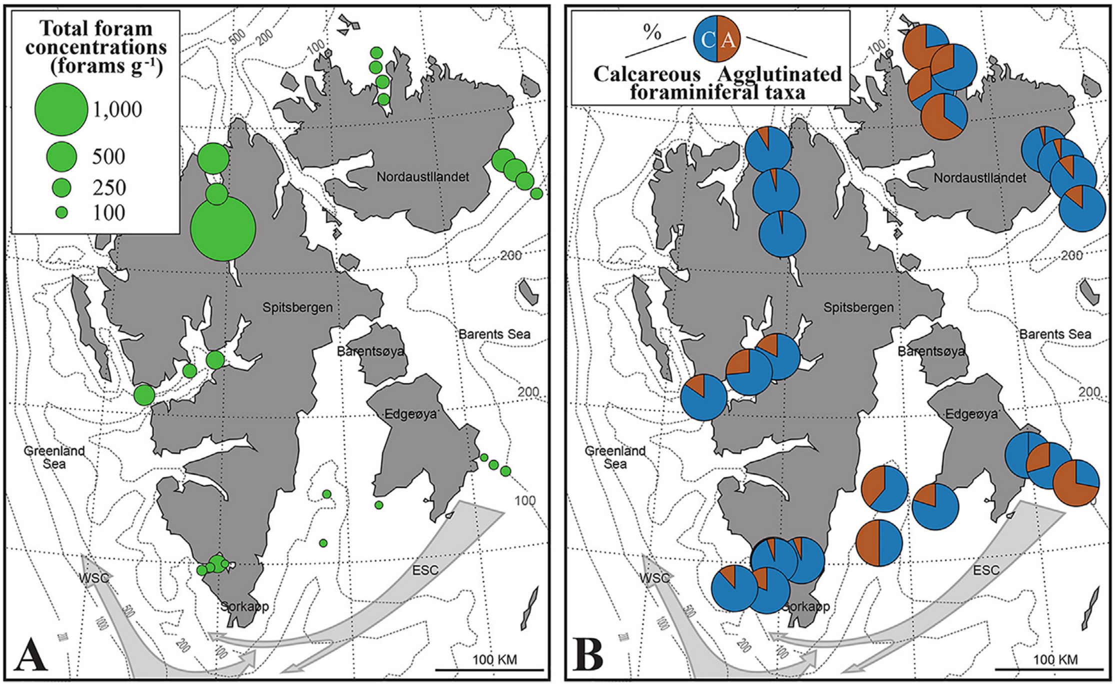

Figure 8 A: Total sedimentary concentrations [forams g^{-1}] of benthic foraminifera at each station. B: Proportion of calcareous/agglutinated foraminifera in each sample.

Melonis barleeanus (57%) and *Quinqueloculina* spp. (31%). The taxa with the best fit for the second axis (CCA 2) are calcareous *Cibicides lobatulus* (42%) and *Nonionellina labradorica* (28%). The CCA scores for each site plotted on the satellite image of the area (NASA; https://landsat.visibleearth.nasa.gov/view.php?id=86468) (Figure 11) show that the highest positive CCA 1 values are in Rijpfjorden and the highest negative values at the coastal sites of Nordaustlandet (NAL 1 and 2). Sites with positive CCA 2 scores are mainly in the northern and northeastern parts of the archipelago, whereas sites with the highest negative scores of CCA 2 are along the eastern and southern sites, as well as near the mouths of most of the fjords.

As mentioned above, the stations can be divided into three major areas. This classification has been confirmed by our dinocyst and benthic foraminiferal results and can be summarized as follows:

4.4. Atlantic Water-dominated stations

This region includes three westward and northward facing fjords: Isfjorden, Wijfjorden, and Rijpfjorden (Figure 1). These fjords are characterized by the presence of a thick layer of AW, usually underlain by TAW and covered by a relatively thin layer of SW and/or IW (Figure 2A). The dinocyst assemblages (Figure 4) are dominated by *Islandinium min-*

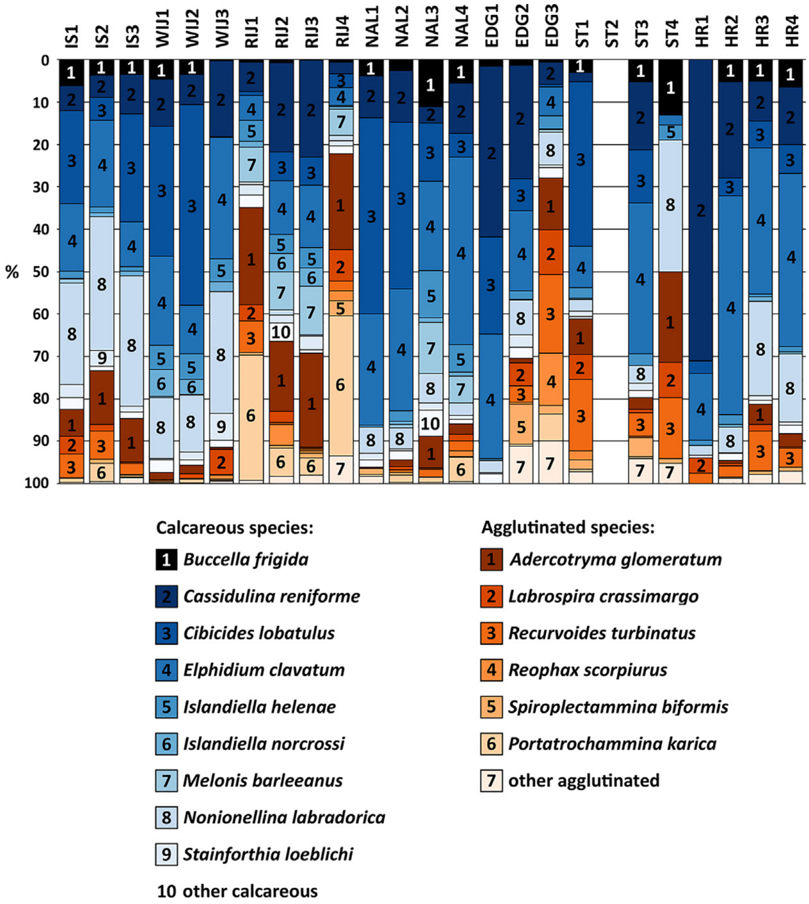

Figure 9 Percentages of the most common calcareous (shades of blue) and agglutinated (shades of brown) benthic foraminiferal species.

utum (an average abundance of ~41% with a maximum of 72% at station IS 3), followed by cysts of *Pentapharsodinium dalei* (~17% with a maximum of 37% at station WIJ 1), *Operculodinium centrocarpum* (~14% with a maximum of 28% at station IS 1), and cysts of *Polarella glacialis* (~8%). The most common benthic foraminiferal species (Figure 9) of the AW-dominated region are *Cibicides lobatulus, Nonionellina labradorica,* and *E. clavatum* (each constituting on average 15% of the assemblages), followed by *Adercotryma glomeratum* (~12%), *Cassidulina reniforme* (~11%), and *Portatrochammina karica* (~8%). *Cibicides lobatulus* reached a maximum abundance of 47% at station WIJ 2, *Nonionellina labradorica* reached 31% at station IS 2, and *Adercotryma glomeratum* reached 23% at station RIJ 1. Other dinocyst and benthic foraminiferal species constituted on average less than 5% of the assemblages, respectively.

4.5. Arctic Water-dominated stations

Fjords characterized by ArW dominance include Storfjorden and Hornsund, both located in southern Svalbard (Figure 1). Even though AW and TAW are also present in the water column at most of the stations, the overlying layer of SW and/or IW is relatively thicker, compared to AW-dominated stations, and the surface water temperatures are lower (Figure 2C). The most common dinocyst species in this region (Figure 4) include *Islandinium minutum* (~40%), cysts of *Polarella glacialis* (~27%), and *Islandinium? cezare* (~9% with a maximum of 22% at station HR 2). The most numerous benthic foraminiferal species (Figure 9) are *E. clavatum* (~27% with a maximum of 52% at station HR 2), *Cassidulina reniforme* (~19% with a maximum of 71% at station HR 1), *Nonionellina labradorica* (~12%), *Cibicides lobatulus* (~10%), *Recurvoides turbinatus* (~8%), *Adercotryma glomeratum* (~6%), and *Buccella frigida* (~5%).

4.6. Locally/glacier-influenced stations

This region groups stations located in the coastal zones of Nordaustlandet and Edgeøya (Figure 1). The oceanographic conditions and, thus, dinocyst and benthic foraminiferal faunas are the most diversified here and depend largely on the distance of the station from the ice front. SW, IW, and TAW dominate the water column in different proportions at all the stations, indicating a dynamic oceanographic regime and the mixing of water masses of different origins (Figure 2B). Two species dominate the dinocyst assemblages (Figure 4) in this region: cysts of *Polarella glacialis* (~41% with a maximum of 72% at station NAL 1) and *Islandinium minutum* (~33%). The most common benthic foraminiferal species (Figure 9) include *E. clavatum* (~25%), *Cibicides lobatulus* (~19%), *Cassidulina reniforme* (~16%), and *Non-*

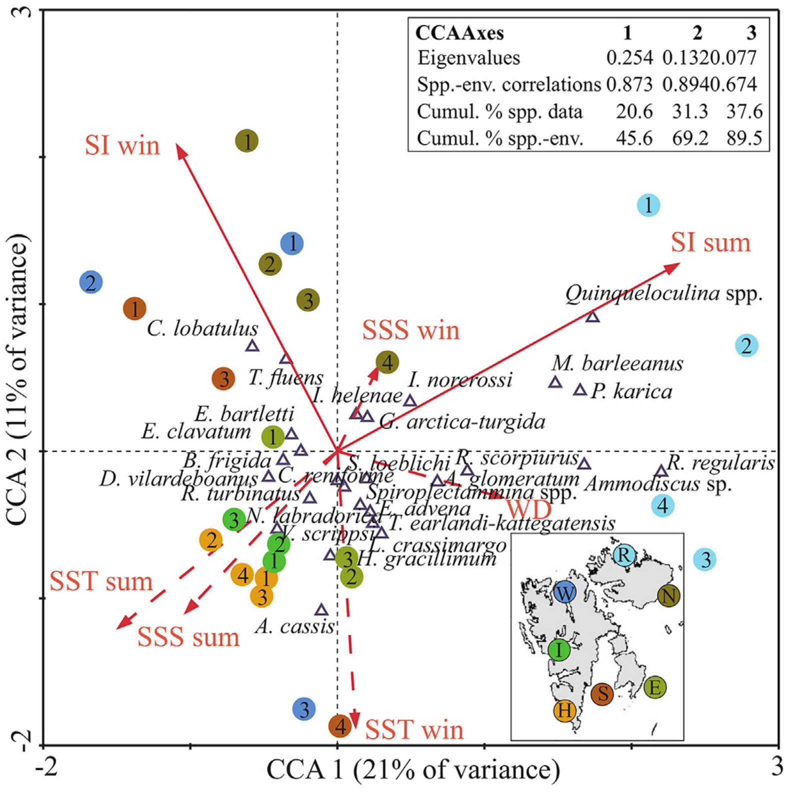

CCAAxes	1	2	3
Eigenvalues	0.254	0.132	0.077
Spp.-env. correlations	0.873	0.894	0.674
Cumul. % spp. data	20.6	31.3	37.6
Cumul. % spp.-env.	45.6	69.2	89.5

Marginal Effects

Variable	Lambda
SI sum	0.20
SST sum	0.12
SI win	0.11
WD	0.09
SSS sum	0.09
SST win	0.07
SSS win	0.04

Conditional Effects

Variable	Lambda	P-value
SI sum	0.20	**0.002**
SI win	0.13	**0.006**
SSS sum	0.07	0.104
WD	0.05	0.287
SST win	0.04	0.384
SST sum	0.03	0.600
SSS win	0.04	0.572

Study areas

Ⓘ Isfjorden (IS 1-3)
Ⓦ Wijdefjord (WIJ 1-3)
Ⓡ Rijpfjorden (RIJ 1-4)
Ⓝ Nordaustlandet (NAL 1-4)
Ⓔ Edgeøya (EGD 1-3)
Ⓢ Storfjorden (ST 1-4)
Ⓗ Hornsund (HR 1-4)

Figure 10 The results of the canonical correspondence analysis (CCA) on the proportions of benthic foraminifera in the assemblages showing the ordination of sites, winter (win) and summer (sum) environmental parameters (SI — sea-ice concentration, SSS — sea surface salinity, SST — sea surface temperature), as well as the most common benthic foraminiferal taxa based on the first two CCA axes (CCA1 and CCA2).

ionellina labradorica (~6%). It is also worth noting that *Melonis barleeanus* reached a maximum of 12% at station NAL 3 although its average share among all identified taxa reached less than 3%.

5. Discussion

Cyst-forming dinoflagellates and benthic foraminifera are two unrelated groups of microorganisms, but both encode environmental parameters of surrounding waters. Most dinoflagellates are planktic (e.g., Taylor et al., 2008; Zonneveld et al., 2013) and for this reason, their spatial distribution is mostly dependent on the upper water masses. In contrast, the composition of the benthic foraminiferal assemblages is strongly influenced by factors such as, e.g., trophic state, type of sediment, and bottom water oxygenation level that might be independent of the dominant water mass. As already mentioned in the introduction, we decided to focus only on surface water conditions, as these are available over extended periods of time from satellite observations, while bottom water parameters are available only from CTD measurements performed during research cruises, mostly in summer. Even though surface water parameters might not affect benthic foraminiferal assemblages in a straightforward way, in the relatively shallow (<300 m) waters around Svalbard they certainly influence them indirectly, e.g., by regulating the food flux reaching the bottom (see, e.g., Seidenkrantz, 2013). This difference is well reflected in our results. For instance, the first and second ordination axes of the RDA on the proportions of dinocyst taxa in the assemblages explain much more of the variance (43% and 19%, respectively, Figure 6) compared to the first two ordination axes of the CCA on the proportions of benthic foraminifera (21% and 11%, respectively, Figure 10).

The dinocyst concentrations (Figure 3A) clearly show that dinoflagellates are highly dependent on the properties of

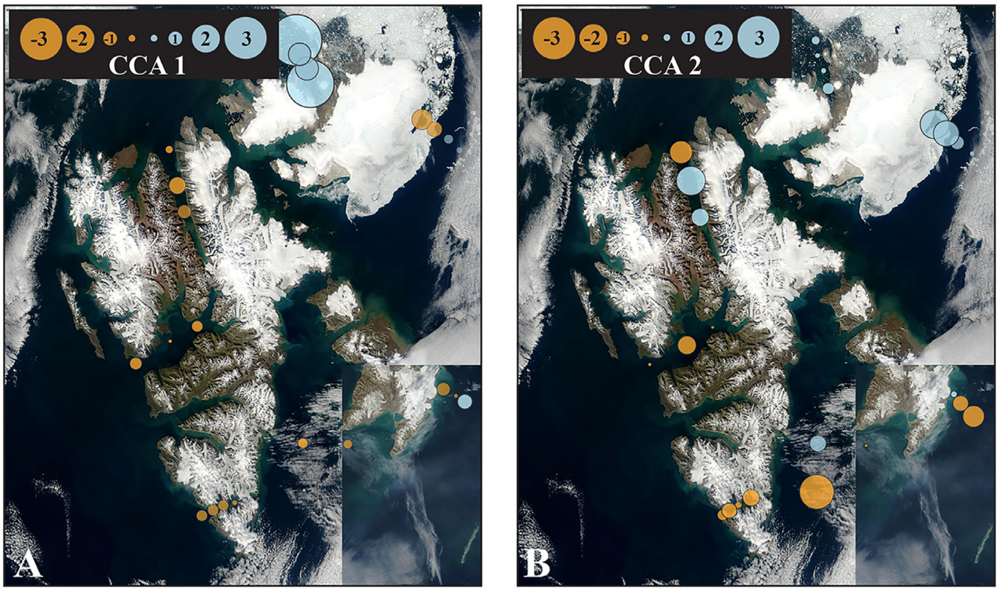

Figure 11 The scores of CCA 1 and CCA 2 for each site plotted on the satellite image of the area (NASA; https://landsat.visibleearth.nasa.gov/view.php?id=86468) showing snow/ice cover in the summer of 2015.

the upper water masses. The concentrations are highest in the western and northern Svalbard, most influenced by the WSC carrying AW. It might seem surprising that the dinocyst abundance is lower in Wijdefjorden than in the Rijpfjorden located farther north and more distant from the AW source. However, it should be noted that while Wijdefjorden is a long and narrow fjord, which limits AW penetration, Rijpfjorden has a wide mouth allowing for an easier exchange of water masses. Additionally, Rijpfjorden is strongly affected by summer sea ice (Figure 6) which might further promote summer dinoflagellate blooms as melting sea ice releases nutrients stimulating productivity in the marginal ice zone (e.g., Hebbeln and Wefer, 1991; Ramseier et al., 1999; Sakshaug, 2004; Smith Jr. et al., 1987). Off Nordaustlandet the dinocyst abundance is also relatively high (comparable to that in Wijdefjorden) indicating that AW reaches this area (Figure 2B). In southern Svalbard, the abundances are generally low. An exception is two stations in Storfjorden (ST 1 and 4) suggesting that the WSC can reach the main axis of this widely open fjord in times when the ESC weakens.

The benthic foraminiferal abundances exhibit a similar general pattern with higher values in western and northern areas influenced mainly by the WSC and lower values in the south affected by the ESC (Figure 8). A peculiar observation is that the highest benthic foraminiferal concentrations were found in Wijdefjorden (with by far the highest values at station WIJ 1 in the inner fjord) and Nordaustlandet. This might suggest that the benthic foraminiferal abundance is also stimulated by organic matter delivered by glaciers as both regions are influenced by tidewater ice fronts.

An important and widely debated aspect of dinocyst and benthic foraminifera distributions in coastal waters around Svalbard is their association with sea ice. Despite the recent development of geochemical proxies of sea-ice coverage (e.g., Belt et al., 2007; Belt and Müller, 2013; Cabedo-Sanz et al., 2013; Müller et al., 2011), its reconstruction in paleo records remains a complicated issue. For this reason, we took a particular interest in investigating the potential use of the two microfossil groups together as sea-ice indicators. More specifically, here we discuss drift ice as fast ice was not present at any station over the studied time.

An analysis of the dinocyst distribution around Svalbard suggests that two species might potentially be associated with sea ice: *Echinidinium karaense* and *Islandinium*? *cezare*. *Echinidinium karaense*, known from the Beaufort Sea, the Baffin Bay, and the northern Hudson Bay, prefers waters with temperatures between −2°C and −8°C and salinity between 20.5 and 33.8. It is found in nutrient-rich waters with lowered salinity due to ice melting and with a well-ventilated layer of bottom waters (e.g., Head et al., 2001; Zonneveld and Pospelova, 2015). Its association with sea ice has previously been investigated, but as it occurred only occasionally in areas with dense sea-ice cover, no definite conclusion have been reached (de Vernal et al., 2020, 2013). *Islandinium*? *cezare* is known from the Kara Sea and appears to have similar environmental preferences to *Echinidinium karaense* (e.g., Head et al., 2001; Zonneveld and Pospelova, 2015). The relative abundances of the two species were low at AW-dominated stations (Isfjorden, Wijdefjorden, Rijpfjorden) as well as off Nordaustlandet (Figure 3). They were much higher off Edgeøya and at ArW-dominated stations (Storfjorden and Hornsund). Nevertheless, they were present in all areas except for Isfjorden (Figure 12), i.e., in areas where sea ice occurs (Supplementary Table 1). Although our environmental data indicate very low sea-ice concentrations in Hornsund, its western and central part is often occupied by pack ice brought there from the Barents Sea by the ESC in late spring and summer (Błaszczyk et al., 2013). Altogether, this suggests that *Echinidinium karaense* and *Islandinium*? *cezare* could be potential regional sea-ice indicators.

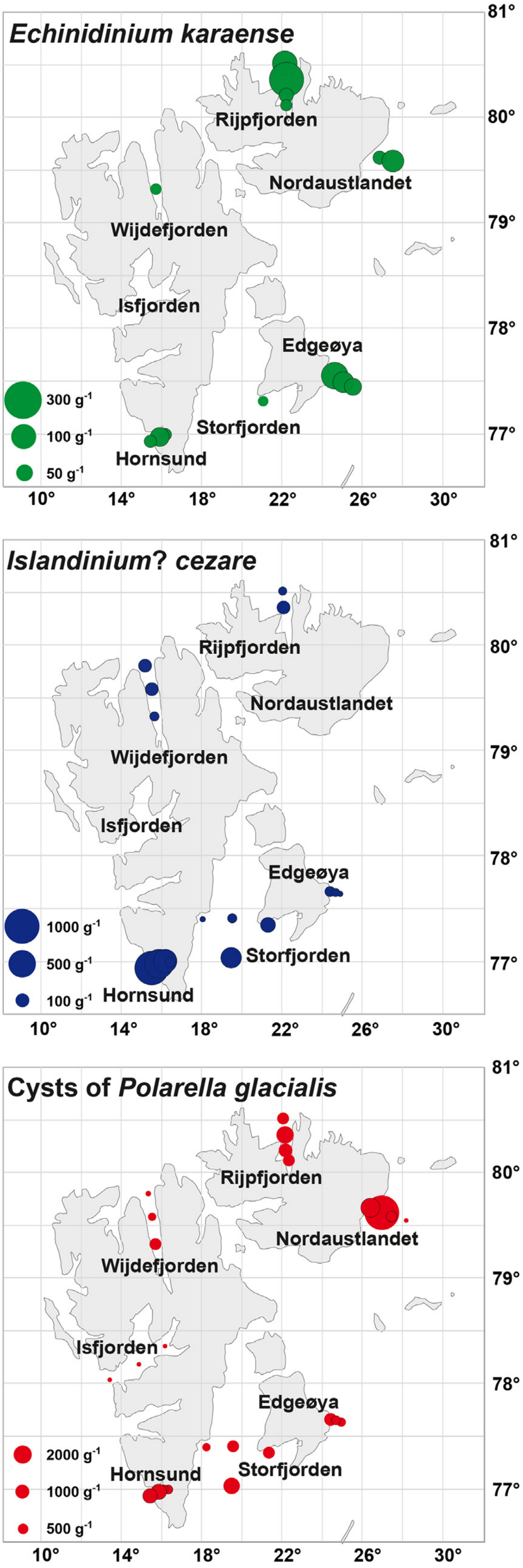

Figure 12 Sedimentary concentrations (cysts g^{-1}) of dinoflagellate cyst taxa potentially associated with sea ice: *Echinidinium karaense*, *Islandinium*? *cezare* and cysts of *Polarella glacialis*.

Our RDA results (Figure 6) show that the dinocyst species that is the most correlated with winter sea ice (drift ice) is *Polarella glacialis*. This species was first described from sea-ice brine channels in Antarctica (Montresor et al., 1999) and its association with sea ice has been observed in the Canadian Arctic (Montresor et al., 2003) and the Arctic Ocean (Matthiessen et al., 2005). However, cysts of *Polarella glacialis* have not been identified in most sediment samples used in paleoenvironmental studies for several potential reasons. Cysts of *Polarella glacialis* likely do not consist of resistant dinosporin (Montresor et al., 1999) and their long-term preservation in sediments is questionable. Furthermore, small (12—17-µm long and 8—15-µm wide) cysts of *Polarella glacialis* could easily pass through the 10—15 µm mesh size typically used in dinocyst sample preparation protocols, thus some but not all of them could be lost during palynological sample preparation (see Heikkilä et al., 2016, 2014). The abundance of this species in our samples (Figures 4 and 11) supports the fact that the cyst walls are resistant enough to be extracted from surface sediments and be used as environmental indicators, at least for modern samples from the Svalbard region. We acknowledge that some of the cysts of *Polarella glacialis* were partly lost during sample preparation. This may have biased our results, but the correlation of this species with sea-ice cover is still strong. *Echinidinium karaense* also shows a correlation with winter sea ice in the RDA plot (Figure 6). Even though it also appears in middle and outer Hornsund (stations HR 2-4) where no sea ice was recorded (Supplementary Table 1), the presence of *Echinidinium karaense* might be in accordance with episodic appearance of pack ice in this area in late spring and summer, as mentioned above. Thus, cysts of *Polarella glacialis* as well as *Echinidinium karaense* can be considered potential winter drift ice indicators in the Svalbard region. Nevertheless, it should be kept in mind that the first ordination axis of the RDA plot, which cysts of *Polarella glacialis* and *Echinidinium karaense* best fit with, is positively but not significantly correlated with the winter sea-ice cover.

No correlation was found between the winter sea-ice cover and the abundance of *Islandinium*? *cezare* (Figure 6). The discrepancy between the "naked eye" correlation of this species' distribution and sea-ice concentration and the RDA results might have several reasons. First of all, the environmental parameters had to be selected and reduced to enable an efficient statistical analysis. This might have led to some of the fauna-environment relationships being missed in the results. For instance, pack ice is brought from the Barents Sea into Hornsund mainly in late spring and summer (Błaszczyk et al., 2013), while our analysis took into account only winter and summer sea-ice concentrations. Secondly, the abundance of *Islandinium*? *cezare* was relatively low, compared to cysts of *Polarella glacialis* (though higher than that of *Echinidinium karaense*), which might have further biased the results. However, our results confirm previous findings (Heikkilä et al., 2016), indicating no direct relationship between *Islandinium*? *cezare* and sea-ice cover.

The CCA results of benthic foraminifera assemblages (Figure 10) show that the first ordination axis which is positively and significantly correlated with the summer sea-ice cover has the best fit mostly with agglutinated foraminifera species. However, before concluding that they can be used as summer sea-ice indicators (e.g., Scott et al., 2008), it should be noted that agglutinated species are most abundant in outer parts of fjords and at sites located farther offshore (Figure 8B) and that the ratio of agglutinated to calcareous foraminifera mainly depends on the absolute abundance of the latter (Supplementary Table 3). Obviously, the summer sea ice that originates mostly from the Arctic Ocean and the Barents Sea is also the most abundant in the outer parts of the fjords. Therefore, our results do not provide a definite answer whether increased sea-ice concentration in summer is indeed an environmental preference of agglutinated species (or a factor that decreases the abundance of calcareous species) or are there other factors that determine lower abundances of calcareous foraminifera in the outer parts of fjords. Although benthic foraminifera are not direct proxies for sea-ice cover, they respond to the surplus of food often available at sea-ice edges (Hebbeln and Wefer, 1991; Seidenkrantz, 2013; Smith Jr. et al., 1987). Furthermore, poor preservation of calcareous tests results from intensive decay of organic matter, leading to a decrease in pH (Majewski and Zajączkowski, 2007), or corrosive brines released during sea-ice formation (Fossile et al., 2020; Nardelli et al., 2023), although the latter occurs mainly during the winter-early spring season.

Interesting exceptions among the calcareous fauna are *Quinqueloculina* spp. and *Melonis barleeanus*, both showing a strong correlation with the summer sea-ice cover (Figure 10). *Quinqueloculina* spp. is an epifaunal porcelaneous foraminifera that belongs to miliolids. In our samples, it consisted mainly of *Quinqueloculina arctica*, a species common in the Arctic Ocean (e.g., Barrientos et al., 2018). It was the most common in the inner Rijpfjorden, where the summer sea-ice concentration was also the highest. Together, it might suggest that *Quinqueloculina* spp. or, more precisely, *Quinqueloculina arctica*, can be used as an indicator of summer sea ice in this particular environmental setting (a fjord facing the Arctic Ocean). *Melonis barleeanus*, in turn, is an infaunal hyaline species that is usually associated with fine-grained sediments containing buried organic matter that supports an infaunal life habit (e.g., Hald and Steinsund, 1992; Jennings et al., 2004). The species was first recorded in Rijpfjorden only recently and its appearance in this fjord was associated with the increasing influence of AW on the northern coast of Svalbard (Kujawa et al., 2021). Although this might be true, we suppose that the relatively high abundance of this species in Rijpfjorden and off Nordaustlandet compared to other stations (Figure 9) results mainly from its known environmental preferences. However, locations with abundant summer sea ice might also be characterised by fine-grained sediments transported by the ice (e.g., Nürnberg et al., 1994), thus making *Melonis barleeanus* an indirect summer sea-ice indicator.

Winter sea ice is the most abundant in the inner parts of the fjords (especially Wijdefjorden and Storfjorden) and off the glaciated shores (Supplementary Table 1). These also happen to be the areas where the relative abundance of calcareous forams is the highest, which is most clearly seen at stations off Edgeøya (Figure 8B). As a result, CCA shows a correlation between winter sea-ice concentration and several species of calcareous benthic foraminifera (Figure 10). However, this does not mean that they can be simply interpreted as winter sea-ice indicators. A good example is *Cibicides lobatulus*, the species the most correlated with winter sea-ice cover according to our CCA results. It dominates at locations with coarse sediments and is usually interpreted as an indicator of high energy/low sedimentation rate environments (e.g., Klitgaard-Kristensen and Sejrup, 1996) in marine environments from the Arctic (e.g., Hald and Korsun, 1997) to the tropics (e.g., Javaux and Scott, 2003; Romano et al., 2022). In Svalbard, such conditions may occur in the vicinity of fjord thresholds and narrows, where sea ice produced in the inner parts may also get stuck for extended periods of time. The species was also common at stations close to the ice fronts of Nordaustlandet and Edgeøya (Supplementary Table 3) where the environment is extremely dynamic. Winter sea ice is also abundant near the ice fronts because of large amounts of freshwater from the glaciers, which freezes at higher temperatures than saline water. Taken together, this could have contributed to the correlation of *Cibicides lobatulus* with winter sea-ice cover in our statistical analysis. However, this correlation occurs only in the particular environmental setting of the Svalbard fjords and glaciated margins.

In contrast, *Nonionellina labradorica* occupies the outer, deeper parts of the western and southern fjords, influenced by stable TAW (Figure 2, Supplementary Table 3) as it is known to feed on fresh phytodetritus and thus is indicative of high-productivity environments (e.g., Hald and Korsun, 1997; Majewski et al., 2009; Polyak and Mikhailov, 1996; Zajączkowski et al., 2010). Therefore, its strong negative correlation with winter and summer sea-ice cover is not surprising.

A direct relationship between net primary production and the abundance of heterotrophic dinoflagellate species can be expected. This relationship is more complex for autotrophic species, as they produce part of the chlorophyll-*a* (Chl-*a*) registered by the satellites. When Chl-*a* concentrations increase, heterotrophic species generally increase more than autotrophic species, so that the latter decrease in relative abundance (e.g., Zonneveld et al., 2013). A positive correlation between Chl-*a* concentrations and benthic foraminiferal abundance in shallow shelf areas can also be expected (e.g., Ahrens et al., 1997; Yamashita et al., 2020). However, no such relationship can be observed in our data (Figures 3, 7 and 12). First, average sea surface Chl-*a* concentrations around Svalbard are generally low, except for a few areas like Freemansundet (north of Edgeøya), Van Mijenfjorden (on the western coast of Svalbard), or in some of the side-fjords of the Isfjorden system where they reach relatively high values of up to ~68 mg Chl yr^{-1} m^{-3} (Figure 13). Unfortunately, none of our stations is located in these net primary production hotspots and the highest, though moderate Chl-*a* concentrations can be found at Storfjorden stations ST 2 and ST 3. Second, in such complex environments as Arctic fjords (e.g., Cottier et al., 2005; Kujawa et al., 2021; Syvitski and Shaw, 1995) the relationship between the net primary production and the Chl-*a* concentration (e.g., Campbell et al., 2002) might be more complex and/or suppressed by other processes than in the open ocean. Potential factors that might influence the primary productivity in Arctic fjords include, e.g., increased turbidity of the water or enhanced sedimentation of organic matter at glacier fronts during the melting season (e.g., Kujawa et al., 2021; Svendsen et al., 2002).

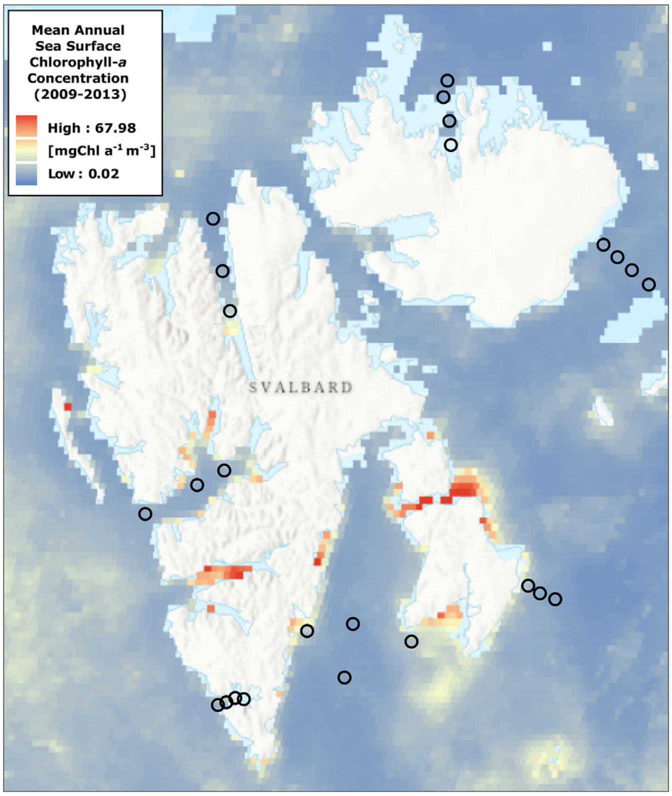

Figure 13 Location of study sites plotted on mean annual sea surface chlorophyll-*a* concentration [mgChl a^{-1} m^{-3}] data from satellite measurements (2009—2013). Data source: NASA Ocean Biology (OB.DAAC, 2014). Mean annual sea surface chlorophyll-*a* concentration for the period 2009—2013 (composite dataset created by UNEPWCMC). Data obtained from the Moderate Resolution Imaging Spectroradiometer (MODIS) Aqua Ocean Colour website (NASA OB.DAAC, Greenbelt, MD, USA). Accessed 28/11/2014. URL: http://oceancolor.gsfc.nasa.gov/cgi/l3. Cambridge (UK): UNEP World Conservation Monitoring Centre. URL: http://data.unep-wcmc.org/datasets/37.

6. Summary and conclusions

The fjords and glaciated coasts of the Svalbard archipelago are complex environments shaped by numerous factors. The most important of them is the AW-carrying WSC which mostly impacts the western coast, but its influence reaches as far as the coast of Nordaustlandet. It carries large amounts of heat, salt, and nutrients which have a tremendous effect on marine ecosystems, glaciers, and coasts. The abundance of both dinocysts and benthic foraminifera is clearly dependent on the strength of AW inflow. However, other factors such as the sea ice exported from the Arctic Ocean and the Barents Sea or even the shape and bathymetry of individual fjords strongly influence the planktic and benthic communities in the region.

The results of multivariate statistical analyses of the relationships between environmental parameters and dinocyst assemblages suggest that cysts of *Polarella glacialis* and *Echinidinium karaense* can be considered winter drift ice indicators. The potential association between *Islandinium*? *cezare* and sea-ice cover was not confirmed.

The relationships between environmental parameters and benthic foraminiferal assemblages are much more difficult to interpret, as the surface water parameters analysed in this study have only indirect influence on them. Furthermore, these bottom dwellers might be influenced by much more factors than just the dominant water mass or sea-ice cover. Although the statistical analysis shows the correlation of some benthic foraminiferal species or groups with winter/summer sea-ice cover, this correlation could be caused by more indirect relationships. For example, the correlation of *Melonis barleeanus* with summer sea-ice cover could be caused by the association of this species with fine-grained sediments, which around Svalbard are more common in areas with abundant summer sea ice.

In general, the analysis of relationships between the environmental parameters and the abundance of dinocyst and benthic foraminiferal species is a complicated task as even a strong correlation does not necessarily mean a causal relationship in such a complex environment as Svalbard fjords. Nevertheless, using two complimentary microfossil groups as (paleo)environmental indicators can provide a more complete picture of the environmental conditions.

Acknowledgements

Study design and data collection (dinocyst analyses) have been supported by grant no. 2014/15/N/ST10/05115 funded by the National Science Centre, Poland. Data collection (foraminiferal analyses) and statistical analysis have been funded by Norwegian Financial Mechanism for 2014-2021, project no. 2019/34/H/ST10/00682. Data interpretation and manuscript preparation have been supported by grant no. 2020/39/B/ST10/01698 funded by the National Science Centre, Poland.

Declaration of competing interest

The authors declare that they have no competing interest.

Supplementary materials

Supplementary material associated with this article can be found, in the online version, at https://doi.org/10.1016/j.oceano.2023.06.007.

References

Aagaard, K., Foldvik, A., Hillman, S.R., 1987. The West Spitsbergen Current: Disposition and Water Mass Transformation. J. Geophys. Res. 92, 3778—3784.

Ahrens, M.J., Graf, G., Altenbach, A.V., 1997. Spatial and temporal distribution patterns of benthic foraminifera in the Northeast Water Polynya. Greenland. J. Marine Syst. 10, 445—465. https://doi.org/10.1016/S0924-7963(96)00052-8

Akimova, A., Schauer, U., Danilov, S., Núñez-Riboni, I., 2011. The role of the deep mixing in the Storfjorden shelf water plume. Deep-Sea Res. Pt. I 58, 403—414. https://doi.org/10.1016/j.dsr.2011.02.001

Ambrose, W.G., Caroll, M.L., Greenacre, M., Thorrold, S.R., McMahon, K.W., 2006. Variation in Serripes groenlandicus (Bivalvia) growth in a Norwegian high-Arctic fjord: Evidence for local- and large-scale climatic forcing. Glob. Change Biol. 12, 1595—1607. https://doi.org/10.1111/j.1365-2486.2006.01181.x

Balazy, P., Kuklinski, P., 2019. Year-to-year variability of epifaunal assemblages on a mobile hard substrate—Case study from high latitudes. Mar. Ecol. 1—17. https://doi.org/10.1111/maec.12533

Bamber, J.L., Krabill, W., Raper, V., Dowdeswell, J.A., 2004. Anomalous recent growth of part of a large Arctic ice cap: Austfonna, Svalbard. Geophys. Res. Lett. 31, 3—6. https://doi.org/10.1029/2004GL019667

Barbieri, R., Hohenegger, J., Pugliese, N., 2006. Foraminifera and environmental micropaleontology. Mar. Micropaleontol. 61, 1—3. https://doi.org/10.1016/j.marmicro.2006.06.004

Barrientos, N., Lear, C.H., Jakobsson, M., Stranne, C., O'Regan, M., Cronin, T.M., Gukov, A.Y., Coxall, H.K., 2018. Arctic Ocean benthic foraminifera Mg/Ca ratios and global Mg/Ca-temperature calibrations: New constraints at low temperatures. Geochim. Cosmochim. Acta 236, 240—259. https://doi.org/10.1016/j.gca.2018.02.036

Belt, S.T., Massé, G., Rowland, S.J., Poulin, M., Michel, C., LeBlanc, B., 2007. A novel chemical fossil of palaeo sea ice: IP25. Org. Geochem. 38, 16—27. https://doi.org/10.1016/j.orggeochem.2006.09.013

Belt, S.T., Müller, J., 2013. The Arctic sea ice biomarker IP 25: a review of current understanding, recommendations for future research and applications in palaeo sea ice reconstructions. Quaternary Sci. Rev. 79, 9—25. https://doi.org/10.1016/j.quascirev.2012.12.001

Błaszczyk, M., Jania, J.A., Kolondra, L., 2013. Fluctuations of tidewater glaciers in Hornsund Fjord (Southern Svalbard) since the beginning of the 20th century. Polish Polar Res. 34, 327—352. https://doi.org/10.2478/popore

Cabedo-Sanz, P., Belt, S.T., Knies, J., Husum, K., 2013. Identification of contrasting seasonal sea ice conditions during the Younger Dryas. Quaternary Sci. Rev. 79, 74—86. https://doi.org/10.1016/j.quascirev.2012.10.028

Campbell, J.W., Antoine, D., Armstrong, R., Arrigo, K., Balch, W., Barber, R., Behrenfeld, M., Bidigare, R., Bishop, J., Carr, M.E., Esaias, W., Falkowski, P., Hoepffner, N., Iverson, R., Kiefer, D., Lohrenz, S., Marra, J., Morel, A., Ryan, J., Vedernikov, V., Waters, K., Yentsch, C., Yoder, J., 2002. Comparison of algorithms for estimating ocean primary production from surface chlorophyll, temperature, and irradiance. Global Biogeochem. Cy. 16. https://doi.org/10.1029/2001gb001444

Carroll, M.L., Denisenko, S.G., Renaud, P.E., Ambrose, W.G., 2008. Benthic infauna of the seasonally ice-covered western Barents Sea: Patterns and relationships to environmental forcing. Deep-Sea Res. Pt. II 55, 2340—2351. https://doi.org/10.1016/j.dsr2.2008.05.022

Comiso, J.C., 2002. A rapidly declining perennial sea ice cover in the Arctic. Geophys. Res. Lett. 29, 2—5. https://doi.org/10.1029/2002GL015650

Cottier, F.R., Tverberg, V., Inall, M., Svendsen, H., Nilsen, F., Griffiths, C., 2005. Water mass modification in an Arctic fjord through cross-shelf exchange: The seasonal hydrography of Kongsfjorden, Svalbard. J. Geophys. Res.-Oceans 110, 1—18. https://doi.org/10.1029/2004JC002757

Curry, J.A., Schramm, J.L., Ebert, E.E. , 1995. Sea Ice-Albedo Climate Feedback Mechanism. J. Clim. 8, 240—247. https://doi.org/10.1175/1520-0442(1995)008⟨0240:SIACFM⟩2.0.CO;2

Dahlke, S., Hughes, N.E., Wagner, P.M., Gerland, S., Wawrzyniak, T., Ivanov, B., Maturilli, M., 2020. The observed recent surface air temperature development across Svalbard and concurring footprints in local sea ice cover. Int. J. Climatol. 40, 5246—5265. https://doi.org/10.1002/joc.6517

Dale, B., 2009. Eutrophication signals in the sedimentary record of dinoflagellate cysts in coastal waters. J. Sea Res. 61, 103—113. https://doi.org/10.1016/j.seares.2008.06.007

Dale, B., 1996. Dinoflagellate cyst ecology: modeling and geological applications. In: Jansonius, J., McGregor, D.C. (Eds.), Palynology: Principles and Applications. AASP Foundation, 1249—1275.

Dale, B., 1983. Dinoflagellate resting cysts: 'benthic plankton'. In: Fryxell, G.A. (Ed.), Survival Strategies of the Algae. Cambridge University Press, New York, 69—136.

Dale, B., 1976. Cyst formation, sedimentation, and preservation: Factors affecting dinoflagellate assemblages in recent sediments from Trondheimsfjord. Norway. Rev. Palaeobot. Palynol. 22, 39—60. https://doi.org/10.1016/0034-6667(76)90010-5

Dale, B., Dale, A.L., 2002. Environmental applications of dinoflagellate cysts and acritarchs. In: Haslett, S.K. (Ed.), Environmental Micropalaeontology. Arnold, London, 207—240.

Darling, K.F., Schweizer, M., Knudsen, K.L., Evans, K.M., Bird, C., Roberts, A., Filipsson, H.L., Kim, J.-H., Gudmundsson, G., Wade, C.M., Sayer, M.D.J., Austin, W.E.N., 2016. The genetic diversity, phylogeography and morphology of Elphidiidae (Foraminifera) in the Northeast Atlantic. Mar. Micropaleontol. 129, 1—23. https://doi.org/10.1016/j.marmicro.2016.09.001

de Vernal, A., Eynaud, F., Henry, M., Hillaire-Marcel, C., Londeix, L., Mangin, S., Matthiessen, J., Marret, F., Radi, T., Rochon, A., Solignac, S., Turon, J.-L., 2005. Reconstruction of sea-surface conditions at middle to high latitudes of the Northern Hemisphere during the Last Glacial Maximum (LGM) based on dinoflagellate cyst assemblages. Quaternary Sci. Rev. 24, 897—924. https://doi.org/10.1016/j.quascirev.2004.06.014

de Vernal, A., Henry, M., Matthiessen, J., Mudie, P.J., Rochon, A., Boessenkool, K.P., Eynaud, F., Grøsfjeld, K., Guiot, J., Hamel, D., Harland, R., Head, M.J., Kunz-Pirrung, M., Levac, E., Loucheur, V., Peyron, O., Pospelova, V., Radi, T., Turon, J.-L., Voronina, E., 2001. Dinoflagellate cyst assemblages as tracers of sea-surface conditions in the northern North Atlantic, Arctic and sub-Arctic seas: the new "n = 677" data base and its application for quantitative palaeoceanographic reconstruction. J. Quaternary Sci. 16, 681—698. https://doi.org/10.1002/jqs.659

de Vernal, A., Marret, F., 2007. Organic-Walled Dinoflagellate Cysts: Tracers of Sea-Surface Conditions. In: Hillaire-Marcel, C., de Vernal, A. (Eds.), Developments in Marine Geology, Elsevier. B.V., 371—408. https://doi.org/10.1016/S1572-5480(07)01014-7

de Vernal, A., Radi, T., Zaragosi, S., Van Nieuwenhove, N., Rochon, A., Allan, E., De Schepper, S., Eynaud, F., Head, M.J., Limoges, A., Londeix, L., Marret, F., Matthiessen, J., Penaud, A., Pospelova, V., Price, A., Richerol, T., 2020. Distribution of common modern dinoflagellate cyst taxa in surface sediments of the Northern Hemisphere in relation to environmental parameters: The new n=1968 database. Mar. Micropaleontol. 159, 101796. https://doi.org/10.1016/j.marmicro.2019.101796

de Vernal, A., Rochon, A., Fréchette, B., Henry, M., Radi, T., Solignac, S., 2013. Reconstructing past sea ice cover of the Northern Hemisphere from dinocyst assemblages: Status of the approach. Quaternary Sci. Rev. 79, 122—134. https://doi.org/10.1016/j.quascirev.2013.06.022

Dowdeswell, J.A., 1989. On the nature of Svalbard icebergs. J. Glaciol. 35, 224—234.

Dowdeswell, J.A., Drewry, D.J., 1985. Place Names on the Nordaustlandet Ice Caps, Svalbard. Polar Rec. (Gr. Brit). 22, 519—523. https://doi.org/10.1017/S0032247400005970

Dowdeswell, J.A., Ottesen, D., Evans, J., Cofaigh, C.Ó., Anderson, J.B., 2008. Submarine glacial landforms and rates of ice-stream collapse. Geology 36, 819—822. https://doi.org/10.1130/G24808A.1

Fensome, R.A., Taylor, F.J.R., Norris, G., Sarjeant, W.A.S., Wharton, D.I., Williams, G.L., 1993. A classification of fossil and living dinoflagellates. Micropaleontol. Spec. Publ. 7, 351.

Fer, I., Skogseth, R., Haugan, P.M., Jaccard, P., 2003. Observations of the Storfjorden overflow. Deep. Res. Part I Oceanogr. Res. Pap. 50, 1283—1303. https://doi.org/10.1016/S0967-0637(03)00124-9

Filipowicz, C., 1990. Textural parameters and classification of deposits in the modern glaciomarine environment, Hornsund Fjord, Spitsbergen. Acta Geol. Pol. 40, 29—67.

Fossile, E., Nardelli, M.P., Howa, H., Baltzer, A., Poprawski, Y., Baneschi, I., Doveri, M., Mojtahid, M., 2022. Influence of modern environmental gradients on foraminiferal faunas in the inner Kongsfjorden (Svalbard). Mar. Micropaleontol. 173, 19. https://doi.org/10.1016/j.marmicro.2022.102117

Fossile, E., Pia Nardelli, M., Jouini, A., Lansard, B., Pusceddu, A., Moccia, D., Michel, E., Péron, O., Howa, H., Mojtahid, M., 2020. Benthic foraminifera as tracers of brine production in the Storfjorden "sea ice factory". Biogeosciences 17, 1933—1953. https://doi.org/10.5194/bg-17-1933-2020

Glud, R.N., Holby, O., Hoffmann, F., Canfield, D.E., 1998. Benthic mineralization and exchange in Arctic sediments (Svalbard, Norway). Mar. Ecol. Prog. Ser. 173, 237—251.

Grøsfjeld, K., Harland, R., Howe, J., 2009. Dinoflagellate cyst assemblages inshore and offshore Svalbard reflecting their modern hydrography and climate. Norw. J. Geol. 89, 121—134.

Haarpaintner, J., Gascard, J.-C., Haugan, P.M., 2001. Ice production and brine formation in Storfjorden, Svalbard. J. Geophys. Res.-Oceans 106, 14001—14013. https://doi.org/10.1029/1999JC000133

Hagen, J.O., Liestøl, O., Roland, E., 1993. Glacier atlas of Svalbard and Jan Mayen. Nor. Polarinsitutt Meddelelser 129, 141.

Hald, M., Dahlgren, T., Olsen, T.-E., Lebesbye, E., 2001. Late Holocene palaeoceanography in Van Mijenfjorden, Svalbard. Polar Res. 20, 23—35. https://doi.org/10.3402/polar.v20i1.6497

Hald, M., Korsun, S., 1997. Distribution of modern benthic foraminifera from fjords of Svalbard, European Arctic. J. Foraminifer. Res. 27, 101—122. https://doi.org/10.2113/gsjfr.27.2.101

Hald, M., Steinsund, P.I., 1992. Distribution of surface sediment benthic Foraminifera in the southwestern Barents Sea. J. Foraminifer. Res. 22, 347—362. https://doi.org/10.2113/gsjfr.22.4.347

Hansen, A., Knudsen, K.L., 1995. Recent foraminiferal distribution in Freemansundet and Early Holocene stratigraphy on Edgeøya, Svalbard. Polar Res. 14, 215—238. https://doi.org/10.1111/j.1751-8369.1995.tb00690.x

Harland, R., 1982. Recent dinoflagellate cyst assemblages from the Southern Barents Sea. Palynology 6, 9—18. https://doi.org/10.1080/01916122.1982.9989231

Hayward, B.W., Coze, F.Le, Vandepitte, L., Vanhoorne, B., 2020. Foraminifera in the World Register of Marine Species (WoRMS) Taxonomic Database. J. Foraminifer. Res. 50, 291—300. https://doi.org/10.2113/gsjfr.50.3.291

Head, M.J., Harland, R., Matthiessen, J., 2001. Cold marine indicators of the late Quaternary: The new dinoflagellate cyst genus Islandinium and related morphotypes. J. Quaternary Sci. 16, 621—636. https://doi.org/10.1002/jqs.657

Hebbeln, D., Wefer, G., 1991. Effects of ice coverage and ice-rafted material on sedimentation in the Fram Strait. Nature 350, 409—411. https://doi.org/10.1038/350409a0

Heikkilä, M., Pospelova, V., Forest, A., Stern, G.A., Fortier, L., Macdonald, R.W., 2016. Dinoflagellate cyst production over an annual cycle in seasonally ice-covered Hudson Bay. Mar. Micropaleontol. 125, 1—24. https://doi.org/10.1016/j.marmicro.2016.02.005

Heikkilä, M., Pospelova, V., Hochheim, K.P., Kuzyk, Z.Z.A., Stern, G.A., Barber, D.G., Macdonald, R.W., 2014. Surface sediment dinoflagellate cysts from the Hudson Bay system and their relation to freshwater and nutrient cycling. Mar. Micropaleontol. 106, 79—109. https://doi.org/10.1016/j.marmicro.2013.12.002

Howe, J.A., Harland, R., Cottier, F.R., Brand, T., Willis, K.J., Berge, J.R., Grøsfjeld, K., Eriksson, A., 2010. Dinoflagellate cysts as proxies for palaeoceanographic conditions in Arctic fjords. In: Howe, J.A., Austin, W.E.N., Forwick, M., Paetzel, M. (Eds.), Fjord Systems and Archives. Geological Society, London, 61—74. https://doi.org/10.1144/SP344.6

Husum, K., Hald, M., 2004. Modern foraminiferal distribution in the subarctic Malangen fjord and adjoining shelf, Northern Norway. J. Foramin. Res. 34, 34—48. https://doi.org/10.2113/0340034

Jacobson, D.M., Anderson, D.M., 1996. Widespread phagocytosis of ciliates and other protists by marine mixotrophic and heterotrophic thecate dinoflagellates. J. Phycol. 32, 279—285. https://doi.org/10.1111/j.0022-3646.1996.00279.x

Javaux, E.J., Scott, D.B., 2003. Illustration of Modern Benthic Foraminifera from Bermuda and Remarks on Distribution in other Subtropical/Tropical Areas. Palaeontologia Electronica 6, 29 pp.

Jennings, A.E., Weiner, N.J., Helgadottir, G., Andrews, J.T., 2004. Modern Foraminiferal Faunas of the Southwestern To Northern Iceland Shelf: Oceanographic and Environmental Controls. J. Foramin. Res. 34, 180—207. https://doi.org/10.2113/34.3.180

Jeong, H.J., 1999. The ecological roles of heterotrophic dinoflagellates in marine planktonic community. J. Eukaryot. Microbiol. 46, 390—396. https://doi.org/10.1111/j.1550-7408.1999.tb04618.x

Jernas, P., Klitgaard-Kristensen, D., Husum, K., Koç, N., Tverberg, V., Loubere, P., Prins, M., Dijkstra, N., Gluchowska, M., 2018. Annual changes in Arctic fjord environment and modern benthic foraminiferal fauna: Evidence from Kongsfjorden, Svalbard. Glob. Planet. Change 163, 119—140. https://doi.org/10.1016/j.gloplacha.2017.11.013

Jima, M., Jayachandran, P.R., Bijoy Nandan, S., Krishnapriya, P.P., Aswathy, N.K., Krishnan, K.P., Harikrishnan, M., Radhakrishnan, C.K., 2021. Stable isotopic signatures of sediment carbon and nitrogen sources and its relation to benthic meiofaunal distribution in the Arctic Kongsfjord. Mar. Ecol. 42, 1–11. https://doi.org/10.1111/maec.12648

Klitgaard-Kristensen, D., Sejrup, H.P., 1996. Modern benthic foraminiferal biofacies across the Northern North Sea. Sarsia 81, 97–106. https://doi.org/10.1080/00364827.1996.10413615

Korsun, S., Hald, M., 2000. Seasonal dynamics of benthic foraminifera in a glacially fed fjord of Svalbard, European arctic. J. Foramin. Res. 30, 251–271. https://doi.org/10.2113/0300251

Korsun, S., Pogodina, I.A., Forman, S.L., Lubinski, D.J., 1995. Recent foraminifera in glaciomarine sediments from three arctic fjords of Novaja Zemlja and Svalbard. Polar Res. 14, 15–32. https://doi.org/10.1111/j.1751-8369.1995.tb00707.x

Kowalewski, W., Rudowski, S., Zalewski, S.M., 1990. Seismoacoustic studies within Wijdefjorden, Spitsbergen. Polish Polar Res. 11, 287–300.

Kucharska, M., Kujawa, A., Pawłowska, J., Łącka, M., Szymańska, N., Lønne, O.J., Zajączkowski, M., 2019. Seasonal changes in foraminiferal assemblages along environmental gradients in Adventfjorden (West Spitsbergen). Polar Biol. 42, 569–580. https://doi.org/10.1007/s00300-018-02453-5

Kujawa, A., Łącka, M., Szymańska, N., Pawłowska, J., Telesiński, M.M., Zajączkowski, M., 2021. Could Norwegian fjords serve as an analogue for the future of the Svalbard fjords? State and fate of high latitude fjords in the face of progressive "atlantification". Polar Biol. 44, 2217–2233. https://doi.org/10.1007/s00300-021-02951-z

Kunz-Pirrung, M., 1998. Rekonstruktion der Oberflächenwassermassen der östlichen Laptevsee im Holozän anhand von aquatischen Palynomorphen. Berichte zur Polarforsch 281, 1–117.

Lepš, J., Šmilauer, P., 2003. Multivariate analysis of ecological data using CanocoTM. Cambridge University Press, Cambridge, UK.

Leu, E., Søreide, J.E., Hessen, D.O., Falk-Petersen, S., Berge, J., 2011. Consequences of changing sea-ice cover for primary and secondary producers in the European Arctic shelf seas: Timing, quantity, and quality. Prog. Oceanogr. 90, 18–32. https://doi.org/10.1016/j.pocean.2011.02.004

Loeblich Jr., A.R., Tappan, H., 1987. Foraminiferal Genera and their Classification. Van Nostrand Reinhold Company, New York.

Loeng, H., Ozhigin, V., Ådlandsvik, B., 1997. Water fluxes through the Barents Sea. ICES J. Mar. Sci. 54, 310–317. https://doi.org/10.1006/jmsc.1996.0165

Łącka, M., Zajączkowski, M., 2016. Does the recent pool of benthic foraminiferal tests in fjordic surface sediments reflect interannual environmental changes? The resolution limit of the foraminiferal record. Ann. Soc. Geol. Pol. 86, 59–71. https://doi.org/10.14241/asgp.2015.019

Mackensen, A., Schmiedl, G., Thiele, J., Damm, E., 2017. Microhabitat preferences of live benthic foraminifera and stable carbon isotopes off SW Svalbard in the presence of widespread methane seepage. Mar. Micropaleontol. 132, 1–17. https://doi.org/10.1016/j.marmicro.2017.04.004

Majewski, W., Szczuciński, W., Zajączkowski, M., 2009. Interactions of Arctic and Atlantic water-masses and associated environmental changes during the last millennium, Hornsund (SW Svalbard). Boreas 38, 529–544. https://doi.org/10.1111/j.1502-3885.2009.00091.x

Majewski, W., Zajączkowski, M., 2007. Benthic foraminifera in Adventfjorden, Svalbard: Last 50 years of local hydrograpic changes. J. Foramin. Res. 37, 107–124. https://doi.org/10.2113/gsjfr.37.2.107

Manley, T.O., 1995. Branching of Atlantic Water within the Greenland-Spitsbergen Passage: An estimate of recirculation. J. Geophys. Res. 100. https://doi.org/10.1029/95JC01251, 20,627-20,634

Marret, F., Bradley, L., de Vernal, A., Hardy, W., Kim, S.Y., Mudie, P.J., Penaud, A., Pospelova, V., Price, A.M., Radi, T., Rochon, A., 2020. From bi-polar to regional distribution of modern dinoflagellate cysts, an overview of their biogeography. Mar. Micropaleontol. 159, 101753. https://doi.org/10.1016/j.marmicro.2019.101753

Maslowski, W., Marble, D., Walczowski, W., Schauer, U., Clement, J.L., Semtner, A.J., 2004. On climatological mass, heat, and salt transports through the Barents Sea and Fram Strait from a pan-Arctic coupled ice-ocean model simulation. J. Geophys. Res. 109, C03032. https://doi.org/10.1029/2001jc001039

Matthiessen, J., de Vernal, A., Head, M.J., Okolodkov, Y., Zonneveld, K.A.F., Harland, R., 2005. Modem organic-walled dinoflagellate cysts in Arctic marine environments and their (paleo-) environmental significance. Paläontologische Zeitschrift 79, 3–51. https://doi.org/10.1007/bf03021752

Mertens, K.N., Price, A.M., Pospelova, V., 2012a. Determining the absolute abundance of dinoflagellate cysts in recent marine sediments II: Further tests of the *Lycopodium* marker-grain method. Rev. Palaeobot. Palyno. 184, 74–81. https://doi.org/10.1016/j.revpalbo.2012.06.012

Mertens, K.N., Rengefors, K., Moestrup, Ø., Ellegaard, M., 2012b. A review of recent freshwater dinoflagellate cysts: Taxonomy, phylogeny, ecology and palaeocology. Phycologia 51, 612–619. https://doi.org/10.2216/11-89.1

Mertens, K.N., Takano, Y., Gu, H., Yamaguchi, A., Pospelova, V., Ellegaard, M., Matsuoka, K., 2015. Cyst-theca relationship of a new dinoflagellate with a spiny round brown cyst, *Protoperidinium lewisiae* sp. nov., and its comparison to the cyst of *Oblea acanthocysta*. Phycol. Res. 63, 110–124. https://doi.org/10.1111/pre.12083

Mertens, K.N., Verhoeven, K., Verleye, T., Louwye, S., Amorim, A., Ribeiro, S., Deaf, A.S., Harding, I.C., De Schepper, S., González, C., Kodrans-Nsiah, M., De Vernal, A., Henry, M., Radi, T., Dybkjaer, K., Poulsen, N.E., Feist-Burkhardt, S., Chitolie, J., Heilmann-Clausen, C., Londeix, L., Turon, J.L., Marret, F., Matthiessen, J., McCarthy, F.M.G., Prasad, V., Pospelova, V., Kyffin Hughes, J.E., Riding, J.B., Rochon, A., Sangiorgi, F., Welters, N., Sinclair, N., Thun, C., Soliman, A., Van Nieuwenhove, N., Vink, A., Young, M., 2009. Determining the absolute abundance of dinoflagellate cysts in recent marine sediments: The *Lycopodium* marker-grain method put to the test. Rev. Palaeobot. Palyno. 157, 238–252. https://doi.org/10.1016/j.revpalbo.2009.05.004

Mertens, K.N., Yamaguchi, A., Takano, Y., Pospelova, V., Head, M.J., Radi, T., Pieńkowski, A.J., De Vernal, A., Kawami, H., Matsuoka, K., 2013. A new heterotrophic dinoflagellate from the north-eastern pacific, *Protoperidinium fukuyoi*: Cyst-theca relationship, phylogeny, distribution and ecology. J. Eukaryot. Microbiol. 60, 545–563. https://doi.org/10.1111/jeu.12058

Moestrup, Ø., Lindberg, K., Daugbjerg, N., 2009. Studies on woloszynskioid dinoflagellates IV: The genus *Biecheleria* gen. nov. Phycol. Res. 57, 203–220. https://doi.org/10.1111/j.1440-1835.2009.00540.x

Montresor, M., Lovejoy, C., Orsini, L., Procaccini, G., Roy, S., 2003. Bipolar distribution of the cyst-forming dinoflagellate *Polarella glacialis*. Polar Biol. 26, 186–194. https://doi.org/10.1007/s00300-002-0473-9

Montresor, M., Procaccini, G., Stoecker, D.K., 1999. *Polarella glacialis*, gen. nov., sp. nov. (Dinophyceae): Suessiaceae are still alive!. J. Phycol. 35, 186–197.

Mudie, P.J., Rochon, A., 2001. Distribution of dinoflagellate cysts in the Canadian Arctic marine region. J. Quaternary Sci. 16, 603–620. https://doi.org/10.1002/jqs.658

Murray, J.W., 1991. Ecology and Palaeoecology of Benthic Foraminifera. Longman Scientific and Technical.

Murray, J.W., Alve, E., 2016. Benthic foraminiferal biogeography in NW European fjords: A baseline for assessing future change. Estuar. Coast. Shelf Sci. 181, 218—230. https://doi.org/10.1016/j.ecss.2016.08.014

Müller, J., Wagner, A., Fahl, K., Stein, R., Prange, M., Lohmann, G., 2011. Towards quantitative sea ice reconstructions in the northern North Atlantic: A combined biomarker and numerical modelling approach. Earth Planet. Sci. Lett. 306, 137—148. https://doi.org/10.1016/j.epsl.2011.04.011

Nardelli, M.P., Fossile, E., Péron, O., Howa, H., Mojtahid, M., 2023. Early taphonomy of benthic foraminifera in Storfjorden 'sea-ice factory': the agglutinated/calcareous ratio as a proxy for brine persistence. Boreas 52, 109—123. https://doi.org/10.1111/bor.12592

Nilsen, F., Cottier, F.R., Skogseth, R., Mattsson, S., 2008. Fjord-shelf exchanges controlled by ice and brine production: The interannual variation of Atlantic Water in Isfjorden, Svalbard. Cont. Shelf Res. 28, 1838—1853. https://doi.org/10.1016/j.csr.2008.04.015

Nilsen, F., Skogseth, R., Vaardal-Lunde, J., Inall, M., 2016. A Simple Shelf Circulation Model: Intrusion of Atlantic Water on the West Spitsbergen Shelf. J. Phys. Oceanogr. 46, 1209—1230. https://doi.org/10.1175/JPO-D-15-0058.1

Nürnberg, D., Wollenburg, I., Dethleff, D., Eicken, H., Kassens, H., Letzig, T., Reimnitz, E., Thiede, J., 1994. Sediments in Arctic sea ice: Implications for entrainment, transport and release. Mar. Geol. 119, 185—214. https://doi.org/10.1016/0025-3227(94)90181-3

Obrezkova, M.S., Pospelova, V., Kolesnik, A.N., 2023. Diatom and dinoflagellate cyst distribution in surface sediments of the Chukchi Sea in relation to the upper water masses. Mar. Micropaleontol. 178, 102184. https://doi.org/10.1016/j.marmicro.2022.102184

Pawłowska, J., Łącka, M., Kucharska, M., Szymańska, N., Koziorowska, K., Kuliński, K., Zajączkowski, M., 2017. Benthic foraminifera contribution to fjord modern carbon pools: A seasonal study in Adventfjorden. Spitsbergen. Geobiology 15, 704—714. https://doi.org/10.1111/gbi.12242

Pfirman, S.L., Bauch, D., Gammelsrød, T., 1994. The Northern Barents Sea: Water Mass Distribution and Modification. In: Johannessen, O.M., Muench, R.D., Overland, J.E. (Eds.), The Polar Oceans and Their Role in Shaping the Global Environment, Vol. 85. American Geophysical Union, 77—94.

Polyak, L., Mikhailov, V., 1996. Post-glacial environments of the southeastern Barents Sea: foraminiferal evidence. Geol. Soc. London, Sp. Publ., Vol. 111, 323—337.

Pospelova, V., Chmura, G.L., Boothman, W.S., Latimer, J.S., 2005. Spatial distribution of modern dinoflagellate cysts in polluted estuarine sediments from Buzzards Bay (Massachusetts, USA) embayments. Mar. Ecol. Prog. Ser. 292, 23—40. https://doi.org/10.3354/meps292023

Pospelova, V., Esenkulova, S., Johannessen, S.C., O'Brien, M.C., Macdonald, R.W., 2010. Organic-walled dinoflagellate cyst production, composition and flux from 1996 to 1998 in the central Strait of Georgia (BC, Canada): A sediment trap study. Mar. Micropaleontol. 75, 17—37. https://doi.org/10.1016/j.marmicro.2010.02.003

Pospelova, V., Head, M.J., 2002. *Islandinium brevispinosum* sp. nov. (Dinoflagellata), a new organic-walled dinoflagellate cyst from modern estuarine sediments of New England (USA). J. Phycol. 38, 593—601. https://doi.org/10.1046/j.1529-8817.2002.01206.x

Ramseier, R.O., Garrity, C., Bauerfeind, E., Peinert, R., 1999. Sea-ice impact on long-term particle flux in the Greenland Sea's Is Odden-Nordbukta region, 1985—1996. J. Geophys. Res. 104, 5329—5343. https://doi.org/10.1029/1998jc900048

Rasmussen, T.L., Forwick, M., Mackensen, A., 2012. Reconstruction of inflow of Atlantic Water to Isfjorden, Svalbard during the Holocene: Correlation to climate and seasonality. Mar. Micropaleontol. 94—95, 80—90. https://doi.org/10.1016/j.marmicro.2013.03.011

Rochon, A., de Vernal, A., Turon, J.-L., Matthiessen, J., Head, M.J., 1999. Distribution of recent dinoflagellate cysts in surface sediments from the North Atlantic Ocean and adjacent seas in relation to sea-surface parameters. Am. Assoc. Stratigr. Palynol. Contrib. Ser. 35, 1—146.

Romano, E., Bergamin, L., Parise, M., 2022. Benthic Foraminifera as Environmental Indicators in Mediterranean Marine Caves: A Review. Geosciences 12, 42. https://doi.org/10.3390/geosciences12010042

Rudels, B., Friedrich, H.J., 2000. The Transformations of Atlantic Water in the Arctic Ocean and Their Significance for the Freshwater Budget. In: Lewis, E.L., Jones, E.P., Lemke, P., Prowse, T.D., Wadhams, P. (Eds.), The Freshwater Budget of the Arctic Ocean. Springer, Dordrecht, 503—532. https://doi.org/10.1007/978-94-011-4132-1_21

Rudels, B., Jones, E.P., Anderson, L.G., Kattner, G., 1994. On the Intermediate Depth Waters of the Arctic Ocean. In: Johannessen, O.M., Muench, R.D., Overland, J.E. (Eds.), The Polar Oceans and Their Role in Shaping the Global Environment, Vol. 85. American Geophysical Union, 33—46. https://doi.org/10.1029/gm085p0033

Sakshaug, E., 2004. Primary and Secondary Production in the Arctic Seas. In: Stein, R., Macdonald, R.W. (Eds.), The Organic Carbon Cycle in the Arctic Ocean. Springer, Berlin, Heidelberg, 57—81. https://doi.org/10.1007/978-3-642-18912-8_3

Saloranta, T.M., Svendsen, H., 2001. Across the Arctic front west of Spitsbergen: high-resolution CTD sections from 1998—2000. Polar Res. 20, 177—184. https://doi.org/10.1111/j.1751-8369.2001.tb00054.x

Schiermeier, Q., 2007. Polar research: The new face of the Arctic. Nature 446, 133—135. https://doi.org/10.1038/446133a

Scott, D.B., Schell, T., Rochon, A., Blasco, S., 2008. Benthic foraminifera in the surface sediments of the Beaufort Shelf and slope, Beaufort Sea, Canada: Applications and implications for past sea-ice conditions. J. Marine Syst. 74, 840—863. https://doi.org/10.1016/j.jmarsys.2008.01.008

Seidenkrantz, M.-S., 2013. Benthic foraminifera as palaeo sea-ice indicators in the subarctic realm — examples from the Labrador Sea-Baffin Bay region. Quaternary Sci. Rev. 79, 135—144. https://doi.org/10.1016/j.quascirev.2013.03.014

Serreze, M.C., Barry, R.G., 2011. Processes and impacts of Arctic amplification: A research synthesis. Global Planet. Change 77, 85—96. https://doi.org/10.1016/j.gloplacha.2011.03.004

Serreze, M.C., Francis, J.A., 2006. The Arctic amplification debate. Clim. Change 76, 241—264. https://doi.org/10.1007/s10584-005-9017-y

Skogseth, R., Haugan, P.M., Haarpaintner, J., 2004. Ice and brine production in Storfjorden from four winters of satellite and in situ observations and modeling. J. Geophys. Res.-Oceans 109, 1—15. https://doi.org/10.1029/2004JC002384

Skogseth, R., Haugan, P.M., Jakobsson, M., 2005. Watermass transformations in Storfjorden. Cont. Shelf Res. 25, 667—695. https://doi.org/10.1016/j.csr.2004.10.005

Ślubowska, M.A., Koç, N., Rasmussen, T.L., Klitgaard-Kristensen, D., 2005. Changes in the flow of Atlantic water into the Arctic Ocean since the last deglaciation: Evidence from the northern Svalbard continental margin, 80°N. Paleoceanography 20, 1—16. https://doi.org/10.1029/2005PA001141

Smith Jr., W.O., Baumann, M.E.M., Wilson, D.L., Aletsee, L., 1987. Phytoplankton Biomass and Productivity in the Marginal Ice Zone of the Fram Strait During Summer 1984. J. Geophys. Res. 92, 6777—6786. https://doi.org/10.1029/JC092iC07p06777

Søreide, J.E., Leu, E.V.A., Berge, J., Graeve, M., Falk-Petersen, S., 2010. Timing of blooms, algal food quality and Calanus glacialis reproduction and growth in a changing Arctic. Glob. Change Biol. 16, 3154—3163. https://doi.org/10.1111/j.1365-2486.2010.02175.x

Stoecker, D.K., 1999. Mixotrophy among dinoflagellates. J. Eukaryot. Microbiol. 46, 397—401. https://doi.org/10.1111/j.1550-7408.1999.tb04619.x

Svendsen, H., Beszczyńska-Möller, A., Hagen, J.O., Lefauconnier, B., Tverberg, V., Gerland, S., Ørbøk, J.B., Bischof, K., Papucci, C., Zajączkowski, M., Azzolini, R., Bruland, O., Wiencke, C., Winther, J.G., Dallmann, W., 2002. The physical environment of Kongsfjorden-Krossfjorden, and Arctic fjord system in Svalbard. Polar Res. 21, 133—166. https://doi.org/10.1111/j.1751-8369.2002.tb00072.x

Syvitski, J.P.M., Shaw, J., 1995. Sedimentology and Geomorphology of Fjords. In: Perillo, G.M.E. (Ed.), Geomorphology and Sedimentology of Estuaries. Developments in Sedimentology. Elsevier Science B.V., 113—178. https://doi.org/10.1016/S0070-4571(05)80025-1

Szymańska, N., Łącka, M., Koziorowska-Makuch, K., Kuliński, K., Pawłowska, J., Kujawa, A., Telesiński, M.M., Zajączkowski, M., 2021. Foraminifera-derived carbon contribution to sedimentary inorganic carbon pool: A case study from three Norwegian fjords. Geobiology 19, 631—641. https://doi.org/10.1111/gbi.12460

Taylor, F.J.R., 1987. The Biology of Dinoflagellates. Blackwell Scientific, Oxford.

Taylor, F.J.R., Hoppenrath, M., Saldarriaga, J.F., 2008. Dinoflagellate diversity and distribution. Biodiversity Conservation 17, 407—418. https://doi.org/10.1007/s10531-007-9258-3

ter Braak, C.J.F., Šmilauer, P., 2002. CANOCO Reference Manual and CanoDraw for Windows user's Guide. Software for Canonical Community Ordination.

Wall, D., Dale, B., 1966. Living Fossils" in Western Atlantic Plankton. Nature 211, 1025—1026. https://doi.org/10.1038/2111025a0

Wallace, M.I., Cottier, F.R., Berge, J., Tarling, G.A., Griffiths, C., Brierley, A.S., 2010. Comparison of zooplankton vertical migration in an ice-free and a seasonally ice-covered Arctic fjord: An insight into the influence of sea ice cover on zooplankton behavior. Limnol. Oceanogr. 55, 831—845. https://doi.org/10.4319/lo.2009.55.2.0831

Węsławski, J.M., Jankowski, A., Kwasniewski, S., Swerpel, S., Ryg, M., 1991. Summer hydrology and zooplankton in two Svalbard fiords. Polish Polar Res. 12, 445—460.

Włodarska-Kowalczuk, M., Pawłowska, J., Zajączkowski, M., 2013. Do foraminifera mirror diversity and distribution patterns of macrobenthic fauna in an Arctic glacial fjord? Mar. Micropaleontol. 103, 30—39. https://doi.org/10.1016/j.marmicro.2013.07.002

WMO, 2014. Sea Ice Nomenclature.

Yamashita, C., Omachi, C., Santarosa, A.C.A., Iwai, F.S., Araujo, B.D., Disaró, S.T., Alves Martins, M.V., Vicente, T.M., Taniguchi, N., Burone, L., Mahiques, M.M., Bícego, M.C., Figueira, R.C.L., Sousa, S.H.M., 2020. Living benthic foraminifera of Santos continental shelf, southeastern Brazilian continental margin (SW Atlantic): chlorophyll-a and particulate organic matter approach. J. Sediment. Environ. 5, 17—34. https://doi.org/10.1007/s43217-019-00001-7

Zajączkowski, M., Szczuciński, W., Plessen, B., Jernas, P.E., 2010. Benthic foraminifera in Hornsund, Svalbard: Implications for paleoenvironmental reconstructions. Polish Polar Res. 31, 349—375. https://doi.org/10.2478/v10183

Zajączkowski, M., Włodarska-Kowalczuk, M., 2007. Dynamic sedimentary environments of an Arctic glacier-fed river estuary (Adventfjorden, Svalbard). I. Flux, deposition, and sediment dynamics. Estuar. Coast. Shelf Sci. 74, 285—296. https://doi.org/10.1016/j.ecss.2007.04.015

Zgrundo, A., Wojtasik, B., Convey, P., Majewska, R., 2017. Diatom communities in the High Arctic aquatic habitats of northern Spitsbergen (Svalbard). Polar Biol. 40, 873—890. https://doi.org/10.1007/s00300-016-2014-y

Zonneveld, K.A.F., 1997. New species of organic walled dinoflagellate cysts from modern sediments of the Arabian Sea (Indian Ocean). Rev. Palaeobot. Palyno. 97, 319—337. https://doi.org/10.1016/S0034-6667(97)00002-X

Zonneveld, K.A.F., Marret, F., Versteegh, G.J.M., Bogus, K., Bonnet, S., Bouimetarhan, I., Crouch, E., de Vernal, A., Elshanawany, R., Edwards, L., Esper, O., Forke, S., Grøsfjeld, K., Henry, M., Holzwarth, U., Kielt, J.F., Kim, S.Y., Ladouceur, S., Ledu, D., Chen, L., Limoges, A., Londeix, L., Lu, S.H., Mahmoud, M.S., Marino, G., Matsuoka, K., Matthiessen, J., Mildenhal, D.C., Mudie, P.J., Neil, H.L., Pospelova, V., Qi, Y., Radi, T., Richerol, T., Rochon, A., Sangiorgi, F., Solignac, S., Turon, J.L., Verleye, T., Wang, Y., Wang, Z., Young, M., 2013. Atlas of modern dinoflagellate cyst distribution based on 2405 data points. Rev. Palaeobot. Palyno. 191, 1—197. https://doi.org/10.1016/j.revpalbo.2012.08.003

Zonneveld, K.A.F., Pospelova, V., 2015. A determination key for modern dinoflagellate cysts. Palynology 39, 387—409. https://doi.org/10.1080/01916122.2014.990115

Oceanologia 65 (2023) 595—611

Available online at www.sciencedirect.com

ScienceDirect

journal homepage: www.journals.elsevier.com/oceanologia

ORIGINAL RESEARCH ARTICLE

Assessment of human interventions presence and their impact on shoreline changes along Nile delta, Egypt

May R. ElKotby[a,*], Tharwat A. Sarhan[b], Mahmoud El-Gamal[c]

[a] *Irrigation and Hydraulics Engineering Department, Mansoura University, Mansoura, Egypt*
[b] *Harbor and Coastal Engineering, Mansoura University, Mansoura, Egypt*
[c] *Water structure, Mansoura University, Mansoura, Egypt*

Received 25 December 2022; accepted 14 June 2023
Available online 8 July 2023

KEYWORDS
Shoreline changes;
Nile Delta;
Landsat image;
DSAS software;
LRR model

Abstract Coastal erosion is a natural process, that contributed to shaping the Nile Delta shoreline in Egypt over history. The objective of this research is to investigate shoreline changes, accretion, and erosion and to detect particularly vulnerable locations that require immediate attention. Another goal is to assess the efficiency of coastal installations that have been recently implemented along the study area and determine whether they have performed their role to the fullest or need additional modifications. Several Landsat images (TM, ETM+, and OLI) were utilized over 37 years to track the shoreline changes and were analysed using remote sensing (RS) and Geographic Information System (GIS). The digital shoreline analysis system (DSAS) was integrated with the LRR model for assessing historical changes for shorelines from 1985 to 2022 and forecasting future shoreline positions in 2030, 2050, and 2100. Most of the eight zones that make up the Delta region have lately seen the establishment of coastal projects, such as the development of the Abu Qir port's breakwater in 2021. From the results, it was found that the areas around Rosetta promontory, Burullus headland, and Damietta promontory experienced a significant and rapid retreat and with large rates over the study period, with average values of −15.7, −3.25, and −16.8 m/y, respectively. However, both the

---

* Corresponding author at: Mansoura University, Mansoura, Egypt.
E-mail addresses: may_ramdan@mans.edu.eg (M.R. ElKotby), prof_tharwat@mans.edu.eg (T.A. Sarhan), Mmelgamel@hotmail.com (M. El-Gamal).

Peer review under the responsibility of the Institute of Oceanology of the Polish Academy of Sciences.

ELSEVIER Production and hosting by Elsevier

https://doi.org/10.1016/j.oceano.2023.06.008

coast of Alexandria, and Gamasa embayment were subjected to accretion as a prevailing case, with average rates of 2.85, and 4.03 m/y, respectively. Many groins were installed in the east of the Rosetta promontory (zone 3) in 2016 to decrease the erosion process; however, it didn't pay off and could not solve the problem. In contrast, the groins system, which was implemented at the East Kitchener Drain (zone 5) in the same year, lowered erosion rates from 17.6 m/y from 2000 to 2010 to 7 m/y from 2010 to 2022. In 2019, Y-groins built in zone 7, east of Damietta Port, succeeded in slowing rates of erosion. Finally, inlet jetties at El-Gamil (zone 8) were constructed in 2016, resulting in the coastline advancing at 14.7 m/y on average in the period of 2010—2022. The findings of this study confirmed that hard structures are dangerous because they exacerbate the problem of shoreline erosion by disseminating it to the neighbouring beaches and acting as an impediment to the movement of longshore sediments. According to the expected future shoreline patterns, it is necessary for authorities to implement both short-term and long-term protective measures to stop the erosion of several areas of the beach.

1. Introduction

Natural processes and human interventions as well as coastal development itself, have all contributed to continuous changes in coastal zones (Niya et al., 2013; Thieler and Hammar-Klose, 1999). The Nile Delta, like other deltas around the world, is susceptible to rapid changes in its shorelines, including erosion problems (Rosette, Burullus, Damietta headland, Ras El-bar), siltation problems in estuaries and lake outlets, pollution problems, salt water intrusion, subsidence of land, and rising sea levels SLR due to global climate change, all of which are brought worse by human interventions, such as the interruption in sediment supply since the completion of the Aswan High Dam, (Elshinnawy and Almaliki, 2021; Masria et al., 2014). In the years prior to the building of the Aswan high dam, the Rosetta and Damietta promontories, and even the beaches of the intervening embayment, all received the 100—115 million m^3/y of sediments that were released into the Mediterranean (El-Asmar et al., 2014). These sands provided ongoing replenishing to the coast in the face of long-shore currents, resulting in net coastal progression. However, the Mediterranean no longer received most of the sediment discharge as a result of the building of the Aswan High Dam in 1964 (El-Asmar et al., 2014). The Nile Delta coastline, which stretches from Alexandria City in the west to Port Said in the east, is lined with numerous coastal structures including groins, jetties at inlets, detached breakwaters, and seawalls. These primarily intended to slow down the erosion process in the delta zone, but because they completely or partially blocked sand passage, they caused up-drift accretion and severely eroded down-drift sides (El Sayed and Khalifa, 2017). According to El-Asmar et al. (2014) sand dunes that existed in Abo-Qir Bay and Burullus headland, are considered the first natural barrier against erosion processes. The pace of erosion in the coastal region would worsen due to the anticipated changes in climate and sea level rise. According to the Intergovernmental Panel on Climate Change (IPCC) estimations, which predict a 59 cm increase in sea level and 2.5 mm/y land subsidence by 2100, twenty percent of the Nile Delta region will be severely susceptible to floods (Ali and El-Magd, 2016). El-Hattab (2015) reported after a vulnerability assessment that about 29.64% of the Nile Delta shoreline is having a very high vulnerability.

Geographic information systems (GIS) and remote sensing (RS) have recently proven to be quite helpful in grasping the entire processes associated with coastal erosion, accretion, and consequences of protection structures, and based on that, necessary mitigation measures are proposed (El-Masry, 2022). Several authors have estimated shoreline alterations trend along the Nile Delta coast (Balbaa et al., 2020; Dewidar and Frihy, 2010; Elsayed et al., 2005; Elshinnawy and Almaliki, 2021; Frihy et al., 1988; Frihy and Lawrence, 2004; Ghoneim et al., 2015; Sanhory et al., 2022; Torab and Azab, 2007). Deabes (2017) applied ArcGIS model builder to estimate shoreline change rates, particularly after building coastal structures along the Nile Delta coast. His results deduced that the erosion patterns between 1970—2010 were centralized around delta promontories Rosetta, Damietta, and along Burullus headland with average rates of −60 m/y, −6 m/y, and −6 m/y respectively. The Digital Shoreline Analysis System (DSAS), a statistics tool, has demonstrated its efficiency in studying coastal changes through many studies on the Nile Delta coast, in addition to many locations around the world. Niya et al. (2013) calculated the shoreline changes from 1990 to 2005 on Iran's coast. Kaliraj et al. (2015) estimated accretion and erosion rates along the coast of Kanyakumari, South India. Basheer Ahammed and Pandey (2019) monitored shoreline changes along the Eastern Coast of India between 1973 to 2015. Gümüs et al. (2021) investigated coastline change rates in Lake Beyşehir, Turkey from 1984 to 2018. Quang et al. (2021) analyzed shoreline morphology along the Quang Nam coastline, Vietnam.

Using remote sensing and the DSAS program, the current study sought to evaluate the shoreline's regressive displacement along the coastal region of the Nile Delta over 37 years to compare and verify the efficacy and protection role of various types of existing countermeasures.

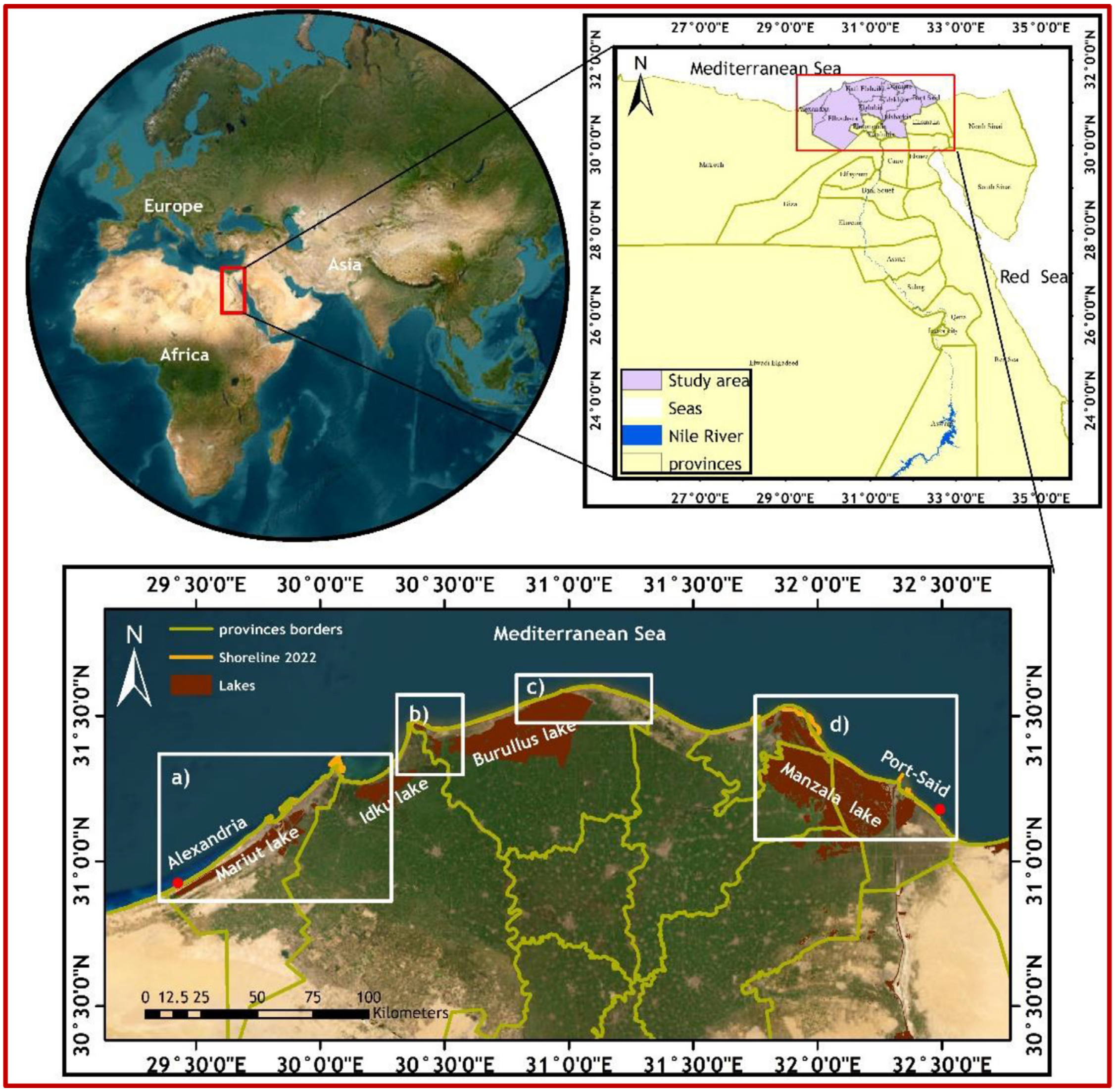

Figure 1 Location of the research area, a) Alexandria and Abo-Qir coast, b) Rosetta promontory, c) Burullus headland, d) Damietta promontory and Port Said coast.

2. Study area

The Nile Delta shoreline is situated in the south-eastern Mediterranean, north of Egypt, and stretches from Alexandria city in the west at 29°23′32.17″E and 30° 53′23.68″N to Port Said in the east at 32°34′7.86″E and 31°4′27.55″N (Figure 1). It composes of beaches, coastal dunes, deserts, and Lakes (Dewidar and Bayoumi, 2021). The Nile Delta coast is recognised for its four major coastal Lakes. These lakes are Mariut and Idku Lake in the west, Burullus Lake in the middle, and Al-Manzalah Lake in the east, which represent approximately 25% of the wetland area covered by extensive fishing farms (Iskander, 2013). Since the Aswan High Dam's construction in 1964, the Nile Delta has seen a significant deficit in the quantity of accumulated sand, and therefore, substantial erosion rates have been monitored (Masria et al., 2014). There are several coastal structures, including (jetties, breakwaters, groins, and seawalls) erected in an attempt to slow the erosion processes in the study region. According to Frihy et al. (1988), the most prevalent wind direction during the year is from the NNW or NW. It is typically dominated by waves and currents, where tides are almost tideless and semidiurnal, with a tidal range of between 25 and 30 cm. The prevailing current direction in most Burullus and Damietta region records is from west to east, except in the spring season when the current changes its direction due to wave direction and bottom terrain (Frihy et al., 1996). Iskander (2013) analysed wave records at Abu-Qir Bay station from 1985 to 1990 and discovered that the significant wave height, or Hs, was 1.91 m with an average peak wave period of 6.0 sec coming from the northwest. While between 1997 and 2010, waves in front of Damietta harbour had Hs of 1.02 m with an average peak wave period of 6.3 sec. Because of its low elevation, the Nile Delta is particularly vulnerable to sea level rising (SLR) and climate change. Digital elevation models (DEMs) have been analysed (Hereher, 2010) and the results showed that 18.1% of the delta is below mean sea level, 12.7% has an elevation between 0 and 1 m, and 13.1% has an elevation between 1 and 2 m above sea level. Around 30 million people reside in this region, making it extremely populated (Abou Samra and Ali, 2021).

Table 1 Specifics about the satellite images used in this study.

Satellite data	Acquisition date	Spatial resolution (m)
Landsat5 TM	03/06/1985	30
	10/06/1985	
	29/03/1985	
Landsat5 TM	01/07/1995	30
	22/06/1995	
	21/07/1995	
Landsat5 TM	14/07/2000	30
	22/08/2000	
	29/08/2000	
Landsat7 ETM	18/06/2005	30
	03/05/2005	
	13/04/2005	
Landsat7 ETM	31/05/2010	30
	06/05/2010	
	27/04/2010	
Landsat8 OLI	08/06/2016	30
	18/05/2016	
	24/07/2016	
Landsat8 OLI	27/07/2022	30
	17/07/2022	
	04/04/2022	

3. Methodology

3.1. Data collection and shoreline extraction

The Nile Delta's shoreline positions were analysed from satellite images captured over 37 years. In the current research, a set of digital images (Landsat TM, ETM+, and OLI) was collected at a spatial resolution of 30 m acquired via the USGS Global Visualization website (https://earthexplorer.usgs.gov/) between 1985 and 2022 intervals (Table 1). These data were projected to the Universal Transverse Mercator UTM, World Geodetic System WGS 84, zone 36. Also, they were radiometrically calibrated which combines sensor calibration, as well as atmospheric correction. To cover the total study area in a single scene image, various Landsat images for all selected dates have been mosaicked by using ENVI v.5.3 software. The Normalized Difference Water Index (NDWI) technique was employed to extract shorelines and exported as a shapefile to ArcGIS v.10.7 software then converted from feature to polyline. The jagged edges (blocky shape) of all shorelines of the selected dates were smoothed (Figure 2) and merged as a single polyline in one length.

3.2. Shoreline changes

To analyse shoreline changes the Digital Shoreline Analysis System (DSAS), an extension of ArcGIS, was applied. Based on previous studies, such as (Abd-Elhamid et al., 2023), DSAS is known as an efficient and precise measuring tool for identifying changes in the coastline. For each set of shorelines, a coastal length of about 324 km was covered by 4050 transects with an 80-m spacing. DSAS computed shoreline changes at each transect by using four different methods. To calculate the overall distance of the shoreline displacement throughout the whole study period, the Net Shoreline Movement (NSM) model is applied. The Shoreline Change Envelope (SCE) model calculates the distance between the closest and farthest shorelines to the baseline. End Point Pates EPR and Linear Regression Rates LRR estimate rates of shoreline change. The spatial changes in the study region's coastline were measured by using the LRR model for the three intermediate periods (1985–2000, 2000– 2010, 2010–2022), and for the overall long-term period from 1985 to 2022. Figure 3 summarizes the total method of work followed in this research.

Table 2 Ranking of erosion and accretion rates LRR.

Rank	LRR rates (m/y)	Classification
1	> 2.0	very high accretion
2	1.0–2.0	high accretion
3	1.0– −1.0	moderate erosion
4	−1.0– −2.0	high erosion
5	< -2.0	very high erosion

3.3. Shoreline prediction by using LRR

To validate the LRR model in the prediction process, the predicted shoreline 2022 was generated using Eq. (1), but with LRR calculated for historic changes between 1985 and 2016. Normalized root-mean-square error, or NRMSE, was determined by using the values of the positional variation between the predicted coastline for 2022 and the digitalized shoreline from the 2022 satellite image at each transect. Next, by determining the error distance (NSM), the LRR model was used to predict future shorelines in 2030, 2050, and 2100:

$$P_F = LRR * (T_F - T_R) + P_R \tag{1}$$

where P_F – future shoreline position, T_F – future date, T_R – recent date, P_R – recent shoreline position.

4. Results and discussion

The Nile Delta shoreline was divided into eight zones, all of which have relatively similar geomorphological changes patterns: (1) Al Hammam city to Abo-Qir port as explained in Figure 4, (2) Abu-Qir embayment, (3) Rosetta Promontory, (4) Abo-khashba embayment, (5) Burullus Headland, (6) Gamasa embayment, (7) Damietta Promontory, (8) Port Said coast. In this study, LRR was selected to represent shoreline changes in four periods: 1985–2000, 2000–2010, 2010–2022, and 1985–2022. As shown in Table 2, Thieler and Hammar-Klose (1999) divided accretion and erosion rates LRR into five categories: very high, high accretion, and moderate, high, very high erosion, with > 2.0 m/y, 1.0–2.0 m/y,

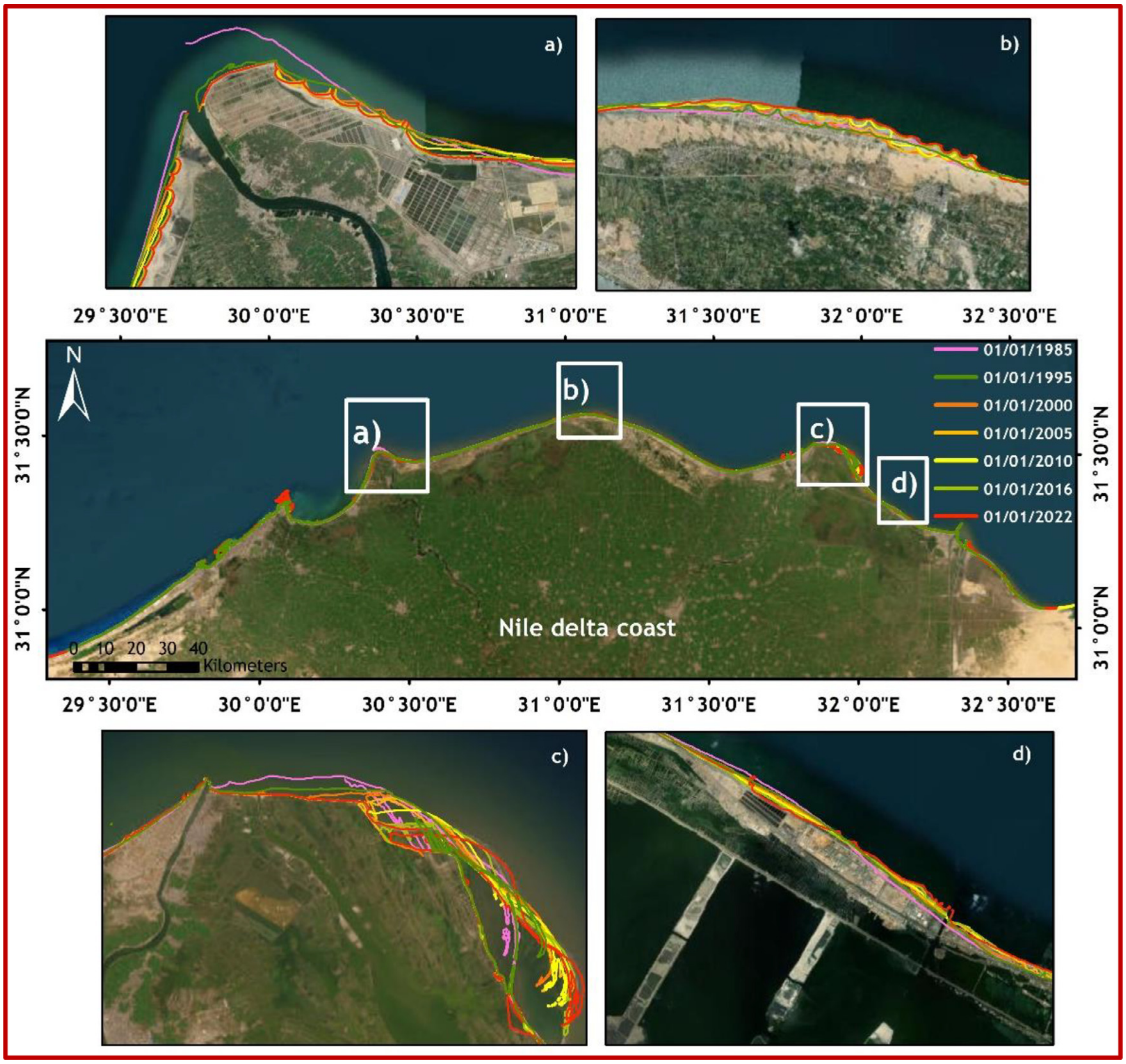

Figure 2 Shorelines extraction from 1985 to 2022, a) Rosetta promontory, b) Burullus headland, c) Damietta promontory, d) El-Gamil inlets.

1.0— —1.0 m/y, —1.0— —2.0 m/y, and <—2.0 m/y change rate, respectively. The findings indicated that the erosion beaches existed along the Nile promontories, and an accretion pattern was present inside the embayment between the promontories. The coastal changes for all zones are presented in Figures 5—6. Also, Figure 7 summarizes all structures implemented along the Nile Delta coast. The average rates of accretion and erosion along the research region are listed in Table 3 for each zone.

4.1. Analysis of shoreline changes for different zones

Zone 1 covers approximately 25% of the coastline. It is the most western section extending from ELhammam city to Abo Qir port, constituting 1000 transects that span 80 kilometres of coastline. The results depicted that LRR had a positive value for all examined periods except the period of 2000—2010 which had dominated erosion for around 842 transects with an average value of —1.5 m/y and a maximum value of —10.47 m/y. Erosion occurred along one 1 over the 1985—2000 and 2010—2022 periods albeit on a small number of transects (287 and 221, respectively). The average accretion rates of three periods (1985—2000, 2000—2010, and 2010—2022) ranged from 1.23 m/year occurred in the 1985—2000 period to 3.73 m/year in the 2010—2022 period. This zone suffered from moderate to high erosion rates, with average values ranging from —0.62 m/y happened in the 1985—2000 period to —1.5 m/y in the 2000—2010 period. In 2010—2022, the mean erosion rate was —1.03 m/y. This region was shown to be likewise characterised as a very high accretion zone during the Long-term period of the research, with an average NSM value of 105.45 m and an LRR rate of 2.85 m/y.

The protection structures executed in this zone contributed dramatically to controlling erosion processes. Some of the structures identified in this region: breakwaters for four ports (El-Dekhila, Abo Qir, Alexandria, Sidi-Kerair port) to provide safe shipping maneuvering, Nobaria Drain jetties to prevent siltation inside inlet, Al agami-emerged detached breakwaters to dissipate wave energy and helping in advance shoreline, submerged break-

Figure 3 Flowchart of the overall technique conducted in this research.

water installed in 2006–2008 to the eroded beach along El-Mandara area, groins constructed at El-Chatby, El-Asafra, El-Mandara (El-Masry, 2022; Frihy et al., 2010; Frihy and El-Sayed, 2013). Nourishment activities are also accomplished periodically by adding desert sand to compensate for sand losses at some affected beaches (Darwish et al., 2017). Figure 8a shows the changes that occurred in the breakwater of Abu Qir port in the year 2021, which will certainly have an impact on the morphology of the shoreline. The results were also comparable to those calculated by Abd-Elhamid et al. (2022), Elbagory et al. (2019) and Soliman et al. (2014) for the same shoreline of the study region. El-Masry (2022) evaluated the influence of coastal structures on the Agami–Sidi Kerair coast throughout the period 1995–2020. According to the author's observations, the majority of the studied region underwent accretion, which is consistent with the findings of the current study. Darwish et al. (2017) examined shoreline changes along Zone 1 from 1972 to 2015. The researcher divided this zone into two segments, separating them by El Dekheila port. The analysis for the first segment revealed accretion rates with an average value of 1.4 m/y from 1984 to 2001, and 1.2 m/y between 2000 and 2015. when compared to the current study, the final findings demonstrated a high degree of convergence, with average accretion rates reaching 1.35 m/y, 1.45 m/y, and 1.29 m/y in intermediate periods 1985–2000, 2000–2010, and 2010–2022 respectively. Similarly, the second segment stretched from El-Dekheila to Abo Qir port, recorded an average accretion rate of 3.3 m/y between 2001 and 2015, while 4.2m/y during the 2000–2010 period and 5.3 m/y during the 2010–2022 period in the current study.

Zone 2 comprises about 6.94% of the study area's coastline in the most western section, stretching from Abo Qir port to the western part of Rosetta promontory. It began in the first period (1985–2000) with an accretion trend on more than 243 transects and erosion recorded on just 17 transects. The average and maximum accretion rates were approximately 3.33 m/y and 25.18 m/y, respectively. The coastline movement has seen an increase in erosion rates in the two following intermediate periods 2000–2010 and 2010–2022, where average values were −1.97 m/y, and −2.48 m/y, respectively. A long-term estimation of coastline changes along zone 2 was also performed from 1985 to 2022. The overall number of transects that demonstrated accretion was 177, covered a total length of 14.16 km, and

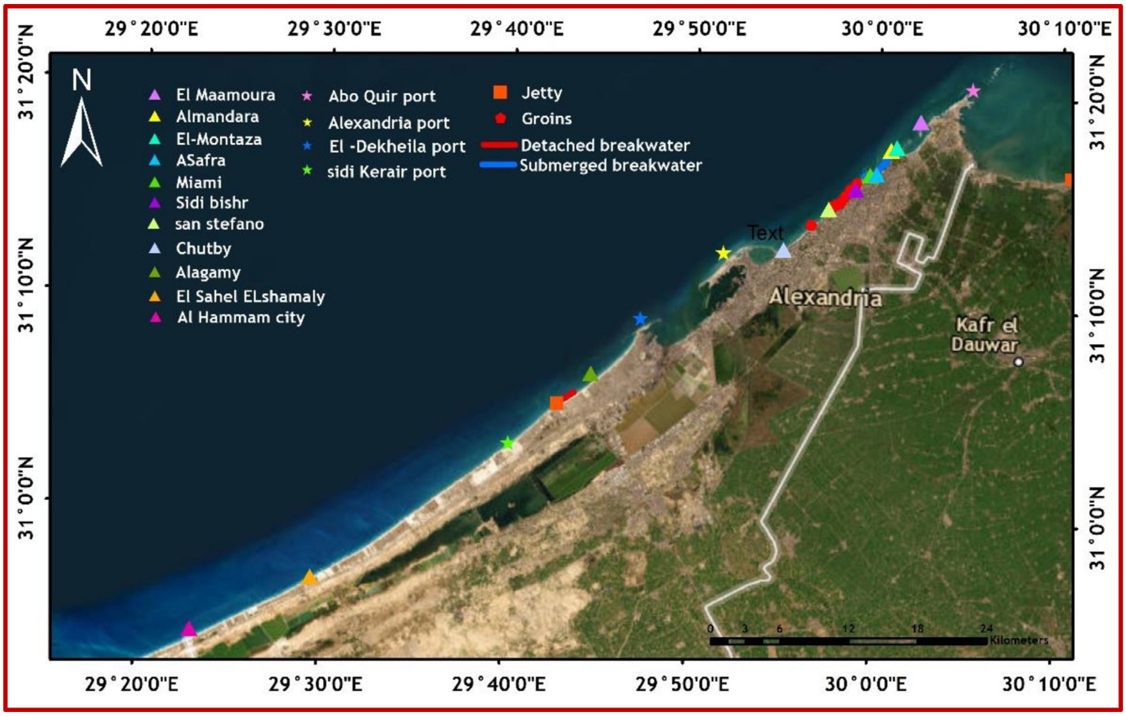

Figure 4 Alexandria coast (zone 1).

Table 3 Shoreline change rates LRR in different periods.

	Short-term periods						Long-term period	
	1985—2000		2000—2010		2010—2022		1985—2022	
	mean erosion (m/y)	mean accretion (m/y)	mean erosion (m/y)	mean accretion (m/y)	mean erosion (m/y)	mean accretion (m/y)	mean erosion (m/y)	mean accretion (m/y)
Zone 1	−0.62	1.23	−1.5	3.35	−1.03	3.73	−0.4	2.85
Zone 2	−0.46	3.33	−1.97	5.35	−2.48	4.14	−0.78	3.21
Zone 3	−36.2	7.94	−10.2	4.55	−7.55	2.33	−15.7	5.12
Zone 4	−2.97	4.24	−2.48	4.55	−3.31	3.6	−2.56	4.82
Zone 5	−4.52	4.68	−6.57	7.04	−5.67	5.09	−3.25	4.25
Zone 6	−2.27	3.98	−1.94	4.7	−3.45	6.76	−1.2	4.03
Zone 7	−22.8	27.13	−17.1	25.06	−21.7	24.27	−16.8	17.81
Zone 8	−8.1	5.23	−6.92	6.52	−5.1	7.78	−13.2	7.2

accounted for nearly 70% of the shoreline in the area under study. This is because the whole length of the coastline in this region is covered by a variety of natural and man-made protective systems. For example, Mohammed Ali seawall was constructed in 1830 on the western side of Abo-Qir Bay and was maintained in 1981 and 2011 to protect the low-elevation land of El-Tahr city (1.5—2.5 m below MSL) from inundation (Ismail et al., 2012). Coastal dunes are considered a natural protection system and represent about 60% of the length of the bay's middle portion. Jetties were structured during the year 1986 to protect the Idku inlet from shoaling. In addition, the breakwaters of Idku Port, located in the eastern portion of Abo-Qir Bay, were built to provide a calm area in the harbor. Several of the previous studies investigated and examined shoreline changes in the same zone (Darwish et al., 2017; Smith and Abdel-Kader, 1988). Emam and Soliman (2020) quantified shoreline changes in the same region using Landsat images (1987—2017). The observations showed very high accretion rates on about 78% of transects.

Along Rosetta promontory, 330 transects were applied to cover 26.4 km of shoreline length (zone 3). It experienced noticeable shifts in coastline displacement between the various intermediate periods. In the 1985—2000 period analysis, erosion was the dominant factor where average erosion rates reached −36.2 m/y with a max value of −99.18 m/y. There were a few parts that accreted with an average value of 7.94 m/y, centralized on the eastern side of the promontory. In the 2000—2010 period, erosion continued to occur but with lower values. Where it was revealed that the average shoreline retreat rate of this section was −10.21 m/y while the average advance rate was 4.55 m/y.

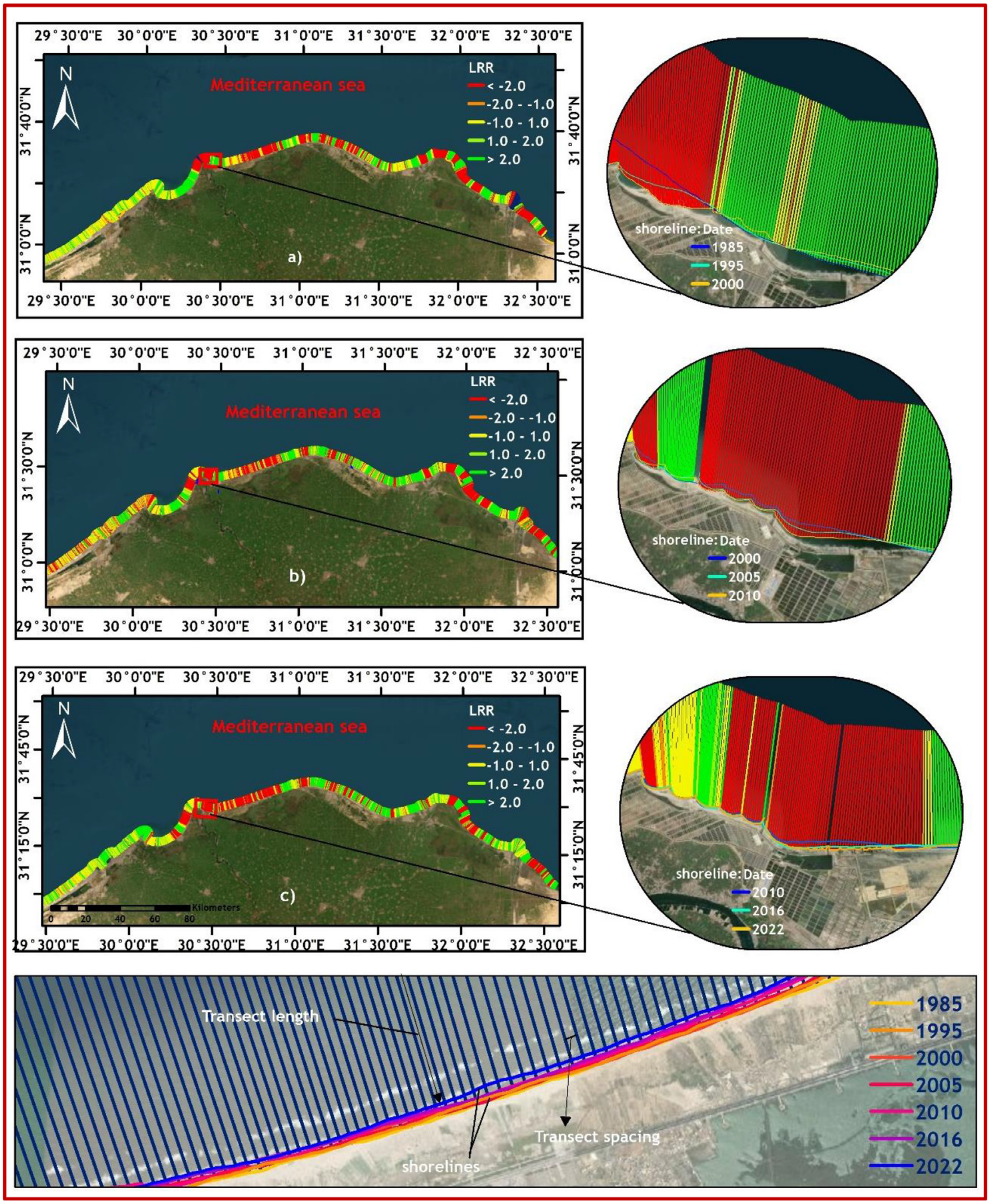

Figure 5 Rates of erosion and accretion LRR along Nile delta coast in a) 1985—2000, b) 2000—2010, c) 2010—2022.

It also revealed that the maximum erosion rate was about −30.7 m/y between 2010 and 2022. Erosion in this zone occurred by the action of waves and longshore currents, which carried sand away from the Rosetta promontory, as well as sand supplementation from the Nile River, which has been halted due to the building of the Aswan high dam. Eroded sand travelled east along the beach of Abu-Khashaba Bay and west along Abu Qir Bay's shoreline. More structures were implemented in this region to mitigate the erosion pattern; for example, a five-kilometre seawall was constructed between 1988 and 1991 at the western and eastern sides of Rosetta promontory to stop the erosion pattern at this promontory (Abou Samra and Ali, 2021). Additional structures were established at the downward drift of the eastern seawall in 2003. These included five groins ranging in length from 400 to 500 m seaward, spaced 800 to 900 m apart. Following that, in 2005, nine more short groins (80—150 m long) were erected with 500—600 m spacing at the downdrift of the western seawall (Dewidar and Frihy, 2007).

The results indicated that the building of nine groins mitigated erosion processes significantly, where shoreline retreat rates decreased from −36.27 m/y in 1985—2000 to −16.3 m/y and −2.81 m/y in two intermediate periods, 2000—2010 and 2010—2022. In 2016, fish farms GFF were

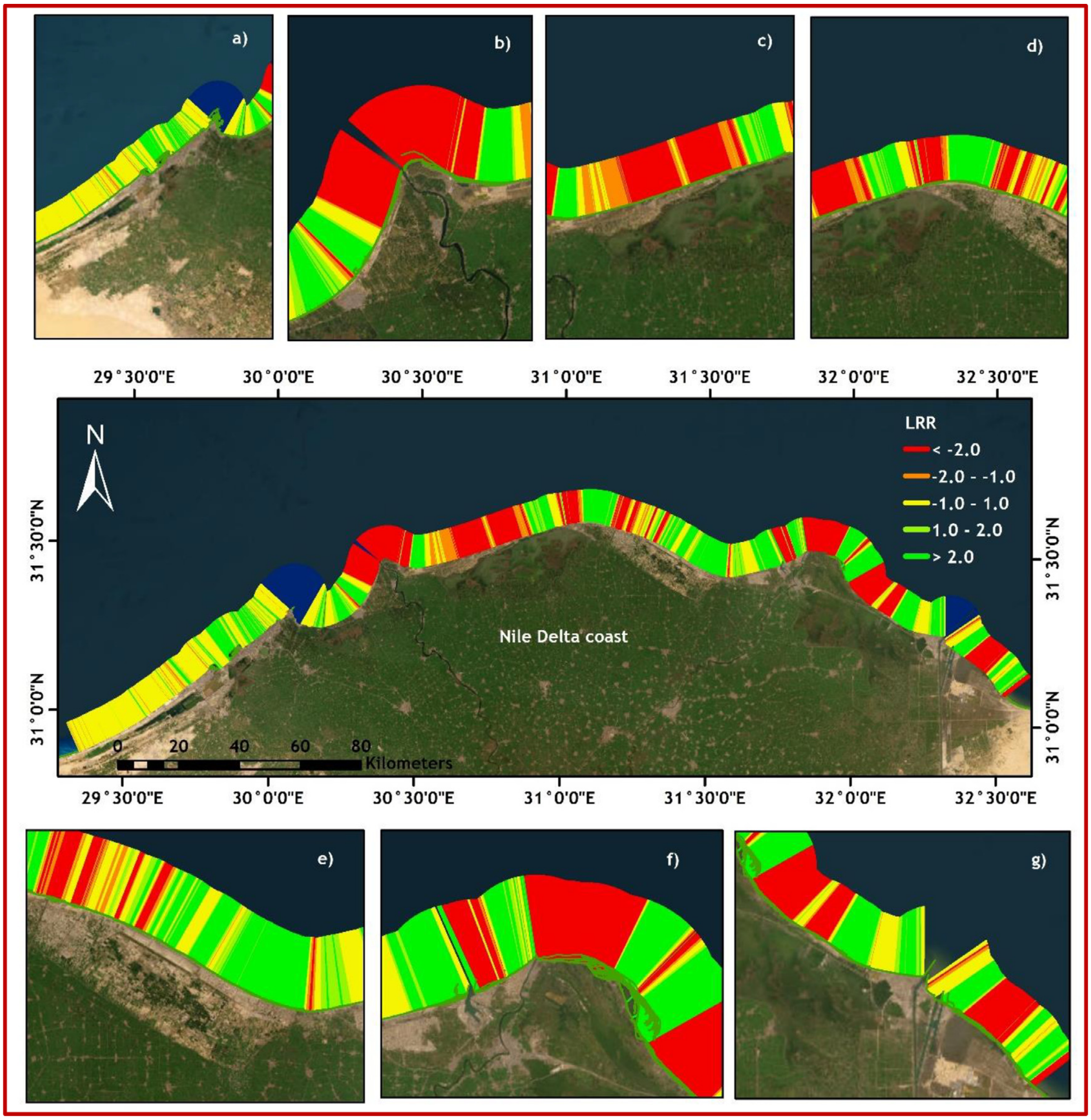

Figure 6 Shoreline changes "LRR" for the long-term period 1985—2022 at different locations: a) Alexandria coast and Abo-Qir Bay (zones 1—2), b) Rosetta promontory (zone 3), c) Abo-Kashaba Bay (zone 4), d) Burullus headland (zone 5), e) Gamasa Bay (zone 6), f) Damietta promontory (zone 7), g) Port Said coast (zone 8).

constructed and extended to about 25 thousand feddan. GFF influenced the balance of the coastline. So, another groin system was installed, as shown in Figure 8b. Between the inlet and outlet of GFF, 8 groins were spaced about 100 m apart, which were completed in 2018. The observations found that this region experienced dominant erosion reduction from —29.3 m/y in 2000—2010 to —18.3 m/y in 2010—2022. Another 8 groins on the eastern side of the outlet were also constructed by the Egyptian shore protection authority. The erosion problem persists with an average value of —12.3 m/y during the 2010—2022 period, as shown in Figure 9a. Sanhory et al. (2022) also investigated how recently built groins along the GFF fish farm influenced shoreline alterations between 1984 and 2020. The results showed that installing an 8-groin system between the GFF's inlet and outlet, reduced erosion rates from —36.22 m/y to —17 m/y. Furthermore, 8 groins at the eastward outlet of the GFF reduced erosion, but it still occurred, and there is a strong resemblance to the present research. For the long-term period from 1985 to 2022, average shoreline movement NSM showed an erosion value of —579.3 m and an accretion value of 189.57 m. Ghoneim et al. (2015) also reached the same conclusion that the shoreline of Rosetta promontory witnessed significant erosion, but rates were reduced as a result of the protection installations that were implemented in this area. Abou Samra and Ali (2021) observed that the average erosion rates were —13.64 m/y from 1984 to 2018 period in the same region.

Zone 4's shoreline consists of 500 transects with an overall length of 40 km of shoreline. This zone witnessed a dominant and continuous erosion throughout the study periods. In the 1985—2000 period, the erosion pattern significantly spread, with average rates reaching —2.97 m/y and peaking at —8.37 m/y. There were very few numbers of transects

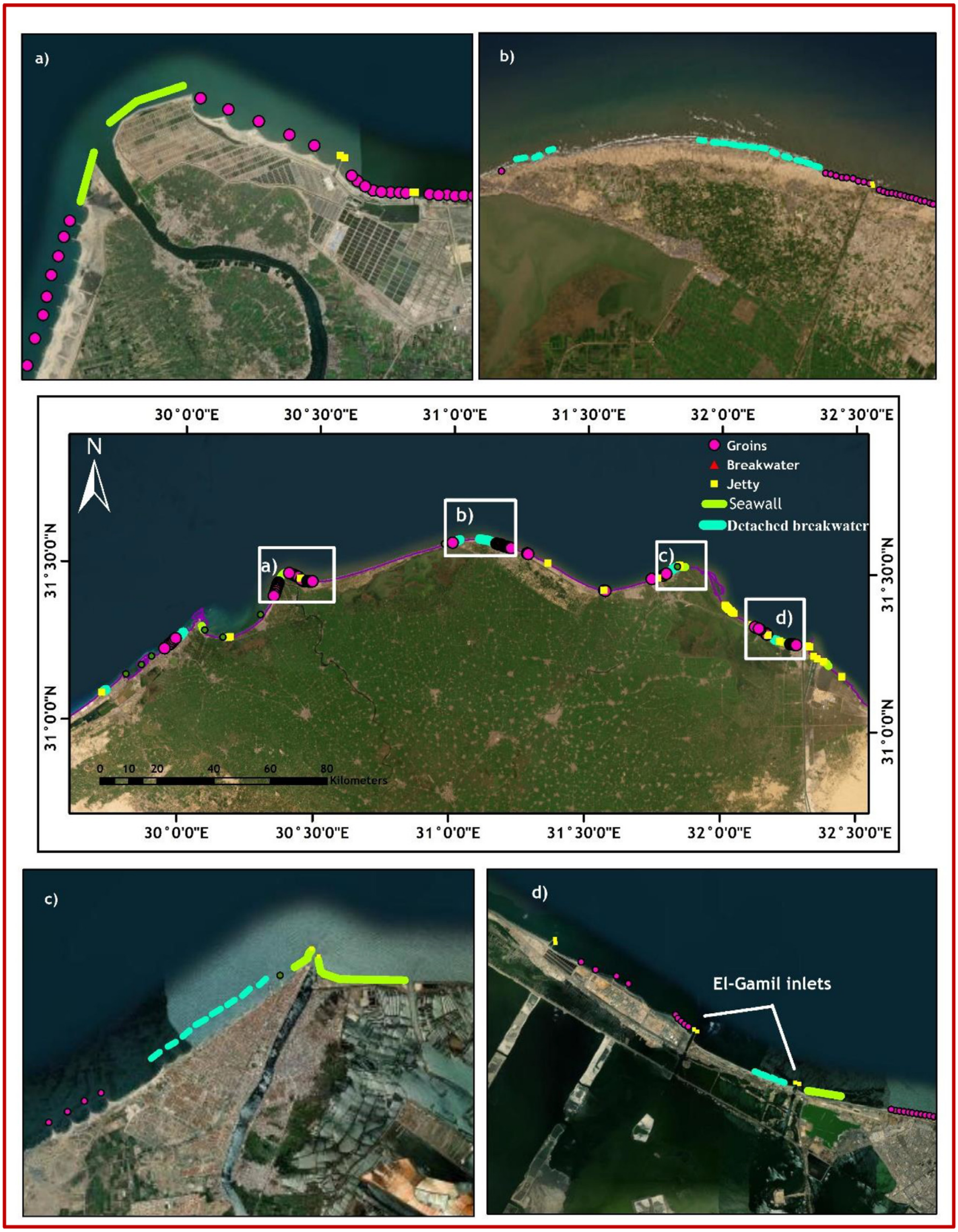

Figure 7 Summary of protection structures along Nile delta coast: a) Rosetta promontory (zone 3), b) Burullus headland (zone 5), c) Damietta promontory (zone 7), d) Port Said coast (zone 8).

showing accretion with an average value of 4.24 m/y. The total number of transects between the 2000—2010 period that show erosion is 393, representing 78.6% of the shoreline. In contrast, a minor accretion was recorded with a maximum rate of 14.87 m/y. From 2010 to 2022, erosion continued with higher rates where an average value reached −3.31 m/y and a maximum value was −9.35 m/y. The total number of transects showing accretion was only 64 transects representing 12.8% of the shoreline. The long-term shoreline movement from 1985 to 2022 showed dominant erosion at 419 transects with an average value of −2.6 m/y. The reason for all these high erosion rates in this zone was the absence of protection structures. These findings were consistent with those of Dewidar and Bayoumi (2021), who stated that this area has completely suffered from erosion problems.

Figure 8 Recent development along the study area: a) Abo-Qir port, b) the eastern side of Rosetta promontory, c) Kitchener drain, d) Gamasa drain outlet, e) the western side of Damietta promontory, f) El-Gamil inlets.

Zone 5 is the middle section extended along Baltim—Burullus headland, which constitutes 533 transects that span 42.5 kilometres of coastline. The result of shoreline change rates showed that the average erosion from 1985 to 2000 was about −4.52 m/y. The studied region possessed more erosion than accretion over this period, with 58% of the area eroded. In the 2000—2010 period, the number of transects that showed an accretion was 301 transects, with average accretion rates of 7.04 m/y. The average erosion was about −6.6 m/y, and the maximum value was −32.73 m. The shoreline change rates of the period from 2010 to 2022 showed that average accretion and erosion rates were about 5.09 m/y and −5.67 m/y, respectively.

Burullus Headland is a changing location prone to a variety of natural and artificial variables that exacerbate the erosion process, necessitating the development of

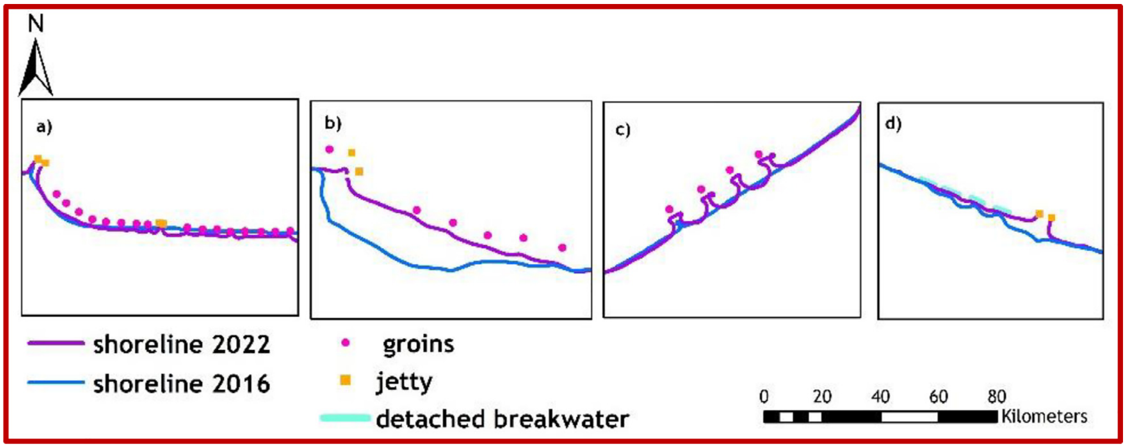

Figure 9 Shoreline changes between 2016—2022 at the recently executed structures: a) group of groins at GFF farms, b) jetties and groins system at the east of Kitchener drain, c) Y-groins at the eastern side of Damietta port, d) jetties at El-Gamil second inlet.

numerous efficient forms of coastal structures along the coast. Protection works along the Burullus coast began in 1947 with the erection of a 6-km seawall to safeguard the Burullus Lake inlet downdrift. A basalt rock wall was installed on Baltim village's east side to protect it in 1975. The western jetty of Burullus Lake inlet, on the other hand, was erected between 1971 and 1972, while the eastern jetty was completed between 1982 and 1983. On the western side of this zone, despite the construction of three detached breakwaters, the erosion in this area was increasing, and this proves that these breakwaters were not sufficient to stop the erosion due to their number concerning the length of the area to be protected. The deposition only occurred in the shadow area of these breakwaters. The rates of erosion were —6.08 m/y between 1985 and 2000 and continued to reach —6.83 m/y between 2000 and 2010 and decreased to —3.15 m/y between 2010 and 2022. Seventeen detached breakwaters have been installed in sea depths ranging from 3 to 4 meters along the Baltim coastal resort. Pre-construction stage of 17 detached breakwaters, this area experienced erosion processes from a period of 1985—2000, where the average shoreline retreat was about —6 m/y. However, this erosion converted into local accretion as a result of forming tombolo and salient in the 2000—2010, and 2010—2022 periods with average shoreline advance of about 13.5 m/y and 8.95 m/y, respectively.

The downdrift part of these detached breakwaters witnessed erosion due to the lack of sediment amount. Therefore, 9 groins were established in the eastern half of this zone in 2004 to safeguard the eroded shoreline west of the Kitchener drain (Elkafrawy et al., 2021). Even after the construction of these groins, the result revealed continued erosion with rates of —8.3 m/y and —5.86 m/y in 2000—2010, and 2010—2022, respectively. In 2016, a group of groins was installed at the eastern side of Kitchener drain, as shown in Figures 8c, and 9b, to control eroded beaches. And therefore, the results showed erosion rates reached —17.6 m/y on average in the 2000—2010 period, then decreased to —7 m/y in the 2010—2022 period. All of these results were consistent with the observations made by Elkafrawy et al. (2021). Emam and Soliman (2020) reported that the overall trend of shoreline change rate from 1987 to 2017 in Burullus region was —2.95 m/y (EPR).

Zone 6′s shoreline representing Gamasa embayment, consists of 440 transects totalling 35.2 km in length. This area was referred to as a very strong accretion zone with average rates of 4.03 m/y between 1985—2022. The average accretion rates of the three periods (1985—2000, 2000—2010, and 2010—2022) ranged from 3.98 m/year in the 1985—2000 period to 6.76 m/year in the 2010—2022 period. Also, the average value of accretion rates in the 2000—2010 period was 4.6 m/y. This zone also suffered from high to very high erosion rates, with average values ranging from —1.94 m/year happened in the 2000— 2010 period to —3.45 m/year in the 2010—2022 period. The maximum erosion rates of the three periods varied between —8.46 m/year in the 1985—2000 period to —10.63 m/year in the 2010—2022 period. This zone is considered a sediment sink receiving sediments from all eroded beaches along the Burullus shoreline (Dewidar and Bayoumi, 2021). Jetties at the Gamasa drain outlet and a group of groins on the eastern side of this drain are two recently added coastal structures 2019 to this zone (Figure 8d).

440 transects were utilized to study shoreline change rates along Damietta promontory (zone 7), representing 10.8% of the shoreline of the research region. Between 1985 and 2022 period, the findings indicated that this segment retreated at a rate of —16.76 m/y on average with a max value of —45.4 m/y. The mean accretion rate was 17.8 m/y. Abou Samra and Ali (2021) revealed that the average shoreline accretion and erosion rates were about 29.36 m/y and —20.61 m/y for the total period of 1984—2018. Abd-Elhamid et al. (2023) declared that the Damietta promontory experienced average rates of erosion ranging from —10 to —25 m/y between 1974 and 2022. At the beginning of this zone, there is Damietta Port, consisting of a western breakwater with a length of 1500 meters, and another eastern breakwater with a length of 800 meters that was extended in the year 2021. The results stated that the building of the two breakwaters enhanced accretion on the port's western side by 10.7 m/y and 3.4 m/y at intermediated periods 2000—2010 and 2010—2022, respectively, and caused local erosion at downdrift of the port's eastern breakwa-

ter with average —5.64 m/y and —4.12 m/y between 2000—2010 and between 2010—2022 respectively. A comparable rate of erosion between —9.9 and —13.5 m/y east of the Damietta port was quoted by El-Asmar et al. (2014) from 1984 to 2011. Four Y groins were constructed in 2019 as shown in Figure 8e to decrease this erosion. Rates of shoreline retreat decreased from —17.4 m/y between 1985—2000 to —2.31 m/y in the 2010—2022 period, Figure 9c. From 2000 to 2010 period, the mean erosion rate was —5.13 m/y. It should be mentioned that Damietta port's eastern breakwater extension will prevent a significant quantity of sand from reaching this beach, and this is what will cause a problem, and affect these groins' functionality.

Because of Ras-Elbar resort, 8 detached breakwaters with a length of 200 m and 200 m spacing were installed to control in the eroded beach. Dominated erosion in the period of 1985—2000 was —2.38 m/y and converted into accretion with average rates of 3.8 m/y, and 1.72 m/y in 2000—2010 and 2010—2022, respectively. Esmail et al. (2019) indicated that the shoreline advanced behind detached breakwaters with rates of 6.25 m/y and 4.25 m/y through the 1999—2003 and 2003—2015 periods. Our measured maximum erosion rates at Damietta promontory were —39.7 m/y in 1985—2000 then decreased to —6.77 m/y and —2.98 m/y in 2000—2010 and 2010—2022. Two jetties were constructed at Damietta inlet to prevent siltation. Also, two seawalls were installed on both the eastern and western sides of the inlet to stop erosion; however, erosion has begun at the eastern jetty with average rates of —27 m/y between 1985—2000 then significantly decreased to —0.81 m/y and —0.224 m/y in 2000—2010 and 2010—2022 respectively. The accretion pattern replaced the erosion pattern with an average of 0.4 m/y and 1.26 m/y during the period 2000—2010 and 2010—2022, respectively. More monitoring of Damietta spit reflects the presence of reciprocal changes between erosion and accretion. The western part of spit, this area suffered from erosion with average rates of —25 m/y during the period of 1985—2000. The erosion shifted distance and recorded average rates of —11.86 m/y in the 2000—2010 period, then converted into an accretion pattern with average rates of 56 m/y from 2010 to 2022. In the middle part of the spit, accretion was dominated in 1985—2000 with rates of 61 m/y on average and but erosion and accretion patterns were observed in the 2000—2010 period with average rates of —18 m/y and 34.55 m/y, respectively. From 2010 to 2022, the erosion pattern was dominated by values of —26.2 m/y on average. Accretion rates were observed with an average of 17.9 m/y. On the eastern side of Damietta spit, the shoreline accreted with average values of 17.7 m/y during the period of 198—2022. These results concurred with those of Aly et al. (2012) who mentioned that the eastern part of the sand spit increased in width during the study period.

Zone 8 extends from the eastern side of Damietta spit to the end of port said city which represents about 44 km, covers 13.5% of the shoreline. From 1985 to 2022, the shoreline advanced at a rate of 7.2 m/y on average. The average rate of coastline erosion was —13.2 m/y. The results of the coastline trend analysis were congruent with those of Abou Samra and Ali (2021). This region displayed different variations in coastline displacement between the various intermediate periods, including accretion and erosion. Shoreline retreat with average rates was —8.1 m/y, —6.92 m/y, and —5.1 m/y for intermediated periods 1985—2000, 2000—2010, and 2010—2022 respectively. In the 1985—2000 period, this section was prone to the impact of accretion with an average rate of 5.23 m/y. Accretion was also observed in the 2000—2010, and 2010—2022 periods, with average rates of 6.52m/y, and 7.78 m/y respectively.

After Damietta spit, this area experienced dominant erosion through three intermediated periods with average rates of —11.57 m/y, —7.48 m/y, and —4.25 m/y respectively. The reason for that is the presence of Damietta spit trapped the eastward sediments, therefore the area behind it suffered from a strong erosion, and also because the presence of jetties at the entrance to the fish farms trapped the long-shore sediments transport (Tharwat Sarhan et al., 2022).

Between 1985 and 2000, the region extending to the entrance of the Suez Canal had erosion and accretion with average values of roughly —6.36 m/y and 4.18 m/y, respectively. Accretion rates in the 200—2010 and 2010—2022 periods were 6.77 m/y and 3.53 m/y, respectively. Significant erosion rates were also observed in this region and were about —5.82 m/y, and —7.39 m/y in the intermittent intervals 2000—2010 and 2010—2022, respectively. As consequently, many protective structures have been established to lessen the erosion that already exists. One such measure is a group of groins installed in 2016, Figure 8f at the western side of El-Gamil's first inlet of El-Manzala Lake which increased accretion rates from 7.9 m/y in 2000—2010 to 11.05 m/y in 2010—2022. This was consistent with the findings of Tharwat Sarhan et al. (2022) who estimated accretion rates due to the implementation of these groins to be 7 m/y between 2002 to 2020. The shoreline was significantly built thanks to the several detached breakwaters installed on the

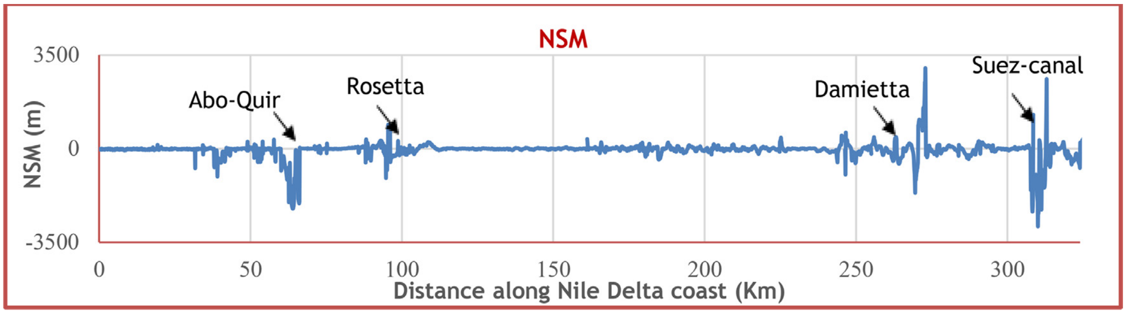

Figure 10 NSM distance between digitalized and predicted shoreline in 2022 at each transect.

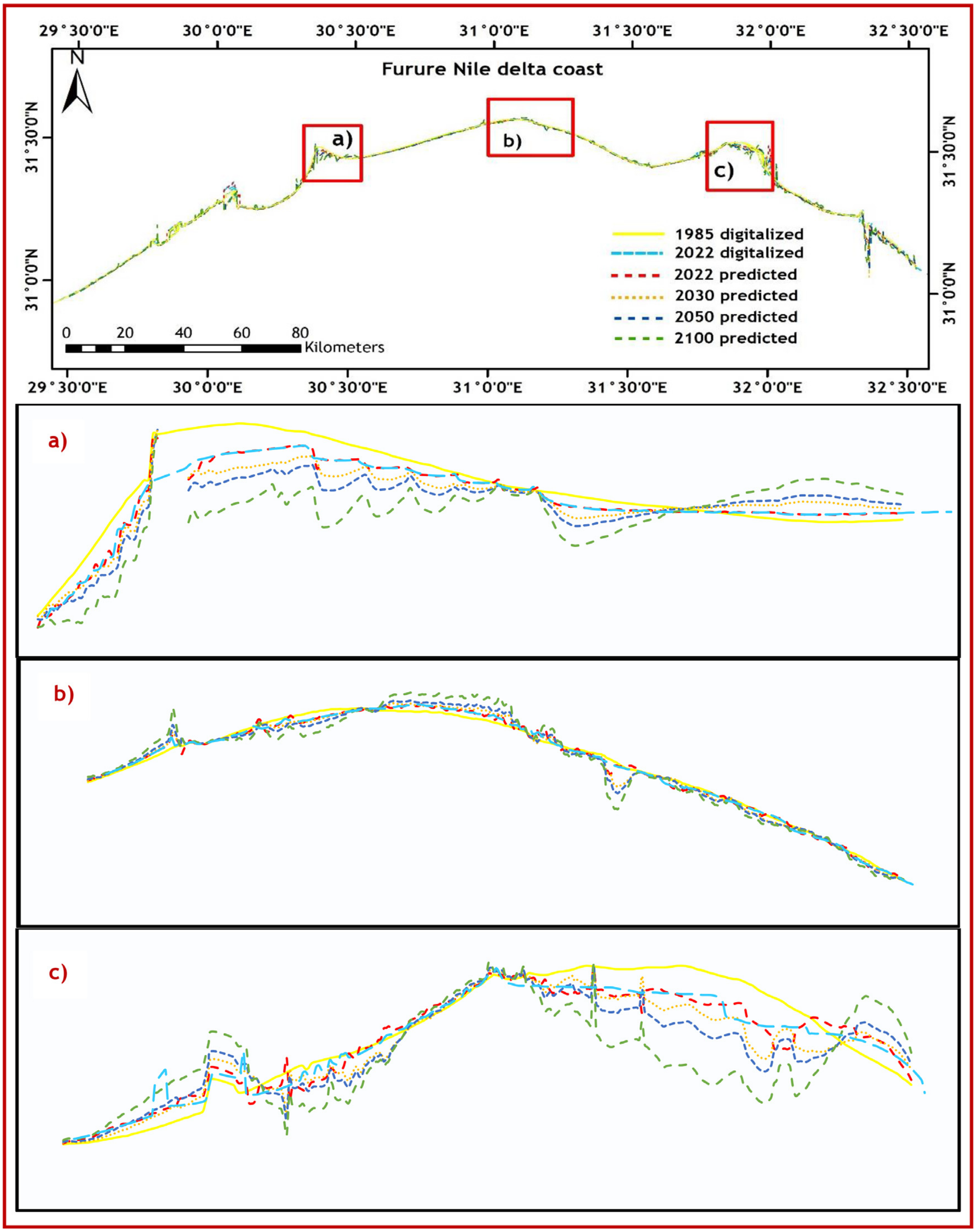

Figure 11 Future shoreline changes from 1985 to 2100: a) Rosetta promontory, b) Burullus headland, c) Damietta promontory.

western side of El-Gamil's second entrance, with accretion rates of 11.65 m/y and 6.44 m/y from 2000 to 2010 and 2010 to 2022, respectively. Jetties at El-Gamil inlets were completed recently as shown in Figure 8f. The results for the jetties' western side at El-Gamil second inlet showed a transition from erosion with an average value of −2.32 m/y in the period of 1985—2000 to an accretion pattern with an average value of 14.7 m/y in the period of 2010—2022, Figure 9d. Rates of erosion decreased from −1.663 m/y in 2000—2010 to −0.64 m/y in 2010— 2022 as a result of the existence of 14 groins with 175 m spacing at the western side of Suez Canal. Dewidar and Frihy (2010) observed erosion rates downdrift of Damietta spit in the long-term period 1972—2007 between −5.1 m/y to −10.16 m/y. Additionally, they mentioned that an accretion pattern occurred at the western of the Suez Canal with an average value of 8 m/y. After the Suez-canal entrance, an erosion pattern was observed with average values of −10.82

m/y, −18.2 m/y, and −29.3 m/y at intermediated periods, respectively.

4.2. Future shore line changes in 2030, 2050 and in 2100

To verify the LRR model, the positional difference between the predicted and extracted shorelines in 2022 was compared using NSM at each transect (Figure 10). The findings of this comparison resulted in a small NRMSE value of 0.0195, demonstrating that the LRR model is a good indicator of future locations of the study region's coastline. Figure 11 depicts the analysis and identification of future shoreline alterations predicted for 2030, 2050, and 2100 at specified locations. The results revealed that zone 1 will advance 128.14 m on average in 2030, then increase to 200.3 m in 2050, and 402.8 m in 2100 years. Furthermore, it will erode by −503.5 m, −550.15 m, and 714.4 m in 2030, 2050, and 2100, respectively. This necessitates the construction of protective structures to mitigate coastline erosion and protect this region. The predicted shoreline positions at zone 2 show accretion changing from 508.15 m in the year 2030 to 1266.48 m for the year 2100, respectively. While, it shows erosion on average of −85.26 m, −156.1 m, and −355.6 m for the years 2030, 2050, and 2100 respectively. Shoreline position at zone 3 (Figure 11a) will advance with about 219.73 m, 412.22 m, and 862.16 m, but it will erode with about −204.59 m, −360.71 m, and −794.139 m for the years 2030, 2050, and 2100 respectively.

The coastline position at zone 4 was estimated to retreat about −66.12 m, −119.5 m, and −286.4 m and to advance by approximately 69.5 m, 104.42 m, and 180.26 m for years 2030, 2050, and 2100 respectively. It was also noticeable that zone 5, Figure 11b, will continue in erosion, and the coastline will retreat with calculated NSM values of −183.88 m, −213.55 m, and −316.89 m for years 2030, 2050, and 2100 respectively. Zone 6 is anticipated to advance with an average shoreline displacement of 134.35 m by 2030, 157.7 m by 2050, and 223.97 m by 2100. The shoreline of zone 7 will erode by average distances of −446.73 m in 2030, −715.98 m in 2050, and −1520.36 m in 2100. As shown in Figure 11c, zone 7 will experience severe erosion, with large sections of the beach disappearing completely by 2100. Zone 8 will need urgent protection structures because it will suffer from severe erosion rates. It will lose land by −702 m in 2030, by about −1038.83 m in 2050, and −1930.17 m in 2100.

5. Conclusions

Erosion and accretion rates were determined over a 324-kilometer stretch of the Nile Delta coast for 37 years. DSAS software was used as an analysis method by casting 4050 transects perpendicular to the digitalized shorelines. The studied region witnessed erosion in 2180 transects and accretion in 1870 transects between 1985 to 2022. Three areas experienced very high erosion rates with a maximum value: Rosetta promontory (−37.2 m/y) and Damietta promontory (−45.4 m/y), as well as Burullus headland (−11.07 m/y). These changes were mostly due to the interruption of the sediment supply via the Aswan High Dam, climate changes, and the negative impacts of coastal installations. The locations with the maximum values of accretion rates were Alexandria coast (25.8 m/y) and Gamasa embayment (37.2 m/y), as well as some portions of Port-said coast (36.9 m/y), centred around El-Gamil inlets throughout the long-term period. This study evaluated the effect of newly installed coastline protection measures on the erosion processes in this region. On the Rosetta promontory's eastern side, a new groin protection system was constructed in 2016. But the impact of these groins on the erosion process was not great. Between the inlet and outlet of GFF, 8 groins were able to lower erosion rates from −29.3 m/y in 2000—2010 to −18.3 m/y in 2010—2022. Despite the erection of additional 8 groins on the eastern side of the outlet, erosion continues to be an issue, with an average rate of −12.3 m/y between 2010 and 2022. On the eastern side of Kitchener Drain, a group of groins was also installed in the same year, and it was noted that erosion rates which peaked at −17.6 m/y on average from 2000 to 2010, decreased by 60.2% in the period from 2010 to 2022. In 2019, a number of Y-groin was executed on Damietta Port's eastern side to mitigate the ongoing erosion in this area. These groins achieved their function and reduced erosion significantly by −2.31 m/y on average between 2010 and 2022. Five groins were erected in 2016 near the western edge of the first El-Gamil inlet, increasing accretion rates from 7.9 m/y in the years 2000—2010 to 11.05 m/y in the years 2010—2022. The estimated shoreline positions for 2030, 2050, and 2100 demonstrate that the past change patterns will be anticipated to continue at nearly similar rates in the future. If the situation does not improve and the Egyptian authorities do not step in and undertake urgent measures, zones 1—2, and 6 will continue to accrete, while zones 3, 4, 5, 7, and 8 will erode at significant rates in the future. These future estimations highlighted the areas of the shoreline that will be significantly lost due to erosion; hence, urgent necessary management solutions will be required.

Declaration of competing interest

The authors declare that they have no known competing financial interests or personal relationships that could have appeared to influence the work reported in this paper.

References

Abd-Elhamid, H.F., Zeleňáková, M., Barańczuk, J., Gergelova, M.B., Mahdy, M., 2023. Historical Trend Analysis and Forecasting of Shoreline Change at the Nile Delta Using RS Data and GIS with the DSAS Tool. Remote Sens. 15 (7). https://doi.org/10.3390/rs15071737

Abd-Elhamid, H.F., Zeleňáková, M., Mahdy, M., 2022. Assessing the impact of climate change and sea level rise on the shoreline of Alexandria city — Recreation area. Public Recreation and Landscape Protection — With Environment Hand in Hand. Proc. 13th Conf., 45—51. https://doi.org/10.11118/978-80-7509-831-3-0045

Abou Samra, R.M., Ali, R.R., 2021. Applying DSAS tool to detect coastal changes along Nile Delta, Egypt. Egypt. J. Remote. Sens. Space Sci. 24 (3), 463—470. https://doi.org/10.1016/j.ejrs.2020.11.002

Ali, E.M., El-Magd, I.A., 2016. Impact of human interventions and coastal processes along the Nile Delta coast, Egypt during the past twenty-five years. Egypt J. Aquat. Res. 42 (1), 1—10.

Aly, M.H., Giardino, J.R., Klein, A.G., 2012. InSAR Study of Shoreline Change along the Damietta Promontory, Egypt. J. Coast. Res. 28 (5), 1263—1269. www.cerl-jcr.org.

Balbaa, S.H., El-Gamal, A.A., Mansour, A.S., Rashed, M.A., 2020. Mapping and Monitoring of Rosetta Promontory Shoreline Pattern Change, Egypt.

Basheer Ahammed, K.K., Pandey, A.C., 2019. Shoreline morphology changes along the Eastern Coast of India, Andhra Pradesh by using geospatial technology. J. Coast. Conserv. 23 (2), 331—353. https://doi.org/10.1007/s11852-018-0662-5

Darwish, K., Smith, S.E., Torab, M., Monsef, H., Hussein, O., 2017. Geomorphological Changes along the Nile Delta Coastline between 1945 and 2015 Detected Using Satellite Remote Sensing and GIS. J. Coast. Res. 33 (4), 786—794. https://doi.org/10.2112/JCOASTRES-D-16-00056.1

Deabes, E.A.M., 2017. Applying ArcGIS to Estimate the Rates of Shoreline and Back-Shore Area Changes along the Nile Delta Coast, Egypt. Int. J. Geosci. 8 (03), 332—348. https://doi.org/10.4236/ijg.2017.83017

Dewidar, K., Bayoumi, S., 2021. Forecasting shoreline changes along the Egyptian Nile Delta coast using Landsat image series and Geographic Information System. Environ. Monit. Assess. 193 (7), 1—11. https://doi.org/10.1007/s10661-021-09192-x

Dewidar, K., Frihy, O., 2007. Pre- and post-beach response to engineering hard structures using Landsat time-series at the northwestern part of the Nile delta, Egypt. J. Coast. Conserv. 11 (2), 133—142. https://doi.org/10.1007/s11852-008-0013-z

Dewidar, K.M., Frihy, O.E., 2010. Automated techniques for quantification of beach change rates using Landsat series along the North-eastern Nile Delta, Egypt. Oceanogr. Mar. Biol. 1 (2), 28—39.

El-Asmar, H.M., El-Kafrawy, S.B., Taha, M.M.N., 2014. Monitoring coastal changes along Damietta Promontory and the barrier beach toward Port Said east of the Nile Delta, Egypt. J. Coast. Res. 30 (5), 993—1005.

Elbagory, I.A., Heikal, E.M., Koraim, A.S., 2019. Shoreline changes using digitizing of Landsat images at Miami to Montaza beach, Alexandria, Egypt Intern. J. Civil Eng. Technol. 10 (5), 75—91.

El-Hattab, M.M., 2015. Improving coastal vulnerability index of the Nile Delta coastal zone, Egypt. J. Earth Sci. Climate Change 6 (8), 293.

Elkafrawy, S.B., Basheer, M.A., Mohamed, H.M., Naguib, D.M., 2021. Applications of remote sensing and GIS techniques to evaluate the effectiveness of coastal structures along Burullus Headland-Eastern Nile Delta, Egypt. J. Remote. Sens. Space Sci. 24 (2), 247—254. https://doi.org/10.1016/j.ejrs.2020.01.002

El-Masry, E.A., 2022. Hard engineering coastal structures; detrimental or beneficial: A case study of Agami—Sidi Kerair coast. Mediterranean Sea, Egypt 26 (1), 505—531. www.ejabf.journals.ekb.eg.

El-Sayed, W.R., Khalifa, A.M., 2017. NILE Delta shoreline protection between past and future. Proceeding of the 20th International Water Technology Conference. International Water Technology Association, Ed. Publisher, London, UK.

Elsayed, M.A., Younan, N.A., Fanos, A.M., Baghdady, K.H., 2005. Accretion and erosion patterns along Rosetta promontory, Nile Delta coast. J. Coast. Res. 21 (3), 412—420.

Elshinnawy, I.A., Almaliki, A.H., 2021. Vulnerability assessment for sea level rise impacts on coastal systems of Gamesa Ras El bar area, Nile delta, Egypt. Sustainability (Switzerland) 13 (7), 3624. https://doi.org/10.3390/su13073624

Emam, W.W.M., Soliman, K.M., 2020. Quantitative analysis of shoreline dynamics along the Mediterranean coastal strip of Egypt. Case study: Marina El-Alamein Resort. Environ. Remote Sens. Egypt 575—594. https://doi.org/10.1007/s10661-020-08432-w

Esmail, M., Mahmod, W.E., Fath, H., 2019. Assessment and prediction of shoreline change using multi-temporal satellite images and statistics: Case study of Damietta coast, Egypt. Appl. Ocean Res. 82, 274—282. https://doi.org/10.1016/j.apor.2018.11.009

Frihy, O.E., Deabes, E.A., Shereet, S.M., Abdalla, F.A., 2010. Alexandria-Nile Delta coast, Egypt: update and future projection of relative sea-level rise. Environ. Earth Sci. 61, 253—273.

Frihy, O.E., Dewidar, K.M., E, M.M., Pharaana St, E., 1996. Evaluation of coastal problems at Alexandria, Egypt. Ocean Coast. Manage. 30 (2—3), 281—295.

Frihy, O.E., El-Sayed, M.K., 2013. Vulnerability risk assessment and adaptation to climate change induced sea level rise along the Mediterranean coast of Egypt. Mitig. Adapt. Strategy Global. Change. 18, 1215—1237. https://doi.org/10.1007/s11027-012-9418-y

Frihy, O.E., Pharaana St, E., Shallalat Alexandria, E., 1988. Nile Delta Shoreline Changes: Aerial Photographic Study of a 28-Year Period. J. Coast. Res. 4 (4), 597—606.

Frihy, O., Lawrence, D., 2004. Evolution of the modern Nile delta promontories: Development of accretional features during shoreline retreat. Environ. Geol. 46 (6—7), 914—931. https://doi.org/10.1007/s00254-004-1103-3

Ghoneim, E., Mashaly, J., Gamble, D., Halls, J., AbuBakr, M., 2015. Nile Delta exhibited a spatial reversal in the rates of shoreline retreat on the Rosetta promontory comparing pre- and post-beach protection. Geomorphology 228 (1), 1—14. https://doi.org/10.1016/j.geomorph.2014.08.021

Gümüs, M.G., Durduran, S.S., Gümüs, K., 2021. Investigation of shoreline change rates using the digital shoreline analysis system in Lake Beyşehir, Turkey, Bull. Geophys. Oceanogr. 63 (1), 119—142.

Hereher, M.E., 2010. Vulnerability of the Nile Delta to sea level rise: An assessment using remote sensing. Geomatics, Nat. Hazards Risk 1 (4), 315—321. https://doi.org/10.1080/19475705.2010.516912

Iskander, M.M., 2013. Wave climate and coastal structures in the Nile Delta coast of Egypt. Emirates J. Eng. Res. 18 (1), 43—57.

Ismail, N.M., Asce, M., El-Sayed, W., 2012. Assessment of coastal flooding at the southern Mediterranean with a global outlook for lowland coastal zones. Coast. Eng. Proc. (33) 83—83.

Kaliraj, S., Chandrasekar, N., Magesh, N.S., 2015. Evaluation of coastal erosion and accretion processes along the southwest coast of Kanyakumari, Tamil Nadu using geospatial techniques. Arab. J. Geosci. 8 (1), 239—253. https://doi.org/10.1007/s12517-013-1216-7

Niya, A.K., Asghar Alesheikh N, A.K., Soltanpour Khaje Nasir, M., 2013. Shoreline Change Mapping Using Remote Sensing and GIS Case Study: Bushehr Province Evaluating Citizen Satisfaction and Prioritizing Their Needs View project. J. Remote Sens. Appl. 3 (3), 102—107. www.ijrsa.org.

Masria, A., Negm, A., Iskander, M., Saavedra, O., 2014. Coastal zone issues: A case study (Egypt). Procedia Eng. 70, 1102—1111. https://doi.org/10.1016/j.proeng.2014.02.122

Quang, D.N., Ngan, V.H., Tam, H.S., Viet, N.T., Tinh, N.X., Tanaka, H., 2021. Long-term shoreline evolution using dsas technique: A case study of Quang Nam province, Vietnam. J. Mar. Sci. Eng. 9 (10), 1124. https://doi.org/10.3390/jmse9101124

Sanhory, A., El-Tahan, M., Moghazy, H.M., Reda, W., 2022. Natural and manmade impact on Rosetta eastern shoreline using satellite Image processing technique. Alex. Eng. J. 61 (8), 6247—6260. https://doi.org/10.1016/j.aej.2021.11.053

Smith, S.E., Abdel-Kader, A., 1988. Coastal erosion along the Egyptian delta. J. Coast. Res. 245—255.

Soliman, A., Elsharnouby, B., Elkamhawy, 2014. Shoreline Changes Due to Construction of Alexandria Submerged Breakwater, Egypt. In: ICHE 2014. Proc. 11th Int. Conf. Hydrosci. Eng, 675—684.

Tharwat Sarhan, A., Mina Iskander, M., Nassar, K., El-Gamal, M., 2022. Shoreline changes detection using digital shoreline analysis system: case study Damietta—Port Said coastal area, Egypt. MEJ. Mansoura Eng. J. 47 (1), 35—48.

Thieler, E. R., Hammar-Klose, E. S. 1999. National assessment of coastal vulnerability to sea-level rise: preliminary results for the US Atlantic coast. US Geological Survey.

Torab, M., Torab, M., Azab, M., 2007. Modern shoreline changes along the Nile delta coast as an impact of construction of the Aswan high dam. Geogr. Tech. 2 (2), 69—76. https://www.researchgate.net/publication/284481009

Oceanologia 65 (2023) 612—623

Available online at www.sciencedirect.com

ScienceDirect

journal homepage: www.journals.elsevier.com/oceanologia

ORIGINAL RESEARCH ARTICLE

First survey of metallic distribution in zooplankton from a south Moroccan area

Fatima Zohra Bouthir[a,*], **Imane Afandi**[a], **Sophia Talba**[b], **Maylis Labonne**[c], **Hicham Masski**[a], **Mathieu Waeles**[d], **Raymond Lae**[d]

[a] *National Institute of Fisheries Research (INRH), Casablanca, Morocco*
[b] *Faculty of Sciences Ben M'sik, Casablanca, Morocco*
[c] *UMR MARBEC, University of Montpellier, Montpellier, France*
[d] *UMR LEMAR 6539, European Institute For Marine Studies, Plouzané, Brest, France*

Received 17 June 2022; accepted 30 June 2023
Available online 11 July 2023

KEYWORDS
Zooplankton;
Metals;
Southern Atlantic coast of Morocco;
Upwelling;
EPURE cruises

Abstract The Moroccan Southern Atlantic coast is mainly influenced by upwelling, Saharan dust and anthropogenic micropollutant input. These factors contribute to increasing the availability of metal elements in waters. To differentiate human impact from natural variability, knowledge of background concentrations of metals and their fluctuations in bioindicator organisms such as zooplankton is important. This work aims to determine the levels of metals elements (Zn, Mn, Pb, Cu, Cd, Cr, Co, Ni, Li, As, Sr, U, Fe and Ba) in zooplankton along the southern area of the Atlantic coast of Morocco. Zooplankton samples were collected in the summer (July 2013) and autumn (December 2013) at 27 stations from Sidi Ifni to the south of Dakhla. All stations were located on transects perpendicular to the coast. The analysis of metal elements in zooplankton was determined by ICP—MS. The results revealed that in all transects, metal concentrations were below the regulatory limits. Metal enrichments were observed in the south and decreased gradually to the north. This study can be used as baseline data for the metal contents of zooplankton in Moroccan South Atlantic coastal water. A comparison to

---

[*] Corresponding author at: Institut National de Recherche Halieutique, 2 BD Sidi Abderrahman, Ain Diab, Casablanca 20100, Morocco.
E-mail addresses: fzbouthir@gmail.com (F.Z. Bouthir), afandi.imane@gmail.com (I. Afandi), sophia.talba@gmail.com (S. Talba), Maylis.Labonne@ird.fr (M. Labonne), hmasski@gmail.com (H. Masski), Matthieu.Waeles@univ-brest.fr (M. Waeles), raymond.lae@ird.fr (R. Lae).

Peer review under the responsibility of the Institute of Oceanology of the Polish Academy of Sciences.

Production and hosting by Elsevier

https://doi.org/10.1016/j.oceano.2023.06.009

worldwide reported data on zooplankton did not reveal any suggestions on increased metal presence in the area investigated.

1. Introduction

In marine environments, metals have received considerable attention due to their toxicity and accumulation in biota. Metallic elements exist naturally in the marine environment, but they are further amplified by anthropogenic and industrial inputs, including planting N-fixing crops, fertilizer production, and wastewater disposal. The irreversibility of this pollution is of particular concern, because it is impossible to recover these metals once dissipated in nature. Despite the fact that metals are natural elements in the environment, above a certain threshold of bioavailability, they become toxic (Kucuksezgin et al., 2006). Unlike organic pollutants, metals are not metabolized; they can be transferred through the food chain and then accumulate in living matter. Metallic element contents in seawater vary over time, depending on the variability of the pollution flow and physical parameters such as the temperature, ocean roughness, flow rates and biological effects (Gaudry et al., 2007).

Metallic accumulation by zooplankton is especially achieved either by direct adsorption from water or by absorption from food and detritus. Zooplankton are a very important compartment in the processes of metal bioavailability in coastal waters. In particular, they are a major source of food for marine species, confirming their role in the transfer of metals to higher trophic levels (Robin et al., 2012). Plankton play an important role in the vertical transport of elements in pelagic surface waters; the flux of organic compounds forms a large part of the vertical flux and then influences the residence periods of metal elements adsorbed to particles in the sea (Fisher et al., 1991). Zooplankton are vital to the functioning of ocean food webs due to their sheer abundance and important ecosystem roles (Battuello et al., 2016).

Zooplankton's position as an "intermediary" in the trophic chain of aquatic ecosystems, with a major role in the transfer of material between primary producers and other higher levels, means that these organisms can be good indicators of the general conditions under which aquatic ecosystems function. Accordingly, several studies have successfully used macro- and mesozooplankton organisms as bioindicators. They are applied to assess the bioavailability of metal elements in marine ecosystems at different spatial and temporal scales (Achary et al., 2020; Battuello et al., 2016; Fang et al., 2006; Hsiao et al., 2011; Kahle and Zauke, 2003; Nair et al., 1999; Pempkowiak et al., 2006). Their utility is due to their presence on a global scale, their high contribution to the total biomass of marine systems and their major role in food chains.

The assessment of anthropogenic disturbance by zooplankton has been studied by researchers worldwide; however, information on the quality of zooplankton in aquatic environments along African coasts is limited, including the Moroccan Atlantic coast, which is one of the richest coasts in terms of exploitable biological resources. Indeed, the south Moroccan coastline is characterized by the upwelling of deep waters, which ensures a supply of nutrients contributing to the production of the entire trophic food chain (Makaoui et al., 2020), as well as local contamination by metal elements, especially Cd in bivalve mollusks and in the liver tissue of pelagic fish. Afandi et al. (2018) and Benbrahim et al. (2006) attributed this finding to anthropogenic sources (phosphate industry) and to natural sources (upwelling activities, showing cadmium contamination). To date, no previous studies assessing the concentration of metals in zooplankton carried out in the southern zone of the Atlantic coast of Morocco are available. To fill this gap in this region of the world, we studied the levels of fourteen metallic elements in zooplankton in the lower and upper mixed layers. This study was conducted along nine transects perpendicular to the coast.

The objectives of this study are as follows: (1) Determine the quality of the coastal marine environment below the baseline metal concentrations for the first time in zooplankton samples from the southern zone of the Atlantic coast of Morocco; (2) Differentiating input from human influence versus natural variance; (3) Determine whether the concentrations of metals differ significantly during the season of high or low upwelling; (4) Determine vertical and diurnal variation in metal accumulation in zooplankton; and (5) Development of a new database of metal levels.

2. Material and methods

2.1. Study area

The study area is located in the eastern limit of the North Atlantic subtropical gyre (Figure 1). The southern Moroccan zone between 20° and 25°N is characterized by variable permanent upwelling with intense activity in summer. This zone is limited in the north and south by seasonal upwelling systems in summer and winter, respectively, with an interannual change (Larissi et al., 2013). It is generally in the 0—100 km coastal band that vertical upwelling-induced movements occur, as estimated from the Rossby deformation radius in northwest Africa (Chelton et al., 1998) cited by Auger et al. (2015); therefore, the coastal jet is limited near the coast (Waeles et al., 2016). In addition, the interannual variability in the upwelling index between 2002 and 2010 deviated from the infrared thermal imaging of the Modis-Aqua sensor along the Moroccan upwelling zone (21—33°N), indicating an evident oscillation over the years (Larissi et al., 2013). This study is particularly valuable be-

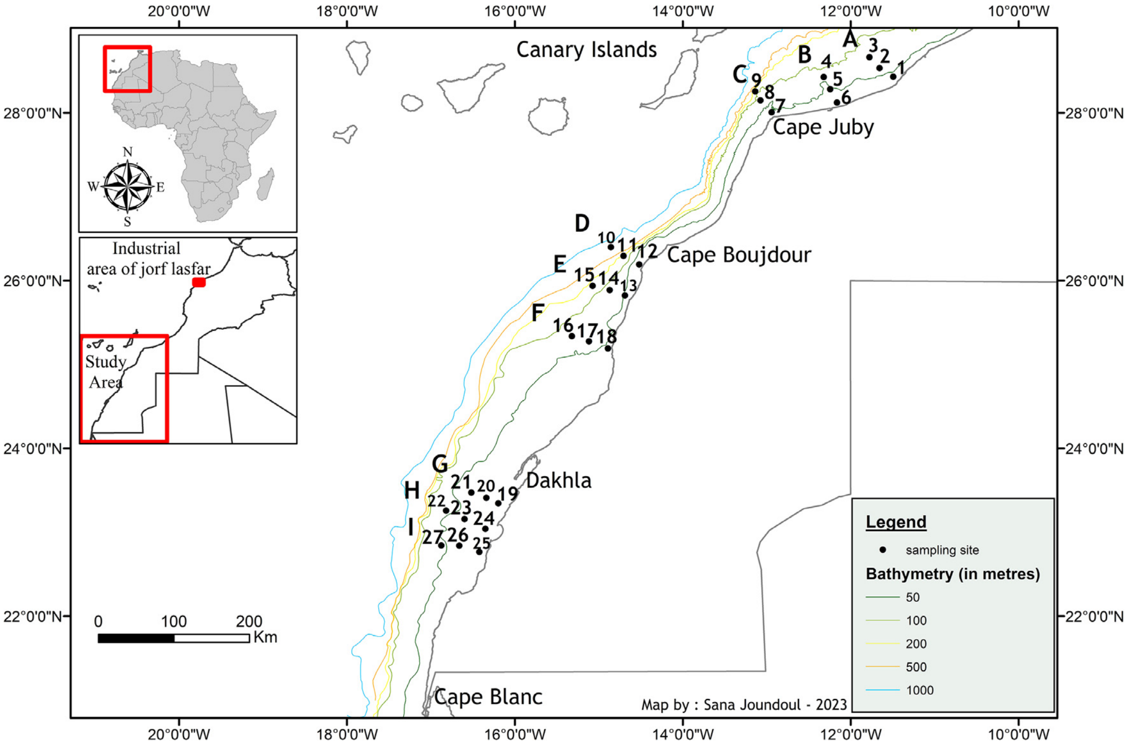

Figure 1 Locations of sampling sites (black dots) and transect definitions (capital letters) along the south Atlantic Moroccan coast, where zooplankton samples were collected during the cruise 2 and 4 aboard the r/v *Antea*.

cause this area of the Canary Current ecosystem represents a considerable fishery potential (Tito de Morais, 2013).

2.2. Sampling and sample preparation

During the EPURE cruises (cruise 2: from 11 to 31 July 2013 and cruise 4: from 21 November to 09 December 2013, r/v *Antea*), 27 hydro-biological stations were sampled. Zooplankton samples were collected using nets with a mesh size of 150 microns. The sampling strategy closely followed the Moroccan coast, integrating different areas of Moroccan upwelling. Specifically, three zones known for their coastal upwelling strength, due to their hydrobiological and bathymetric characteristics, were selected: north of Cape Juby, south of Cape Boujdour and south of Dakhla. In each zone, three sections were conducted (Figure 1), with a total of 111 zooplankton samples, of which 57 were collected in cruise 2 and 54 samples in cruise 4. At each station, samples were collected during the day and night, further 2 levels were typically sampled for 5 min., usually one near the bottom and one in the mixed layer.

The zooplankton samples were passed through a small nylon sieve, briefly rinsed after catching with ultrapure water to remove salts and frozen at −20°C. Subsequently, in the laboratory, samples were freeze-dried for 72 hours at −55°C, homogenized by mixing in rotating glass and stored in glass bottles in vacuum desiccators.

2.3. Analytical procedures

Prior to the use for digestion, all glassware and vessels were cleaned with special detergent (Micro 90), kept covered with HNO_3 (10%) for at least 24 h and rinsed 4 to 5 times with deionized water. To avoid any contamination, vessels were tested individually for blanks and screened before use. Mineralization was carried out in Teflon digestion vessels according to the Association of Official Analytical Chemists (AOAC Official Method 999.10, AOAC, 2002). Zooplankton samples were first mixed, and approximately 0.25 g of zooplankton samples were digested for 30 min. in a microwave oven at 190°C with 5 ml of HNO_3 (65% Merck-Suprapur Grade) and 2 ml of H_2O_2 (30% Fluka). The digested solutions were successively diluted to 50 ml with deionized water.

All elements analyses (Zn, Mn, Pb, Cu, Cd, Cr, Co, Ni, Li, As, Sr, U, Fe and Ba) were performed in an Ocean Spectrometry Pole at LEMAR by means of a magnetic sector inductively coupled plasma mass spectrometer (ELEMENT 2, Thermo) with low- and medium-resolution settings as described in Afandi et al. (2018).

The stock standard solution was prepared gravimetrically from primary standards. An external 6-point standard curve was prepared by serial dilution and analyzed at the beginning, middle and end of each run. We used indium (In) as an internal standard ($\sim 1\ \mu g\ L^{-1}$, as run in the final solution) for all samples, standards and blank solutions. Final concentrations of samples and procedural blanks were calculated from In-normalized data. All results were expressed in $\mu g\ g^{-1}$ dry weight (dw). Precision was estimated through replicated samples (every 10th sample was a replica) and was better than 10% in all cases. A quality control program was performed, including treatment and analysis of Certified Reference Material (the CRM was fish protein DORM-4 from the National Research Council, Canada) (Table 1) and blanks with the samples.

Table 1 Limit of quantification and accuracy of standard (DORM-4) analyzed according to the procedure used for zooplankton metal analysis (μg g^{-1}dw).

CRM Dorm-4	Li	Cd	Cu	Mn	Cr	Co	Fe	Pb	Sr	As	Ni	Zn	U
LQ	5.40 10^{-04}	1.20 10^{-04}	3.03 10^{-03}	9.30 10^{-04}	3.80 10^{-04}	8.10 10^{-05}	0.173	2.99 10^{-03}	4.80 10^{-03}	1.50 10^{-04}	6.54 10^{-03}	4.20 10^{-03}	2.22 10^{-04}
Assigned value	—	0.306 ± 0.015	15.9 ± 0.9	—	1.87 ± 0.16	—	341 ± 27	0.416 ± 0.053	—	6.80 ± 0.64	1.36 ± 0.22	52.2 ± 3.2	—
Measured value	1.09	0.32 ± 0.013	15.93 ± 0.25	2.88	1.86 ± 0.026	0.263	357.58 ± 15.10	0.37 ± 0.017	9.275	6.86 ± 0.06	1.25 ± 0.046	49.61 ± 2.48	0.034

2.4. Statistical procedures

All data were subjected to statistical analysis. One-way analysis of variance (ANOVA) was used to determine the significant differences in metal levels during the two cruises in the three areas, by radials, by day/night and by inshore/offshore. All statistical calculations were performed with XLSTAT for Windows (Version 2015.1.03.15945). Statistical significance was defined at 95% ($p < 0.05$). A Principle Component Analysis (PCA) is performed on standardized data, which is intended to classify the different groups of metals with the same origin.

3. Results

The vertical distribution of physico-chemical parameters along the nine inshore-offshore sections was explained by Waeles et al. (2016), with strong upwelling signatures observed in the northern and southern areas; in the central area, biological activity was less intense, as reflected in the fluorescence concentrations.

Zooplankton collections were examined to determine the biological composition. Copepods were the most dominant (60—98%), and their composition was dominated by *Acartia*, *Centropages*, *Euterpina*, *Oncaea* and *Paracalamus* species in summer and autumn seasons from all nine transect stations. Total density was considerably higher in the south than in the north, with minor variations between day and night. The highest total density was at Station 27 level 5 (night), with 18,158 ind m^{-3} in contrast with total biomass with the highest value at Station 22 level 5 (day), while the lowest density was recorded at Station 15 level 5 (night) with a total density of 10.66 ind m^{-3} and lower total biomass in the same station 15 level 2 (day).

3.1. Metal distribution and concentrations in zooplankton

In the present study, the mean metal concentrations in total zooplankton are given in Tables 2 and 3. The average metal concentrations in the analyzed zooplankton samples were arranged in the following order: Sr > Fe > Zn > Ba > Li > Mn > Cr > As > Cu > Cd > Ni > Pb > Co > U. However, it should be noted that the metal ranges were extremely large (Table 2 and 3). According to the metal concentration in zooplankton, the metals were divided into four classes: (Sr, Fe); (Zn, Li, Ba, Cr and Mn); (As, Cu, Cd, Ni and Pb), and the fourth subgroup included redox-sensitive elements (Co and U). Strontium showed the highest concentration, ranging from 84 to 63887 μg g^{-1} dw. The concentrations of metals in the second and third classes of elements ranged from 0.36—566 μg g^{-1} dw and 0.17—45 μg g^{-1} dw, respectively. The values of the fourth-class elements ranged from 0.08—1.84 μg g^{-1} dw.

By separating the data into various categories, such as diurnal vs. nocturnal samples, by cruise, or by sample location, some noticeable trends were observable (Table 2 and 3). The metal spatial distribution in zooplankton samples showed some particular patterns. ANOVA indicated a significant variation in the metal concentrations in zooplankton between the northern, central and southern zones

Table 2 Concentrations of Li, Cr, Mn, Fe, Co and Ni (in $\mu g\ g^{-1}$ dry weight) determined in zooplankton, reported per season (summer vs. autumn), per sampling zone (north, center or south) and per time (day vs. night). Values are mean ± standard deviation (SD). *N*=number of samples.

Samples	Li	Cr	Mn	Fe	Co	Ni
Mean±SD	15.66 ±43.58	10.25 ±18.31	12.31 ±17.64	1126 ±1169	0.60 ±0.30	5.22 ±8.21
(Min-Max) N=113	0.50–353.09	0.36–101.15	1.64–99.15	84.23–5095	0.12–1.84	0.46–45.02
Summer N=57	$15.70^{a} \pm 47.73$	$6.04^{b} \pm 7.08$	$6.80^{b} \pm 4.31$	$895^{b} \pm 847$	$0.57^{a} \pm 0.31$	$3.00^{b} \pm 3.90$
Autumn N=54	$15.61^{a} \pm 39.00$	$14.86^{a} \pm 24.74$	$18.22^{a} \pm 23.85$	$1379^{a} \pm 1406$	$0.63^{a} \pm 0.28$	$7.64^{a} \pm 10.69$
North N=38	$12.95^{ab} \pm 27.99$	$3.72^{a} \pm 5.30$	$6.88^{b} \pm 3.28$	$611.43^{b} \pm 434.35$	$0.70^{a} \pm 0.33$	$3.05^{b} \pm 3.98$
Center N=30	$32.37^{a} \pm 74.48$	$8.86^{b} \pm 7.85$	$10.39^{b} \pm 6.91$	$1328.18^{b} \pm 1156.44$	$0.58^{ab} \pm 0.23$	$4.16^{ab} \pm 2.95$
South N=44	$62.30^{b} \pm 253.46$	$19.08^{b} \pm 28.28$	$20.25^{a} \pm 28.07$	$1575.47^{a} \pm 1516.23$	$0.49^{b} \pm 0.26$	$8.62^{a} \pm 12.64$
Day N=76	$45.96^{a} \pm 185.22$	$11.04^{a} \pm 18.11$	$12.75^{a} \pm 17.07$	$1154.72^{a} \pm 1146.27$	$0.6^{a} \pm 0.28$	$5.58^{a} \pm 8.3$
Night N=37	$11.59^{a} \pm 23.73$	$8.63^{a} \pm 18.85$	$11.41^{a} \pm 18.96$	$1066.72^{a} \pm 1227.31$	$0.59^{a} \pm 0.32$	$4.48^{a} \pm 8.07$

The mean metal concentrations of different species from all sites sharing a common letter (a, b or ab) for a particular metal are not significantly different, $p < 0.05$.

(ANOVA, $p > 0.05$) (Tables 2 and 3), except for Zn, Sr and Ba. Therefore, we found increases from north to south in the concentrations of Cr, Mn, Fe, Ni, Cu and Pb and a decrease in Co. However, the concentration of Cd was lower in the central zone, whereas the concentrations of Li, As and U were higher.

The results showed that during both the summer and autumn seasons, no significant differences were observed for Li, Co, Cu, Cd, Pb and U concentrations; however, during autumn, we detected relatively high concentrations of Cr, Mn, Fe, Ni and As, whereas the lowest concentrations were recorded for Zn, Sr and Ba (Table 2 and 3).

Statistically significant spatial variations (by transect) were observed among all metal variables, except for Zn, Cd and Li. Transects I and H formed a group with generally noticeable concentrations of Cr, Mn, Fe, Ni, Cu, Sr, Ba and Pb (Figure 2).

However, no significant differences were found between diurnal and nocturnal zooplankton samples ($p > 0.05$). Furthermore, metal concentrations were not significantly different near the coast in comparison with offshore and were not different between surface and deep areas, except for Sr and U.

3.2. Statistical analysis

The results of metals in zooplankton also indicated the same relative origins between some metals. This was confirmed by statistical analysis (PCA) (Figure 3), which showed a very good correlation between Sr and Ba in Group I and a low correlation between Zn and Pb in group II, while Cu, Fe, Cr, Mn, and Ni formed a clustered group III on the right, and Li, Cd, U, As and Co formed a loose group IV on the left, with negative correlations between Cd and other metals, possibly indicating a different source.

4. Discussion

4.1. Essential metal elements in zooplankton

The assessment of metal concentrations in zooplankton is very important, because they are the main diet for many predators and may contribute to transferring a variety of metals to higher trophic levels. As mentioned, this is the first study on the levels of metals in zooplankton in the south Atlantic region of Morocco (North Atlantic). Also, in this area, metal concentrations in sediments are comparable with uncontaminated sediments (Maanan et al., 2015). The absence of previous studies on the composition of metallic elements in zooplankton in the study region complicates the interpretation of our results. Indeed, published zooplankton data on some elements, such as Sr, Li, As, Mn, Fe, U, Co and Ba, are very scarce.

According to results revealed by the principal component analysis in Figure 3, the first group (G-I) contained Sr at a higher concentration, it correlates with Ba. Sr is the fifth most abundant cation after Na^{+}, Mg^{2+}, Ca^{2+} and K^{+}. Strontium is especially used in the reconstruction of environmental history (Fang et al., 2014), it is used as a chemical tracer for oceanic circulation. Related results were reported by Rentería-Cano et al. (2011), with high concentrations of Sr (105–15,450 $\mu g\ g^{-1}$ dw) on zooplankton sampled from the northern Gulf of California, while Fang et al. (2014) in northeastern Taiwan reported an average of 370 $\mu g\ g^{-1}$ dw, with a range of 121–777 $\mu g\ g^{-1}$ dw. This element was followed by iron (Fe), which is an essential micronutrient for the biological requirements of all marine organisms. The high levels of Fe can be attributed to its direct adsorption by zooplankton in seawater or indirect absorption by a digestion of phytoplankton, which metabolize it by photosynthesis (Ho et al., 2003; Rentería-Cano et al., 2011). The Fe concentrations were comparable to those reported by Pempkowiak et al. (2006) from the southern Baltic and by Fang et al. (2014) but higher than those reported by Ben Salem and Ayadi (2017) and Battuello et al. (2016), respectively, on the southern and northern Mediterranean coasts.

Zinc is one of the most important micronutrients, with higher levels in zooplankton than in pelagic fish (Afandi et al., 2018), reflecting the presence of Zn in the marine environment. Furthermore, according to Eisler (1993), nutrition is the main source of Zn for aquatic organisms, and it is significantly more essential than Zn uptake from seawater. Additionally, depending on Paimpillil et al. (2010), this higher concentration may be

Table 3 Concentrations of Cu, Zn, As, Sr, Cd, Sr, Cd, Ba, Pb and U (in μg g^{-1} dry weight) determined in zooplankton, reported per season (summer vs. autumn), per sampling zone (north, center or south) and per time (day vs. night). Values are mean ± standard deviation (SD). *N*=number of samples. The mean metal concentrations of different species from all sites sharing a common letter (a, b or ab) for a particular metal are not significantly different, $p < 0.05$.

Samples	Cu	Zn	As	Sr	Cd	Ba	Pb	U
Mean ± SD	7.32 ±3.35	106.05± 85.57	7.47 ±3.91	6034 ± 10451	6.97 ± 2.72	17.37 ± 20.96	1.31 ±1.58	0.26 ± 0.11
(Min-Max) N=113	1.62–21.75	23.17–566.09	2.05–25.21	147.93–63887	0.86–12.91	0.91–111.05	0.17–9.86	0.08–0.69
Summer N=57	7.58^{a} ± 4.15	126.68^{a} ± 89.79	6.10^{b} ±2.12	8107^{a} ±13129	7.34^{a} ± 3.01	21.50^{a} ± 25.50	1.55^{a} ± 2.02	0.25^{a} ± 0.12
Autumn N=54	7.03^{a} ± 2.15	83.90 ^{b}± 75.48	8.97 ^{a}± 4.79	3806^{b} ± 3795	6.56^{a} ± 2.33	12.94^{b} ± 13.49	1.05^{a} ± 0.83	0.27^{a} ± 0.11
North N=38	6.41^{b}±3.05	102.74^{a}±100.24	6.90^{b}±2.10	7081.99^{a} ± 19096.94	7.39^{a}±2.38	21.11^{a} ± 43.62	0.81^{b}±0.97	0.22^{b}±0.10
Center N=30	7.50^{ab}±4.04	255.40^{a}±841.89	10.79^{a}±5.71	5008.39^{a} ±10777.58	5.93^{b}± 3.00	14.85^{a} ± 21.01	1.51^{ab}±1.98	0.35^{a}±0.13
South N=44	8.26^{a}±2.85	112.92^{a}±78.72	5.54^{b}±1.50	8818.87^{a} ± 14029.17	7.28^{a}±2.74	22.20^{a} ± 26.79	1.75^{a}±1.68	0.24^{b}±0.07
Day N=76	7.5^{a} ± 3.46	173.72^{a} ±535.34	7.49^{a} ± 3.56	8017.57^{a} ± 17971.79	6.83^{a} ± 2.56	21.61^{a} ± 38.35	1.45^{a} ± 1.82	0.26^{a} ± 0.1
Night N=37	6.96^{a} ± 3.1	91.16^{a} ± 36.14	7.43^{a} ± 4.59	5262.78^{a} ± 8379.98	7.24^{a} ± 3.05	16.12^{a} ±19.06	1.02^{a} ± 0.86	0.26^{a} ± 0.14

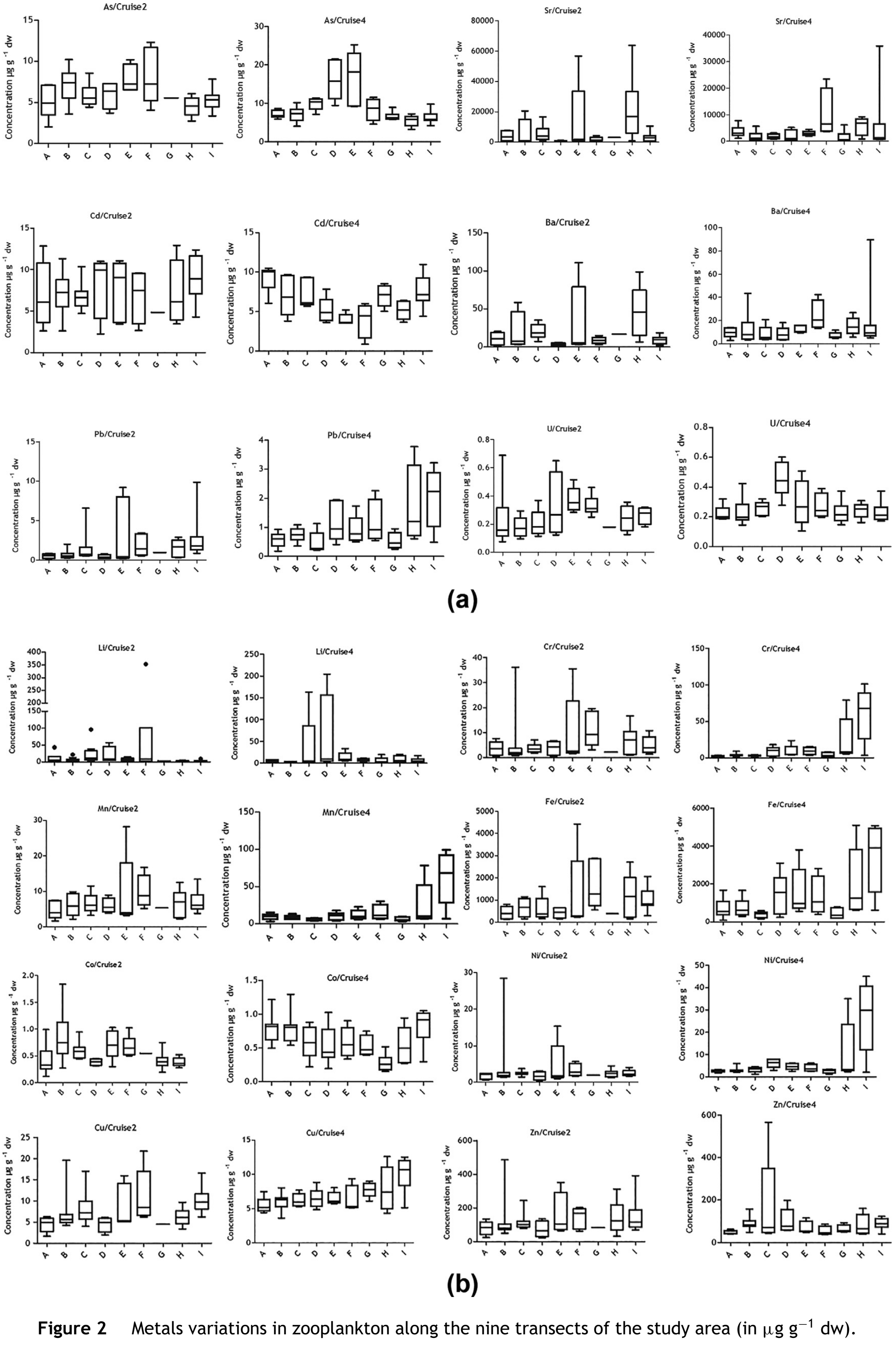

Figure 2 Metals variations in zooplankton along the nine transects of the study area (in $\mu g\ g^{-1}$ dw).

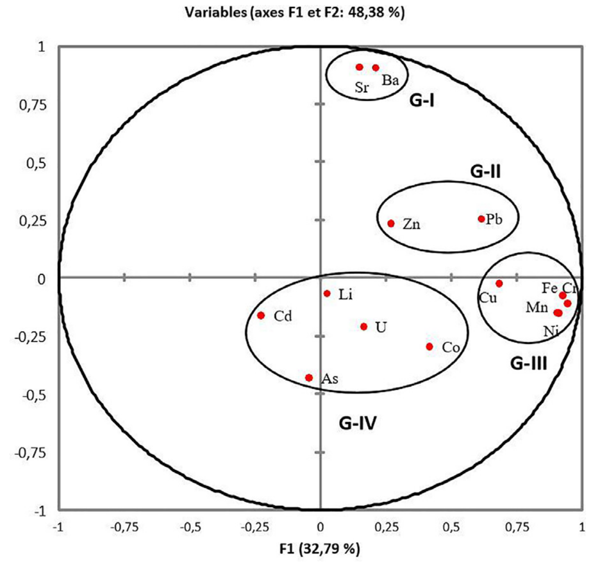

Figure 3 Principal component analysis (PCA) with different groups of metals.

due to its co-precipitation with calcium carbonate. Nevertheless, higher levels have been reported in the literature than those noted in our study (Nair et al., 1999; Pempkowiak et al., 2006; Srichandan et al., 2016).

Manganese is a naturally arising metal in seawater and can be considerably bioconcentrated by aquatic biota at lower trophic levels. In our study, the concentration of this element ranged from 1.64 to 99.15 μg g^{-1} dw. These levels were higher than those of pelagic species analyzed in the same area (Afandi et al., 2018). Similar levels were detected in previous studies, such as Fang et al. (2006) and Kahle and Zauke (2003), but they are still lower than those recorded in more contaminated marine regions, e.g., in the Bay of Bengal (Srichandan et al., 2016) and at the northern coast of Taiwan (Hsiao et al., 2011). At the same order of metal concentrations, the average level of Cr was 10.25 μg g^{-1} dw, which varied from 0.36 to 101.15 μg g^{-1} dw. Seasonally, its accumulation in zooplankton was found to be higher during autumn compared to the summer season (Table 2), this difference may be due to the development cycle of zooplankton, with a short period of reproduction at the beginning of summer and a maximum biomass in autumn (Shi et al., 2020), the same observation was recorded by Battuello et al. (2016) with lower values. However, our values of Cr are noticeably low compared to the reported values, such as Hsiao et al. (2011) and Fang et al. (2014) from Taiwan, Leonova et al. (2013) in the White Sea or Achary et al. (2020) in coastal India (Table 4).

Copper is important in the zooplankton life cycle process, including egg production and growth, and is used as a component of enzymatic activity (Paimpillil et al., 2010). Their levels in zooplankton ranged from 1.62 to 21.75 μg g^{-1} dw (Table 3) and were in accordance with those registered in other marine environments of the world in areas of low anthropogenic impact (Battuello et al., 2016; Kahle and Zauke, 2003). Ni is one of the biologically essential trace elements and has a wide distribution in terrestrial and aquatic environments. The concentration of Ni

Table 4 Metal concentrations (μg g^{-1} dry weight) in zooplankton samples from different areas.

Location	Cu	Zn	Cr	Cd	Pb	Ni	Source
Atlantic coast off Morocco	7.32 ± 3.35	106.05± 85.57	10.25 ±18.31	6.97 ± 2.72	1.31 ± 1.58	5.22 ± 8.21	Present study
	1.62—21.75	24—566	0.36—101.15	0.86—12.91	0.17—9.86	0.46—45	
Mediterranean area	1.90—39.70	14.47—132.33	—	0.05—0.41	1.01—12.38	0.85—5.48	Battuello et al. (2016)
Banc d'Arguin Mauritania	17—92	70—580	—	4—11	12—54	—	Everaarts et al. (1993)
Northeastern Taiwan (*Temora turbinate*)	8.3—180.0	5.6—825.1	7.1—188.3	1.4—141.8	0.06—85.9	2.7—954.9	Hsiao et al. (2011)
White Sea	33—142	284—643	59—620	0.4—3.2	9.1—36.4	3.2—13.4	Leonova et al. (2013)
North Sea (Atlantic ocean)	4.3—13.4	55—171	—	2.7—13.1	0.4—2.3	0.9—6.4	Haarich et al. (1993)
Weddel Sea- Antarctic (Australia)	6—52	131—682	—	2.1—14.4	0.09—1.67	2.9—18	Kahle and Zauke (2003)
Southern Baltic sea	2.33—25.42	84—1600	0.00—16.22	0.07—3.23	0.71—13.68	1.42—11.58	Pempkowiak et al. (2006)
Kalpakkam coast (India)	37.6 ± 24.3	356.8 ± 216.6	60.0 ± 43.4	2.3 ± 2.3	38.6 ± 21.8	43.4 ± 49.8	Achary et al. (2020)
	5.6—105.0	13.1—711.8	4.7—145.3	0.4—8.4	4.4—84.8	1.94—180.3	
Bombay (India)	73.8—151.8	709—1809	—	1.1—2.5	3.6—5.4	4.4—8.6	Nair et al. (1999)
Bay of Bengal (Indian ocean)	2.64—14.38	16.96—1408	—	0.76—1.50	0.22—4.16	1.50—3.10	Srichandan et al. (2016)
Arctic	4.69—36.93	84.14—366.81	1.67—13.29	0.18—4.96	1.43—15.32	2.77—16.07	Mohan et al. (2019)
Arabian Sea	1.31 ± 1.13	2.77 ± 2.25	—	0.04 ± 0.03	2.57 ± 2.66	—	Robin et al. (2012)

in the present study ranged between 0.46 and 45.02 μg g^{-1} dw, and is higher compared to the reported values, such as Battuello et al. (2016) and Ben Salem and Ayadi (2017). The highest Ni concentration is usually entering into the individual cells through the metabolic pathways, it replaces the metals of the metalloenzymes and disrupts metabolism in certain cases (Achary et al., 2020). Thus with the exception of Fe, the concentrations of metals in the group (G-III) (Figure 3) have the same range of magnitude, which could indicate the same metabolic needs for metals or the same pathways of metal ingestion and accumulation, while a high correlation could indicate a common source.

Cobalt is an important metallic element due to its association with vitamin B12. In the present study, the Co concentration in zooplankton varied from 0.12 to 1.84 μg g^{-1} dw. Our findings have shown that Co levels were similar to pelagic species analyzed in the same (Afandi et al., 2018), but lower than those detected in contaminated coastal areas (Fang et al., 2014; Rejomon et al., 2008; Rentería-Cano et al., 2011; Srichandan et al., 2016). These low values indicate that the study area is not contaminated with this metal. This element is part of the redox-sensitive element in the same subgroup (G-IV) (Figure 3) such as uranium.

Published data on minor elements such as Li and Ba, in zooplankton are very limited, the lack of previous information on these elements complicates the interpretation of our results. The concentration ranges of Ba found in the present study are in the same order of magnitude as the reported data by Fang et al. (2014).

4.2. Nonessential metal elements in zooplankton

Cadmium (Cd) is a nonessential metal with no known beneficial effects. Once it is present in the environment, it can remain for a long time and does not break down into less toxic substances. It is well known that the concentrations of Cd in seawater depend on several factors, including upwelling and biogeochemical processes such as direct uptake by living species and decomposition of organic matter. Since Cd has no significant physiological role, it is probably adsorbed on the surface of zooplanktonic debris or fecal pellets (Battuello et al., 2016; Kahle and Zauke, 2003; Paimpillil et al., 2010). In this study, Cd levels ranged from 0.86 to 12.91 μg g^{-1} dw (Table 3). These results are comparable with those reported in other marine organisms from the same area (Afandi et al., 2018; Benbrahim et al., 2006), in the upwelled water zone in Mauritania (Everaarts et al., 1993).

Lead is recognized as a nonessential metal for marine organisms, and the Pb content in the analyzed zooplankton in this study ranged from 0.17—9.86 μg g^{-1} dw. These results are higher than those reported in bivalve mollusks and pelagic fish from the same area (Afandi et al., 2018; Benbrahim et al., 2006), but they are comparable with the data reported in zooplankton (Fang et al., 2014; Pempkowiak et al., 2006). The observed high Pb levels in zooplankton in the south and center could be attributed to high influxes from mineral dust in these regions and the formation of colloids with Pb in seawater adsorbing onto planktonic debris, which can increase the concentration of this element in this species (Robin et al., 2012). Pb and Zn showed a positive correlation (Figure 3) which could be influenced by various processes such as recycling within surface waters from rapid remineralization of biological material.

The uranium contents in the present study were lower, ranging between 0.08 and 0.69 μg g^{-1} dw, while these concentrations ranged from 0.5 to 6.1 μg g^{-1} dw in the Bay of Bengal (Achary et al., 2020) and between 0.24 to 11.3 μg g^{-1} dw in the Northern Gulf of California (Rentería-Cano et al., 2011). This element causes significant toxic effects in animals and humans. According to Skwarzec et al. (2012), the contribution of marine organisms to the geochemical migration of U between seawater and bottom sediments is insignificant, but it was shown that an increase in U accumulation in reducing conditions by comparison with oxidizing conditions (Khaustova et al., 2021).

Arsenic is present in different environmental compartments at very variable concentrations. The highest levels are found in marine organisms that are capable of both accumulating and transforming this element. In zooplankton from the study area, the levels ranged from 2.05 to 25.21 μg g^{-1}. Published data noted large variations in the concentrations registered from other marine environments of the world, e.g., in the Bay of Bengal, values ranged from 2.73 to 5.73 μg g^{-1} dw (Srichandan et al., 2016), and in the Sea of Japan, values varied between 0.21 and 17 μg g^{-1} dw (Shibata et al., 1996). Furthermore, Neff (1997) reported concentrations of total arsenic in zooplankton from all over the world of 0.2—24.4 μg g^{-1} dw; these levels were in accordance with our findings. This element correlates with Cd and Co, it may indicate the same source such as upwelling and removal of surface waters by the biological pump (Figure 3) but generally, Cd may correlate with Cu and Zn in marine organisms. In our study, As and Cd doesn't correlate with other metals, while Mn, Fe, Ni, Cu, Pb, Cr and Zn discerned positive affinity and good relationship, suggesting their strong affinity and coexistence; the same observation was recorded by Srichandan et al. (2016) in contrast with Robin et al. (2012) who recorded inter-metal relationships for essential and non-essential metals.

4.3. Diverse variations in metal accumulation

Geographical variations in the concentrations of the majority of the metals studied follow the biological activity explained above, with increases in the concentrations in the north followed by the south and then the central zone. Furthermore, local upwelling may be related to increased Cd and other metal bioavailabilities in seawater, hence increasing uptake into zooplankton, as hypothesized for these regions. Additionally, despite the presence of phosphate mining activities in the south of Laâyoune, more precisely in the central zone, we did not record enrichment with Cd in this area, in contrast to the other two zones (north and south), which show evidence of permanent upwelling. Additionally, Shelley et al. (2016), in the same project EPURE, studied the metallic element compositions of aerosols at three stations (Agadir, Laâyoune, Dakhla) and quantified atmospheric deposition fluxes in the Canary Current Upwelling System; they did not observe significantly different ratios of Cd/Al between stations. Otherwise, these results correlated with those found for total dissolved Cd in the same cruises by Waeles et al. (2016), with concentrations ranging from 40 to 370 pmol l^{-1} in the northern area and from 40 to 420 pmol l^{-1} in the southern area, and lower values in the central zone varying from 10 to 210 pmol l^{-1}. Furthermore, our results are generally in agreement with those proposed by these two previous studies in terms of the origin of contamination by certain metals such as Cd, suggesting that the importance of atmospheric deposition and anthropogenic inputs of Cd has not been proven in the study area, while it is the upwelling of the North Central Atlantic Waters that mainly influences the distribution of Cd. This diversity in the southern region can be explained by the quality of the environment in this zone. Indeed, according to Robin et al. (2012), the high concentrations of metals in zooplankton at both coastal and offshore stations often coincide with high concentrations of dissolved metals; thus, elevated concentrations may be attributed to their higher availability in seawater. It can be noted, as Erasmus et al. (2021) have indicated, that factors driving the accumulation of metal elements are oceanographic process and diffuse sources, (e.g., geogenic weathering, ocean currents, upwelling, etc.) and not direct point sources of pollution.

It is well documented that the metals contained in zooplankton, especially in copepods, could vary significantly inter- and intraspecies (Hsiao et al., 2011). Hamanaka and Tsujita (1981) reported large variations in Cd concentrations in copepods, amphipods and euphosids, with a lower Cd concentration in euphosids (less than 2.2 μg g^{-1} dw) but a wide Cd range in copepods (1.66—14.55 μg g^{-1} dw), with large similarity to our results. In a more precise way, Achary et al. (2020) reported that zooplankton taxa dominated by copepods are active in accumulating metals from the background. Other reports on metal content from the marine environment determined that zooplankton are more efficient in the accumulation of metals from the environment (Rejomon et al., 2008).

The concentrations of metals in the diurnal samples were slightly higher than those in the nocturnal samples for the main metals (Li, Cr, Mn, Fe, Zn, Sr), with no significant differences. However, for Co, Ni, Cu, As, Cd, Ba, Pb and U, the concentrations were in the same order for both the diurnal and nocturnal zooplankton. These variations between groups of metals were observed by Horowitz and Presley (1977), who recorded biological variations between day and night. In fact, zooplankton are mainly transported by ambient water currents, used to avoid predators as in diel vertical migration or to increase prey encounter rate.

The vertical variation in metal accumulation in zooplankton did not represent any significant difference, except for Sr, because of its higher concentration in surface water; and U because of its lower concentration in surface water. However, some metals have profiles that are nutrient-like, such as Cd, Cu and Zn, which is indicative of their involvement in biological cycles (Waeles et al., 2016) and their strong correlation with zooplankton biomass. Fisher et al. (1991) also indicated that the storage efficiencies of Cd, Zn and Hg indicate their need to be recycled by copepods in surface waters through the organic cycle in the sea, with a direct correlation between the retention efficiency of ingested elements in copepods and the presence of the elements in the cytoplasm of the copepods' diatom food. In contrast, other metals seem to have a scavenged-type behavior, such as Pb, or behave in a conservative way, such as U; In our study, the concentrations of Pb tend to be maximal near mineral dust in the south and center area, it confirms this scavenged-type and conservative character. Then, some other metals, such as Mn, tend to be at maximum concentration level in the south, without any vertical variation, such elements can be considered hybrid-type metals, and their distribution is controlled by both biological uptake and scavenging processes (Bruland and Lohan, 2003). In general, metals with no apparent biological function would be expected to show some assimilation and therefore greater recycling, accounting for their longer residence times. Furthermore, the oceanic behavior of other metals, such as Sr and Ba, is still not well assessed, with limited data on Sr and Ba circulations in the global ocean, especially in the Southern Hemisphere (Fang et al., 2014).

The average metal concentrations in zooplankton during summer and autumn presented significant variations, with higher levels of Cr, Mn, Fe, Ni and As in autumn and higher levels of Zn, Ba and Sr during summer. These increases in metals during both seasons coincide with the presence of a strong upwelling activity, allowing for metal resuspension and making them bioavailable to biota (Larissi et al., 2013). In fact, this zone is limited in the north and south by seasonal upwelling systems with an inter-annual change. It is described as an ecological barrier for planktonic populations and frontal zone where two different water masses NACW (North Atlantic Central Waters) and SACW (South Atlantic Central Water) meet, hence its important richness (Tito de Morais, 2013). The mean concentrations of metals reported in this study (Table 2 and 3) were much higher than those previously reported in water by Waeles et al. (2016) and Afandi (2018), reflecting an efficient bioaccumulation of metals, such as demonstrated by Chevrollier et al. (2022). These differences may be associated with the large surface area of zooplankton relative to their unit mass and with their active metabolism, resulting in rapid adsorption of various metals (Battuello et al., 2016; Ravera, 2001). Moreover, it has been reported that the concentration levels of metals in plankton depend upon different biotic and abiotic factors, such as the physicochemical properties of the water, the productivity of the water body, quantitative and qualitative aspects of the plankton, the bioavailability of metals, and spatiotemporal variations (Dobaradaran et al., 2018; Elmaci et al., 2007).

A general comparison of the present data on the metal concentrations with those from various sea areas is compiled in Table 4. All the metal levels in the zooplankton samples appear to fall within a range of values that have been reported for similar organisms obtained in other areas (Everaarts et al., 1993; Rainbow, 1996; Srichandan et al., 2016). The reported patterns are also in good agreement with the data in the literature obtained from a great number of open ocean areas. The moderately increased Zn concentrations found in this study (Table 2 and 3) followed by Cu, Ni, Pb and Cd are generally in agreement with data from nearer regions, such as Banc Arguin in Mauritania (Everaarts et al., 1993), and indeed with other marine areas, such as the Antarctic, Arctic and the North Sea (Haarich et al., 1993; Kahle and Zauke, 2003; Mohan et al., 2019).

5. Conclusion

This study highlights, for the first time in the Moroccan marine environment, metal accumulation in zooplankton, and it is confirmed that this species plays a significant role in the transfer of metals to higher trophic levels due to its high bioaccumulation of most metals compared to bivalve mollusks and pelagic fish species previously studied in the same area. In the present study, the increases in metal concentrations in zooplankton from the northern zone to the southern zone, which has a very low anthropogenic influence, can be explained by the existence of cold-water upwelling, bringing nutrients and metal elements to the surface and making these elements bioavailable to marine organisms. Metals in zooplankton samples followed the order of Sr > Fe > Zn > Ba > Li > Mn > Cr > As > Cu > Cd > Ni > Pb > Co > U; there were also rather large variations in concentrations between metals and by area, the meaning of which is still poorly understood. Unfortunately, some metal concentrations found in our study were in good agreement with concentrations found in other regions that were not contaminated. The results of this study can be used as baseline data for the metal contents of zooplankton in Moroccan South Atlantic coastal water. Additionally, the results of the present study will be useful for historical evaluations by annual monitoring in the area. Finally, it is highly recommended that further studies be undertaken in the region of the southern Moroccan Atlantic coast to determine the relationship between the metal contents of zooplankton and seawater, the bioaccumulation factor (BAF) of metals in zooplankton, as well as the metal content in different species of zooplankton, to determine which method yields the most sensitive bioindicator.

Declaration of competing interest

The authors declare that they have no conflicts of interest.

Acknowledgments

We are grateful to the helpful captain and crew of the r/v *Antea* and to the engineers of the Pole Spectrometry Ocean Brest (PSO, Brest, France) for their help in running ICP—MS measurements. This work was financially supported by the French National Research Agency project ANR-11-CEPL-0005 EPURE (P.I. L. Tito de Morais) and was coordinated by teams of scientists, including Mr. A. Benhra and Mr. S. Benbrahim. We would also like to thank all teams from Marine Biological Laboratory/ INRH Casablanca and especially Mr Said Charib who provided us zooplanktonic bological data.

References

Achary, S., Panigrahi, S., Panigrahy, R., Prabhu, R., Sekar, J., Satpathy, K., 2020. Concentration factor of metals in zooplankton and their seasonality in Kalpakkam coast, southwest Bay of Bengal. Environ. Chem. Ecotox. 2, 12—23.

Afandi, I., 2018. Thèse de Doctorat «Spéciation chimique des éléments traces métalliques et leur accumulation dans les différents compartiments du milieu marin — Littoral Atlantique Marocain». Université Hassan II, Casablanca, Maroc, 212 pp.

Afandi, I., Talba, S., Benhra, A., Benbrahim, S., Chfiri, R., Labonne, M., Masski, H., Lae, R., De Morais, L., Bekkali, M., Bouthir, FZ., 2018. Trace metal distribution in pelagic fish species from the north-west African coast (Morocco). Int. Aquat. Res. 10, 191—205. https://doi.org/10.1007/s40071-018-0192-7

AOAC, 2002. Official Method 999.10, Lead, Cadmium, Zinc, Copper, and Iron in foods. Atomic adsorption spectrophotometry after microwave digestion first action, 1999 (edited in 2000 and revised in 2002). J. AOAC Int. 83, 1189.

Auger, P.A., Machu, E., Gorgues, T., Grima, N., Waeles, M., 2015. Comparative study of potential transfer of natural and anthropogenic cadmium to plankton communities in the North-West African upwelling. Sci. Total Environ. 505, 870—888.

Battuello, M., Brizio, P., Mussat S, R., Nurra, N., Pessani, D., Abete, M.C., Squadrone, S., 2016. Zooplankton from a North Western Mediterranean area as a model of metal transfer in a marine environment. Ecol. Indic. 66, 440—451.

Ben Salem, Z., Ayadi, H., 2017. First investigation of trace metal distribution in surface seawater and copepods of the south coast of Sfax (Tunisia). Environ. Sci. Pollut. Res. 24, 19662—19670. https://doi.org/10.1007/s11356-017-9536-x

Benbrahim, S., Chafik, A., Chfiri, R., Bouthir, F.Z., Siefeddine, M., Makaoui, A., 2006. Etude des facteurs influençant la répartition géographique et temporelle de la contamination des côtes atlantiques marocaines par les métaux lourds: cas du mercure, du plomb et du cadmium. Mar. Life 16, 37—47.

Bruland, K.W., Lohan, M.C., 2003. Controls of Trace Metals in Seawater. In: Elderfield, H., Ed., Treatise on Geochemistry, Elsevier Science Ltd., Cambridge.

Chelton, D.B., Deszoeke, R.A., Schlax, M.G., El Naggar, K., Siwertz, N., 1998. Geographical variability of the first baroclinic Rossby radius of deformation. J. Phys. Oceanogr. 28, 433—460.

Chevrollier, L.A., Koski, M., Sondegaard, J., Trapp, S., Aheto, D.W., Darpaah, G., Nielsen, T.G., 2022. Bioaccumulation of metals in the planktonic food web in the Gulf of Guinea. Mar. Pollut. Bull. 179. https://doi.org/10.1016/j.marpolbul.2022.113662

Dobaradaran, S., Nabipour, I., Ramavandi, B., Saeedi, R., Spitz, J., Izadi, A., Janahmadi, M., 2018. Trace metals in zooplankton from the northern Persian Gulf. Mar. Pollut. Bull. 137, 9—11. https://doi.org/10.1016/j.marpolbul.2018.10.007

Eisler, R., 1993. Zinc hazards to fish, wildlife, and invertebrates: a synoptic review. In: Cont. Haz. Rev. U.S. Department of the Interior, Fish and Wildlife Service, 1—126 Report 26.

Elmaci, A., Teksoy, A., Topac, FO., Özengin, N., 2007. Assessment of heavy metals in Lake Uluabat, Turkey. Afr. J. Biotechnol. 6 (19), 2236—2244.

Erasmus, A., Smit, N.J., Zimmermann, S., Nachev, M., Sures, B., Wepener, V., 2021. Metal and metalloid concentrations in the southern African endemic inter- and infratidal super klipfish, *Clinus superciliosus*, from the west and south coasts of South Africa. Mar. Pollut. Bull. 172, 112852.

Everaarts, J.M., Heesters, R., Fischer, C.V., 1993. Heavy metals (Cu, Zn, Pb, Cd) in sediment, zooplankton and epibenthic invertebrates from the area of the continental slope of the Banc d'Arguin (Mauritania). Hydrobiologia 258, 41—58.

Fang, TH., Hsiao, SH., Nan, FH., 2014. Nineteen trace elements in marine copepods collected from the coastal waters off northeastern Taiwan. Cont. Shelf Res. 91, 70—81.

Fang, TH., Hwang, JS., Hsiao, SH., Chen, HY., 2006. Trace metals in seawater and copepods in the the ocean outfall area off the northern Taiwan coast. Mar. Environ. Res. 61, 224—243.

Fisher, N.S., Nolan, C.V., Fowler, S.C., 1991. Assimilation of metals in marine copepods and its biogeochemical implications. Mar. Ecol. Prog. Ser. 71, 37—43.

Gaudry, A., Zeroual, S., Gaie-Levrel, F., Moskura, M., Boujrhal, F.Z., El Moursli, R.C., Delmas, R., 2007. Heavy metals pollution of the Atlantic marine environment by the Moroccan phosphate industry, as observed through their bioaccumulation in Ulva lactuca. Water Air Soil Poll. 178 (1—4), 267—285.

Haarich, M., Kienz, W., Krause, M., Schmidt, G.P.Z.D., 1993. Heavy metal distribution in different compartments of the northern North Sea and adjacent areas. Ocean Dynam. 45 (5), 313—336. https://doi.org/10.1007/BF02225884

Hamanaka, T., Tsujita, T., 1981. Cadmium and zinc concentrations in zooplankton in the Subarctic Region of the North Pacific. J. Oceanogr. Soc. Japan 37, 160—172.

Ho, T.-Y., Quigg, A., Finkel, Z.V., 2003. The elemental composition of some marine phytoplankton. J. Phycol. 39, 1145—1159.

Horowitz, A., Presley, B.J., 1977. Trace metal concentrations and partitioning in zooplankton, neuston, and benthos from the south Texas outer continental shelf. Arch. Environ. Con. 5 (2), 241—255.

Hsiao, S.H., Hwang, J.S., Fang, T.J., 2011. Copepod species and their trace metal contents in coastal northern Taiwan. J. Marine Syst. 88, 232—238.

Kahle, J., Zauke, G.-P., 2003. Trace metals in Antarctic copepods from the Weddell Sea (Antarctica). Chemosphere 51, 409—417.

Khaustova, N., Tikhomirova, Y., Korost, S., Poludetkina, E., Voropaev, A., Mironenko, M., Spasennykh, M., 2021. The Study of Uranium Accumulation in Marine Bottom Sediments: Effect of Redox Conditions at the Time of Sedimentation. Geosciences 11 (8), 332. https://doi.org/10.3390/geosciences11080332

Kucuksezgin, F., Kontas, A., Altay, O., Uluturhan, E., Darılmaz, E., 2006. Assessment of marine pollution in Izmir Bay: nutrient, heavy metal and total hydrocarbon concentrations. Environ. Int. 32, 41—51.

Larissi, J., Berraho, A., Makaoui, A., Baibai, T., Somoue, L., 2013. Impact of Inter-annual Coastal Upwelling Variability (2001—2010) on the Productivity of the Moroccan Atlantic South Area (21°—26°N). J. Mar. Biol. Oceanogr. 2 (1). https://doi.org/10.4172/2324-8661.1000107

Leonova, G.A., Bobrov, V.A., Bogush, A.A., Bychinskii, V.A., 2013. Concentration of chemical elements by zooplankton of the White Sea. Oceanology 53 (1), 54—70.

Maanan, M., Zourarah, B., Sahabi, M., Maanan, M., Le Roy, P., Mehdi, K., Salhi, F., 2015. Environmental risk assessment of the Moroccan Atlantic continental shelf: The role of the industrial and urban area. Sci. Total Environ. 511, 407—415.

Makaoui, A., Baibai, T., Agouzouk, A., Belabchir, Y., Bessa, I., Larissi, J., Idrissi, M., Ettahiri, O., Hilmi, K., 2020. Variabilité Océanographique de la zone d'El Jadida — Jorf Lasfar (Maroc). European Sci. J. ESJ 16 (27), 256—267.

Mohan, M., Treasa N, K.A., Kannan, V.M., Gopikrishna, V.G., Abdul S, M., Binish, M.B., Arunbabu, V, Rakesh, P.S., Krishnan, K.P., 2019. Metal content in zooplanktons of two Arctic fjords. Ny-Ålesund, Svalbard. Environ. Nanotech. Monit. Manage. (12) 100251. https://doi.org/10.1016/j.enmm.2019.100251

Nair, V.R., Krishnamurti, A.J., Gajbhiye, S.N., 1999. Trophic structure and levels of selected metals, in the zooplankton community of Thane-Bassein creek, Bombay. Indian J. Mar. Sci. 28, 173—183.

Neff, J.M., 1997. Ecotoxicology of arsenic in the marine environment. Environ. Toxicol. Chem. 16, 917—927.

Indian Paimpillil, J.S., Joseph, T., Rejomon, G., Gerson, V.J., 2010. Metals in coastal zooplanktons — A coastal living resource hazard. In: Varma, O.P., Rajamanickam, G.V., Wilson, E. (Eds.), Coastal Hazards. Indian Geological Congress, Roorkee-247 667 (INDIA), 199—208.

Pempkowiak, J., Walkusz-Miotk, J., Beldowski, J., Walkusz, W., 2006. Heavy metals in zooplankton from the Southern Baltic. Chemosphere 62, 1697—1708.

Rainbow, P.S., 1996. Heavy metals in aquatic invertebrates. In: Beyer, W.N., Heinz, G.A., Redmon- Norwood, A.W. (Eds.), Environmental contaminants in wildlife. Interpreting tissue concentrations. Lewis Publishers, Boca Raton, 405—425.

Ravera, O., 2001. Monitoring of the aquatic environment by species accumulator of pollutants: a review. J. Limnol. 60 (Suppl. 1), 63—78.

Rejomon, G., Balachandran, K.K., Nair, M., Joseph, T., 2008. Trace metal concentrations in marine zooplankton from the western Bay of Bengal. Appl. Ecol. Env. Res. 6 (1), 107—116.

Rentería-Cano, M.E., Sanchez-Velasco, L., Shumilin, E., Lavin, M.F., Gomez-Gutierrez, J., 2011. Major and trace elements in zooplankton from the Northern Gulf during summer. Biol. Trace Elem. Res. 142, 848—864.

Robin, R.S., Mudulli, P.R., Vishmu Vardhan, K., Ganguly, D., Abhilassh, K.R., Balasubramanian, T., 2012. Heavy metal contamination and risk assessment in the marine environment of Arabian Sea, along the southwest coast of India. Amr. J. Chem. 2 (4), 191—208.

Shelley, R.U., Sarthou, G., Tymen, G., Losno, R., Tito de Morais, L., Lae, R., Benhra, A., Bouthir, F.Z., 2016. A case study of aerosol trace element deposition to Moroccan coastal waters. 4th—6th September. 22nd European Aerosol conference, Tours, France (oral presenation).

Shi, Y., Wang, J., Zuo, T., Shan, X., Jin, X., Yuan, W., Pakhomov, E.A., 2020. Seasonal changes in Zooplankton Community Structure and Distribution Pattern in the Yellow Sea, China. Front. Mar. Sci. 7, 391. https://doi.org/10.3389/fmars.2020.00391

Shibata, Y., Sekiguchi, M., Otsuki, A., Morita, M., 1996. Arsenic Compounds in Zoo- and Phyto-plankton of Marine Origin. Appl. Organomet. Chem. 10 (9), 713—719.

Skwarzec, B., Strumińska-Parulska, D.I., Boryło, A., Kabat, K., 2012. Polonium, uranium and plutonium radionuclides in aquatic and land ecosystem of Poland. J. Environ. Sci. Heal. A 47 (3), 479—496. https://doi.org/10.1080/10934529.2012.646153

Srichandan, S., Panigrahy, R.C., Baliarsingh, S.K., Rao B, S., Pati, P., Sahu, B.K., Sahu, K.C., 2016. Distribution of trace metals in surface seawater and zooplankton of the Bay of Bengal, off Rushikulya estuary, East Coast of India. Mar. Pollut. Bull. 111 (1—2), 468—475.

Tito de Morais, L., 2013. Campagne EPURE 1, leg 2. Rapport scientifique de fin de mission. 91. https://www.iuem.univ-brest.fr/epure/figures/compte-rendu-scientifique-epure-1

Waeles, M., Planquette, H., Afandi, I., Delebecque, N., Bouthir, F.Z., Donval, A., Tito de Morais, L., 2016. Cadmium in the waters off South Morocco: Nature of particles hosting Cd and insights into the mechanisms fractionating Cd from phosphate. J. Geophys. Res.-Oceans 121, 3106—3120. https://doi.org/10.1002/2016JC011688